



HAL
open science

Study of the formation of pollutants, in particular NO_x, during the combustion of biogas and bio-oils

Suphaporn Arunthanayothin

► **To cite this version:**

Suphaporn Arunthanayothin. Study of the formation of pollutants, in particular NO_x, during the combustion of biogas and bio-oils. Engineering Sciences [physics]. Université de Lorraine, 2021. English. NNT : 2021LORR0246 . tel-03667927

HAL Id: tel-03667927

<https://hal.univ-lorraine.fr/tel-03667927>

Submitted on 23 Feb 2023

HAL is a multi-disciplinary open access archive for the deposit and dissemination of scientific research documents, whether they are published or not. The documents may come from teaching and research institutions in France or abroad, or from public or private research centers.

L'archive ouverte pluridisciplinaire **HAL**, est destinée au dépôt et à la diffusion de documents scientifiques de niveau recherche, publiés ou non, émanant des établissements d'enseignement et de recherche français ou étrangers, des laboratoires publics ou privés.



AVERTISSEMENT

Ce document est le fruit d'un long travail approuvé par le jury de soutenance et mis à disposition de l'ensemble de la communauté universitaire élargie.

Il est soumis à la propriété intellectuelle de l'auteur. Ceci implique une obligation de citation et de référencement lors de l'utilisation de ce document.

D'autre part, toute contrefaçon, plagiat, reproduction illicite encourt une poursuite pénale.

Contact : ddoc-theses-contact@univ-lorraine.fr

LIENS

Code de la Propriété Intellectuelle. articles L 122. 4

Code de la Propriété Intellectuelle. articles L 335.2- L 335.10

http://www.cfcopies.com/V2/leg/leg_droi.php

<http://www.culture.gouv.fr/culture/infos-pratiques/droits/protection.htm>



UNIVERSITÉ
DE LORRAINE

SIMPPÉ



UNIVERSITE DE LORRAINE-LRGP-ENSIC-NANCY

THESE

Presented at the University of Lorraine

École Doctorale SIMPPÉ : Sciences et Ingénierie des Molécules, des Produits,
des Procédés et de l'énergie

Laboratoire Réactions et Génie des Procédés (UMR 7274 CNRS)

For the acquisition of the grade of

DOCTEUR DE L'UNIVERSITÉ DE LORRAINE

Specialty: « Génie des Procédés, des Produits et des Molécules »

By

Suphaporn ARUNTHANAYOTHIN

**Study of the formation of pollutants, in particular NOx,
during the combustion of biogas and bio-oils**

Defended in public on December 15th, 2021

Examination board:

Jury president	Prof. C. Rousselle	PRISME, CNRS-Université Orléans, Orléans
Reviewers:	Prof. C. Rousselle	PRISME, CNRS-Université Orléans, Orléans
	Dr. G. Vanhove	PC2A, CNRS-Université de Lille, Lille
Examinators:	Prof. K. Van Geem	LCT, University of Ghent, Ghent, Belgium
	Dr. F. Battin-Leclerc	LRGP, CNRS-Université de Lorraine, Nancy
	Dr. O. Herbinet	LRGP, CNRS-Université de Lorraine, Nancy



UNIVERSITÉ
DE LORRAINE

SIMPPÉ



LABORATOIRE
RÉACTIONS
ET GÉNIE
DES PROCÉDÉS

UNIVERSITE DE LORRAINE-LRGP-ENSIC-NANCY

THESE

Présentée à l'Université de Lorraine

École Doctorale SIMPPÉ : Sciences et Ingénierie des Molécules, des Produits, des
Procédés et de l'énergie

Laboratoire Réactions et Génie des Procédés (UMR 7274 CNRS)

Pour l'obtention du grade de

DOCTEUR DE L'UNIVERSITÉ DE LORRAINE

Spécialité: « Génie des Procédés, des Produits et des Molécules »

Par

Suphaporn ARUNTHANAYOTHIN

Étude de la formation de polluants, notamment NO_x, lors de la combustion de biogaz et de bio-huiles

Soutenue publiquement le 15 décembre 2021 devant la Commission d'Examen

Membres du jury:

Présidente du jury	Prof. C. Rousselle	PRISME, CNRS-Université Orléans, Orléans
Rapporteurs:	Prof. C. Rousselle	PRISME, CNRS-Université Orléans, Orléans
	Dr. G. Vanhove	PC2A, CNRS-Université de Lille, Lille
Examineurs:	Prof. K. Van Geem	LCT, University of Ghent, Ghent, Belgium
	Dr. F. Battin-Leclerc	LRGP, CNRS-Université de Lorraine, Nancy
	Dr. O. Herbinet	LRGP, CNRS-Université de Lorraine, Nancy

Acknowledgments

This thesis was carried out within the Radical Kinetics Group of the Laboratory Reaction and Process Engineering (UMR 7274 CNRS - University of Lorraine).

This thesis would not have been possible without the support of many people. I would like to first thank the members of my thesis committee, not only for their time and extreme patience, but also for sharing their wisdom and providing their perspectives and intellectual contributions to my development as a scientist. Thanks to Christine ROUSSELLE for being a supportive and strong guiding force as Chair of my committee. Thanks also to Guillaume VANHOVE and Kevin VAN GEEM, for agreeing for reading my voluminous manuscript with great attention..

Many thanks to Olivier HERBINET, who has been an ideal teacher and my thesis director, offering advice and encouragement with a perfect blend of insight and humor. I'm proud of, and grateful for, my time working with Olivier. Thank you to my co-director, Frédérique BATTIN-LECLERC, for your patience, guidance, and support. I am extremely grateful that you helped for the scientific understanding, read my numerous revisions and continued to have faith in me over the years. Also thanks to my thesis committee members, Tiziano Faravelli and Benedicte Cuenot, who offered guidance and support. Your encouraging words and thoughtful, detailed feedback have been very important to me.

Thanks to the IMPROOF project and the CNRS-LRGP for providing me with the financial means to complete this project and for the material assistance. I would like to thank you to Tiziano Faravelli and Alessandro Stagni for their help with the kinetic modelling. Very special thanks to my teammates: Sylvain, Isma, Joseph, Nicolas, Mathilde, Rachel, Andrés, Jonathan, Zaki, Juan-Carlos, Lucia, Aleix, Ludivine, Tao, Amal, Valérie, Pierre Alexandre, René, Baptiste. Thank you also to all the PhD students, ex-PhD students, post-docs and partners at the coffee breaks, for their sympathy and warm atmosphere, as well as all those whom I did not mention and who have met my road. I would also like to thank all of my friends in France, Kanya, Tuk, Jubjang Smart, Nob, Ning Mac, Ké, Beer.

Last, but not least, my warm and heartfelt thanks go to my family for their tremendous support and hope they had given to me. Without that hope, this thesis would not have been possible. I am thankful for their unconditional love and support throughout the entire thesis process and every day.

Résumé: *Etude de la formation de polluants, en particulier de NO_x, lors de la combustion de biogaz et de bio-huiles.*

En raison de la raréfaction des combustibles fossiles et des enjeux climatiques, les technologies neutres en CO₂ doivent être basées principalement sur des sources d'énergie renouvelables et doivent se substituer progressivement aux combustibles fossiles. Le biogaz et les bio-huiles font partie des sources d'énergie renouvelables sur lesquelles se porte l'attention dans le monde entier en raison de leur utilisation directe avec peu de modifications puisque leurs propriétés sont proches de celles du gaz naturel et du pétrole. Afin d'utiliser les options technologiques les plus prometteuses, des efforts accrus au niveau de la recherche fondamentale et appliquée sont nécessaires. Cette thèse vise à mieux comprendre la formation de polluants, en particulier les NO_x lors de la combustion de biogaz et de bio-huiles à la fois par des études expérimentales et des simulations numériques. La chimie de combustion du biogaz et des bio-huiles en phase gazeuse est encore relativement méconnue. La constitution d'une base de données expérimentale comprenant l'identification des produits et intermédiaires formés permettra une meilleure compréhension des réactions chimiques mises en jeu. L'objectif sera ensuite de développer et de valider des modèles cinétiques détaillés capables de reproduire la combustion de composés modèles des biogaz et des bio-huiles. L'étude de l'oxydation et de la pyrolyse de ces composés modèles a été réalisée en utilisant à la fois un réacteur parfaitement agité et des réacteurs pistons sur une large gamme de températures (jusqu'à 2073 K). Différentes méthodes ont été mises en œuvre au cours de cette thèse afin d'analyser une large gamme de composés. Les méthodes d'analyse utilisées pour cette thèse sont la chromatographie en phase gazeuse (GC), la spectrométrie de masse en ligne (MS), l'analyse des NO_x par chimiluminescence et la spectroscopie infrarouge à transformée de Fourier (FTIR). Les composés modèles étudiés lors de cette thèse sont NH₃, NH₃/CH₄, NH₃/H₂, H₂S, H₂S/CH₄ dans le cas du biogaz et le pyrrole, l'éthylène glycol et le propylène glycol dans le cas des bio huiles. Une étude complémentaire de la formation de NO_x lors de l'oxydation de CH₄ et de l'éthylène en présence d'air a été réalisée. Pour la plupart de ces réactifs, les résultats expérimentaux ont été utilisés pour développer et valider un modèle cinétique, en particulier en collaboration avec Politecnico di Milano pour les carburants azotés et soufrés. Ces modèles ont ensuite été utilisés pour étudier les voies de décomposition des espèces étudiées.

Abstract: *Study of the formation of pollutants, in particular of NO_x, during the combustion of biogas and bio oils.*

Due to the depletion of fossil fuels and climate warnings, CO₂ neutral technologies must be based primarily on renewable energy sources and must increasingly replace fossil fuels. Biogas and bio-oils are one of the renewable energy sources that are gaining attention globally due to their direct applicability without any modification, since their properties are similar to those of natural gas and petroleum. In order to use the most promising technology options, increased efforts in basic and applied research are needed. This thesis aims at obtaining a better understanding of the formation of pollutants, in particular NO_x during biogas and biofuel combustion by means of both an experimental study and numerical simulations. The combustion chemistry of biogas and bio-oils in the gas phase is still relatively unknown. The establishment of an experimental database including the identification of the products and intermediates formed will allow a better understanding of the chemical reactions involved. The objective will then be to develop and validate detailed kinetic models able of reproducing the combustion of biogas components and bio-oil surrogates. The study of fuel oxidation and pyrolysis was carried out using both a jet-stirred reactor and flow tube reactors over a wide range of temperature conditions (up to 2073 K). Different methods were implemented during this thesis in order to analyze the large number of intermediates. The analysis methods used for this thesis are Gas Chromatography (GC), Online-Mass Spectrometry (MS), NO_x analyzer by chemiluminescence, and Fourier-Transform Infrared Spectroscopy (FTIR). The thesis allowed the study the oxidation and pyrolysis of different fuels, from biogas components (NH₃, NH₃/CH₄, NH₃/H₂, H₂S, H₂S/CH₄) to bio-oil surrogates (pyrrole, ethylene glycol, propylene glycol). The study of the formation of NO_x during the oxidation of CH₄ and ethylene in the presence of air was also investigated during my PhD. For most of these reactants, the experimental results were used to develop and validate a kinetic model, especially with Politecnico di Milano for nitrogen and sulfur containing fuels. These models were then used to study the decomposition pathways of the species studied.

RÉSUMÉ EN FRANÇAIS

La maîtrise de l'énergie a toujours joué un rôle majeur dans le développement de l'humanité et dans le développement économique, et a permis une amélioration des conditions de vie de la société. La demande croissante en énergie, l'épuisement des ressources fossiles et l'impact des émissions dues à la combustion, poussent l'Homme à adopter une démarche plus écologique et responsable. La tendance a été à l'adoption de sources d'énergie avec un contenu énergétique plus élevé, comme le passage du charbon (solide) au pétrole (liquide) et au gaz naturel (gazeux). À mesure que la population humaine croît sur terre, les ressources deviennent de plus en plus des denrées précieuses. La croissance démographique incontrôlée est devenue un véritable enjeu ; elle entraîne non seulement une demande plus importante en énergie mais aussi des problèmes environnementaux. La forte demande en énergie contribue à la déforestation, au réchauffement climatique et à d'autres problèmes environnementaux, tels que la pollution et les pluies acides.

De nos jours à 2040, la part des énergies fossiles dans la demande mondiale d'énergie primaire restera supérieure à 80 %. La demande pour toutes les sources d'énergie, à l'exception du charbon, continue d'augmenter comme le montre la Figure 1.

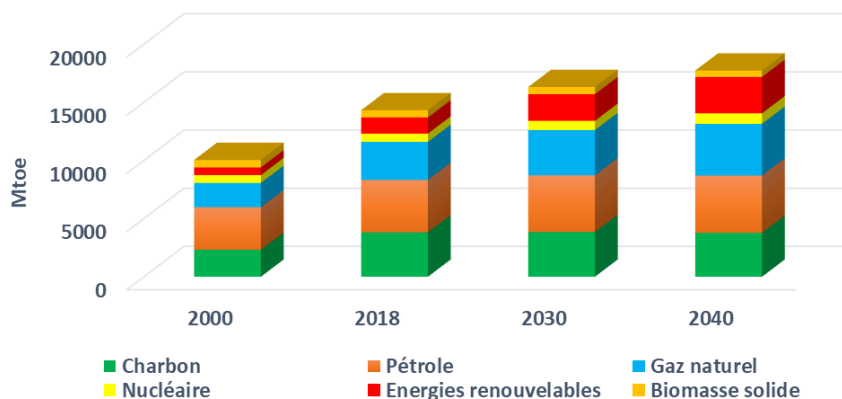
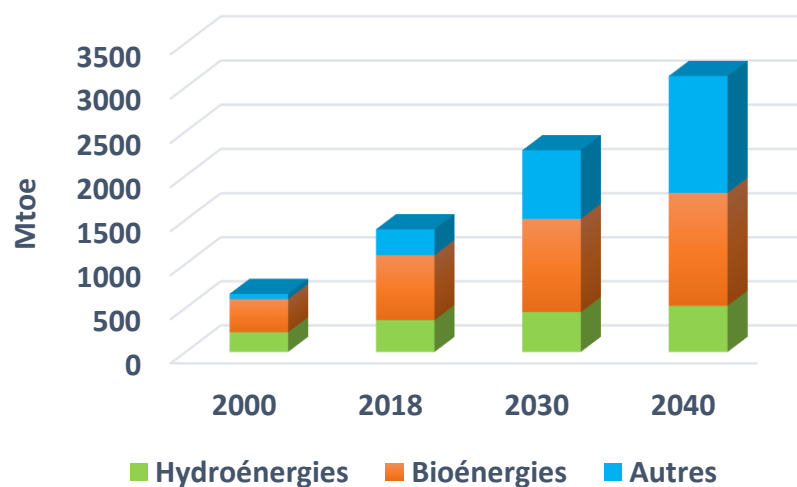


Figure 1 : Demande mondiale totale d'énergie primaire par source au fil des ans en Mtoe (IEA, 2019a).

Le charbon a un impact énorme sur la pollution de l'environnement car sa production implique de fortes émissions de gaz à effet de serre (RTE-France, 2021). En 2021, les émissions de CO₂ par MWh produit en France des centrales au charbon représentent 0,986 tonne de CO₂, alors que les usines de biocarburants émettent 50% de CO₂ en moins (0,494 tonne de CO₂). Ainsi, la demande en charbon en 2040 sera légèrement inférieure à son niveau d'aujourd'hui, et sa part dans le mix primaire sera dépassée par le gaz vers 2030. La demande en gaz augmente de 35%, l'utilisation

industrielle du gaz augmentant deux fois plus vite que celle du gaz pour la production d'énergie. De plus, d'après les prévisions, les sources à faible émission de carbone représenteront plus de la moitié de l'augmentation de la demande jusqu'en 2040. Parmi elles, les énergies renouvelables dominent.

En théorie, les énergies renouvelables ne s'épuiseront jamais car elles peuvent se régénérer, ce qui en font une ressource naturelle durable et abondante. Elles produisent un minimum de CO₂ et de déchets. Cependant, il est aujourd'hui difficile de produire autant d'énergie que celles tirées des sources non renouvelables et des conditions météorologiques peu fiables peuvent également entraver l'approvisionnement en énergie. Les énergies renouvelables vont voir leur capacité augmenter dans les prochaines années selon l'AIE (IEA, 2019a) comme le montre la [Figure 2](#). La source principale est la bioénergie qui correspond à l'énergie générée par la conversion de produits solides, liquides et gazeux dérivés de la biomasse. La bioénergie moderne fait référence à l'utilisation de la biomasse parallèlement aux technologies de chauffage modernes, à la production d'électricité et aux carburants de transport, par opposition aux méthodes traditionnelles de chauffage au bois couramment utilisées pour le chauffage et la cuisson dans les pays en développement. Sa part dans le mix énergétique devrait croître dans les années à venir en raison de sa disponibilité immédiate et des enjeux climatiques. La deuxième source d'énergie renouvelable est l'hydroélectricité, mais elle augmente lentement et les potentialités sont quasiment toutes déjà exploitées.



*Figure 2: Source d'énergie renouvelable en Mtoe au fil des ans (IEA, 2019a).
Remarques : autres comprennent l'énergie éolienne, solaire photovoltaïque, géothermique, solaire à concentration et marine.*

La biomasse est classée comme source d'énergie renouvelable au niveau des cadres juridiques de l'UE et de l'ONU, bien que la combustion de la biomasse d'origine végétale libère du CO₂, car la photosynthèse recycle ce CO₂ au travers de nouvelles cultures. Ce cycle du CO₂ des plantes vers l'atmosphère et de nouveau dans les plantes peut même avoir un bilan négatif en CO₂, car une partie relativement importante du CO₂ est déplacée vers le sol au cours de chaque cycle. La biomasse peut être brûlée directement ou convertie en biocarburants liquides, en bio-huiles ou en biogaz qui peuvent être brûlés comme carburants.

Le biogaz est principalement produit par le procédé de digestion anaérobie (DA) de la biomasse, dont le principe est illustré à la [Figure 3](#). La composition du biogaz dépend de la source de biomasse. Il est principalement composé de méthane et de dioxyde de carbone, contient de plus petites quantités de sulfure d'hydrogène et d'ammoniac et est normalement saturé de vapeur d'eau.

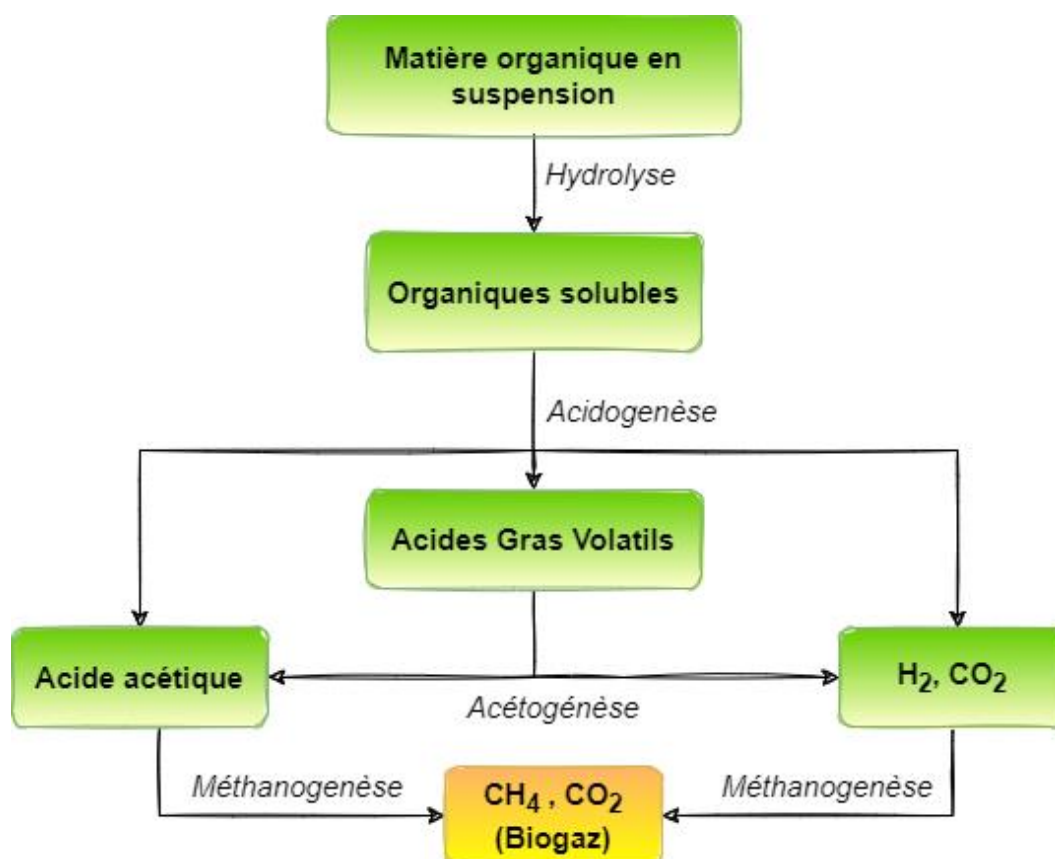


Figure 3: Étapes successives du procédé de digestion anaérobie pour la production du biogaz (Appels et al., 2008)

Le processus de digestion anaérobie conduit à la production de biogaz. Les matières organiques sont d'abord hydrolysées en composés organiques solubles tels

que les acides aminés, les acides gras et les sucres. Ensuite, en fonction des différents types de micro-organismes présents, ces composés organiques solubles sont transformés en produits intermédiaires tels que les alcools et les acides gras (acidogénèse). Lors de l'étape suivante, les produits intermédiaires sont utilisés par les acétogènes pour former du H₂, du CO₂ et de l'acétate (acétogénèse). Enfin, les méthanogènes consomment principalement du CO₂, du H₂ et de l'acétate pour produire du méthane et du CO₂ comme produits finaux métaboliques (méthanogénèse).

La biomasse peut être convertie en bio-huile par deux voies principales : la pyrolyse rapide et la liquéfaction hydrothermale. La pyrolyse rapide implique la décomposition thermique rapide de composés organiques en l'absence d'oxygène pour produire des liquides, des gaz et du charbon (Voir [Figure 4](#)). La pyrolyse rapide est réalisée à un temps de séjour du gaz court (1 s), à la pression atmosphérique et à une température relativement élevée (450–500 °C). Le séchage de la matière première est nécessaire. La teneur en humidité de la charge est très importante pour le processus de pyrolyse, qui devrait être d'environ 10 %. Ce procédé fournit un rendement d'huile élevé jusqu'à 80 % de la matière première sèche. Cependant, les huiles obtenues sont corrosives, et elles possèdent des teneurs en oxygène et en humidité beaucoup plus élevées et un contenu énergétique inférieur, par rapport aux huiles d'origine fossile.

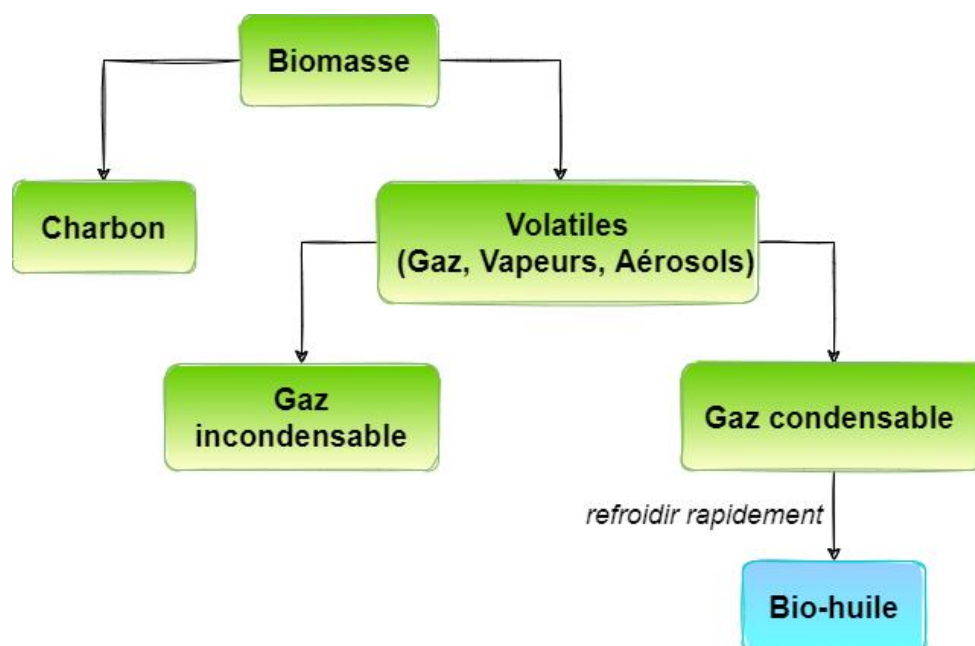


Figure 4: Processus de pyrolyse rapide de la biomasse pour la production de bio-huile.

Cette thèse a été réalisée en partie dans le cadre du projet européen IMPROOF (2016-2020) (CERFACS, 2020) visant à améliorer l'efficacité énergétique des fours de vapocraquage en développant de nouvelles technologies et en utilisant un revêtement à haute émissivité. Le biogaz et les bio-huiles ont été étudiés pour être utilisés comme carburants alternatifs pour alimenter les fours de vapocraquage.

Afin de promouvoir le développement de nouveaux types de fours de vapocraquage proposés dans le projet IMPROOF, cette thèse vise à mieux comprendre la formation de polluants, en particulier les NO_x lors de la combustion de biogaz et de bio-huiles au moyen d'une étude expérimentale combinée à des simulations numériques. La chimie de combustion du biogaz et des bio-huiles en phase gazeuse est encore relativement méconnue. La constitution d'une base de données expérimentale comprenant l'identification des produits et intermédiaires formés permettra une meilleure compréhension des réactions chimiques mises en jeu. L'objectif sera ensuite de développer et de valider des modèles cinétiques détaillés capables de reproduire la combustion de composés modèles des biogaz et des bio-huiles. L'étude expérimentale de l'oxydation et de la pyrolyse de ces composés modèles a été réalisée en utilisant à la fois un réacteur parfaitement agité et des réacteurs tubulaires sur une large gamme de températures (jusqu'à 2073 K). Différentes méthodes ont été mises en œuvre au cours de cette thèse afin d'analyser une large gamme de composés. Les méthodes d'analyse utilisées pour cette thèse sont la chromatographie en phase gazeuse (GC), la spectrométrie de masse en ligne (MS), l'analyse des NO_x par chimiluminescence et la spectroscopie infrarouge à transformée de Fourier (FTIR). Les composés modèles étudiés lors de cette thèse sont NH₃, NH₃/CH₄, NH₃/H₂, H₂S, H₂S/CH₄ dans le cas du biogaz et le pyrrole, l'éthylène glycol et le propylène glycol dans le cas des bio huiles. Une étude complémentaire de la formation de NO_x lors de l'oxydation de CH₄ et de l'éthylène en présence d'air a été réalisée. Pour la plupart de ces réactifs, les résultats expérimentaux ont été utilisés pour développer et valider un modèle cinétique, en collaboration avec Politecnico di Milano (partenaire du projet européen Improof) pour les carburants azotés et soufrés. Ces modèles ont ensuite été utilisés pour étudier les voies de décomposition des espèces étudiées. Le [Tableau 1](#) résume la liste des carburants étudiés et les conditions expérimentales associées.

Tableau 1: sommaire des carburants étudiés et des conditions expérimentales associées.

Réactifs	Expériences	$x_{fioul}^{entrée}$ (ppm)	T (K)	P(MPa)	τ (s)	ϕ	Réacteurs
Etude de l'oxydation des substituts du biogaz							
NH ₃	Pyrolyse	1000	1373-1873	0,113	0,25	∞	RP1
	Oxydation	1000	1073-1973	0,127	0,05	0,375	RP1
NH ₃ +CH ₄	Oxydation	1000 (both fuels)	1223-1973	0,127	0,025	1	RP1
		NH ₃ : 500 CH ₄ : 12 000	500-1200	0,107	1,5	0,5,1,2	RPA
NH ₃ +H ₂	Oxydation	NH ₃ : 1,000 H ₂ : 0-2003	873-1773	0,127	0,05	1	RP1
H ₂ S	Pyrolyse	500	600-1200	0,107	2	∞	RPA
		500	973-1923	0,123	0,25		RP1
		500	900-1600	0,107	2		RP2
	Oxydation	500	400-1200	0,107	2	0,009-0,25	RPA
		500	673-1423	0,127	0,1, 0,25	0,1, 0,25	RP1
		500	400-1200	0,107	2	0,25	RP2
H ₂ S+CH ₄	Oxydation	H ₂ S: 500 CH ₄ : 20 000	650-1200	0,107	2	0,5,1, 2	RPA
Etude de la formation des NOx							
N ₂	Oxydation	791 000	1373-2073	0,120	0,04	3,78	RP1
CH ₄		1,000	1050-2073	0,120	0,04	0,01	
C ₂ H ₄		500	973-1473	0,123	0,04	0,5, 1, 2	
Etude de l'oxydation des substituts du bio-huile							
Pyrrole	Pyrolyse	10 000	950-1200	0,107	2	∞	RPA
	Oxydation		700-1200			0,5,1, 2	
Ethylène Glycol	Pyrolyse		650-1100			∞	
	Oxydation		600-1100			0,5,1, 2	
Propylène glycol	Pyrolyse		650-1100			∞	
	Oxydation		600-1200			1	

L'étude expérimentale de l'oxydation et de la pyrolyse des composés représentatifs du biogaz et des bio-huiles a été réalisée en utilisant trois réacteurs différents, qui sont un réacteur parfaitement agité (RPA) et deux réacteurs tubulaires assimilés à des réacteurs pistons (RP), RP1 et RP2. La [Figure 5](#) présente les trois réacteurs utilisés pour chaque étude des composés modèles des combustibles.

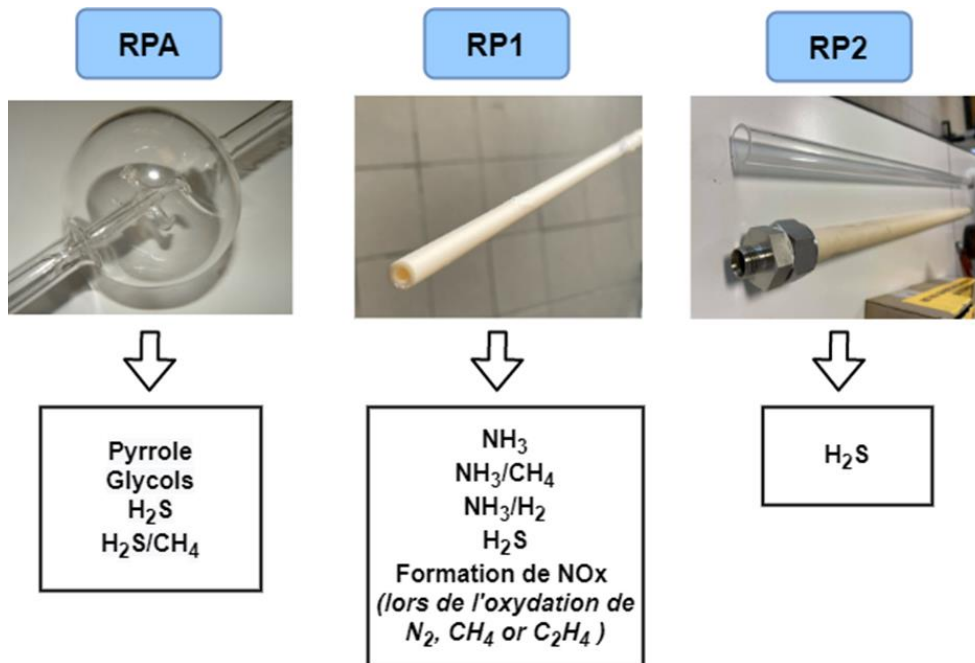


Figure 5: Réacteurs utilisés pour les études de chaque composé modèle de combustible.

Les montages expérimentaux utilisés pour l'étude de l'oxydation du biogaz et des bio huiles sont légèrement différents du fait des propriétés physico-chimiques spécifiques de ces biocarburants (état de la matière, viscosité, point d'ébullition). En particulier, le système de la chambre d'évaporation et de mélange est adapté en fonction des conditions et des combustibles à étudier. Les bio-huiles doivent être vaporisées avant d'être mélangées au gaz vecteur et à l'O₂, tandis que le biogaz peut être directement mélangé au gaz vecteur et à l'O₂.

Trois types de pilotes ont été utilisés pendant ma thèse. Le premier montage (Figure 6) consistait en un réacteur parfaitement agité alimenté par des espèces en phase gazeuse dans des conditions standard, utilisé pour réaliser les expériences de l'oxydation du biogaz à des températures allant jusqu'à 1200 K. Le deuxième type de montage utilisait un réacteur tubulaire placé dans un four. Deux géométries de tubes ont été utilisées pour les expériences. Ce type de montage a également été utilisé pour réaliser l'oxydation et la pyrolyse du biogaz à des températures plus élevées (jusqu'à 2073,15 K). Le dernier type de montage a été utilisé pour réaliser les expériences de bio-huiles à basse température dans un réacteur parfaitement agité par jets gazeux avec le système de chambre d'évaporation-mélange nécessaire pour évaporer les bio-huiles liquides. L'effet de la richesse du mélange carburant-air (ϕ) a été étudié et pour des valeurs de 0,5, 1 et 2, afin de couvrir un large éventail de conditions (des mélanges pauvres en carburant aux mélanges riches en carburant).

L'influence de la température a également été étudiée en réalisant des expériences sur une plage de températures de 650 K à 2073 K. Selon le pilote, la pression a été maintenue constante pour chaque expérience dans la gamme 0,107-0,127 MPa.

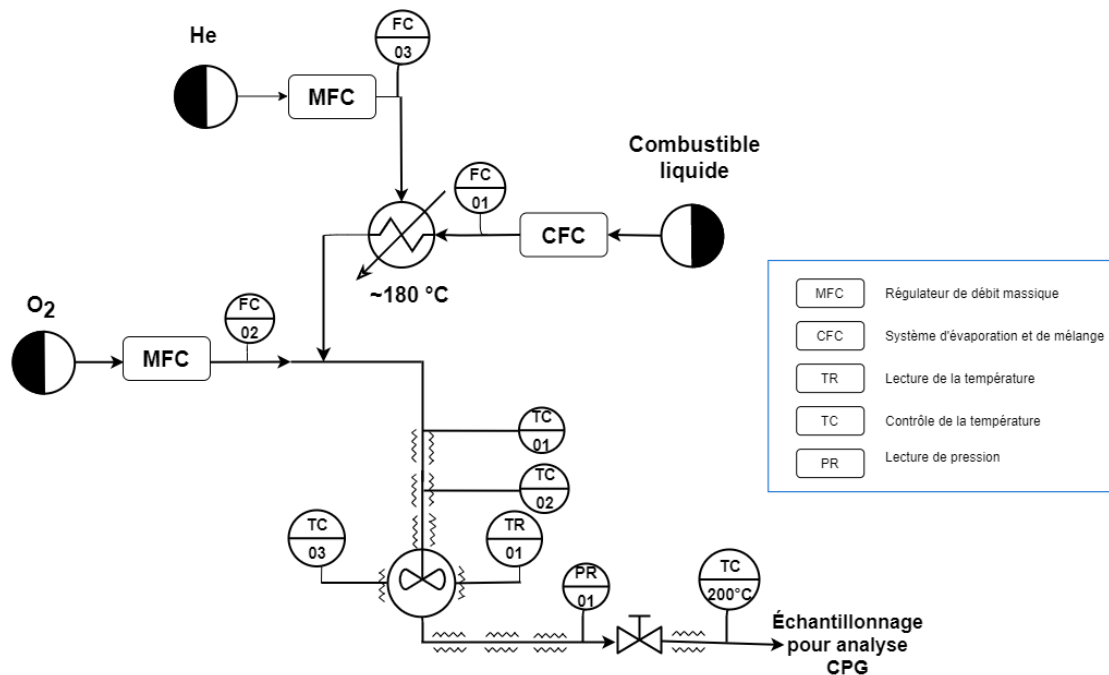


Figure 6: Montage expérimental couplé à un RPA utilisé pour les études d'oxydation des bio-huiles.

Les expériences sur l'oxydation de l'ammoniac (NH_3) et de l'hydrogène sulfuré (H_2S) ont été les plus difficiles à réaliser. Ces espèces ont la particularité de s'adsorber facilement aux parois, nécessitant la répétition des expériences et la vérification des données obtenues, ainsi que la prise de précautions particulières pour obtenir des données fiables. L'étude de la pyrolyse et de l'oxydation de l'ammoniac pur dans le RP1 a permis de mieux comprendre les réactions chimiques mises en jeu. Les modèles actuels sont relativement fiables et permettent de prédire correctement la réactivité de l'ammoniac et la formation des principaux produits stables. Des voies d'améliorations existent néanmoins pour le cas de la pyrolyse de l'ammoniac. La richesse a une influence importante sur la réactivité du système ; un mélange pauvre favorise les réactions avec l'oxygène, conduisant à une réactivité beaucoup plus importante de l'ammoniac.

Afin d'évaluer l'influence de la présence de méthane et d'hydrogène sur la chimie d'oxydation de l'ammoniac, l'oxydation de l'ammoniac en mélange avec H_2 ou CH_4 a été étudiée à l'aide du RP1. La présence de méthane n'affecte presque pas la réactivité de NH_3 (~1450-1500 K). En revanche, NH_3 favorise la réactivité du

méthane à basse température avec un rôle majeur joué par l'intermédiaire NO. Ce dernier joue un rôle important sur l'oxydation du méthane en augmentant sa réactivité, ce qui s'est traduit par décalage d'environ 100 K, en particulier dans les conditions les plus pauvres en réacteur parfaitement agité. La présence de H₂ favorise significativement la réactivité de l'ammoniac et favorise la formation de NO ; plus la proportion de H₂ dans le mélange en entrée est importante, plus la production de NO est grande.

L'oxydation du sulfure d'hydrogène pur dans les trois réacteurs a été étudiée afin de tester le comportement du modèle cinétique dans des conditions rarement explorées jusqu'alors ; à des températures relativement basses et des temps de séjour plus élevés et vice versa. Plusieurs tests ont été réalisés avec des réacteurs dont les parois ont été traitées ou pas, ce qui a permis de mettre en évidence des effets catalytiques parfois très importants. La comparaison entre les résultats expérimentaux jugés les plus fiables et les données calculées à partir du modèle donne des résultats globalement très satisfaisants, même si des voies d'amélioration sont possibles pour certains intermédiaires comme H₂. L'influence de l'ajout de H₂S sur l'oxydation du méthane en RPA a été étudiée pour mieux comprendre les interactions entre ces deux carburants. D'après les données expérimentales obtenues, l'ajout de H₂S affecte très peu la réactivité du méthane, même si un effet a été observé au travers de la formation de quantité non négligeable d'éthane à plus basse température que dans le cas de l'oxydation du méthane pur.

Les mécanismes cinétiques des réactions impliquant des composés azotés ont été largement étudiés dans la littérature. Néanmoins, à ma connaissance, les expériences de formation de NO_x thermiques ont été réalisées uniquement en flamme. Par conséquent, l'expérience réalisée au cours de ma thèse sera la première utilisant un réacteur tubulaire à haute température (jusqu'à 2073 K) pour étudier la formation de NO_x thermique. L'étude de la formation de NO_x a été réalisée en FR1 (0,12 MPa, 1350-2073 K) en utilisant trois combustibles différents ; N₂, méthane et éthylène. Deux expériences différentes d'oxydation de N₂ (sans et avec 1% d'H₂O) ont été réalisées pour mieux comprendre l'effet de l'eau sur la formation de NO_x thermique. Le NO a été détecté par la spectrométrie de masse. Il a été constaté aucune influence de H₂O sur la formation de NO. La formation de NO au cours de ces deux expériences a le même maximum de ~120 ppm à 2073 K, alors que la simulation conduit à une formation de NO_x trois fois plus élevée (340 ppm) en cas de présence

de 1% de H₂O. Le NO thermique est formé pour ~100 ppm lors de l'oxydation du méthane dans l'air, alors qu'aucun NO_x précoce n'a été observé en raison de la trop faible quantité de méthane en entrée (0,1%). Cependant, la formation de NO_x précoce a été remarquée lors de l'oxydation de l'éthylène (0,05 %) mais seulement dans le cas de conditions riches et stœchiométriques. Cette expérience doit être répétée pour mieux observer la formation de CO et de NO en utilisant respectivement le GC-Méthaniseur et l'analyseur de NO_x.

La pyrolyse et l'oxydation du pyrrole en RPA ont permis de valider le modèle cinétique du pyrrole développé par les collègues de Milan, fournissant un bon accord général. La formation importante d'hydrocarbures insaturés pose certaines questions quant à l'utilisation de bio-huile, car ces espèces favorisent la formation des oxydes d'azote et sont aussi des précurseurs de HAP et de particules.

La pyrolyse et l'oxydation de l'éthylène glycol ont été étudiées expérimentalement et théoriquement en partant du modèle cinétique proposé par Kathrotia et al. (2017). La comparaison entre les résultats expérimentaux et les données calculées a fourni un bon accord pour la réactivité du carburant mais moins pour les produits. Certaines réactions sont probablement manquantes dans le modèle (probablement certaines voies moléculaires par des mécanismes concertés). De plus, en raison de problème de condensation dans la ligne de transfert, certains produits n'ont pas pu être détectés par nos techniques analytiques, ce qui explique pourquoi le bilan en atome de carbone n'est pas aussi bon (< 60 %) que d'habitude. Dans la littérature, il existe très peu d'études expérimentales sur ce type d'espèces; par conséquent, de nouvelles études avec divers dispositifs expérimentaux sont nécessaires pour obtenir une meilleure compréhension de la chimie en phase gazeuse de ce type d'espèces. De plus, le manque d'informations sur la chimie de l'éthénol est probablement responsable de la surestimation de l'acétaldéhyde par le modèle.

L'étude expérimentale du propylène glycol a été réalisée pour comparer sa réactivité avec celle de l'EG. Les structures de ces deux molécules sont assez simples mais en fait, leur chimie a semblé beaucoup plus compliquée que ce qui était attendu. A ma connaissance, ce travail expérimental sur le PG est le premier montré dans la littérature. Le développement d'un modèle cinétique nécessitera une étude beaucoup plus approfondie de la chimie spécifique impliquée dans la cinétique en phase

gazeuse du PG à l'aide de calculs avancés comme ceux reposant sur la mécanique quantique pour explorer les surfaces d'énergie potentielle de ces systèmes spécifiques.

Ce travail a conduit à la publication de trois articles dans des journaux scientifiques internationaux à comité de lecture :

✓ Stagni, A., Cavallotti, C., Arunthanayothin, S., Song, Y., Herbinet, O., Battin-Leclerc, F., & Faravelli, T. (2020). *An experimental, theoretical and kinetic-modeling study of the gas-phase oxidation of ammonia*. Reaction Chemistry & Engineering (5), 696-711.

✓ Arunthanayothin, S., Stagni, A., Song, Y., Herbinet, O., Faravelli, T., & Battin-Leclerc, F. (2020). *Ammonia–methane interaction in jet-stirred and flow reactors: An experimental and kinetic modeling study*. Proceedings of the Combustion Institute (38), 345-353.

Pelucchi, M., Arunthanayothin, S., Song, Y., Herbinet, O., Stagni, A., Carstensen, HH., Faravelli, T., Battin-Leclerc, F., 2021. Pyrolysis and Combustion Chemistry of Pyrrole, a Reference Component for Bio-oil Surrogates: Jet-Stirred Reactor Experiments and Kinetic Modeling. Energy & Fuels 35 (9), 7265-7284.

Et à un acte de congrès:

✓ Stagni, A., Arunthanayothin, Y., Herbinet, O., Battin-Leclerc, F., & Faravelli, T. (2021). *An experimental and kinetic-modeling study of H₂S combustion in ideal reactors*, a été présenté à la 10ème réunion européenne de la combustion (ECM 2021).

TABLE OF CONTENTS

RÉSUMÉ EN FRANÇAIS	i
NOMENCLATURE	1
I. INTRODUCTION	4
I.1 Environmental and problematic context in energy	6
I.2 Alternative solution	12
I.2.1 Renewable energy	12
I.2.2 Biomass	14
<i>I.2.2.1 Biogas</i>	14
<i>I.2.2.2 Bio-oil</i>	18
I.3 Thesis objective	22
II. STATE OF THE ART ON OXIDATION OF THE MOLECULES STUDIED AS PART OF THE THESIS	27
II.1 Biogas	30
II.1.1 Ammonia.....	30
II.1.2 Methane doped with ammonia	36
II.1.3 Ammonia doped with hydrogen	43
II.1.4 Hydrogen sulfide	46
II.1.5 Methane doped with hydrogen sulfide	50
II.2 Formation of NO_x	54
II.3 Bio-Oils	59
II.3.1 Pyrrole	59
II.3.2 Ethylene glycol.....	63
II.4 Conclusion of the state of art	64
III. EXPERIMENTAL SET-UPS AND METHODS	67
III.1 Experimental set-ups	69
III.1.1 Experimental set-up for the studies of biogas components in a JSR	70
III.1.2 Experimental set-up for the studies of biogas components in a FR	71
III.1.3 Experimental set-up for the studies of bio-oil surrogates in a JSR	72
III.2 Liquid storage, flow control and evaporation system	73

III.2.1	Liquide storage and flow control.....	73
III.2.2	Evaporation and mixing system	74
III.3	Gas inlet.....	75
III.3.1	Mass Flow Controller (MFC)	75
III.3.2	Determination of the inlet gas flow rates.....	76
III.4	Reactors	79
III.4.1	Jet-Stirred Reactor	79
III.4.2	Flow Reactor (FR1)	80
a)	Calculation of the Peclet number (Pe).....	81
III.4.3	Flow Reactor (FR2)	83
III.4.4	Reactor wall treatment.....	85
III.5	Analytical methods	86
III.5.1	Gas chromatography analysis	86
III.5.2	Online Mass Spectrometry (MS).....	89
III.5.3	NOx analyzer.....	90
III.5.4	FTIR spectrometer	91
III.6	Conclusion of the experimental set-ups and methods.....	92
IV.	PYROLYSIS AND OXIDATION OF BIOGAS COMPONENTS	94
IV.1	Ammonia pyrolysis and oxidation.....	96
IV.1.2	<i>Kinetic modeling</i>	<i>97</i>
IV.1.2	<i>Experimental results</i>	<i>100</i>
IV.1.3	<i>Conclusion.....</i>	<i>103</i>
IV.2	Oxidation of methane doped with ammonia	104
IV.2.1	Experimental results	104
a)	Jet-Stirred Reactor	104
b)	Flow reactor	106
IV.2.2	Kinetic modeling.....	109
IV.2.3	Conclusion	113
IV.3	Ammonia doped with hydrogen oxidation.....	114
IV.3.1	Experimental results	115

<i>IV.3.2 Kinetic analysis</i>	117
<i>IV.3.3 Conclusion</i>	119
IV.4 Neat hydrogen sulfide pyrolysis and oxidation	120
<i>IV.4.1 Kinetic modeling</i>	120
<i>IV.4.2 Experimental results</i>	122
<i>IV.4.3 Kinetic analysis</i>	129
<i>IV.4.3 Conclusion</i>	133
IV.5 Methane doped with hydrogen sulfide oxidation	134
<i>IV.5.1 Experimental results</i>	135
<i>IV.5.2 Kinetic analysis</i>	139
<i>IV.5.3 Conclusion</i>	140
V. NO_x FORMATION AT HIGH TEMPERATURES	142
V.1 Study of the formation of NO_x from synthetic air	144
V.2 Study of the NO_x formation during the oxidation of CH₄ (in air)	146
V.3 Study of the NO_x formation during the oxidation of C₂H₄	150
V.4 Conclusion	152
VI. PYROLYSIS AND OXIDATION OF BIO-OIL SURROGATES	154
VI.1 Pyrrole pyrolysis and oxidation	156
<i>VI.1.1 Kinetic modeling</i>	156
<i>VI.1.2 Experimental results</i>	162
<i>* H and O atom balances are not significant because water was not quantified.</i>	166
<i>VI.1.3 Kinetic analysis</i>	167
<i>VI.1.4 Conclusion</i>	169
VI.2 Ethylene glycol pyrolysis and oxidation	170
<i>VI.2.1 Experimental results</i>	171
<i>VI.2.2 Conclusion</i>	176
VI.3 Propylene glycol pyrolysis and oxidation	177
<i>VI.3.1 Experimental results</i>	177
<i>VI.3.2 Comparison of PG and EG experimental results</i>	181
<i>VI.3.3 Conclusion</i>	184

VII. CONCLUSION AND PERSPECTIVES	186
VIII. COMMUNICATIONS AND PUBLICATIONS DURING THE THESIS	199
IX. REFERENCES	204
X. APPENDIX	222
X.1 Example of a calculation sheet for the determination of the initial conditions	224
X.2 Experimental data of biogas components	225
<i>X.2.1 Pyrolysis of neat ammonia in the FR1</i>	225
<i>X.2.2 Oxidation of neat ammonia</i>	226
<i>X.2.3 Oxidation of methane-ammonia</i>	228
<i>X.2.4 Oxidation of ammonia-hydrogen in the FR1</i>	231
<i>X.2.5 Oxidation of neat hydrogen in the FR1</i>	236
<i>X.2.6 Oxidation of neat hydrogen sulfide</i>	237
<i>X.2.7 Oxidation of neat H₂S in the FR</i>	238
<i>X.2.8 Pyrolysis of neat H₂S in the JSR</i> :.....	239
<i>X.2.9 Pyrolysis of neat H₂S in the FR</i> :.....	240
<i>X.2.10 Oxidation of methane-hydrogen sulfide in the JSR</i>	241
<i>X.2.11 Oxidation of neat methane in the FR: simulation of a leak of N₂ (unpublished data)</i>	244
X.3 Experimental data of the formation of NO_x	246
<i>X.3.1 Oxidation of N₂ in the FR1</i>	246
<i>X.3.2 Oxidation of CH₄ in the FR1</i>	247
<i>X.3.3 Oxidation of C₂H₄ in the FR1</i>	248
X.4 Experimental data of bio-oils surrogates	249
<i>X.4.1 Pyrolysis of pyrrole in a JSR</i>	249
<i>X.4.2 Oxidation of pyrrole in the JSR</i>	250
<i>X.4.3 Pyrolysis of ethylene glycol in the JSR</i>	255
<i>X.4.4 Oxidation of ethylene glycol in the JSR</i>	256
<i>X.4.5 Pyrolysis of propylene glycol in the JSR</i>	258
<i>X.4.6 Oxidation of propylene glycol in the JSR</i>	260

TABLE OF FIGURES

FIGURE 1 : DEMANDE MONDIALE TOTALE D'ENERGIE PRIMAIRE (STEPS) PAR SOURCE AU FIL DES ANS EN MTOE (IEA, 2019A).	III
FIGURE 2: SOURCE D'ENERGIE RENOUVELABLE EN MTOE AU FIL DES ANS (IEA, 2019A).	
REMARQUES : AUTRES COMPRENENT L'ENERGIE EOLIENNE, SOLAIRE PHOTOVOLTAÏQUE, GEOTHERMIQUE, SOLAIRE A CONCENTRATION ET MARINE.	IV
FIGURE 3: ÉTAPES SUCCESSIVES DU PROCEDE DE DIGESTION ANAEROBIE POUR LA PRODUCTION DU BIOGAZ (APPELS ET AL., 2008)	V
FIGURE 4: PROCESSUS DE PYROLYSE RAPIDE DE LA BIOMASSE POUR LA PRODUCTION DE BIO-HUILE.	VI
FIGURE 5: REACTEURS UTILISES POUR LES ETUDES DE CHAQUE COMPOSE MODELE DE COMBUSTIBLE.	IX
FIGURE 6: MONTAGE EXPERIMENTAL COUPLE A UN RPA UTILISE POUR LES ETUDES D'OXYDATION DES BIO-HUILES.	X
FIGURE 7: POPULATION GROWTH FROM 2015 TO 2100 (UNITED NATION, 2019)	6
FIGURE 8: TOTAL PRIMARY ENERGY DEMAND OVER THE YEARS BY STATED POLICIES SCENARIO (STEPS) FOR DIFFERENT COUNTRIES IN MTOE (MILLION TONS OF OIL EQUIVALENT) (IEA, 2019A).	7
FIGURE 9: WORLD TOTAL PRIMARY ENERGY DEMAND (STEPS) BY SOURCE OVER THE YEARS IN MTOE (IEA, 2019A).	8
FIGURE 10: GLOBAL CO ₂ EMISSIONS IN MILLION TONS (MT) BY SECTOR IN 2017, (ORANGE GRAPHS) AND SOURCE IN 2018 (YELLOW GRAPHS), (IEA, 2019B).	9
FIGURE 11: SO ₂ , NO _x , FINE PARTICULATE MATTER (PM _{2.5}) EMISSIONS IN MILLION TONS (MT) BY SOURCE IN 2018 (IEA, 2019A).	10
FIGURE 12: SO ₂ , NO _x , FINE PARTICULATE MATTER (PM _{2.5}) EMISSIONS IN MILLION TONS (MT) BY SECTOR IN 2018 (IEA, 2019A).	10
FIGURE 13: SOURCE OF RENEWABLE ENERGY IN MTOE OVER THE YEARS (IEA, 2019A).	NOTES:
OTHER INCLUDES WIND, SOLAR PV, GEOTHERMAL, CONCENTRATING SOLAR POWER AND MARINE.	13
FIGURE 14: SUBSEQUENT STEPS IN THE ANAEROBIC DIGESTION PROCESS (APPELS ET AL., 2008)	15
FIGURE 15: REACTION PATHWAY FOR THE BIOMASS FLASH PYROLYSIS PROCESS .	19
FIGURE 16: REACTION PATHWAY FOR THE HYDROTHERMAL LIQUEFACTION OF CELLULOSE.	20
FIGURE 17: DISTILLATION SCALE OF BIO-OIL AND OTHER LIQUID HYDROCARBON MIXTURES (FAGERNÄS, 1995; DOE EIA., 2012).	21
FIGURE 18: SURROGATES USED IN MY BIO-OIL AND BIOGAS STUDIES.	29

FIGURE 19 : LAMINAR BURNING VELOCITY OF NH ₃ /AIR FLAMES AT 0.101 MPa, (B) 298 K, (C) 448 K, DATA COMPARING WITH LITERATURE EXPERIMENTAL (POINTS ARE EXPERIMENTS AND LINES ARE SIMULATIONS). FIGURE EXTRACTED FROM HAN ET AL., 2020.	34
FIGURE 20: COMPARISON OF MEASURED UNSTRETCHED LAMINAR BURNING VELOCITY OF CH ₄ /NH ₃ /AIR FLAMES TO SIMULATED RESULTS AT (A) 0.10 MPa (B) 0.30 MPa (C) 0.50 MPa. THE MEASUREMENTS AT 0.10 MPa ARE DATA FROM OKAFOR ET AL., 2018. FIGURE DRAWN FROM OKAFOR ET AL., 2019.	38
FIGURE 21: MEASURED NH ₂ PROFILES IN THE METHANE DOPED WITH 1.05% NH ₃ AND CH ₃ NH ₂ FLAMES, AND CALCULATED PROFILES FOR THE FOUR DOPANTS (T= 600-2000 K, P= 0.001 MPa). FIGURE EXTRACTED FROM WILLIAMS AND FLEMING, 1997.	39
FIGURE 22: EXPERIMENTAL DATA AND MODELING PREDICTIONS FOR OXIDATION OF CH ₄ /NH ₃ IN FUEL-RICH CONDITIONS, UNDER 0.101 MPa. CLOSED SYMBOLS REPRESENT THE EXPERIMENTAL DATA, BALANCE IN N ₂ AND OPEN SYMBOLS FOR CO ₂ TO BALANCE. MODELING PREDICTIONS ARE SHOWN AS SOLID LINES FOR N ₂ AND DASHED LINES FOR CO ₂ . FIGURE EXTRACTED FROM MENDIARA AND GLARBORG, 2009.	42
FIGURE 23: LBV OF STOICHIOMETRIC NH ₃ /H ₂ /AIR FLAMES (P= 0.101 MPa), AS A FUNCTION OF H ₂ MOLE FRACTION, MEASURED IN THE WORKS OF HAN ET AL. (2019), KUMAR ET AL. (2013), LI ET AL. (2014) , LEE ET AL. (2010) , ICHIKAWA ET AL. (2015) , AND PREDICTED LBV USING THREE MECHANISMS. FIGURE EXTRACTED FROM HAN ET AL., 2019.	44
FIGURE 24: EFFECT OF H ₂ ADDITION ON THE IGNITION DELAY TIMES OF NH ₃ /H ₂ MIXTURES AT ϕ = 0.5 (CIRCLES) AND ϕ = 1.0 (TRIANGLES). (A) ISOBARS, (B) ISOTHERMS. FIGURE EXTRACTED FROM DAI ET AL., 2020.	46
FIGURE 25: H ₂ S (~ 800-PPM) OXIDATION UNDER OXIDIZING CONDITIONS (ϕ = ~0.285) AT 3 MPa (A) AND 10 MPa (B). EXPERIMENTAL DATA WERE OBTAINED IN A QUARTZ (BLACK SYMBOLS) AND AN ALUMINA (SMALLER RED SYMBOLS) TUBULAR REACTOR, RESPECTIVELY. MODELING PREDICTIONS ARE SHOWN AS SOLID LINES. THE DASHED LINE DENOTES PREDICTIONS OMITTING THE H ₂ S + O ₃ REACTION. FIGURE EXTRACTED FROM SONG ET AL., 2017.	48
FIGURE 26: EXPERIMENTAL RESULTS OF H ₂ S (505 PPM) OXIDATION IN A FLOW REACTOR AT 0.06 MPa FOR ϕ =0.503 (A). EXPERIMENTAL RESULTS OF H ₂ S (500PPM) OXIDATION AT 4 MPa FOR ϕ =0.485 (B). EXPERIMENTAL DATA ARE SHOWN AS SYMBOLS, MODELING PREDICTIONS AS LINES. FIGURE EXTRACTED FROM COLOM-DÍAZ ET AL., 2019.....	49
FIGURE 27 : CONCENTRATION OF H ₂ S AND SO ₂ AS FUNCTION OF TEMPERATURES. SYMBOLS REPRESENT EXPERIMENTAL CONCENTRATION, WHILE LINES DENOTE MODEL PREDICTIONS. (FIGURE RETRIEVED FROM COLOM-DÍAZ ET AL., 2021).....	49

FIGURE 28: RESULTS OF EXPERIMENTS WITH CH ₄ /H ₂ S FOR $\Phi= 1.1$ IN A FLOW REACTOR AT 5 MPa. INLET COMPOSITION: 1500 PPM CH ₄ , 3010 PPM O ₂ , 200 PPM H ₂ S; BALANCE IN N ₂ . T (s) =5920/T (K). EXPERIMENTAL DATA ARE SHOWN AS SYMBOLS, MODELING PREDICTIONS AS LINES. FIGURE EXTRACTED FROM GERSEN ET AL., 2017.	52
FIGURE 29: LAMINAR FLAME SPEED MEASUREMENTS OF NEAT CH ₄ AND 8.25% H ₂ S/CH ₄ IN 14.5% O ₂ , 85.5% AR. SOLID LINE: MODEL PREDICTION (MULVIHILL ET AL., 2019), DASH-DOT LINE: (METCALFE ET AL., 2013), DOTTED LINE: (BONGARTZ AND GHONIEM, 2015). ALSO SHOWN FOR COMPARISON IS A CH ₄ /AIR CURVE FROM (METCALFE ET AL., 2013). FIGURE EXTRACTED FROM MULVIHILL ET AL., 2019.	53
FIGURE 30: NO CONCENTRATIONS IN CH ₄ /O ₂ /N ₂ FLAMES UNDER 0.10 TO 1.42 MPa. FIGURE EXTRACTED FROM KLASSEN ET AL., 1995.	56
FIGURE 31: EXPERIMENTAL (SYMBOLS) AND MODELLED (LINES) MOLE FRACTION PROFILES OF CH AND NO IN CH ₄ (A) AND CH ₄ /C ₃ H ₈ (B) FLAMES. FIGURE EXTRACTED FROM PILLIER ET AL., 2005.	57
FIGURE 32: NO MOLE FRACTIONS AS A FUNCTION OF HEIGHT ABOVE THE BURNER SURFACE (HAB) FOR THE $\Phi= 1.28$ (TOP) AND $\Phi= 1.07$ (BOTTOM) C1–C4 ALKANE FLAMES. FIGURE EXTRACTED FROM SUTTON ET AL., 2012.	58
FIGURE 33: IGNITION DELAY TIMES FOR 0.5% PYRROLE, 350 kPa IN A SHOCK TUBE FIGURE EXTRACTED FROM MACNAMARA AND SIMMIE, 2003.	61
FIGURE 34: COMPARISON OF EXPERIMENTAL DATA WITH MODEL PREDICTIONS FOR PYRROLE UNDER DIFFERENT RESIDENCE TIMES (136/T, 251/T AND 343/T s), WITH 8 VOL% H ₂ O AND 20,000 PPM O ₂ . SYMBOLS DENOTE EXPERIMENTAL DATA AND LINES DENOTE MODEL PREDICTIONS. FIGURE EXTRACTED FROM YAMAMOTO ET AL., 2012.	62
FIGURE 35: MOLE FRACTION PROFILES OF FUEL, O ₂ , AND MAJOR PRODUCTS CO, CO ₂ , H ₂ O AND H ₂ FOR $\Phi= 1$ IN A FLOW REACTOR AS A FUNCTION OF THE RESPECTIVE OVEN TEMPERATURES. RED SYMBOLS REPRESENT EXPERIMENTAL DATA AND BLUE LINES MODELING RESULTS. FIGURE EXTRACTED FROM KATHROTIA ET AL., 2017.	64
FIGURE 36: EXPERIMENTAL SET-UP USING A JSR FOR THE STUDIES OF BIOGAS OXIDATION.	70
FIGURE 37: EXPERIMENTAL SET-UP COUPLED WITH A FR USED FOR THE STUDIES OF BIOGAS OXIDATION.	71
FIGURE 38: EXPERIMENTAL SET-UP COUPLED WITH A JSR USED FOR THE STUDIES OF BIO-OILS OXIDATION.	72
FIGURE 39: LIQUID FUEL STORAGE.	73
FIGURE 40: LIQUID FLOW REGULATION DISPLAY DURING THE START OF AN EXPERIMENT.	74
FIGURE 41: PICTURE OF CONTROLLED EVAPORATION AND MIXING (CEM) SYSTEM.	75
FIGURE 42: REACTORS USED FOR THE STUDIES OF EACH FUEL SURROGATE.	79

FIGURE 43: PICTURE OF A JET-STIRRED REACTOR.	80
FIGURE 44: OVEN USED TO HEAT FR1 IN HIGH-TEMPERATURE EXPERIMENTS.	80
FIGURE 45: TEMPERATURE PROFILES MEASURED AS A FUNCTION OF THE SET TEMPERATURE AND THE POSITION IN THE REACTOR.....	82
FIGURE 46: FUSED SILICA AND ALUMINA FLOW TUBES (FR2).	83
FIGURE 47 : OVEN USED DURING THE EXPERIMENTAL STUDIES IN A FR2.....	83
FIGURE 48: TEMPERATURE PROFILES MEASURED AS A FUNCTION OF THE SET POINT TEMPERATURE AND THE POSITION IN THE FR2 (SOURCE: VIN, 2019).....	84
FIGURE 49: PE NUMBER AS A FUNCTION OF TEMPERATURES (A) AND RESIDENCE TIMES (B) (SOURCE: VIN, 2019).	84
FIGURE 50: H ₂ S QUANTIFICATION DURING THE H ₂ S OXIDATION USING COATED AND NON-COATED JSRS. (500 PPM INLET H ₂ S, PHI = 0.25, 0.107MPa, T=2s).	85
FIGURE 51: PICTURE OF THE GC-MS USED FOR THE ANALYSIS.	87
FIGURE 52: PICTURE OF THE ONLINE MASS SPECTROMETER (A) AND MS DISPLAY DURING THE OXIDATION OF NEAT H ₂ S (500 PPM INLET H ₂ S, PHI=0.5, 0.107 MPa, T= 2 s) (B).	89
FIGURE 53: MS DISPLAY OF CATALYTIC WALL EFFECT DURING THE OXIDATION OF DIETHYL ETHER (DEE).	90
FIGURE 54: PICTURE OF THE NO _x ANALYZER.	91
FIGURE 55: PICTURE OF THE FTIR SPECTROMETER (A) AND EXAMPLE OF THE FTIR SPECTRUM (B).	91
FIGURE 56: OXIDATION OF 500 PPM OF NH ₃ WITH 2% AND 4 % OF O ₂ IN A JSR, P = 0.107 MPa. T = 1.5 s. EXPERIMENTAL DATA OBTAINED BEFORE MY PHD. BY SONG Y. (SYMBOLS). COMPUTED DATA (LINES).....	99
FIGURE 57: MOLE FRACTIONS OF NH ₃ , N ₂ AND H ₂ AS A FUNCTION OF TEMPERATURE (FR1 DATA, P= 0.113 MPa, RESIDENCE TIME OF ABOUT 250 MS).....	100
FIGURE 58: OXIDATION OF 1000 PPM NH ₃ WITH 2000 PPM O ₂ IN A FR ($\phi=0.375$). EXPERIMENTAL AND MODELING RESULTS. P = 950 TORR. AVERAGE τ IN THE REACTIVE ZONE IS 50 MS.	101
FIGURE 59: REACTION FLUX ANALYSIS IN FR AT T= 1523 K AND x= 55 CM. ARROW THICKNESS IS PROPORTIONAL TO THE REACTION FLUX.....	102
FIGURE 60: SENSITIVITY COEFFICIENTS TO NO AND N ₂ MOLE FRACTIONS IN FR CASE AT T = 1523 K – x = 58.5 CM (~100% AMMONIA CONVERSION).	103
FIGURE 61: MOLE FRACTIONS OF REACTANTS AND MAIN REACTION PRODUCTS AT DIFFERENT TEMPERATURES AND EQUIVALENCE RATIOS IN THE JSR. SYMBOLS: EXPERIMENTS. LINES: DATA COMPUTED WITH THE MODEL (DASHED LINES ARE AVERAGED MOLE FRACTIONS DUE TO OSCILLATION REGIME).....	106

FIGURE 62: MOLE FRACTIONS OF THE FUELS AND MAIN REACTION PRODUCTS RECORDED DURING THE OXIDATION OF METHANE AND AMMONIA IN THE FLOW TUBE REACTOR ($\Phi=1$). SYMBOLS: EXPERIMENTS (CLOSE SYMBOLS IN PANEL A) ARE FOR METHANE-AMMONIA CO-OXIDATION, OPEN SYMBOLS ARE FOR NEAT METHANE OXIDATION). LINES: DATA COMPUTED WITH THE MODEL.	107
FIGURE 63: A) CONSUMPTION PATHWAYS OF METHANE AND AMMONIA, AND B) SENSITIVITY ANALYSIS FOR METHANE MOLE FRACTION AT VARIABLE Φ FOR $\sim 1\%$ CH_4 CONVERSION. SENSITIVITY COEFFICIENTS ARE NORMALIZED WITH RESPECT TO THE VALUE OF $\text{H}+\text{O}_2=\text{O}+\text{OH}$ (NOT INCLUDED).	112
FIGURE 64: A) SENSITIVITY DIAGRAM FOR METHANE UNDER THE FR CONDITIONS. B) AND C) FORMATION ROUTES TO NO AND N_2 ($T = 1560 \text{ K}$, $\phi=1$, $x = 46 \text{ cm}$ (LENGTH FROM THE TUBE INLET)). THE ARROW THICKNESS IS PROPORTIONAL TO THE REACTION FLUX.	113
FIGURE 65: EVOLUTION OF THE TEMPERATURE AT MID CONVERSION AS A FUNCTION OF THE PERCENTAGE OF H_2 IN THE NH_3/H_2	115
FIGURE 66: EFFECT OF PROGRESSIVE ADDITION OF H_2 TO THE OXIDATION OF 1000 PPM NH_3 IN A FR. SYMBOLS: EXPERIMENTS. LINES: DATA COMPUTED WITH THE MODEL. $P = 0.128\text{MPa}$. THE AVERAGE RESIDENCE TIME IN THE REACTIVE ZONE IS 50 MS.	116
FIGURE 67: REACTION FLUX ANALYSIS IN FR AT TEMPERATURES OF 1073 K, 1173 K, AND 1573 K CORRESPONDING TO H_2 COMPOSITION OF 66.7% (A), 35% (B) AND 0% (C), RESPECTIVELY.	118
FIGURE 68: SENSITIVITY COEFFICIENTS TO NH_3 MOLE FRACTIONS IN FR1 CASE AT TEMPERATURES OF 1073 K, 1173 K, AND 1573 K CORRESPONDING TO H_2 COMPOSITION OF 66.7% (A), 35% (B) AND 0% (C), RESPECTIVELY.	119
FIGURE 69: SOLID SULFUR FOUND AT THE OUTLET OF FR2.	122
FIGURE 70: PYROLYSIS OF 500 PPM H_2S IN THE JSR. $P = 0.107\text{MPa}$. $\tau = 2 \text{ s}$. SYMBOLS ARE FOR EXPERIMENTS AND LINES FOR DATA COMPUTED WITH THE MODEL.	123
FIGURE 71: PYROLYSIS DATA IN FR2 ($P = 0.107\text{MPa}$, $T \sim 2 \text{ s}$, $x_{\text{FUELIN}} = 500 \text{ PPM}$). SYMBOLS ARE FOR EXPERIMENTS AND LINES FOR DATA COMPUTED WITH THE MODEL.	123
FIGURE 72: PYROLYSIS OF 500 PPM H_2S IN FR1. $P = 0.123 \text{ MPa}$. $\tau = 0.25 \text{ s}$. SYMBOLS ARE FOR EXPERIMENTS AND LINES FOR DATA COMPUTED WITH THE MODEL.	124
FIGURE 73: JSR OXIDATION DATA ($P = 800 \text{ Torr}$, $T = 2 \text{ s}$) FOR TWO CASES, $x_{\text{FUELIN}} = 500 \text{ PPM} / \phi = 0.25$, AND $x_{\text{FUELIN}} = 800 \text{ PPM} / \phi = 0.50$. THE REACTOR WALL WAS TREATED TO MINIMIZE CATALYTIC EFFECTS. SYMBOLS ARE FOR EXPERIMENTS AND LINES FOR DATA COMPUTED WITH THE MODEL.	125
FIGURE 74: OXIDATION OF 500 PPM H_2S WITH 3000, 20400 AND 40800 PPM O_2 IN JSR. $P = 0.107 \text{ MPa}$. $\tau = 2 \text{ s}$. SYMBOLS ARE FOR EXPERIMENTS AND LINES FOR DATA COMPUTED WITH THE MODEL.	126

FIGURE 75: OXIDATION OF 500 PPM H ₂ S IN FR1. P = 0.127 MPa. SYMBOLS ARE FOR EXPERIMENTS AND LINES FOR DATA COMPUTED WITH THE MODEL. SOLID LINES: $\tau = 0.25$ s, $\Phi = 0.1$. DASHED LINES: $\tau = 0.1$ s, $\Phi = 0.25$.	128
FIGURE 76: OXIDATION OF 500 PPM H ₂ S IN 0.3% O ₂ (FR2). P = 0.107 MPa, $\tau = 2$ s, $\Phi = 0.25$. SYMBOLS ARE FOR EXPERIMENTS AND LINES FOR DATA COMPUTED WITH THE MODEL.	129
FIGURE 77 : CONSUMPTION PATHWAY OF H ₂ S UNDER OXIDATIVE CONDITION AT 725 K IN JSR, P= 0.107 MPa, 500 PPM H ₂ S, 3000 PPM O ₂ , T= 2 s.	130
FIGURE 78: SENSITIVITY COEFFICIENTS TO H ₂ S MOLE FRACTION FOR H ₂ S PYROLYSIS IN JSR. T = 1200 K, P= 0.107 MPa, 500 PPM H ₂ S, T= 2 s,	131
FIGURE 79 : SENSITIVITY COEFFICIENTS TO H ₂ S MOLE FRACTION FOR H ₂ S OXIDATION IN JSR. T = 675 K, P= 0.107 MPa, 500 PPM H ₂ S, 40800 PPM O ₂ , T= 2 s.	131
FIGURE 80: SENSITIVITY (OF FUEL MOLE FRACTION TO REACTIONS) ANALYSIS OF H ₂ S OXIDATION TO RATE CONSTANTS AT T=725 K IN JSR, P= 0.107 MPa, 500 PPM H ₂ S, 3000 PPM O ₂ , T= 2 s.	132
FIGURE 81: COMPARISON OF EXPERIMENTAL RESULTS OF NH ₃ /H ₂ OXIDATION USING THE FR1 AFTER H ₂ S EXPERIMENTS (FULL SYMBOLS) AND THE NEW FR1 (HOLLOW SYMBOLS). NO WAS DETECTED BY THE MS FOR THE FIRST EXPERIMENTS AND BY THE NO _x ANALYZER FOR THE SECOND EXPERIMENT (NEW FR1).	134
FIGURE 82: OXIDATION OF 20 000 PPM CH ₄ WITH 500 PPM H ₂ S IN A JSR UNDER 0.107MPa. SYMBOLS: EXPERIMENTS. LINES: DATA COMPUTED WITH THE MODEL.	136
FIGURE 83: OXIDATION OF 20 000 PPM CH ₄ WITH 500 PPM H ₂ S IN A JSR UNDER 0.107MPa. SYMBOLS: EXPERIMENTS. LINES: DATA COMPUTED WITH THE MODEL.	137
FIGURE 84: EFFECT OF ADDITION OF 500 PPM H ₂ S TO THE OXIDATION OF 20 000 PPM CH ₄ IN JSR, O ₂ INLET MOLE FRACTION: 40 800 PPM. BLACK SYMBOLS: NEAT CH ₄ . BLUE SYMBOLS: NEAT H ₂ S. RED SYMBOLS: CH ₄ /H ₂ S.	138
FIGURE 85: CONSUMPTION PATHWAYS OF METHANE (A) AND HYDROGEN SULFIDE (B) UNDER 0.107MPa, STOICHIOMETRIC CONDITION (975K).	139
FIGURE 86: SENSITIVITY COEFFICIENTS TO CH ₄ (A) AND H ₂ S (B) MOLE FRACTIONS IN JSR AT TEMPERATURES OF 950 K, 975 K, AND 1100 K CORRESPONDING TO FUEL LEAN, STOICHIOMETRIC AND RICH CONDITIONS, RESPECTIVELY.	140
FIGURE 87: NO MOLE FRACTION PROFILES IN SYNTHETIC DRY AND HUMID AIR (1% H ₂ O ON A MOLE BASIS) UNDER 0.12 MPa, T= 0.04 s. SYMBOLS: EXPERIMENTS. LINES: DATA COMPUTED WITH THE MODEL.	146

FIGURE 88: OXIDATION OF 1000-PPM METHANE IN FR1 UNDER 0.12 MPa AND $T = 0.04$ s. COMPARISON BETWEEN EXPERIMENTAL (SYMBOLS) AND PREDICTED (LINES) MOLE FRACTION PROFILES OF FUEL, INTERMEDIATE AND PRODUCT SPECIES.	147
FIGURE 89: OXIDATION OF METHANE IN N_2 ENRICHED AIR IN FR1 BY SONG AND CO-WORKERS (PRIVATE COMMUNICATION). 1000 PPM OF METHANE, $\Phi = 0.4, 1.0$ AND 1.25 (DILUTION IN N_2), $P = 0.12$ MPa AND $T = 0.03$ s.....	148
FIGURE 90: NO FORMATION PATHWAYS DURING THE OXIDATION OF N_2 [DRY AIR (A) AND HUMID AIR (B)] AND N_2 [DRY AIR] + CH_4 (C), IN FR1 AT 2023 K. $x = 50$ CM (LENGTH FROM THE TUBE INLET).	149
FIGURE 91: SENSITIVITY COEFFICIENTS TO NO MOLE FRACTION IN FR DURING THE OXIDATION OF DRY AIR (GREEN), HUMID AIR (BLUE) AND AIR DOPED WITH CH_4 (RED) AT 2023 K. $x = 50$ CM (LENGTH FROM THE TUBE INLET).	149
FIGURE 92: OXIDATION OF 500-PPM ETHYLENE IN FR1 UNDER 0.123 MPa AND $T = 0.04$ s. COMPARISON BETWEEN EXPERIMENTAL (SYMBOLS) AND PREDICTED (LINES) MOLE FRACTION PROFILES OF REACTANTS AND PRODUCT SPECIES.	151
FIGURE 93: FORMATION PATHWAYS OF PROMPT NO DURING THE OXIDATION OF ETHYLENE FOR $\Phi = 1$ AT 1273 K. THE SIZE OF THE ARROWS IS PROPORTIONAL TO THE PERCENTAGES.	151
FIGURE 94: SENSITIVITY ANALYSIS OF NO DURING THE OXIDATION OF ETHYLENE FOR $\Phi = 1$ AT 1273 K.	152
FIGURE 95: PYROLYSIS OF PYRROLE (700 PPM LEFT PANEL, 5000 PPM RIGHT PANEL IN ARGON) IN A SINGLE PULSE SHOCK TUBE AT $P=13$ ATM AND $T = 550$ MS. COMPARISON BETWEEN EXPERIMENTAL (SYMBOLS)(MACKIE ET AL., 1991) AND PREDICTED (LINES) (PELUCCHI ET AL., 2021) MOLE FRACTION PROFILES OF INTERMEDIATE AND PRODUCT SPECIES.	161
FIGURE 96: PYROLYSIS OF ~ 10000 PPM PYRROLE IN THE JSR UNDER $P=0.107$ MPa AND $T= 2$ s. COMPARISON BETWEEN EXPERIMENTAL (SYMBOLS) AND PREDICTED (LINES) MOLE FRACTION PROFILES OF FUEL, INTERMEDIATE AND PRODUCT SPECIES	164
FIGURE 97 : MOLE FRACTION OF SPECIES FROM PYRROLE (10000 PPM AT THE INLET) OXIDATION IN JSR AS A FUNCTION OF TEMPERATURE (0.107 MPa, $T= 2$ s, $\Phi = 0.5, 1$ AND 2). SYMBOLS ARE EXPERIMENTAL DATA AND LINES SIMULATIONS.....	165
FIGURE 98 : RATE OF PRODUCTION ANALYSIS AT $T=950$ K, FOR PYRROLE OXIDATION JSR AT $\Phi=1.0$, $P=0.107$ MPa AND $T = 2.0$ s. ARROW'S WIDTH QUALITATIVELY REPRESENTS THE IMPORTANCE OF EACH REACTIVE FLUX.	168
FIGURE 99 : SENSITIVITY ANALYSIS OF FUEL CONSUMPTION TO MODEL RATE CONSTANTS AT $T=950$ K FOR THE $\Phi = 0.5, 1.0$ AND 2.0 MIXTURES. SENSITIVITY COEFFICIENTS ARE NORMALIZED OVER THAT OF $\dot{H} + O_2 \leftrightarrow \dot{O} +$	

ÓH. A NEGATIVE SENSITIVITY COEFFICIENT STANDS FOR A REACTION INCREASING REACTIVITY (I.E., CONTRIBUTING TO FUEL CONSUMPTION) AND VICE VERSA.....	168
FIGURE 100: MOLE FRACTIONS OF REACTANTS AND MAIN REACTION PRODUCTS DURING THE PYROLYSIS OF EG OVER THE TEMPERATURE RANGE 650-1100 K IN THE JSR (P = 0.107 MPa AND T = 2 s). SYMBOLS: EXPERIMENTS. LINES: DATA COMPUTED WITH THE MODEL.	172
FIGURE 101: MOLE FRACTIONS OF REACTANTS AND MAIN REACTION PRODUCTS DURING THE OXIDATION OF 10000 PPM EG IN THE JSR ($\phi = 0.5, 1$ AND $2, P = 0.107$ MPa AND $T = 2$ s) OVER THE TEMPERATURE RANGE 600-1100 K. SYMBOLS: EXPERIMENTS. LINES: DATA COMPUTED WITH THE MODEL.	174
FIGURE 102: REACTION PRODUCT SELECTIVITY ANALYSIS FOR EG PYROLYSIS AND OXIDATION (800 K FOR $\phi = 2$, 775 K FOR $\phi = 0.5$ AND 1 , AND 900K FOR $\phi = \infty$). ~50 % OF FUEL CONVERSION.	175
FIGURE 103: MOLE FRACTIONS OF REACTANTS AND MAIN REACTION PRODUCTS DURING THE PYROLYSIS AND OXIDATION OF PG OVER THE TEMPERATURE RANGE 600-1200 K IN THE JSR (P = 0.107 MPa AND T = 2 s). BLUE SYMBOLS: PYROLYSIS EXPERIMENTS. RED SYMBOLS: OXIDATION EXPERIMENTS.	178
FIGURE 104: REACTION PRODUCT SELECTIVITY ANALYSIS FOR PG PYROLYSIS AND OXIDATION (775 K FOR $\phi = \infty$ AND 825 K FOR $\phi = 1$). ~50 % OF FUEL CONVERSION.	181
FIGURE 105: MOLE FRACTIONS OF REACTANTS AND MAIN REACTION PRODUCTS DURING THE PYROLYSIS OF PG AND EG OVER THE TEMPERATURE RANGE 600-1200 K IN THE JSR ($X_{\text{FUELINLET}} = P = 0.107$ MPa AND T = 2 s). RED SYMBOLS: PG EXPERIMENTS. BLACK SYMBOLS: EG EXPERIMENTS.....	181
FIGURE 106: MOLE FRACTIONS OF REACTANTS AND MAIN REACTION PRODUCTS DURING THE OXIDATION ($\phi = 1$) OF PG AND EG OVER THE TEMPERATURE RANGE 600-1200 K IN THE JSR ($X_{\text{FUELINLET}} = 1\%$, P = 0.107 MPa AND T = 2 s). RED SYMBOLS: PG EXPERIMENTS. GREEN SYMBOLS: EG EXPERIMENTS.	183
FIGURE 107: EFFECT OF ADDITION OF 1000 PPM H ₂ AND CH ₄ TO THE OXIDATION OF 1000 PPM NH ₃ IN FR. SYMBOLS: EXPERIMENTS.	191

TABLE OF TABLES

TABLE 1 : BIOGAS COMPOSITION ACCORDING TO THE BIOMASS SOURCE.	16
TABLE 2 : CHEMICAL AND PHYSICAL PROPERTIES OF TWO SELECTED BIOGASES AND NATURAL GAS.	17
TABLE 3 : COMPARISON OF PROPERTIES OF BIO-OIL AND THREE LIQUID FUELS (BASU, 2018).	20
TABLE 4 : COMPOSITION OF BIO-OIL (BRIDGWATER ET AL., 2001).	22
TABLE 5: LISTS OF GASEOUS REACTANTS STUDIED DURING THE THESIS.	24
TABLE 6: LISTS OF REACTANTS FOR THE NOX FORMATION STUDIED DURING THE THESIS.	25
TABLE 7: LISTS OF BIO-OIL SURROGATES STUDIED DURING THE THESIS.	25
TABLE 8: THERMAL PROPERTIES AND FUNDAMENTAL COMBUSTION CHARACTERISTICS OF AMMONIA AND HYDROCARBON FUELS (^A HAN ET AL., 2020; ^B FLOCKENHAUS, 1969; ^C DAHOE, 2005; ^D DIRRENBERGER ET AL., 2011; ^E ENGINEERINGTOOLBOX, 2020; ^F KOBAYASHI ET AL., 2019; ^G NIST CHEMISTRY WEBBOOK, 2020).	30
TABLE 9: SUMMARY OF LAMINAR BURNING VELOCITY OF AMMONIA FLAME STUDIES	31
TABLE 10: SUMMARY OF SPECIATION STUDIES DURING AMMONIA OXIDATION.	32
TABLE 11 : SUMMARY OF LBV OF METHANE-AMMONIA FLAMES STUDIES	36
TABLE 12 : SUMMARY OF SPECIATION STUDIES DURING METHANE-AMMONIA OXIDATION.	37
TABLE 13: SUMMARY OF LBV STUDIES OF AMMONIA-HYDROGEN FLAMES.	43
TABLE 14: SUMMARY OF IGNITION DELAY TIME STUDIES DURING AMMONIA-HYDROGEN OXIDATION.	44
TABLE 15: SUMMARY OF HYDROGEN SULFIDE OXIDATION STUDIES.	47
TABLE 16: SUMMARY OF METHANE DOPED WITH HYDROGEN SULFIDE OXIDATION STUDIES.	50
TABLE 17: SUMMARY OF THE FORMATION OF NOX STUDIES, ALL PERFORMED USING LAMINAR PREMIXED FLAME BURNERS.	55
TABLE 18: SUMMARY OF PYRROLE OXIDATION STUDIES.	60
TABLE 19: SUMMARY OF ETHYLENE GLYCOL OXIDATION STUDIES.	63
TABLE 20: MAXIMAL FLOW RATE DEPENDING ON THE GAS USED AND CONVERSION FACTOR FOR EACH GAS (SOURCE: BRONKHORST MANUAL).	76
TABLE 21: UNCERTAINTY QUANTIFICATION OF THE EXPERIMENTAL SETUP.	88
TABLE 22: UNCERTAINTY OF THE EXPERIMENTAL METHODS.	92
TABLE 23: LIST OF CRITICAL REACTIONS IN THE NH ₃ OXIDATION MECHANISM. REACTION RATE EXPRESSION IS MODIFIED ARRHENIUS $K = AT^{\beta} \exp[-E_{ACT}/(RT)]$. UNITS ARE CM ³ , CAL, MOL, K, S.	98
TABLE 24: SUMMARY OF THE CONDITIONS INVESTIGATED IN THIS STUDY.	114

TABLE 25: LIST OF KEY REACTIONS IN THE H ₂ S PYROLYSIS AND OXIDATION MECHANISM. REACTION RATE EXPRESSION IS MODIFIED ARRHENIUS $k = AT^b \exp[-E_a/(RT)]$. UNITS ARE CM ³ , CAL, MOL, K, S.	121
TABLE 26: SUMMARY OF CONDITIONS INVESTIGATED IN THIS STUDY.	135
TABLE 27: SUMMARY OF EXPERIMENTAL CONDITIONS USED IN THE NO _x FORMATION STUDY.	144
TABLE 28: NOMENCLATURE OF RELEVANT SPECIES IN PYRROLE PYROLYSIS AND OXIDATION.	157
TABLE 29: RATE COEFFICIENTS FOR RELEVANT REACTIONS IN THE FOLLOWING DISCUSSION ON PYRROLE PYROLYSIS AND OXIDATION.	159
TABLE 30: SUMMARY OF EXPERIMENTAL CONDITIONS USED IN THE PRESENT PYRROLE STUDY.	163
TABLE 31: C-, H-, N- AND O-ATOM BALANCES.	166
TABLE 32: SUMMARY OF JSR EXPERIMENTAL CONDITIONS USED IN THE PRESENT STUDY	171
TABLE 33: CARBON BALANCE OF THE EXPERIMENTAL RESULTS OF EG.	175
<i>TABLE 34: SUMMARY OF JSR EXPERIMENTAL CONDITIONS USED IN THE PRESENT STUDY.</i>	<i>177</i>
TABLE 35: CARBON BALANCE OF THE EXPERIMENTAL RESULTS OF PG.	180
TABLE 36: EXPERIMENTS PERFORMED DURING MY THESIS.	188

NOMENCLATURE

Abbreviations

CRDS	Cavity Ring-Down Spectroscopy
ECN	Effective Carbon Number
FID	Flame Ionization Detector
FTIR	Fourier-transform infrared spectroscopy
FR	Flow reactor
GC	Gas Chromatography
IEA	International Energy Agency
JSR	Jet-stirred reactor
LBV	Laminar Burning Velocity
PAH	Polycyclic Aromatic Hydrocarbons
MS	Mass Spectrometry
TCD	Thermal Conductivity Detector

Symbols and units

E_a	Energy of activation
K	Thermodynamic equilibrium constant
k	Kinetic constant
P	Pressure
ppm	Parts per million
R	Universal ideal gas constant (8,314 J.mol ⁻¹ .K ⁻¹)
T	Temperature
τ	Residence time
x	Mole fraction
φ	Fuel air equivalence ratio

$$\varphi = \frac{x_{fuel}/x_{O_2}}{(x_{fuel}/x_{O_2})_{stoichio}}$$

I. INTRODUCTION

Energy has always played a major role in human and economic development, as well as in the well-being of society. The growing demand for energy, the depletion of fossil resources and the impact of emissions due to combustion, push humans to adopt a more ecological and responsible approach. The tendency has been towards the adoption of energy sources with a higher energy content, as the shift from coal (solid) to oil (liquid) and natural gas (gas).

I.1 Environmental and problematic context in energy

As each human is added to the Earth, resources become more of a precious commodity. Population growth is a problem, it not only leads to a more important demand in energy but also environmental issues. The substantial demand for energy contributes to deforestation, global warming and other environmental issues, such as pollution and acid rain. The United Nation has reported that the world's population is expected to increase by 2 billion persons in the next 30 years, from 7.8 billion (May 2020) currently to 9.7 billion in 2050 and could peak at nearly 11 billion around 2100 as shown in [Figure 7](#).

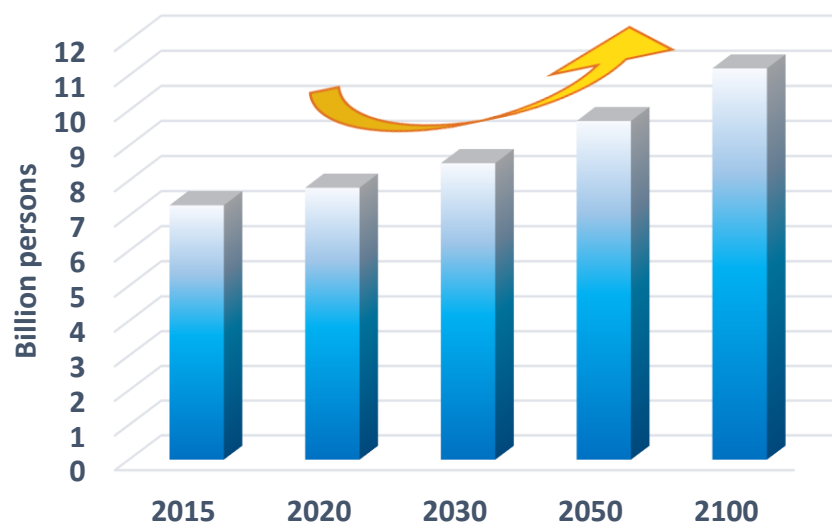


Figure 7: Population growth from 2015 to 2100 (United Nation, 2019)

Experts believe it will be needed 50 percent more energy to sustain humanity needs by 2050 (Howstuffworks, 2020). The United States has a population of just over 300 million people (5% of the people on Earth). They consume 20% of the world's energy and cause 19% of the world's greenhouse gases. 20% of the world's

population is in China that is responsible for 33% of its greenhouse emissions. Developing nations like India and some African countries tend to consume much less energy but add to the population crisis. India is almost the exact opposite of the USA, using only 5% of the world's energy. But with nearly 1.2 billion people, it's comprising almost 17% of the Earth's population.

As shown in [Figure 8](#), the International Energy Agency (IEA) estimates the world demand to grow from around 14,000 Mtoe in 2018 to around 18,000 Mtoe in 2024. China, the United States of America, and India account for 70% of the total energy demand growth. China remains the world's largest energy consumer in this scenario, but its demand grows slowly. India, where energy demand doubles, is the single largest source of demand growth to 2040 in the Stated Policies Scenario (STEPS¹). The European Union is almost the exact opposite of China, decreasing energy demand from 1,600 Mtoe in 2018 to 1,300 Mtoe in 2024.

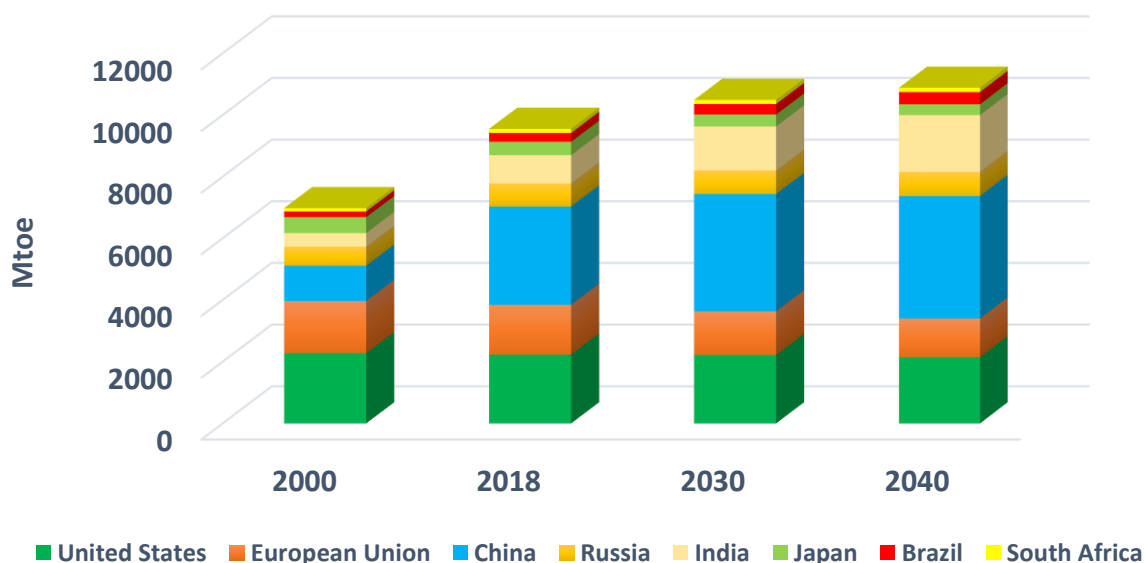


Figure 8: Total primary energy demand over the years by Stated Policies Scenario (STEPS) for different countries in Mtoe (Million tons of oil equivalent) (IEA, 2019a).

¹ The Stated Policies Scenario, by contrast, incorporates today's policy intentions and targets. Previously known as the New Policies Scenario, it has been renamed to underline that it considers only specific policy initiatives that have already been announced.

From 2018 to 2040, the share of fossil fuels in global primary energy demand will remain above 80%. Demand for all sources of energy, except coal, continues to increase as shown in Figure 9. Coal has a huge impact on the environment pollution because its production involves high greenhouse gases emissions (RTE-France, 2021). In 2021, CO₂ emissions per MWh generated in France from coal-fired plants represent 0.986 tons of CO₂, whereas biofuel plants emit 50% less CO₂ (0.494 tons of CO₂). So, its demand in 2040 will be slightly below today's level, and its share in the primary mix will be overtaken by gas around 2030. Gas demand rises by 35%, with industrial use of gas increasing at more than twice the pace of gas in power generation. Moreover, low-carbon sources are over half of the increase in demand to 2040, where renewables dominate investment and capacity additions.

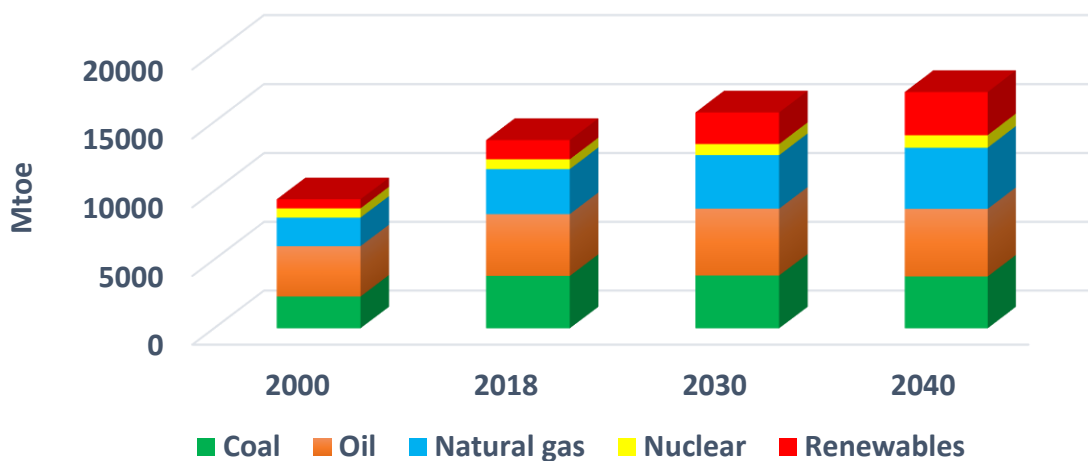


Figure 9: World total primary energy demand (STEPS) by source over the years in Mtoe (IEA, 2019a).

Not only the problem of energy demand that we are facing today but also that of environment, especially Global warming which occurs when greenhouse gases collect in the atmosphere and absorb sunlight and solar radiation. These gases trap the heat and cause the planet to get hotter (NRDC, 2016). Global warming causes a climate change, which disturbs the existing ecosystems and leads to a range of consequences, such as adverse weather events, resource depletion, and decreasing biodiversity (IPCC, 2019; Verplanken et al., 2020). It is predicted that the planet's average temperature will increase 1.8 - 5.8 °C by the end of the twenty-first century if the current trend of CO₂ emission levels remains stable (Shope, 1991). Carbon dioxide, CO₂, the main greenhouse gases which is mostly produced by the power

sector (Electricity and heat production) and the energy source that produced mainly CO₂ is coal as shown in [Figure 10](#) (IEA, 2019b).

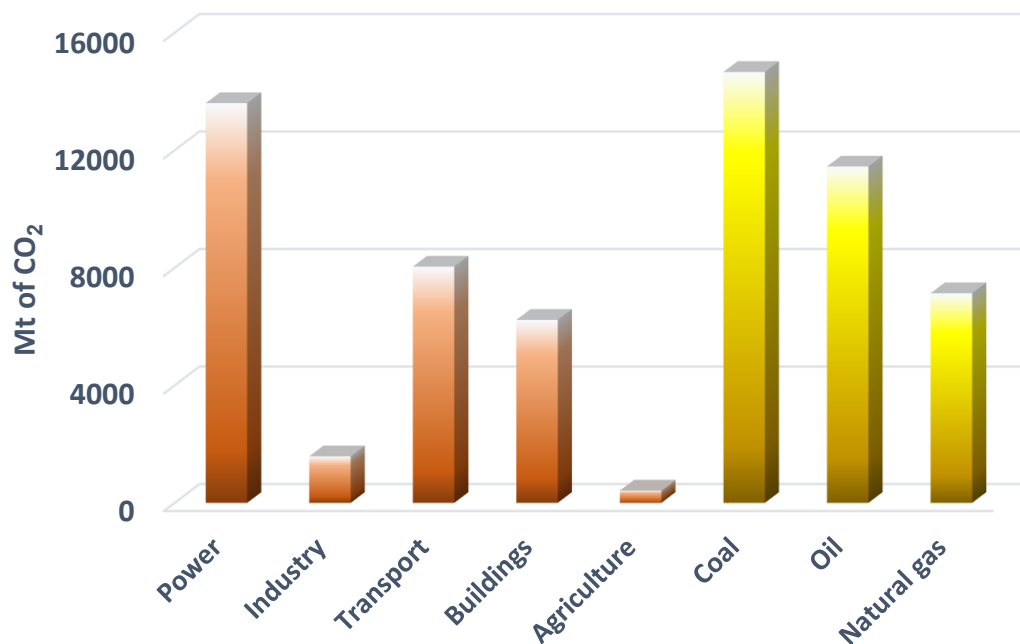


Figure 10: Global CO₂ emissions in Million tons (Mt) by sector in 2017, (Orange graphs) and source in 2018 (Yellow graphs), (IEA, 2019b).

The supply and use of coal and natural gas has a number of environmental impacts. Coal is responsible for over 40% of global emissions of energy-related sulfur dioxide (SO₂) emissions, a cause of respiratory illness and a precursor of acid rain and nearly 15% of particulate emissions. In contrast, SO₂ and particulate emissions from the use of natural gas are close to zero. Combustion of natural gas does produce nitrogen oxides (NO_x), which can trigger respiratory problems and the formation of other hazardous particles and pollutants, but it accounts for less than 10% of global energy-related NO_x emissions compared with around 15% for coal. However, the combustion of oil is the main source of NO_x as shown in [Figure 11](#).

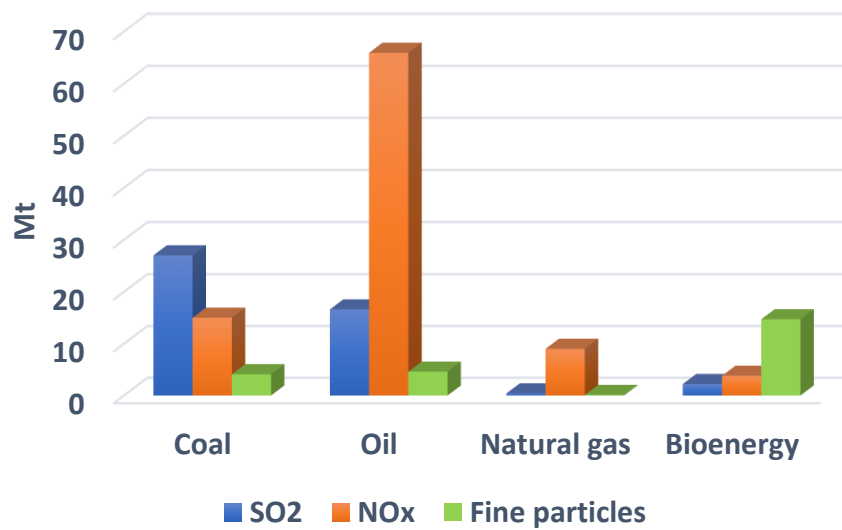


Figure 11: SO₂, NO_x, fine Particulate Matter (PM_{2.5}) emissions in Million tons (Mt) by source in 2018 (IEA, 2019a).

The main sector producing NO_x is transportation. While SO₂ is produced mainly from the industrial and power sectors. In contrast, these both sectors produced less PM_{2.5} than buildings sector as shown in Figure 12 (IEA, 2019a). The buildings sector includes energy used in residential, commercial and institutional buildings, and non-specified other. Building energy use includes space heating and cooling, water heating, lighting, appliances and cooking equipment.

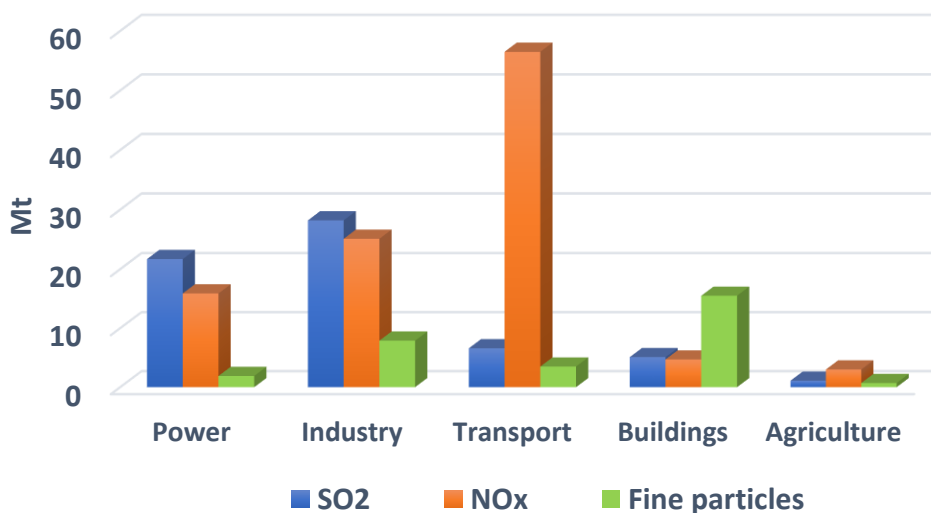


Figure 12: SO₂, NO_x, fine Particulate Matter (PM_{2.5}) emissions in Million tons (Mt) by sector in 2018 (IEA, 2019a).

NO_x is the generic term that encompasses a group of highly reactive gases, which contain nitrogen and oxygen in different amounts, such as nitric oxide (NO) and nitrogen dioxide (NO₂). It can in particular have impacts in terms of greenhouse effect, acidification of the air, etc. NO_x comes mainly from the combustion of fossil fuels in the air (which contains almost 80% nitrogen) at a temperature above 1400°C. Combustion installations (thermal power stations, heaters, etc.) are also responsible for a large share of its emissions.

Other types of pollutants produced from the power sector and transportation are Polycyclic Aromatic Hydrocarbons (PAHs). The PAHs are comprised of two or more benzene rings bonded in linear, cluster, or angular arrangements. It is well known that PAHs can be formed during the incomplete combustion of organic substances, such as motor fuels in cars and fuel oils in heating systems (Abdel-Shafy and Mansour, 2016).

Therefore, it is important to reduce the impact of environmental pollution. That is why alternative energy is gaining more and more attention in the industry and transportation, as well as from the refinery sector in order to drastically reduce CO₂ emissions. The global refining sector contributes around 4% of the total anthropogenic CO₂ emissions. In 2015, the total CO₂ emitted by mainstream refineries was estimated to be around 970 Mt per year (Ensys Energy, 2016). CO₂ emissions at refineries can be reduced through a number of routes. A way to reduce these emissions is through carbon capture and storage. Moreover, a refinery switching from refinery fuel oil to natural gas can reduce its emissions quickly by up to 20% (DigitalRefining, 2006) because CO₂ emissions from heaters and boilers are dependent on refinery fuel. Therefore, the *IMPROOF*² project (CERFACS, 2020; Djokic et al., 2017) aims to investigate biogas and bio-oils to be used as alternative fuels in refinery because these fuels are considered renewable, and hence, decrease net carbon dioxide production. However, this comes at significant cost and our knowledge about their impact on the

² Integrated Model Guided Process Optimization of Steam Cracking Furnaces: <https://improof.cerfacs.fr> a European project aiming at improving the energy efficiency of steam cracking furnaces starting from September 2016 to November 2020

emission of other pollutants, like NO_x and PAHs remains limited and needs to be investigated to validate these biofuels as a sustainable energy source.

I.2 Alternative solution

Nowadays, human beings are facing the dual pressure of economic growth and environmental protection. The growing concern over climate change and dependency of fossil fuels has encouraged people to look for renewable energy sources. The warnings of climate researchers are highly worrying and the goal of transforming the entire energy conversion processes into CO₂-free or CO₂-neutral technologies as quickly as possible is largely undisputed worldwide with the United Nations' *Sustainable Development Goals*³ and the *European Green Deal*⁴ presented in 2019. In particular, a competition between possible technology paths should be sought that ensures that the ecological goals are achieved in the best economic way. The European commission's goal is to reach net-zero greenhouse gas emissions in 2050 by prioritizing energy efficiency and developing a power sector based largely on renewable sources, especially the development of full potential of Europe's offshore wind energy. Moreover, decarbonizing the gas sector and boosting eco-design of products are the one of their solutions. The emissions that will not be eliminated by 2050 will be removed e.g., via natural carbon sinks such as forests, carbon capture and storage technologies.

I.2.1 Renewable energy

Renewable energy is gaining more and more attention, especially in Europe. Renewable energy is derived from natural processes that are replenished constantly. It derives directly from solar, wind, ocean, hydropower, biomass, geothermal resources, and biofuels and hydrogen derived from renewable resources.

³ UN Sustainable Development Goals: <https://www.un.org/sustainabledevelopment/sustainable-development-goals/>, retrieved on 22.04.2020

⁴ https://ec.europa.eu/info/strategy/priorities-2019-2024/european-green-deal_en By the year 2050, Europe is aiming for CO₂ neutrality, retrieved on 29.03.2021

Renewable energy will never run out because it can regenerate itself, making it a sustainable and abundant natural resource. It produces minimal CO₂ and waste products. However, it is hard to produce the same amount of energy as non-renewable sources and unreliable weather can affect energy supply. For some technologies, like wind turbines, EU manufacturers accounted for at least 41 % of the new global installed capacity in 2016 (JRC, 2017). In 2017, the EU reached a share of 17.52% of renewable energy in gross final energy consumption, against a target of 20% for 2020 (European commission, 2019). The renewable energy is going to increase in the next years according to the IEA (IEA, 2019a) as shown in [Figure 13](#). The main source is bioenergy⁵ which correspond to the energy generated from the conversion of solid, liquid and gaseous products derived from biomass. Modern bioenergy refers to the use of biomass alongside modern heating technologies, power generation, and transport fuels as opposed to the traditional methods of wood burning commonly used for heating and cooking in developing countries. Its part in the energy mix is estimated to grow in the future years because of its immediate availability and to the environmental concern. The second largest source of renewable energy is hydropower, but it slowly increases.

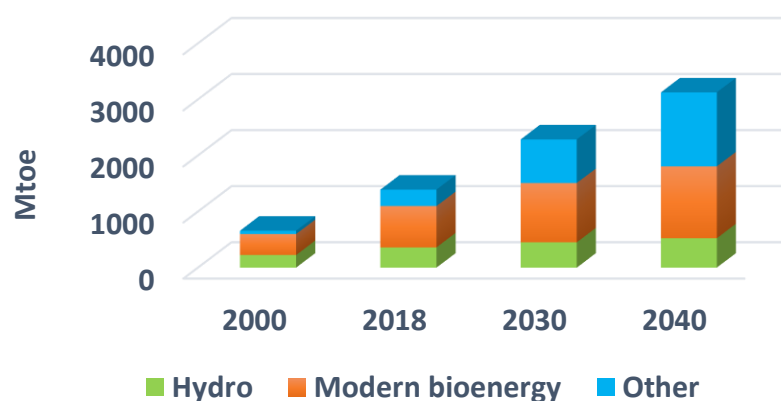


*Figure 13: Source of renewable energy in Mtoe over the years (IEA, 2019a).
Notes: Other includes wind, solar PV, geothermal, concentrating solar power and marine.*

⁵ There is a slight tendency for the word **bioenergy** to be favored in Europe compared with **biofuel** in America.

I.2.2 Biomass

Biomass is organic material that comes from plants and animals. Biomass has been used as a fuel source ever since humanity learned to make fire. Biomass served as the primary source of energy before fossil fuels became common in the twentieth century. Biomass contains stored energy from the sun. Plants absorb the sun's energy in a process called photosynthesis. When biomass is burned, the chemical energy in biomass is released as heat. Biomass has still been classified as a renewable energy source in the EU and UN legal frameworks, although burning plant-derived biomass releases CO₂, because photosynthesis cycles the CO₂ back into new crops. This recycling of CO₂ from plants to atmosphere and back into plants can even be CO₂ negative, as a relatively large portion of the CO₂ is moved to the soil during each cycle. Biomass can be burned directly or converted to liquid biofuels, bio-oils or biogas that can be burned as fuels.

I.2.2.1 Biogas

a) Biogas production and composition

In the context of a global energy demand, biogas from household and agriculture wastes, sewage sludge, and animal manure is foreseen playing an important role in future (Nallathambi Gunaseelan, 1997; Holm-Nielsen et al., 2009; Weiland, 2010; Demirbas, 2008). The strict laws and regulations for environmental consideration require increasingly sustainable solutions for handling and recycling animal manure and organic wastes. To prevent emissions of greenhouse gases (GHG) and leaching of nutrients and organic matter to the natural environment, it is necessary to close the loops from production to utilization by optimal recycling measures (as shown in [Figure 14](#)). Biogas is an environmentally friendly energy source, which can take the place of fossil fuels in power and heat generation. Moreover, it has attracted attention for being used as a vehicle fuel.

Biogas is mainly produced by the anaerobic digestion (AD) process of biomass, the principle of which is shown in [Figure 14](#). The composition of biogas depends on the biomass source (see [Table 1](#)). It is primarily composed of methane and carbon dioxide, contains smaller amounts of hydrogen sulfide and ammonia, and is normally saturated with water vapor. Small amounts of aromatics and organo-chlorinated and

–fluorinated compounds can be found in biogas from household waste. Biogas must be desulfurized and dried before utilization to prevent corrosive damage. Since the sources of biogas anaerobic digestion are different, the methane composition derived from the biogas varies from 50-75% with content in hydrogen sulfide of 100-10000 ppm, and in ammonia of 50-100 ppm.

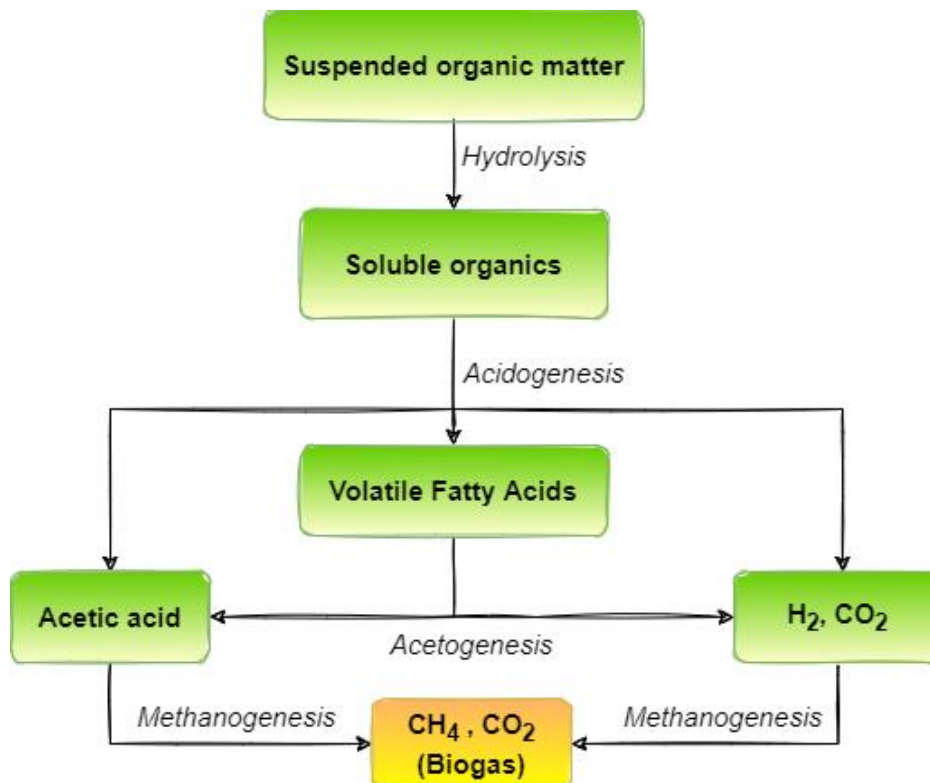


Figure 14: Subsequent steps in the anaerobic digestion process (Appels et al., 2008).

H₂S can be removed from biogas by three common technologies; *absorption into a liquid* either water or caustic solution, *biological conversion* by which sulfur compounds are converted into elemental sulfur by sulfide oxidizing microorganisms with the addition of air/oxygen and *adsorption on a solid* such as iron oxide-based materials, activated carbon, or impregnated activated carbon. Adsorption on nanomaterials is recognized to be an energy-efficient technology for hydrogen sulfide removal. Because of the high surface areas of nanomaterials, developing a nanoscale adsorbent with high adsorption capacity for hydrogen sulfide removal (Li et al., 2007; Yan et al., 2010).

Moreover, scrubbers (water and polyethylene glycol) can remove NH_3 from biogas. Since NH_3 molecules are soluble in water, their removal in aqueous chemical scrubbers becomes effective up to 99% (Munoz et al., 2013; Lien et al., 2014)

Table 1: Biogas composition according to the biomass source.

Components	Household waste	Wastewater treatment plant sludge	Agricultural wastes	Waste of agri-food industry
CH_4 (%vol)	50-60	60-75	60-75	68
CO_2 (%vol)	34-38	19-33	19-33	26
N_2 (%vol)	0-5	0-1	0-1	-
O_2 (%vol)	0-1	<0.5	<0.5	-
H_2O (%vol)	6 (at 40 °C)	6 (at 40 °C)	6 (at 40 °C)	6 (at 40 °C)
Total (%vol)	100	100	100	100
H_2S (mg/m ³)	100-900	1000-4000	3000-10000	400
NH_3 (mg/m ³)	-	-	500-100	-
Aromatics (mg/m ³)	0-200	-	-	-
Organochlorinated or Organofluorated (mg/m ³)	100-800	-	-	-

b) Biogas properties

The composition of biogas has a strong influence on its physical properties. [Table 2](#) gives the main properties of two biogases as well as those of natural gas. The main result from the comparison with natural gas is the lower heating value and larger density for biogas, which leads to a factor of about two in the Wobbe Index.

Table 2: Chemical and physical properties of two selected biogases and natural gas.

Types of gas	Biogas from Household	Biogas from Agri-food industry	Natural gas
Composition	60% CH ₄	68% CH ₄	97% CH ₄
	33% CO ₂	26% CO ₂	2.2% C ₂
	1% N ₂	1% N ₂	0.3% C ₃
	0% O ₂	0% O ₂	0.1% C ₄
	6% H ₂ O	5% H ₂ O	0.4% N ₂
HHV ^a (kWh/m ³)	6.6	7.5	11.3
LHV ^b (kWh/m ³)	6.0	6.8	10.3
Density (kg/m ³)	1.21	1.11	0.73
Relative density, d	0.93	0.85	0.57
Wobbe Index (LHV/ \sqrt{d})	6.9	8.1	14.9

^a Higher Heating Value

^b Lower Heating Value

Biogas provides less energy than natural gas because of its lower methane amount. Another alternative to replace natural gas with high amount of methane is biomethane, which is a near-pure source of methane. There are two main biomethane production pathways: the first involves upgrading biogas and the second involves the gasification of biomass. There are over 700 biomethane production plants in operation today producing around 2.5 Mtoe of biomethane globally. Most of these plants are in Europe and North America. Three quarters of biomethane are injected into existing gas networks (Cedigaz, 2019).

c) Biogas applications

Biogas is mainly used for the generation of heat and energy. The major applications already running are:

- The generation of heat in the industry (boiler, process, ...),
- The production of electricity as well as heat (cogeneration for household),
- Fuel in engines.

As already mentioned, these applications need purified biogas. Dehydration and desulphurization are systematically performed. The use of biogas as fuel also requires the removal of organo-halogen and heavy metals. Another application of biogas, which is currently studied, is the direct injection in the natural gas grid.

I.2.2.2 Bio-oil

Bio-oil is a highly oxygenated, free-flowing, dark brown organic liquid. It contains a large amount of water (~40) that comes from the moisture in the biomass and the reaction products. Bio-oil has several environmental advantages over fossil fuels as a clean fuel. No SO_x emissions are generated, because plant biomass contains insignificant amounts of sulfur. Bio-oil fuels generate more than 50% lower NO_x emissions than diesel oil in a gas turbine (Xiu and Shahbazi, 2012).

a) Bio-oil production

Biomass can be converted to bio-oil by two main routes: flash pyrolysis and hydrothermal liquefaction (HTL). Flash pyrolysis involves the rapid thermal decomposition of organic compounds in the absence of oxygen to produce liquids, gases, and char (see [Figure 15](#)). Flash pyrolysis is performed at a short gas residence time (1s), atmospheric pressure, and a relatively high temperature (450–500 °C). Furthermore, feedstock drying is necessary. The moisture content of the feedstock is very important for the pyrolysis process, which should be around 10%. At higher moisture contents, high levels of water are produced and at lower levels, there is a risk that the process only produces dust instead of oil. This process provides a high oil yield up to 80% on dry feed. However, oils obtained have much higher corrosiveness, oxygen and moisture contents and lower energy value, as compared to heavy petroleum fuel oil.

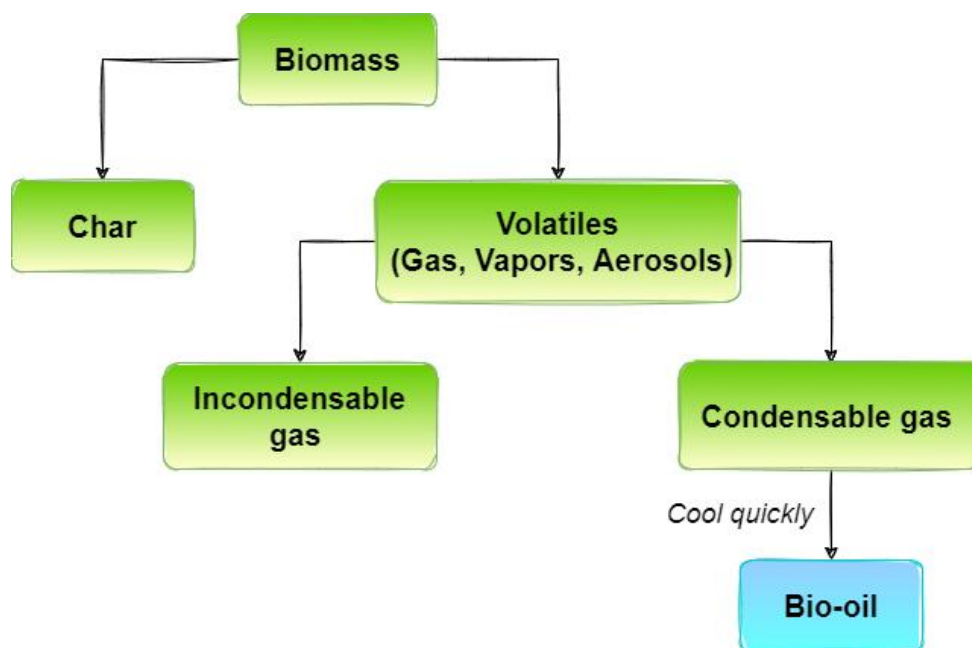


Figure 15: Reaction pathway for the biomass flash pyrolysis process.

Hydrothermal liquefaction (HTL) involves the reaction of biomass in water at high temperature and pressure with or without the presence of a catalyst (Ross et al., 2010). Hydrolysis can play an important role in forming glucose/oligomer, which can quickly decompose into non-glucose aqueous products, oil, char and gases (Minowa et al., 1995). Without a catalyst, char and gases were produced through oil as intermediates (see Figure 16). However, in the presence of an alkali catalyst, char production was inhibited because the oil intermediates were stabilized, resulting in oil production. Reduced nickel was found to catalyze the steam reforming reaction of aqueous products as intermediates and the methanation reaction. HTL is usually characterized by lower temperatures (300–400 °C), longer residence times (0.2–1h.), and high pressure (5–20 MPa). Contrary to flash pyrolysis and gasification processes, drying the feedstock is not needed in the HTL process, which makes it especially suitable for naturally wet biomass. However, the oil yield is relatively low (20-60 %).

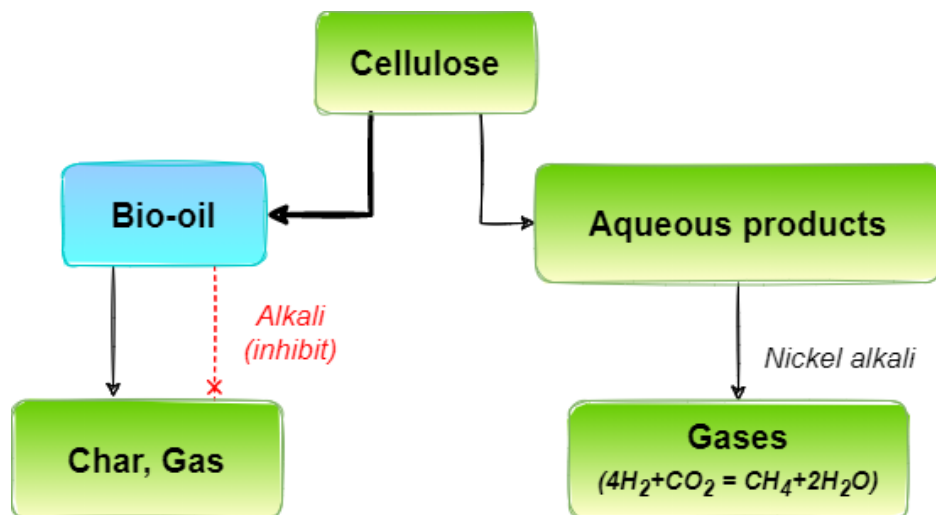


Figure 16: Reaction pathway for the hydrothermal liquefaction of cellulose.

b) Bio-oil properties

Bio-oil is a free-flowing liquid. Its low viscosity because of its high-water content as shown in Table 3. According to its density (1200 kg/m³), bio-oil is heavier than water or any oil derived from petroleum. Bio-oil properties can change with time because of polymerization, condensation, esterification, and etherification. This feature makes bio-oil different from mineral oils, the properties of which do not change with time.

Table 3: Comparison of properties of Bio-oil and three liquid fuels (Basu, 2018).

Property	Bio-oil	Heating oil	Gasoline	Diesel
Heating value (MJ/kg)	18-20	45.5	44	42
Density at 15 °C (kg/m ³)	1200	865	737	820-950
Flash point (°C)	48-55	38	40	42
Pour point (°C)	-15	-6	-60	-29
Viscosity at 40 °C (cP)	40-100	1.8-3.4 per cSt	0.37-0.44	2.4
	(25% water)	-		
pH	2-3	-	-	-
Solids (%wt)	0.2-1		0	0

cP, Centipoise; cSt, centistokes. Gasoline and diesel values can vary

Property	Bio-oil	Heating oil	Gasoline	Diesel
Elemental analysis (%wt)				
Carbon	42-47	86.4	84.9	87.4
Hydrogen	6-8	12.7	14.76	12.1
Nitrogen	<0.1	0.006	0.08	392 ppm
Sulfur	<0.02	0.2-0.7	-	1.39
Oxygen	46-51	0.04	-	-
Ash	<0.02	<0.01	-	-

Figure 17 compares bio-oil with petroleum distillate compounds, which can be separated, using fractional distillation (Fagernäs, 1995; DOE EIA., 2012). Low distillation temperature indicates the respective molecular size, volatility, viscosity, and combustion temperature of each fraction (Brook et al., 1997; Ma et al., 2018).

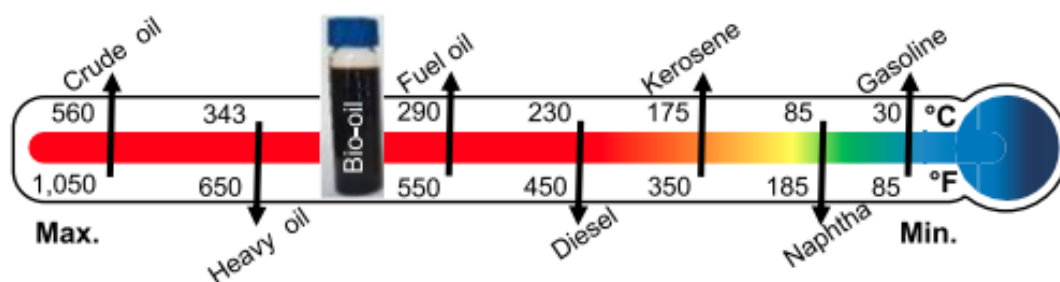


Figure 17: Distillation scale of bio-oil and other liquid hydrocarbon mixtures (Fagernäs, 1995; DOE EIA., 2012).

c) Bio-oil composition

Bio-oil composition depends on the biomass that bio-oil is made from as well as on the process used. Table 4 presents a typical composition of bio-oil.

Table 4: Composition of Bio-oil (Bridgwater et al., 2001).

Major group	Compounds	Mass (%)
Water	-	20-30
Lignin fragments	Insoluble pyrolytic lignin	15-30
Aldehydes	Formaldehyde, acetaldehyde, hydroxy acetaldehyde, glyoxal and methyl glyoxal	10-20
Carboxylic acids	Formic, acetic, propionic, butyric, pentanoic, hexanoic and glycolic	10-15
Carbohydrates	Cellobiosan, α -D-levoglucosan, oligosaccharides and 1.6 anhydroglucofuranose	5-10
Phenols	Phenol, cresols, guaiacols and syringols	2-5
Furans	Furfural	1-4
Alcohols	Methanol, ethanol	2-5
Ketones	Acetol (1-hydroxy-2-propanone), cyclopentanone	1-5

d) Bio-oil application

As a renewable liquid fuel, bio-oil can be readily stored and transported. It can serve as a substitute for fuel oil or diesel in many applications (combustion fuel in boiler/burner/furnace systems for heat, etc.). Bio-oil contains less hydrogen per carbon (H/C) atom than do conventional transport fuels such as diesel and gasoline. To increase H/C ratio, bio-oil can be hydrogenated (hydrogen added) to be used as transportation fuels with a high H/C ratio. Furthermore, most of the chemicals produced from petroleum can be derived from bio-oil such as resins, food flavorings, agrichemicals, fertilizers, and adhesives (Rachel-Tang et al., 2017).

I.3 Thesis objective

This PhD thesis was partly performed as a part of the European project named IMPROOF (2016-2020) (CERFACS, 2020) aiming at improving the energy efficiency of steam cracking furnaces by developing new technologies and by using a high emissivity coating. Biogas and bio-oils were investigated to be used as alternative fuels because they are considered as renewable, thus decreasing the net carbon dioxide production.

To promote the development of new the types of steam cracking furnaces proposed in the IMPROOF project, this thesis aims at obtaining a better understanding of the formation of pollutants, in particular NO_x and Polycyclic Aromatic Hydrocarbons (PAHs) during biogas and biofuel combustion by means of both an experimental study and numerical simulations. The combustion chemistry of biogas and bio-oils in the gas phase is still relatively unknown. The establishment of an experimental database including the identification of the products and intermediates formed will allow a better understanding of the chemical reactions involved. The objective will then be to develop and validate detailed kinetic models able of reproducing the combustion of biogas components and single compound bio-oil surrogates. These models made available to industrials and academics will help the studies performed in order to reduce fuel consumption (through a better efficiency) and polluting emissions.

In order to obtain reliable experimental results, it is necessary on the one hand to well define and control the operating conditions and on the other hand to analyze the compounds obtained during the reaction as completely and accurately as possible. The study of fuel oxidation was carried out using both a jet-stirred reactor and a flow tube reactor to reach high temperature conditions (up to 2073 K). A **jet-stirred reactor**, which can be considered *ideal*, allows to overcome physical phenomena such as the species diffusion and heat transfers. In a **flow tube reactor**, which is considered as *piston flow reactor*, the fluid is perfectly mixed in the radial direction but not in the axial one. Temperature in this reactor is inhomogeneous and the temperature profile needs to be measured. Therefore, the assumption of the reactors to be ideal makes it possible to model them the most simply possible. Biofuel oxidation leads to the product formation of a wide range of species with varied natures. Different methods were implemented during this thesis in order to analyze this large number of compounds. The analysis methods used for this thesis are Gas Chromatography (GC), Online-Mass Spectrometry (MS), NO_x analyzer, and Fourier-Transform Infrared Spectroscopy (FTIR).

The manuscript is divided into six main separate parts:

- The first chapter presents generalities about the chemistry of combustion and a state of the art about the investigation of the gas-phase kinetics of the oxidation of the various molecules studied within the framework of this thesis, as presented in [Table 5](#) to [Table 7](#).

- The second chapter concerns the description of the experimental setup and of the different analytical techniques used.

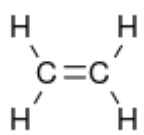
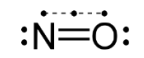
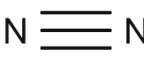
- The third chapter deals with the results obtained on the oxidation of biogas components: ammonia, hydrogen sulfide and the mixtures of methane doped with ammonia, hydrogen sulfide, and the mixture of ammonia doped with hydrogen.

Table 5: Lists of gaseous reactants studied during the thesis.

Fuel name	Structure	Chemical formula	Molar mass (g/mol)	Boiling point (°C)
Methane	$\begin{array}{c} \text{H} \\ \\ \text{H}-\text{C}-\text{H} \\ \\ \text{H} \end{array}$	CH ₄	16.04	-161.52
Ammonia	$\begin{array}{c} \text{H}-\ddot{\text{N}}-\text{H} \\ \\ \text{H} \end{array}$	NH ₃	17.00	-33.35
Hydrogen Sulfide	$\begin{array}{c} \cdot \quad \cdot \\ \diagdown \quad \diagup \\ \text{H} \quad \text{S} \quad \text{H} \\ \diagup \quad \diagdown \end{array}$	H ₂ S	34.08	-60.70
Hydrogen	H—H	H ₂	2.02	-252.76

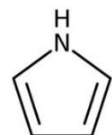
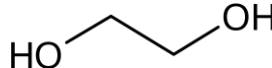
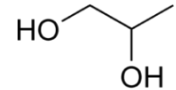
- The fourth chapter concerns the study of the NO_x formation at high temperatures during the oxidation of nitrogen (N₂), methane, and ethylene.

Table 6: Lists of reactants for the NO_x formation studied during the thesis.

Fuel name	Structure	Chemical formula	Molar mass (g/mol)	Boiling point (°C)
Ethylene		C ₂ H ₄	28.05	-103.7
Nitric Oxide		NO	30.00	-151.80
Nitrogen		N ₂	28.01	-195.80

- The fifth chapter presents the results obtained for oxidation of bio-oil surrogates: pyrrole, ethylene glycol and propylene glycol.

Table 7: Lists of bio-oil surrogates studied during the thesis.

Fuel name	Structure	Chemical formula	Molar mass (g/mol)	Boiling point (°C)
Pyrrole		C ₄ H ₅ N	67.09	129.70
Ethylene Glycol		C ₂ H ₆ O ₂	62.07	197.30
Propylene Glycol		C ₃ H ₈ O ₂	76.10	188.20

- The last chapter concludes and presents some perspectives to this work.

II. STATE OF THE ART ON OXIDATION OF THE MOLECULES STUDIED AS PART OF THE THESIS

II. State of the art on the molecules studied as part of the thesis

Due to the complexity of organic compounds in bio-oils and biogas as shown in previous part and the limitation of analysis techniques, it is necessary to surrogate the composition. Combustion of surrogates allows to better understand the reactivity of bio-oils and biogas, and to also understand the formation pathways of the products.

There are many interesting surrogates to be studied on the subject. The surrogates studied depend on the previous works in IMPROOF project performed by Sylvain Namysl and Yu Song (Namysl et al., 2019&2020; Pelucchi et al., 2019a&b; Marrodán et al., 2019; Stagni et al., 2020a&b) and also depend on the literature works. Our surrogate composition is graphically summarized in [Figure 18](#).

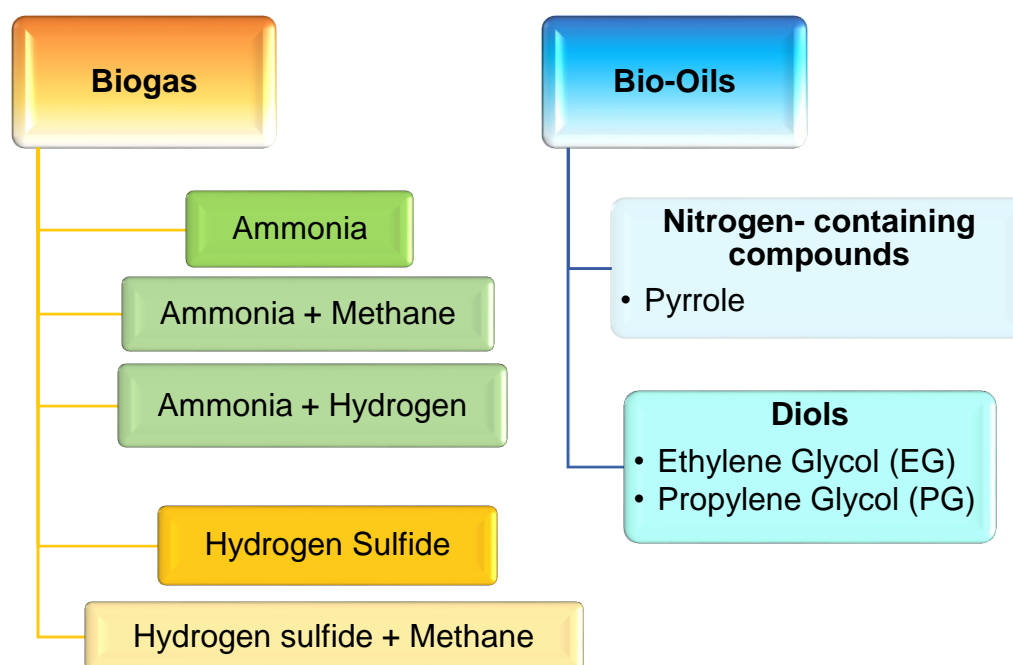


Figure 18: Surrogates used in my bio-oil and biogas studies.

A literature review has been carried out for each surrogate in the following part. This state of the art is presented in detail about the experimental oxidation, combustion and pyrolysis studies concerning these chemical families as well as the study of NO_x formation. The objective is to identify the experimental results and kinetic models already published and to establish what can be missing for a complete assessment of the reactivity of those compounds.

II.1 Biogas

The composition of biogas, a mixture primarily composed of methane and carbon dioxide, has a significant impact on its chemical and physical properties. Minor species in biogas also have an effect on the reactivity of this fuel and on the potential pollutants produced during its oxidation. In the following part, literature studies about the oxidation and pyrolysis of ammonia and hydrogen sulfide under different conditions (types of reactors, temperature, pressure, bath gases, reactive mixture composition) are presented. Moreover, studies focusing on the interaction between biogas compounds (CH_4/NH_3 and $\text{CH}_4/\text{H}_2\text{S}$) and the effect of additions such as hydrogen (NH_3/H_2) are examined.

II.1.1 Ammonia

Carbon free compounds, i.e., hydrogen and ammonia, are recognized as promising alternative fuels, since they can be oxidized without CO_2 emissions. However, NH_3 physical and chemical properties (flame velocity, low calorific value, minimum ignition temperature (See [Table 8](#))) and the high NO_x levels production in combustion processes could represent a limit for the application of ammonia as alternative fuel.

Table 8: Thermal properties and fundamental combustion characteristics of ammonia and hydrocarbon fuels (^aHan et al., 2020; ^bFlockenhaus, 1969; ^cDahoe, 2005; ^dDirrenberger et al., 2011; ^eEngineeringtoolbox, 2020; ^fKobayashi et al., 2019; ^gNIST Chemistry WebBook, 2020).

Types of gas	NH_3	H_2S	H_2	CH_4	Natural Gas
Laminar Burning Velocity (LBV), (298 K, $\Phi \sim 1.1$) (cm/s)	7 ^a	3 ^b	25 ^x	38 ^d	40 ^d
HHV ^e (MJ/kg)	22.50	17.4	141.8	55.5	52.2
LHV ^e (MJ/kg)	18.65	-	119.96	50	47.1
Autoignition temperature (K)	924	505	844	810	853
Adiabatic flame temperature ^f (K)	2073	-	2383	2223	-
Boiling temperature ^g at 1 atm (K)	239.6	213	20	112	111

II. State of the art on the molecules studied as part of the thesis

Fuel–air equivalence ratio, Φ (phi) is defined as the ratio of the fuel-to-oxidizer ratio to the stoichiometric fuel-to-oxidizer ratio as shown mathematically in Equation 1.

$$\Phi = \frac{\text{fuel to oxidizer ratio}}{(\text{fuel to oxidizer ratio})_{st}} = \frac{m_{fuel}/m_{ox}}{(m_{fuel}/m_{ox})_{st}} = \frac{n_{fuel}/n_{ox}}{(n_{fuel}/n_{ox})_{st}}$$

Equation 1: Fuel-Air equivalence ratio (Φ) formula

where, m represents the mass, n represents number of moles, suffix st stands for stoichiometric conditions.

For these reasons, a deeper understanding of NH₃ oxidation mechanisms is necessary to identify optimal operating conditions and minimize NO_x emissions. Table 9 and Table 10 present the experimental studies of the oxidation of neat ammonia from premixed flames, flow and jet-stirred reactors. The experimental conditions are temperature (T), pressure (P) and fuel–air equivalence ratio (Φ).

Table 9: Summary of laminar burning velocity of ammonia flame studies.

Instrument	Experimental Conditions	Bath gas	NH ₃	Reference
	T=293 K; P= 0.101 MPa; Φ = 0.74–1.35	Air	~ 22-23 %	(Zakaznov et al., 1979)
	T=300 K; P= 0.007–0.2 MPa; Φ ≈ 0.58–1.79	Air	14–32.2%	(Ronney, 1988)
Constant volume	T=295 K; P= 0.101 MPa; Φ = 0.49–1.19	Air	5 – 68 %	(Pfahl et al., 2000)
	T=298 K; P=0 .101 MPa; Φ = 0.9–1.30	Air	-	(Jabbour & Clodic,2004)
Bomb (CVB)	T=298 K; P= 0.101 MPa; Φ = 0.89–1.20	Air	-	(Takizawa et al., 2008)
	T=298 K; P= 0.1–0.5 MPa; Φ = 0.70–1.30	Air	-	(Hayakawa et al., 2015)
	T=298 K; P= 0.101 MPa; Φ = 0.6–1.5	N ₂	-	(Mei et al., 2019)
	T=298-473K; P= 0.101 MPa; Φ = 0.8-1.4	Air	-	(Lhuillier et al., 2020)
Burner	T=298 K; P=0.101 MPa; Φ = 0.85–1.25	Air	-	(Han et al., 2019)
	T=298-448 K; P=0.101 MPa; Φ = 0.85–1.25	Air	-	(Han et al., 2020)

II. State of the art on the molecules studied as part of the thesis

Table 10: Summary of speciation studies during ammonia oxidation.

Instrument	Experimental Conditions	Bath gas	NH ₃	Reference
	T=450–925 K; P= 3–10 MPa; Φ= 0.023–1.04	N ₂	714 - 789 ppm	(Song et al., 2016)
Flow Reactor	T=900–1350K; P= 0.122 MPa; Φ=1	Ar	8% & 14% in NH ₃ /O ₂	(Manna et al., 2020)
	T=900–1800K; P= 0.101 MPa; Φ=∞	Ar or N ₂	0.1-1.0%	(Benés et al., 2020)
Jet-Stirred Flow Reactor	T=900–1350 K; P= 0.122 MPa; Φ=1 T=1000–1350 K; P= 0.122 MPa; Φ=1	Ar & Water	8% & 14% in NH ₃ /O ₂	(Manna et al., 2020)
	T=1260-1350 K; P= 0.122 MPa; Φ=0.4-1.6	N ₂ & Water	0.4%	(Manna et al., 2021)
Shock tube	T=1560– 2455 K; P= 0.142–3.04 MPa; Φ=0.5–2.0	Ar	1%	(Mathieu and Petersen, 2015)

Zakaznov et al. (1979) were the first to study the laminar burning velocities⁶ (LBVs) of NH₃/air mixtures. They used the cylindrical-tube method (ambient condition). It was found that a mixture with 23% NH₃ (equivalence ratios (Φ) of 1.07) had the maximum LBV value of 7 cm/s, whereas the LBV value for the mixture close to the lower flammability limit (17–17.5% NH₃) was 3 cm/s. **Ronney et al. (1988)** measured the LBVs of NH₃/air mixtures using a CVB at five initial pressures under microgravity conditions, i.e., 0.066, 0.132, 0.329, 1 and 1.974 atm. Their results showed that initial pressure only had little influence on the LBV values of NH₃/air mixtures.

Pfahl et al. (2000) performed the experiments on flammability limits, ignition energies, and flame speeds in a 11.25- and a 400-liter CVB at initial pressures and temperatures of 100 kPa and 295 K, respectively. It was concluded that increasing the

⁶ The Laminar burning velocity is the speed at which a laminar (planar) combustion wave propagates relative to the unburned gas mixture ahead of it. LBV provides supplements of basic diffusion and chemical reaction information of combustible mixtures, and verification information for chemical reaction kinetics (Aung K.T. et al., 1997).

initial amount of nitrous oxide in flammable gases increased the laminar burning velocity at high temperature (>1200 K). **Jabbour et al. (2004)** measured the LBVs of NH_3/air mixtures at ambient pressure and temperature using a vertical tube. **Takizawa et al. (2008)** studied the LBVs of NH_3/air mixtures at atmospheric pressure and room temperature in a CVB. The flame propagation was measured using both direct and schlieren photography. A red NH_3/air flame was observed in direct photography. After that, **Hayakawa et al. (2015)** measured the LBVs and Markstein lengths⁷ of NH_3/air mixtures at 1, 3 and 5 atm and Φ from 0.9 to 1.2 using a CVB. They found that the trends of LBVs of NH_3 with varying initial pressure and equivalence ratio were the same as those of hydrocarbon fuels, which was different from the observation of **Ronney et al. (1988)**. In 2019, **Han et al. (2019)** also measured the LBVs of NH_3/air , $\text{NH}_3/\text{H}_2/\text{air}$, $\text{NH}_3/\text{CO}/\text{air}$ and $\text{NH}_3/\text{CH}_4/\text{air}$ mixtures using a burner. **Lhuillier et al. (2020)** performed the experiments on the LBV values of NH_3/air mixtures measured using a CVB at atmospheric pressure, from 298 to 473 K, in the fuel and equivalence ratios in the range from 0.8 to 1.4. It was found that, the LBV of NH_3/Air flame ($\Phi=1.1$, 298K) was 7 cm/s.

Recently, **Han et al. (2020)** again measured the laminar burning velocity of NH_3/air mixtures at unburnt gas temperatures from 298 K to 448 K, covering equivalence ratios from 0.85 to 1.25 and at 1 atm using a burner. It was found that their experimental results of the laminar burning velocity at 298 K and 448K, agree well with the literature data from Han et al. (2019), Takizawa et al. (2008), Ronney (1988), Pfahl et al. (2000), Jabbour and Clodic (2004), Hayakawa et al. (2015), Ichikawa et al. (2015), Mei et al. (2019), and Lhuillier et al. (2020) as shown in [Figure 19](#).

⁷ Markstein length introduced by Clavin (Clavin, 1985) for gaseous fuels, is a mixture specific constant with a magnitude of the order of the flame thickness and serves as a measure of the sensitivity of the laminar burning velocity to the influence of flame shape modifications (Dahoe et al., 2002).

II. State of the art on the molecules studied as part of the thesis

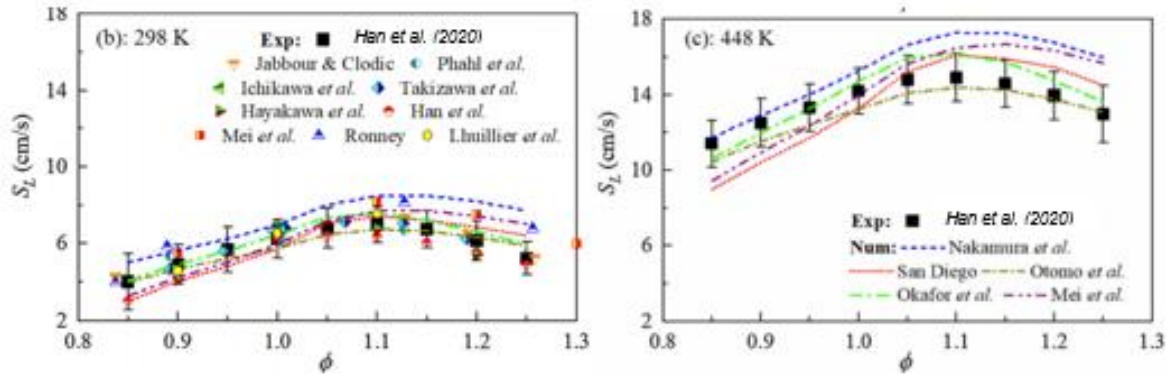


Figure 19: Laminar burning velocity of NH_3/air flames at 0.101 MPa, (b) 298 K, (c) 448 K, data comparing with literature experimental (Points are experiments and lines are simulations). Figure extracted from Han et al., 2020.

In summary, it is recognized that the LBVs of NH_3/air mixtures under atmospheric pressure are extremely low (6 cm/s at $\Phi = 1.1$), which are very less than that of CH_4/air mixtures (36 cm/s at $\Phi = 1.1$) due to the weak reactivity and low adiabatic flame temperatures (2073 K). As a result, the laminar flame propagation of NH_3/air mixtures is strongly affected by buoyancy effect, while a great influence of the experimental uncertainties can hardly be avoided, especially at elevated pressures.

In 2019, **Mei et al. (2019)** performed an experimental and kinetic modeling investigation on the laminar flame propagation of ammonia in a high-pressure CVB under oxygen enrichment and elevated pressure conditions ($\Phi = 0.6\text{--}1.5$, 298 K). It was found that the LBVs of NH_3/air mixtures peak around $\phi = 1.1$, while the maximum measured LBV values are between 6.6 and 8.1 cm/s. For the $\text{NH}_3/\text{O}_2/\text{N}_2$ mixtures, LBVs peak also at $\Phi = 1.1$. The peak values of the measured LBVs are 27.4, 24.8 and 21.4 cm/s at 1, 2 and 5 atm, respectively, which are much higher than the peak LBV values of NH_3/air mixtures. It can be concluded that the oxygen enrichment greatly accelerates the laminar flame propagation of NH_3 .

Since 2015, high-temperature results at increased pressures are available in shock tubes and flow reactors. **Mathieu and Petersen (2015)** measured ignition delay times for ammonia diluted in argon in a shock tube at 1.4, 11, and 30 bar, respectively, while Hayakawa et al. (2015) determined the burning velocity of ammonia/air mixtures at pressures of 1–5 bar. After that, studies of ammonia oxidation at low-to-medium temperatures and high pressure were performed by **Song et al. (2016)**. They investigated the oxidation of ammonia under 30 and 100 bar, 450–925 K with

stoichiometric and lean NH_3/O_2 mixtures, highly diluted in N_2 , in a laminar flow reactor. It was shown that ammonia oxidation was slow under stoichiometric conditions. Under oxidizing conditions the onset temperature for reaction was 850–875 K at 30 bar, while at 100 bar it was about 800 K, with complete consumption of NH_3 at 875 K.

After the start of my PhD, **Manna et al. (2020)** studied the oxidation and thermal pyrolysis of a highly diluted stoichiometric $\text{NH}_3/\text{O}_2/\text{Ar}$ and NH_3/Ar mixtures in a quartz jet-stirred reactor as a function of the inlet temperature (900–1350 K), at atmospheric pressure. Additionally, experimental tests were replicated in a quartz and in an alumina tubular flow reactor to examine the chemical heterogeneous interactions with different materials. Recently, **Benès et al., (2021)** performed the pyrolysis of NH_3 (1000-10000 ppm) in a quartz tubular flow reactor and a non-porous alumina tubular flow under atmospheric pressure. **Manna et al. (2021)** studied the oxidation of ammonia diluted in N_2 in a jet-stirred reactor under 0.122 MPa ($\phi=0.4-1.6$). The second experiments were carried out by replacing N_2 with different amounts of H_2O (to 3, 6, 10, 12, 15 vol%). Water helps to slow down the reactivity of the process (Sabia and Joannon, 2020; Sabia et al., 2015; Sabia et al., 2020), therefore to extend the time interval where dynamic behaviors occur, and to stabilize oscillations.

In the literature, a large number of publications on ammonia oxidation was published during the last years. However, only a few studies concerned the species concentration profiles during the oxidation of ammonia in jet-stirred and flow reactors. Complementary data about the species concentration profiles could be useful to improve kinetic models for the combustion of ammonia. Therefore, more experiments with speciation on ammonia oxidation and pyrolysis need to be carried out.

II.1.2 Methane doped with ammonia

Ammonia is known as a trace compound among biogas components. Moreover, ammonia is an important combustion intermediate deriving from the formation of nitric oxide from nitrogen organic fuels. For most solid fuels, NH_3 is formed directly during devolatilization (Glarborg et al., 2003), and it has also been reported as a product of gasification (Hasegawa and Sato, 1998). The selectivity for forming NO or N_2 from N volatiles in combustion depends largely on the fate of amine radicals such as NH_2 , NH , and N . Therefore, it is important to understand the mutual interaction of ammonia with hydrocarbons, such as methane, in combustion processes. [Table 11](#) and [Table 12](#) present the results on the experimental studies of the oxidation of methane doped with ammonia available in the literature. These are only from premixed/diffusion flames and flow reactors.

Table 11: Summary of LBV of methane-ammonia flames studies.

Instrument	Experimental Conditions	Bath gas	NH_3	Reference
Burner	T= 298-2000 K; P= 0.101 MPa; Φ = 0.5-1.5	Air	5% in the fuel	(Henshaw et al., 2005)
	T= 298-2300 K; P= 0.101 MPa; Φ = 0.7-1.5	Air	0.5%	(Konnov et al., 2006)
CVB	T= 298-2200 K; P= 0.1 MPa; Φ = 0.8-1.3	Air	0-30% in the fuel	(Okafor et al., 2018)
	T= 298-2200 K; P= 0.1-0.5 MPa; Φ = 0.7-1.3	Air	0-30% in the fuel	(Okafor et al., 2019)
	T=445 K; P= 0.54 MPa; Φ =0.9,1.0,1.1	Air	0–15% in the fuel	(Lhuillier et al., 2021)

II. State of the art on the molecules studied as part of the thesis

Table 12: Summary of speciation studies during methane-ammonia oxidation.

Instrument	Experimental Conditions	Bath gas	NH ₃	Reference
	T= 1500-2100 K; P= 0.003 MPa; Φ = 0.8-1.16	-	5-6%	(Garo et al., 1992)
	T= 600-2000 K; P= 0.001 MPa; Φ = 1.007	Ar	0.35%, 1.05%	(Williams and Fleming, 1997)
	T= 400-1800 K; P= 0.005-0.013 MPa; Φ = 0.7-1.6	Ar	1.3%	(Hughes et al., 2002)
	T= 298-2000 K; P= 0.101 MPa; Φ = 0.5-1.5	Air	5% in the fuel	(Henshaw et al., 2005)
Burner	T= 373-2000 K; P= 0.004 MPa; Φ = 0.8-1.17	N ₂	0.14%	(Rahinov et al., 2006)
	T= 298-2300 K; P= 0.101 MPa; Φ = 0.048-0.0625	N ₂ or CO ₂	0.5%	(Konnov et al., 2006)
	T= 1250-2050 K; P= 0.004 MPa; Φ = 0.62-1	Ar	1.9-11.4%	(Tian et al., 2009)
	T= 1980-2200 K; P= 0.101 MPa; Φ = 0.65-1.45	Air	0.44%	(Li et al., 2013)
	T= 1200-1900 K; P= 0.101 MPa; Φ = 0.8-0.95	Air or CO ₂	1.8%	(Barbas et al., 2015)
	T= 300-1800 K; P= 0.101 MPa; non-premixed	Air	0.1%	(Sullivan et al., 2002)
Flow reactor	T= 900-1500 K; P= 0.12 MPa; Φ = 0.67-3	N ₂	0.03%	(Grcar et al., 2005)
	T= 973-1773 K; P= 0.101 MPa; Φ = 0.13-1.55	N ₂ or CO ₂	0.05%	(Mendiara and Glarborg, 2009)
Gas turbine combustor	T= 300-2300 K; P=0.1-0.25 MPa; Φ = 0.6-1.4	Air	30% in the fuel	(Okafor et al., 2020)

Henshaw et al. (2005) investigated the burning velocities and NO_x mole fraction with the ammonia addition to methane-air flames at atmospheric pressure. A sampling probe was fitted to the metal probe of a 5-gas analyzer (IMR model 2800P, FL) and inserted inside the chimney above the burner. They pointed out that adding ammonia to methane-air flames resulted in an increase in NO concentrations especially for stoichiometric composition, with a minor effect on the carbon monoxide formation. In 2006, **Konnov et al. (2006)** measured the adiabatic burning velocities in CH₄+NH₃ flames at atmospheric pressure and initial gas temperature of 298 K. The

II. State of the art on the molecules studied as part of the thesis

results were compared to those measured in methane flame (Dyakov et al., 2001). It was found that no influence of the ammonia admixture on the flame burning velocities.

Recently, **Okafor et al. (2018)** studied the LBV of CH₄/NH₃/air premixed flames under 0.10 MPa over a wide range of equivalence ratios and ammonia concentrations. Ammonia concentration in the fuel was varied from 0 to 0.3, while the equivalence ratio was varied from 0.8 to 1.3. It was found that the LBV decreased with an increase in ammonia concentration. In 2019, **Okafor et al. (2019)** investigated the LBV and Markstein lengths of CH₄/NH₃/air at high pressures (0.1-0.5 MPa) for the first time. A reduced reaction mechanism for modelling CH₄/NH₃/air was proposed, which is optimized and validated with results of present measurement and data from the literature. **Figure 20** showed the reduced mechanism satisfactorily reproduces the measured LBV of CH₄/NH₃/air flames over a wide range of pressures (0.1-0.5 MPa) and equivalence ratios.

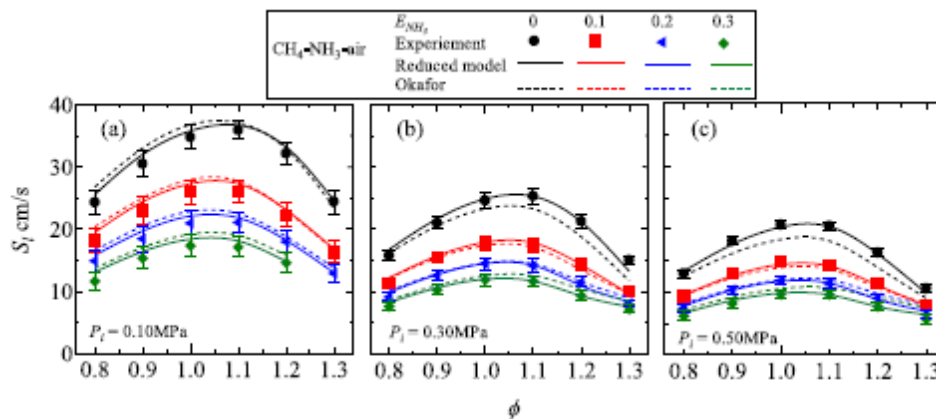


Figure 20: Comparison of measured unstretched laminar burning velocity of CH₄/NH₃/air flames to simulated results at (a) 0.10 MPa (b) 0.30 MPa (c) 0.50 MPa. The measurements at 0.10 MPa are data from Okafor et al., 2018. Figure drawn from Okafor et al., 2019.

More recently, **Lhuillier et al. (2021)** investigated the ammonia combustion behavior in a spark-ignition engine and the effect of hydrogen and methane enrichment on the LBV at 445 K, P= 0.54 MPa, ϕ = 0.90-1.10. It was noticed that adding H₂ or CH₄ to the NH₃ fuel induces the same LBV increase at ϕ = 0.9 and similar effects at ϕ = 1.0 and 1.1. However, the effects of hydrogen or methane enrichment observed in the SI engine could not be sufficiently explained by the LBV of the mixtures.

II. State of the art on the molecules studied as part of the thesis

In 1992, **Garo et al.** investigated premixed laminar $\text{CH}_4\text{-O}_2$ flames doped with ammonia and nitrogen oxide at a pressure of 0.003 MPa under various equivalence ratios. Molecular beam mass spectrometry and laser-induced fluorescence were used to measure the intermediate species (CH , CH_3 , OH , O , H radicals). The mechanism of **Miller and Bowman, 1989** was used with a few reactions added. Sensitivity and reaction path analysis indicated that the reactions ($\text{CH}_i + \text{NO} = \text{HCN} + \text{H}_{i-1}\text{O}$, $i=1-3$) were underestimated in the model.

After that, **Williams and Fleming (1997)** measured nitrogen compounds with temperatures ranging from 500-2000 K in premixed methane/oxygen/argon flames doped with NH_3 , CH_3NH_2 , CH_3CN and NO . Laser-induced fluorescence was used to measure the intermediate species. Due to a low NH_2 radical fluorescence signal, dopant should be added at three times its normal concentration (1.05%) to be able to measure it as shown in [Figure 21](#). The experimental data were interpreted with the GRI 2.11 model modified by adding reactions between CH_3 and NH . It was found that the agreement with the measured intermediate profiles was much better with the modified model.

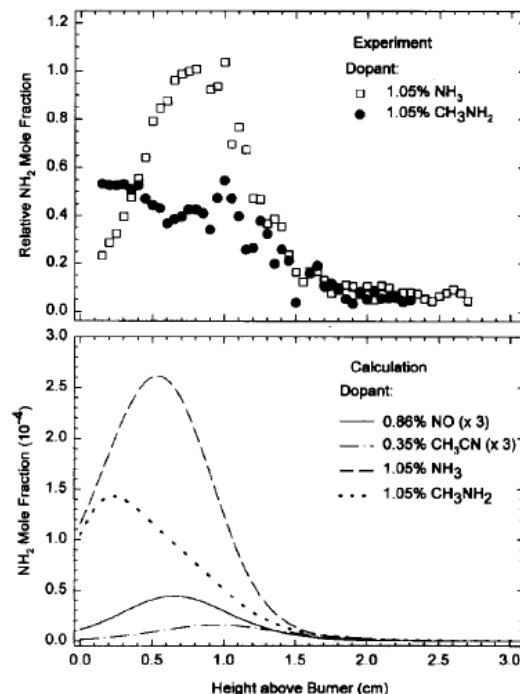


Figure 21: Measured NH_2 profiles in the methane doped with 1.05% NH_3 and CH_3NH_2 flames, and calculated profiles for the four dopants ($T= 600\text{-}2000$ K, $P= 0.001$ MPa). Figure extracted from Williams and Fleming, 1997.

II. State of the art on the molecules studied as part of the thesis

In 2002, **Hughes et al.** used laser-induced fluorescence to observe NO in methane/oxygen/argon laminar flames doped with ammonia and sulfur dioxide at low pressure ($P=0.005-0.013$ MPa) and intermediate temperature (400-1400 K). The proposed detailed chemical mechanism consists of the Leeds methane oxidation mechanism (Hughes et al., 2001) with added reactions that describe both NO_x and SO_x chemistry in combustion systems. Sensitivity analysis has been used to highlight the important reactions ($NH + SO = NO + SH$, $N + SO = NO + S$) for NO formation.

Later, **Rahinov et al. (2006)** measured the absolute NH₂ radical mole fraction by intracavity laser absorption spectroscopy (ICLAS) in methane/air laminar flat flames doped with ammonia ($T=373-2000$ K, $P= 0.004$ MPa). **Compared to Williams et al. (1997)**, they were able to obtain a good signal-to-noise ratio when only 0.14% NH₃ was added to methane/air flame. They pointed out that the peak NH₂ radical concentration was independent of the equivalence ratio. The use of the detailed ammonia oxidation mechanism proposed by **Skreiberg et al. (2004)** predicted the experimental data well. In 2009, **Tian et al.** investigated NH₃/CH₄/O₂/Ar flames at low pressure under stoichiometric conditions with the combustion products identified by molecular-beam mass spectrometry with tunable synchrotron vacuum ultraviolet photoionization. The reaction zone was widened with the increase of the NH₃/CH₄ ratio. Computational results showed that the mechanism proposed by **Skreiberg et al. (2004)** could predict the concentration profiles of major species and intermediates. More recently, **Li et al. (2013)** performed an experimental study of CH₄ + air flames doped with NH₃ at atmospheric pressure and temperature ranging from 1980-2200 K. Laser-induced fluorescence and probe sampling were adopted to measure NO concentrations. Ammonia conversion data were accurately reproduced by the models developed by **(Konnov, 2009)** and **(Skreiberg et al., 2004)**, which indicated that these models were reliable.

For non-premixed flame, **Sullivan et al. (2002)** investigated ammonia conversion and NO_x formation in laminar coflowing non-premixed methane-air flames with temperatures ranging from 300-1800 K. Flue gases from the reactor were dehumidified through a water trap upstream of Hartmann & Braun gas analyzers for measurement of O₂, NO, CO₂ and CO concentrations. It was found that the conversion efficiency of NH₃ to NO decreased from 50% at low ammonia mole fraction (<100 ppm)

to less than 30% at higher ammonia mole fraction (>800 ppm). Better agreement between experiment and model was found using the mechanism (Glarborg et al., 1998) compared to GRI 3.0 mechanism (Smith et al., 1999).

In 2005, **Grcar et al.** studied the effects of mixing on ammonia oxidation at temperatures below those in self-sustaining flames (900-1500 K) in a flow reactor. Dilute streams of methane-ammonia and oxygen-steam were commingled in an isothermal environment. The concentrations of NO, CO, CO₂ and O₂ were determined by continuous gas analyzers. It was found that NO was sensitive to mixing. At low temperatures, high levels of NO were found only in the premixed reaction zone, at higher temperatures a much lower NO production was found in a non-premixed reaction zone.

With the increasing interest in biogas fuels as substitutions for fossil fuels, reliable experimental data for oxidation of methane doped with ammonia under bath gas carbon dioxide become essential. **Konnov et al. (2006)** studied CH₄ flames doped with ammonia and measured NO mole fraction at atmospheric pressure in the post-flame zone. A Fisher Rosemount Model 951A NO/NO₂ chemiluminescence analyzer was used for measuring the concentration of NO_x. It was found that the NO_x mole fractions differed qualitatively between CH₄/O₂/N₂ flames and CH₄/O₂/CO₂ flames. NO mole fraction peaked around $\Phi=1$ under CH₄/O₂/N₂ flames, which peaked in the fuel-rich side under CH₄/O₂/CO₂ flames.

After that, **Mendiara and Glarborg (2009)** investigated experimentally the oxidation of NH₃ during the oxy-fuel combustion of methane in a plug flow reactor (T=973-1773 K, P=0.101 MPa) and interpreted the results in terms of a detailed chemical kinetic model. The composition of the gas leaving the reactor was analyzed through a series of continuous gas analyzers. Two Rosemount NGA 2000 MLT infrared gas analyzers determined the concentration of NO and CO/CO₂, respectively. The results showed that a high CO₂ level (90%) enhanced NO formation under reducing conditions, while it inhibited NO production under stoichiometric and lean conditions. According to the authors, the enhanced CO concentrations and alteration in the amount and partitioning of O/H radicals were responsible for the effect of the high CO₂ concentration on the NH₃ conversion as shown in [Figure 22](#).

II. State of the art on the molecules studied as part of the thesis

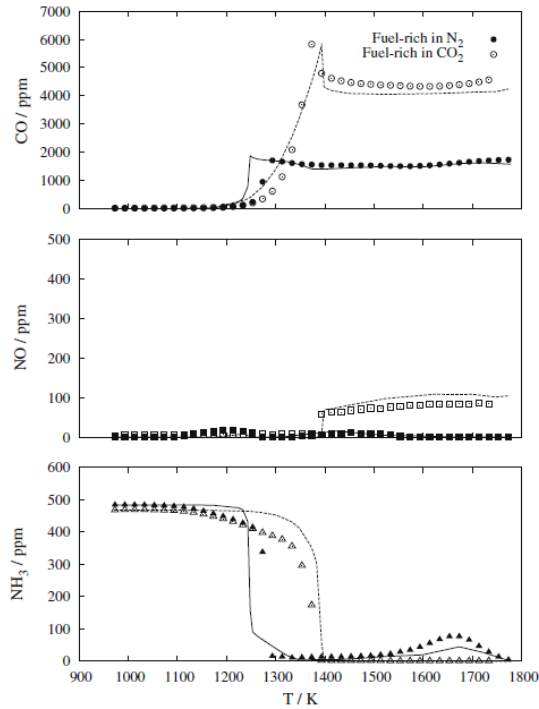


Figure 22: Experimental data and modeling predictions for oxidation of CH_4/NH_3 in fuel-rich conditions, under 0.101 MPa. Closed symbols represent the experimental data, balance in N_2 and open symbols for CO_2 to balance. Modeling predictions are shown as solid lines for N_2 and dashed lines for CO_2 . Figure extracted from Mendiara and Glarborg, 2009.

Recently, **Barbas et al. (2015)** focused on the oxy-fuel combustion of methane doped with ammonia at temperatures ranging from 1200-1900 K in a premixed laminar flame. The analytical instrument included a magnetic pressure analyzer for O_2 , a non-dispersive infrared gas analyzer for CO_2 and CO , a flame ionization detector for hydrocarbons and a chemiluminescent analyzer for NO_x . It was found that the mole fractions of CO and NO decreased under fuel-lean conditions. The chemical kinetic mechanism used in this work was developed by **Mendiara and Glarborg (2009)**. HNO is the main intermediate which reacts with H to form NO .

After the start of my PhD, **Okafor et al. (2020)** investigated the formation and control of emissions from the combustion of $\text{CH}_4/\text{NH}_3/\text{air}$ with up to 30% ammonia by heat fraction in gas turbine combustors. They studied the flow field, flame structure and emissions characteristics of a micro gas turbine swirl combustor using Particle Image Velocimetry (PIV), and Planar Laser Induced Fluorescence (PLIF) imaging, in addition to Fourier Transform Infrared (FTIR) spectroscopy. It was found that the higher flame speed of $\text{CH}_4/\text{NH}_3/\text{air}$ mixtures ensured lower NO_x production in the

II. State of the art on the molecules studied as part of the thesis

secondary combustion zone. Rich-lean premixed combustion at 0.25 MPa provided low emissions such as 49 ppmv of NO_x, 2 ppmv of CO and approximately zero N₂O, HCN and NH₃ with a combustion efficiency of 99.8%.

Despite the abundant experimental data on ammonia addition during methane combustion, to our knowledge, there is no systematic experimental study of the influence of operating variables (ammonia concentration, low to intermediate temperatures) on the oxidation of methane doped with ammonia in a jet-stirred reactor.

II.1.3 Ammonia doped with hydrogen

Due to its weak combustion properties, co-firing of ammonia with a combustion enhancer (e.g., hydrogen, methane or coal) is one of the proposed solutions to allow its use in gas turbines, engines or industrial furnaces (Kobayashi et al., 2019; Xiao et al., 2017; Reiter and Kong, 2011). A comprehensive understanding of ammonia mutual interaction with species like hydrogen is essential for designing efficient industrial processes and controlling undesired emissions. Several studies have dealt with the oxidation of ammonia doped with hydrogen as shown in [Table 13](#) and [Table 14](#).

Table 13: Summary of LBV studies of ammonia-hydrogen flames.

Instrument	Experimental Conditions	Bath gas	H ₂	Reference
Burner	T=293 K; P= 0.101 MPa; Φ =0.5-1.10	Air	0-20 % in the fuel	(Kumar and Meyer, 2013)
	T=293 K; P= 0.101 MPa; Φ =1.0 - 1.25	Air	33.3-60% in the fuel	(Li et al., 2014)
	T=300–1100 K; P=0.1-25 MPa; Φ =0.5–1.7	Air	0–60 mol% in thr fuel	(Goldmann et Dinkelacker, 2018)
	T=298 K; P= 0.101 MPa; Φ =0.7-1.6	Air	15-40% in the fuel	(Han et al., 2019)
	T=298-473 K; P= 0.101 MPa; Φ =0.8–1.4	Air	0–60 vol% in the fuel	(Lhuillier et al., 2020)
CVB	T=293 K; P= 0.101 MPa; Φ =0.6-1.67	Air	-	(Lee et al., 2010)
	T=298 K; P= 0.101-0.507 MPa; Φ =1.0	Air	-	(Ichikawa et al., 2015)
	T=445 K; P= 0.54 MPa; Φ =0.9,1.0,1.1	Air	0–15 vol% in the fuel	(Lhuillier et al., 2021)

II. State of the art on the molecules studied as part of the thesis

Table 14: Summary of ignition delay time studies during ammonia-hydrogen oxidation.

Instrument	Experimental Conditions	Bath gas	H ₂	Reference
Rapid Compression Machine	T=1000-1100 K; P=4.3 & 6.5 MPa; Φ=0.2-0.5	Ar & N ₂	0-25 vol % in fuel	(Pochet et al., 2019)
	T=950-1150 K; P=2-6 MPa; Φ=0.5- 2.0	Ar & N ₂	0-20% in fuel	(He et al., 2019)
	T=1040–1210 K; P 2-7.5 MPa; Φ=0.5-3.0	Ar & N ₂	0-10% in fuel	(Dai et al., 2020)

Several experimental studies have considered enhancing the combustion of NH₃ by mixing it with H₂, which could conveniently be obtained from ammonia decomposition, leading to a significant increase in the LBV and extending the flammability ranges as shown in Figure 23.

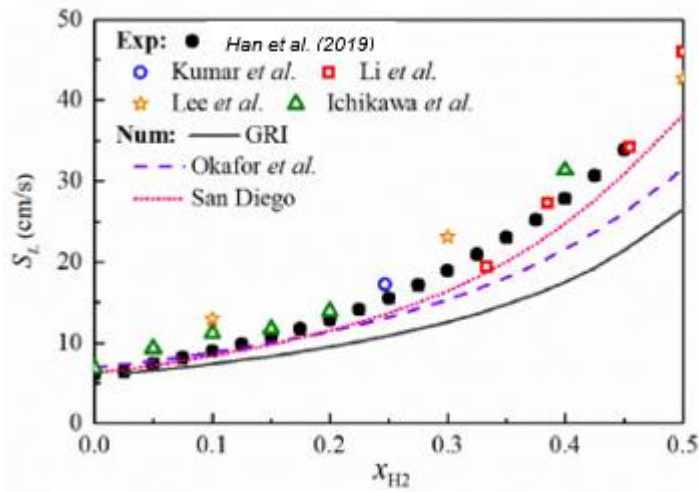


Figure 23: LBV of stoichiometric NH₃/H₂/air flames ($P= 0.101$ MPa), as a function of H₂ mole fraction, measured in the works of Han et al. (2019), Kumar et al. (2013), Li et al. (2014), Lee et al. (2010), Ichikawa et al. (2015), and predicted LBV using three mechanisms. Figure extracted from Han et al., 2019.

Lee et al. (2010) investigated the combustion properties of NH₃/H₂/air in CVB as a function of the hydrogen fraction in the fuel blend, for several equivalence ratios from fuel-lean to fuel-rich at Normal Temperature and Pressure (NTP). After that, Kumar and Meyer (2013) conducted experimental and modeling study of laminar flame speeds for premixed NH₃/H₂/air jet flames for 0–80% NH₃ in H₂ by energy and

for equivalence ratios from 0.5 to 1. **Li et al. (2014)**, by using the Bunsen burner method, provided LBV measurements for various $\text{NH}_3/\text{H}_2/\text{air}$ mixtures at NTP as a function of the equivalence ratio. **Ichikawa et al. (2015)** studied the LBV and Markstein length of several $\text{NH}_3/\text{H}_2/\text{air}$ stoichiometric mixtures by means of the OPSF method also at 298 K but for an initial pressure ranging from 0.1 to 0.5 MPa. Recently, **Han et al. (2019)** reported LBV measurements obtained by means of the heat flux method, with NH_3 blended with H_2 , CO or CH_4 as fuels and air as the oxidizer at NTP. Kumar and Meyer conducted Bunsen burner experiments for different NH_3/H_2 blends at NTP, but their results contradict those of the previously mentioned studies. Recently, **Lhuillier et al. (2020)** reported LBV data for $\text{NH}_3/\text{H}_2/\text{air}$ mixtures measured by means of the outwardly propagating spherical flame method at 1 atm, for previously unseen unburned gas temperatures ranging from 298 to 473 K, hydrogen fractions ranging from 0 vol% to 60 vol% in the fuel and equivalence ratios. It was concluded that increasing hydrogen fraction and temperature increases velocities, with maximum values obtained for rich mixtures near stoichiometry. More recently, **Lhuillier et al. (2021)** investigated the effect of hydrogen and methane enrichment on the LBV at 445 K, $P=0.54$ MPa, $\phi=0.90-1.10$. It was noticed that adding H_2 or CH_4 to the NH_3 fuel induces the same LBV increase at $\phi = 0.9$ and similar effects at $\phi = 1.0$ and 1.1.

There was also research on the oxidation of NH_3/H_2 in a Rapid Compression Machine (RCM). **Pochet et al. (2018)** investigated the ignition delay times of NH_3/H_2 mixtures (0, 10 and 25% vol. H_2) at fuel lean conditions ($\Phi = 0.2, 0.35, 0.5$), high pressures (43 and 65 bar) and intermediate temperatures (1000–1100 K) in an RCM. In 2019, **He et al. (2019)** studied the ignition delay times of NH_3 and NH_3/H_2 mixtures (1–20% vol. H_2) measured in an RCM at pressures from 2 to 6 MPa, temperatures from 950 to 1150 K, and equivalence ratios from 0.5 to 2. More recently, **Dai et al. (2020)** measured auto-ignition delay times of NH_3 and NH_3/H_2 mixtures in a rapid compression machine at pressures from 2–7.5 MPa and temperatures in the range 1040–1210 K. It was shown that hydrogen addition has a significant ignition-enhancing effect on NH_3 , 5% H_2 addition can reduce the ignition delay times by a factor of ~ 28 at $\Phi = 1$ as shown in [Figure 24](#).

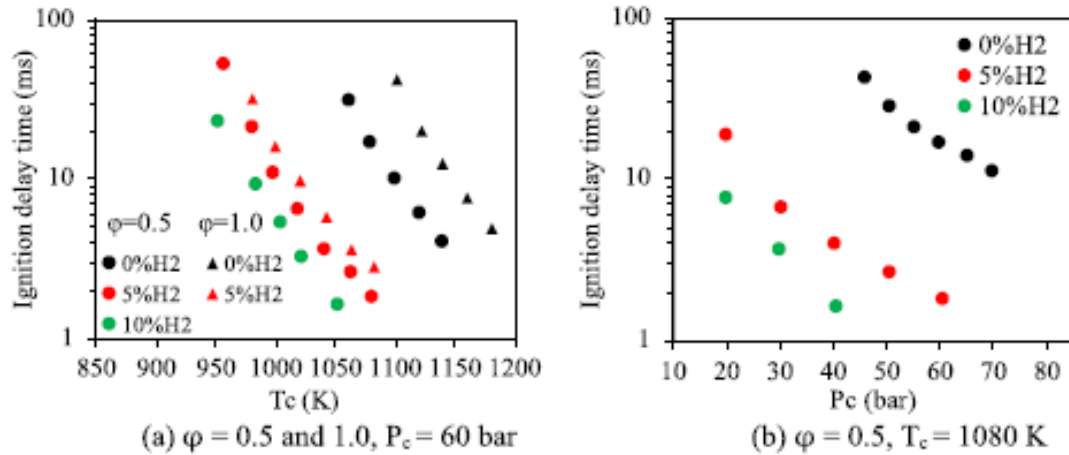


Figure 24: Effect of H₂ addition on the ignition delay times of NH₃/H₂ mixtures at $\phi = 0.5$ (circles) and $\phi = 1.0$ (triangles). (a) isobars, (b) isotherms. Figure extracted from Dai et al., 2020.

The oxidation and pyrolysis of ammonia doped with hydrogen in jet-stirred and flow reactors are still missing in the literature. These data will be valuable for refining detailed kinetic models though more constrained validation tests.

II.1.4 Hydrogen sulfide

Hydrogen sulfide is also a trace compound present in biogas. Moreover, the increasing importance of unconventional fuel sources, such as sour and shale gas (biogas with significant amounts of H₂S up to 3% content in volume), brings interest to the direct use of these fuels, developing technologies and combustion processes focused on their knowledge and understanding under high temperature and pressure conditions. The literature reviews on the experimental studies of the oxidation of neat hydrogen sulfide are shown in Table 15.

II. State of the art on the molecules studied as part of the thesis

Table 15: Summary of Hydrogen sulfide oxidation studies.

Instrument	Experimental Conditions	Bath gas	H ₂ S	Reference
Shock tube	T= 950–1200 K; P= 0.101 MPa	Air	4-22 % in Air	(Frenklach et al., 1981)
Ignition vessel	T= 293 K; P= 0.1 MPa	Air	-	(Pahl and Holtappels, 2005)
Flow reactor	T= 950–1150 K; P= 0.101 MPa; Fuel lean condition	N ₂	100-520 ppm	(Zhou et al., 2013)
	T= 450–925 K; P = 3-10 MPa; $\Phi = 0.029-0.94$	N ₂ or CO ₂	750-800ppm	(Song et al., 2017)
	T= 700–1400 K; P= 0.101 MPa; $\Phi = 0.05-3.0$	N ₂	476-514 ppm	(Colom-Díaz et al., 2019a)
	T= 500–1000 K; P= 0.06–4 MPa; $\Phi = \sim 0.5$	N ₂	500 ppm	(Colom-Díaz et al. 2019b)

In 1972, **Cullis and Mulcahy (1972)** studied the kinetics of combustion of gaseous sulphur compounds. In 2000, the significant progress in the understanding of the kinetics and mechanisms of the atmospheric oxidation chemistry of sulfur in the last decades was reviewed by **Gardiner et al. (2000)**, which indicated the less effort placed on developing and understanding sulfur combustion kinetics. After that, **Bongartz and Ghoniem (2015)**, optimized a detailed chemical kinetics mechanism for oxy-fuel combustion of mixtures of hydrogen sulfide and methane. Recently, **Cong et al. (2016)** developed a detailed and reliable reaction mechanism for the high temperature pyrolysis of H₂S to form H₂ and S₂ under different operating conditions.

Hydrogen sulfide oxidation has been studied since 1981, **Frenklach et al. (1981)** performed the experiments and studied the kinetic models of the oxidation of hydrogen sulfide in a shock tube (950-1200 K, 1 atm). They determined the ignition delays in dry air from 40 runs in order to be subjected to a regression analysis to determine the best Arrhenius type fit for ignition delay. After that, **Pahl and Holtappels (2005)** studied the explosion limits of the two ternary gas systems H₂S/CO₂/air and H₂S/N₂/air determined at 293 K and 1 bar according to the bomb method of the new European standard EN 1839. In 2014, **Selim et al. (2014)** investigated the effect of

acid gas (H_2S and CO_2) addition in hydrogen/air flame. It was found that the presence of carbon monoxide triggered the formation of other sulfurous–carbonaceous compounds, such as COS and CS_2 . Additionally, **Zhou et al. (2013)** conducted the oxidation of H_2S in a flow reactor under fuel-lean conditions (950-1150 K, 1 atm).

Last few year, **Song et al. (2017)** performed the oxidation of H_2S under lean to stoichiometric conditions in a flow reactor, at high pressure (3–10 MPa) as a function of temperature (600–925 K). The results were analyzed in terms of a detailed chemical kinetic model based on the work of Zhou et al. as shown in [Figure 25](#). It was shown that modeling predictions generally overpredicted the onset of reactivity (H_2S & SO_2).

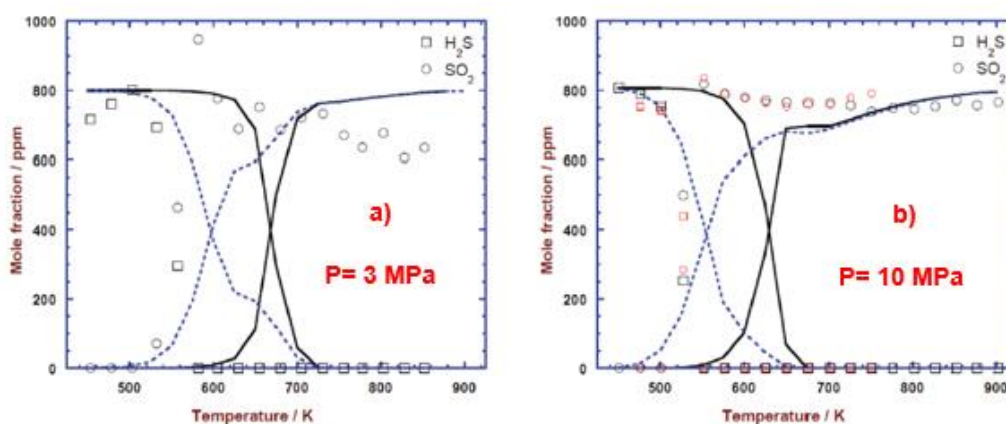


Figure 25: H_2S (~ 800-ppm) oxidation under oxidizing conditions ($\phi = \sim 0.285$) at 3 MPa (a) and 10 MPa (b). Experimental data were obtained in a quartz (black symbols) and an alumina (smaller red symbols) tubular reactor, respectively. Modeling predictions are shown as solid lines. The dashed line denotes predictions omitting the $\text{H}_2\text{S} + \text{O}_3$ reaction. Figure extracted from Song et al., 2017.

After the start of my PhD, **Colom-Díaz et al. (2019a)** conducted H_2S oxidation in a tubular flow reactor at atmospheric pressure, in the 700-1400 K temperature range. They developed the mechanism that had been used to simulate their experimental results, together with data from the literature, obtaining a fairly good agreement under the different conditions. Furthermore, **Colom-Díaz et al. (2019b)** performed the oxidation of H_2S under high pressure (0.06–4 MPa), in the temperature range of 500–1000 K and under slightly oxidizing conditions. It was shown that the pressure has a larger role than gas residence time on the oxidation rate. The kinetic model for high pressures seems to work fairly well at different pressures, except for the experiment at 4 MPa, there is a gap of 50 K in temperature between experimental concentrations and model predictions as shown in [Figure 26](#).

II. State of the art on the molecules studied as part of the thesis

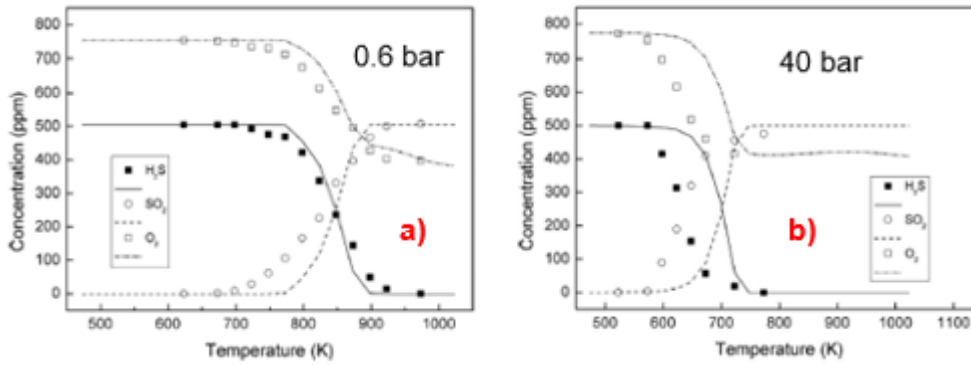


Figure 26: Experimental results of H₂S (505 ppm) oxidation in a flow reactor at 0.06 MPa for $\phi=0.503$ (a). Experimental results of H₂S (500 ppm) oxidation at 4 MPa for $\phi=0.485$ (b). Experimental data are shown as symbols, modeling predictions as lines. Figure extracted from Colom-Díaz et al., 2019.

During my PhD, Colom-Díaz et al. (2021) published a paper in which they investigated H₂S and CH₃SH oxidation in a JSR under atmospheric pressure with $\phi = 1, 0.5$ and 0.25 . The inlet mole fraction of H₂S was about 2000 ppm and the residence time was 1 s, using N₂ as bath gas. SO₂ was the only product which was detected. The model developed by Colom-Díaz et al. (2019) was used in the case of H₂S oxidation. The simulation data matched very well their experimental results but less for $\phi = 0.2$ as shown in Figure 27. These authors did not report any catalytic effects and no wall coating procedure was applied.

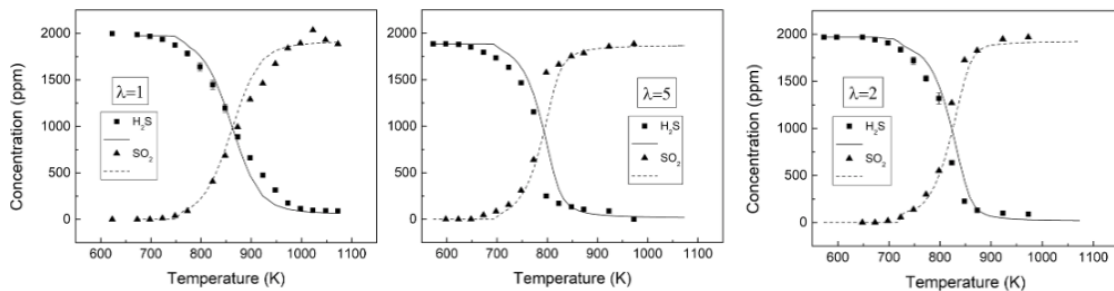


Figure 27 : Concentration of H₂S and SO₂ as function of temperatures. Symbols represent experimental concentration, while lines denote model predictions. (figure retrieved from Colom-Díaz et al., 2021).

The lack of data in literature justified the investigation of the oxidation and pyrolysis of hydrogen sulfide in a jet-stirred reactor.

II.1.5 Methane doped with hydrogen sulfide

Hydrogen sulfide (H_2S) is a by-product from cleaning of natural gas and synthesis gas produced from gasification of coal or biomass, from hydrodesulfurization of light hydrocarbons, and from upgrading heavy oils and coals. It is also released from sulfur-containing fuels during pyrolysis or formed under very reducing conditions in combustion processes. Hydrogen sulfide is detected from various biomass sources generating biogas. Several literature studies have dealt with the oxidation of methane doped with hydrogen sulfide as shown in Table 16.

Table 16: Summary of Methane doped with hydrogen sulfide oxidation studies.

Instrument	Experimental Conditions	Bath gas	H_2S	Reference
Burner	T= 500-1500 K; P= 0.101 MPa; Φ =0.5-3.0	Air	0.2-1.3%	(Selim et al., 2011)
	T= 500-1500 K; P= 0.101 MPa; Φ =0.5-3.0	Air	0.2-1.3%	(Selim et al., 2012)
	T= 700-1100 K; P= 0.101 MPa; Φ =1.0-2.0	Air	5.4-9.7%	(Li et al., 2017)
CVB	T= 295K; P= 0.101 MPa; Φ =0.7-1.4	Ar	8.25%	(Mulvihill et al., 2019)
Clause furnace	T= 1050-1600 K; P= 0.11-0.18 kPa; Φ =2.45-3.68	N_2	1.65-2.45%	(Chin et al., 2001)
Flow reactor	T= 1223-1423 K; P= 0.1 MPa; Φ =0.4-0.6	CO_2	131 ppm	(Jerzak et al., 2016)
	T= 600-900 K; P= 5 MPa; Φ =1.1-22.8	N_2	200 ppm	(Gersen et al., 2017)
	T= 500-1400 K; P= 0.1-4 MPa; Φ = 0.22-5.73	N_2	279-1295 ppm	(Colom-Díaz et al., 2020)
Shock tube	T= 930-1050 K; P= 3-8 MPa; Φ =0.5	Ar	0.052%	(Gersen et al., 2017)
	T= 1538-2144 K; P ~ 0.101 MPa ; Φ =0.5	Ar	0.0638%	(Mulvihill et al., 2019)

In 2011, **Selim et al.** investigated the hydrogen sulfide oxidation in methane/air mixture. A double concentric tubular reactor burner was used wherein air is premixed with methane and injected into the annulus of the burner and hydrogen sulfide was injected into the central tube. A suction pump was connected to the sampling line to introduce the sampled gas to GC (TCD, FPD). Samples were taken along the

longitudinal centerline of the reactor. The analysis of combustion products revealed that H₂S reaction started with thermal and chemical decomposition to form hydrogen. The role of sulfur dioxide as a coupling catalyst enhanced the dimerization of CH₃ radical to form a series of higher hydrocarbons under fuel-rich conditions. Later, **Selim et al. (2012)** ran another set of experiments with spatial gas sampling carried out both axially and radially along the reactor. Reactant and bath gases were injected into the annulus of the burner; the center tube was not used here. The absence of higher hydrocarbons around the centerline validated the hypothesis of SO₂ effect as a coupling catalyst. Reactants being premixed prior to combustion enhanced the oxidation competition between H₂S and CH₄, which led the reaction of H₂S to form SO₂ rather than S₂. Methane reacted with sulfide compounds to form CS₂.

For non-premixed flames studies, **Li et al. (2017)** conducted H₂S and CH₄ (molar ratio, 1:1) oxidation experiment under stoichiometric to fuel-rich flames at atmospheric pressure. The initial concentration of CH₄ was much higher than that of acid gas. However, it allows to focus on the competition between H₂S and CH₄ under fuel-rich conditions. The gas composition was analyzed by GC-TCD/FID/FPD. It was found that the primary conversion of H₂S occurred at the burner tip, and mainly consisted of partial oxidation, while CH₄ oxidation occupied further in the flame. The formation of SO₂ was promoted by sufficient oxygen supply. The initial formation of CS₂ and COS occurred mainly due to reactions between H₂S and S₂ with hydrocarbons.

In 2001, Chin et al. investigated the competition between hydrogen sulfide and methane with oxygen in the reaction furnace environment of a Claus plant. A stream of the quenched product gas was analyzed by GC. It was found that the hydrogen sulfide reaction was much faster than the methane oxidation reaction in the temperature range from 1273-1473 K. There was an increased consumption of H₂S and SO₂ in the presence of methane. After that, **Jerzak et al. (2016)** studied the effect of the CO₂ content of biogas on the process of oxidation of H₂S to SO₂ with temperature ranging from 1223-1423 K in a flow reactor. H₂S concentration was determined by LAND Lancom Series analyzer; CO, CO₂ and SO₂ concentrations were detected by Horiba PG350 analyzer. It demonstrated that the oxidation of H₂S was

II. State of the art on the molecules studied as part of the thesis

inhibited by an increase of CO₂ concentration in biogas. The decisive role in the SO₂ formation process was by the reactions: $\text{SH} + \text{O}_2 = \text{H} + \text{SO}_2$ and $\text{SO} + \text{O}_2 = \text{SO}_2 + \text{O}$.

After that, **Gersen et al. (2017)** investigated the autoignition and oxidation behavior of CH₄/H₂S mixtures (T=600-1050 K, P=30-80 bar) in a shock tube and flow reactor, respectively. The product analysis was conducted by GC-TCD/FID. A model was drawn from recent work of **Hashemi et al. (2016)** and **Song et al. (2017)**. It was found that the addition of 1% H₂S to methane reduced the ignition delay times by a factor of 2 compared to neat methane. Moreover, flow reactor results showed that a large part of H₂S was consumed already at 600 K, while temperatures around 775 K were needed to oxidize 10% methane as shown in [Figure 28](#). It was concluded that more work would be desirable on the reactions of H₂S and SH with peroxy radicals (HO₂ and CH₃OO).

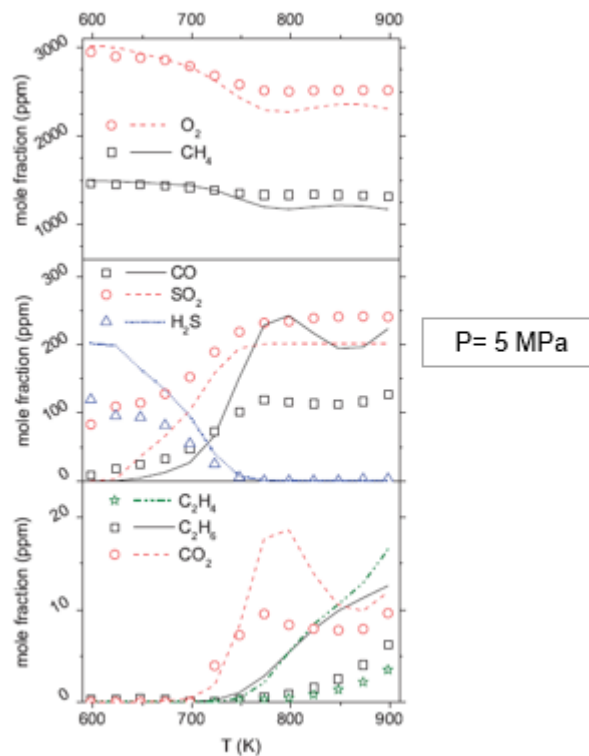


Figure 28: Results of experiments with CH₄/H₂S for $\Phi = 1.1$ in a flow reactor at 5 MPa. Inlet composition: 1500 ppm CH₄, 3010 ppm O₂, 200 ppm H₂S; balance in N₂. τ (s) = 5920/T (K). Experimental data are shown as symbols, modeling predictions as lines. Figure extracted from Gersen et al., 2017.

More recently, **Mulvihill et al. (2019)** studied the first shock-tube data as well as laminar flame speeds measured in the H₂S/CH₄ system. The study demonstrated

that the added H₂S has an inhibiting effect on $S_{L,u}^0$ as compared to pure CH₄, though only at $\Phi \geq 1$ as shown in Figure 29. This result is due to competition for H atoms by several sulfur reactions. The reaction $SO+H(+M) = HSO (+ M)$ was particularly important at $\Phi \geq 1$. Moreover, several of the most-sensitive sulfur reactions contained C/S species, which may contribute to the slight differences between the present model and an older model that did not contain such species.

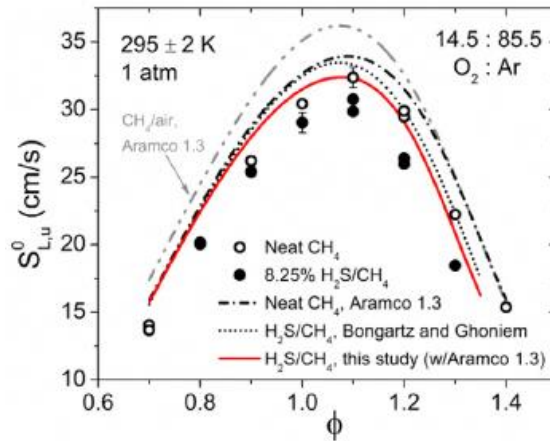


Figure 29: Laminar flame speed measurements of neat CH₄ and 8.25% H₂S/CH₄ in 14.5% O₂, 85.5% Ar. Solid line: model prediction (Mulvihill et al., 2019), dash-dot line: (Metcalf et al., 2013), dotted line: (Bongartz and Ghoniem, 2015). Also shown for comparison is a CH₄/air curve from (Metcalf et al., 2013). Figure extracted from Mulvihill et al., 2019.

After the start of my PhD, **Colom-Díaz, et al. (2020)** investigated the oxidation of CH₄/H₂S mixtures in two different flow reactor setups, at different pressures, in the temperature range of 500–1400 K. It was found that H₂S promotes CH₄ oxidation to lower temperatures. The presence of CH₄ inhibits the oxidation of H₂S under near atmospheric pressure, being this inhibition less important at higher pressures. The kinetic model predicts fairly well the trend of CH₄ and H₂S evolution. However, in the case of H₂S, the model does not capture accurately the experimental results under near atmospheric pressure and 40 bar, which might be related to H₂S conversion chemistry.

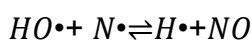
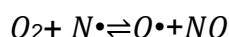
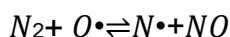
Nevertheless, the above-mentioned studies were mostly conducted under nitrogen dilution atmospheres, the studies for oxidation of methane doped with hydrogen sulfide under bath gas carbon dioxide are scarce. To our best knowledge, no experiments concerning the oxidation of methane doped with hydrogen sulfide

were conducted in a jet-stirred reactor. Considered as the second main component (CO₂) of biogas, it is of great interest to perform experimental and model work for methane and hydrogen sulfide interaction under bath gas carbon dioxide. Note that the above-mentioned studies highlighted a high reactivity of hydrogen sulfide compared to that of methane.

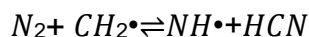
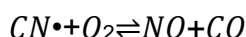
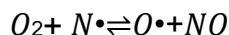
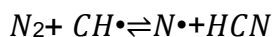
II.2 Formation of NO_x

The origin of the pollutant nitric oxides (NO_x) comes from the combustion systems of nitrogen in air or the fuel. NO_x essentially consist of two molecules: NO and NO₂. Two processes have been identified whereby atmospheric N₂ produces NO;

- The Zel'dovich mechanism (Thermal NO_x (Zeldovich, 1946)) requires nitrogen in air to combine with O and OH radicals;



- Fenimore's prompt (1971) scheme is an attack on N₂ by some hydrocarbon fragment;



In 2000, **Moskaleva and Lin (2000)** theoretically investigated the kinetics and mechanism for the CH + N₂ reaction. It was found that the major pathway of the CH + N₂ reaction to prompt NO formation occurs by the spin-conserved ground electronic doublet surface, forming H + NCN instead of HCN + N, products first suggested by **Fenimore (1971)**. Since that time, many studies have focused on NCN radical. Research studies on the formation of NO_x during the oxidation of hydrocarbons and alcohols have been reported as shown in [Table 17](#).

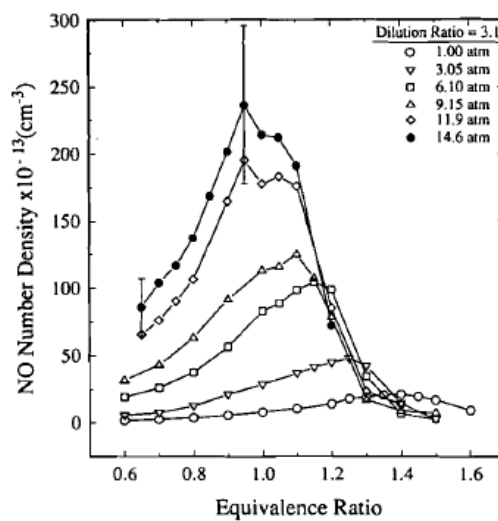
II. State of the art on the molecules studied as part of the thesis

Table 17: Summary of the formation of NO_x studies, all performed using laminar premixed flame burners.

Experimental Conditions	Bath gas	Fuels	Reference
T= 2112–2367 K; P=0.1-0.3 MPa; Φ = 0.8-1.6	N ₂ , Air	CH ₄ , C ₂ H ₆ , C ₃ H ₈ , CO	(Fenimore, 1971)
T= 1900-2350 K; P=0.101 MPa; Φ = 0.05-1.18	N ₂ /H ₂	CH ₄ , C ₂ H ₂ , CH ₃ CCH	(Hayhurst and Vince, 1977)
T=1100–1400 K; P=0.004 MPa; Φ = 0.5, 1 & 1.5	Ar	HCN/H ₂	(Miller et al., 1984)
T= 405–1672 K; P=0.004, 0.009 & 0.015 MPa; Φ = 1.13	Air	CH ₄	(Heard et al., 1992)
T= 1000-2000 K; P=0.001 MPa; Φ = 0.94-1.0	Ar	CH ₄ /NO _x	(Williams and Fleming, 1994)
T= 1660-1960 K; P=0.101-1.42 MPa; Φ = 0.5-1.6	N ₂	CH ₄	(Klassen et al., 1995)
T= 1750-2060 K; P=0.003-0.004 MPa; Φ = 0.8, 1.07 and 1.27	N ₂	CH ₄	(Berg et al., 1998)
T= 300-1800 K; P=0.001 MPa; Φ = 0.8-1.2	N ₂	CH ₄	(Gasnot et al., 1999)
T= 1550–1830 K; P=0.004 MPa; Φ = 0.7, 1, and 1.25	N ₂	CH ₄ , C ₂ H ₆ , C ₃ H ₈	(Pillier et al., 2005)
T= 1700-2000 K; P=0.001 MPa; Φ = 0.6-1.2	N ₂	CH ₄ , C ₃ H ₈	(Williams and Fleming, 2007)
T= 1890 K; P=0.005 MPa; Φ = 0.76-0.94	N ₂	CH ₄	(Lamoureux et al., 2008)
T= 1575-1830 K; P=0.005 MPa; Φ = 1 and 1.25	N ₂	CH ₄ , C ₂ H ₂	(Lamoureux et al., 2010)
T= 1900-2000 K; P=0.003-0.004 MPa; Φ = 1 and 1.25	N ₂	CH ₄ , C ₂ H ₆ , C ₃ H ₈ , C ₄ H ₁₀ ,	(Sutton et al., 2012)
T=2000 K; P=0.101 MPa; Φ = 1 and 1.3	Air	C ₁ –C ₃ alkanes and alcohols	(Watson et al., 2016)
T=2000 K; P=0.101 MPa; Φ = 1.3	Air	C ₁ –C ₄ alkanes, alcohols	(Watson et al., 2017)
T= 1841–2251 K; P=0.1-0.7 MPa; Φ = 0.7, 1 and 1.2	N ₂	CH ₄	(De Persis et al., 2020)

II. State of the art on the molecules studied as part of the thesis

In 1971, **Fenimore (1971)** studied the formation of NO in hydrocarbon flames (methane, ethylene, propane diluted with N₂-O₂ mixtures) under 0.1 to 0.3 MPa, $\phi=0.8-1.6$. It was found that high pressures and fuel-rich mixtures promote the formation of NO. In 1976, **Hayhurst and Vince (1976)** reported NO mole fraction profiles in hydrocarbon flames (CH₄, C₂H₂, CH₃CCH), under 0.1 MPa, $\phi=0.05-1.18$. It was observed that the larger the hydrocarbon molecule, the more the formation of NO increases. After that, **Miller et al. (1984)** studied the conversion of HCN to NO and N₂ in H₂/O₂/HCN/Ar flames at low pressures (0.004 MPa). It was deduced that the nitrogen atom in HCN predominantly follows the following route to NO and N₂; HCN → NCO → NH → N → NO → N₂. In 1992, **Heard et al. (1992)**, studied the Prompt-NO formation in methane/air flames under low pressures (0.004-0.015 MPa) and $\phi=1.13$. It was reported that the key reactions controlling prompt NO are CH + N₂. However, the CH concentration profile is not in such good agreement with the experiment. In 1994, **Williams and Fleming (1994)** investigated the formation of NO in methane flames doped with NO_x under 0.001 MPa, $\phi=0.94-1.0$ diluting in argon. The results showed that only a small fraction of the NO participates in the reburn reactions. However, the amount of reburn was under predicted (factor of 1.5-2) by the kinetic mechanism. After that, **Klassen et al. (1995)**, performed the measurements of NO formation in high-pressure premixed methane flames (up to 1.42 MPa, $\phi=0.5-1.6$). It was observed that, NO measurements under lean conditions ($\phi=0.55-0.8$) showed higher NO emissions with increasing pressure as shown in [Figure 30](#).



*Figure 30: NO concentrations in CH₄/O₂/N₂ flames under 0.10 to 1.42 MPa.
Figure extracted from Klassen et al., 1995.*

II. State of the art on the molecules studied as part of the thesis

Moreover, **Berg et al. (1998)** also studied the prompt NO formation and reburn in methane flames but at low pressures (0.003-0.004 MPa), $\Phi = 0.8$ and 1.07. The experimental results were compared to computations from the GRI-Mech 2.11 chemical mechanism and it was found that more prompt NO formed than predicted for all flames studied, ranging from fuel lean to fuel rich. After that, in 1999, the prompt NO formation in methane flames at low-pressure (0.001 MPa, $\Phi = 0.8-1.2$) was also studied by **Gasnot et al. (1999)**. Measurements were compared with computed data from three different mechanisms (MB, MBGRI 1.2, and GRI 2.11). Very satisfactory agreement was obtained with the three mechanisms for the major species and the reactive species O, H, and OH.

Pillier et al. (2005) reported CH and NO mole fraction profiles in CH_4 , $\text{CH}_4/\text{C}_2\text{H}_6$, $\text{CH}_4/\text{C}_3\text{H}_8$, and $\text{CH}_4/\text{C}_2\text{H}_6/\text{C}_3\text{H}_8$ flames, under 0.004 MPa, $\Phi = 0.7, 1$, and 1.25. It was shown that the prompt-NO mechanism is the major path leading to NO formation in stoichiometric and rich flames. It appears that NO formation is not affected when methane is substituted by low quantities (<10%) of ethane and/or propane as shown in [Figure 31](#). NO mole fraction was under predicted in lean and stoichiometric flames.

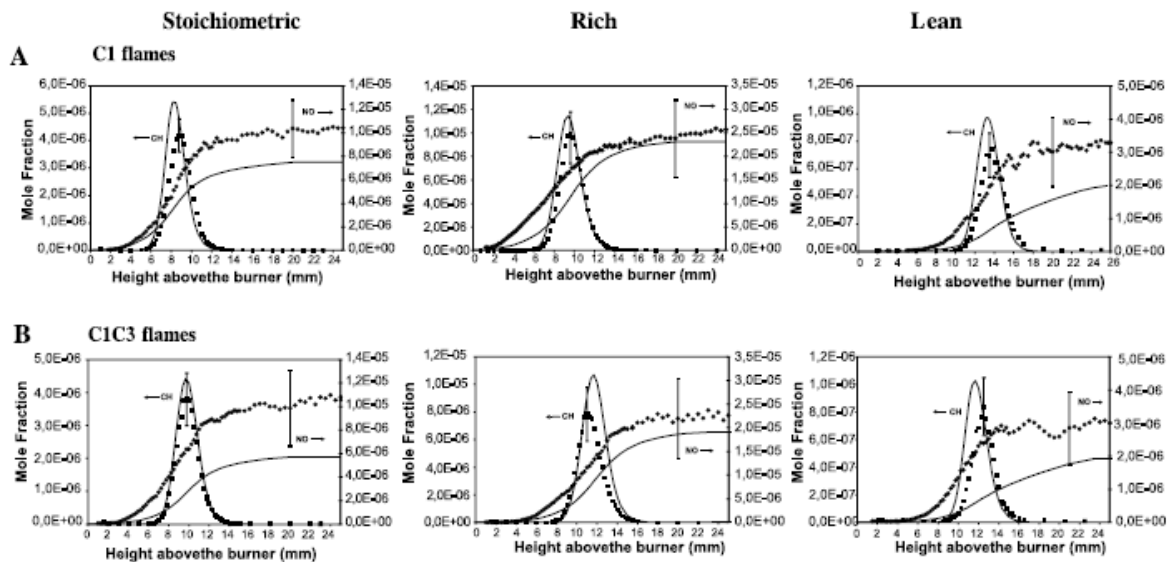


Figure 31: Experimental (symbols) and modelled (lines) mole fraction profiles of CH and NO in CH_4 (A) and $\text{CH}_4/\text{C}_3\text{H}_8$ (B) flames. Figure extracted from Pillier et al., 2005.

In 2007, **Williams and Fleming (2007)** investigated the NO formation in methane and propane flames under 0.001 MPa, $\Phi = 0.6-1.2$. It was observed that the reactions of CH_2 and C_2O with N_2 support the inclusion of these two species into NO formation schemes in these flames. The formation of prompt NO_x in methane flames seeded with methyl ethyl ketone or ethyl acetate was studied in by **Lamoureux et al, (2008)**. In 2010, **Lamoureux et al. (2010)**, also studied the role of NCN in prompt-NO formation in low-pressure ($P=0.005$ MPa) CH_4 and C_2H_2 flames ($\Phi = 1$ and 1.25). This work emphasized that possible other routes leading to NO exist in acetylene flames. The formation of NCN and prompt-NO formation in low-pressure (0.003-0.004 MPa) C1–C4 alkane flames ($\Phi = 1$ and 1.25) was studied by **Sutton et al. (2012)**. This work showed that NO concentrations ([Figure 32](#)) steadily increase as the fuel changes from methane to ethane to propane to butane for both the near-stoichiometric and rich flame conditions.

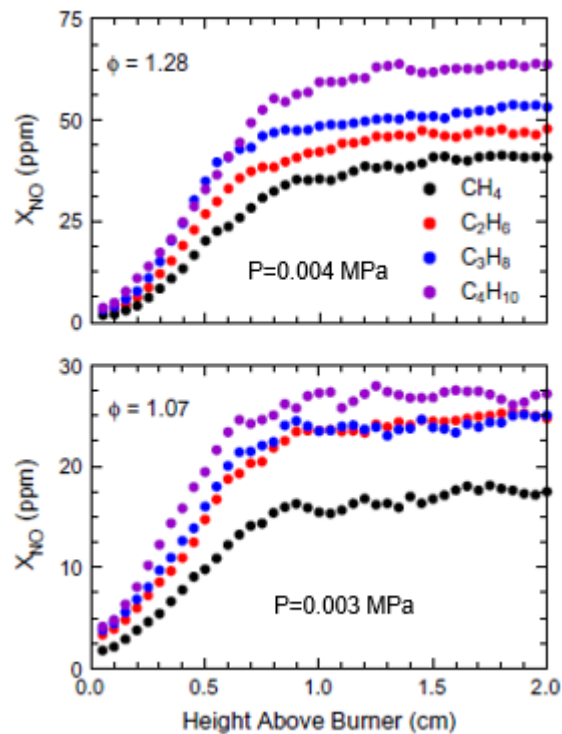


Figure 32: NO mole fractions as a function of height above the burner surface (HAB) for the $\phi = 1.28$ (top) and $\phi = 1.07$ (bottom) C1–C4 alkane flames. Figure extracted from Sutton et al., 2012.

Watson et al. (2016) investigated the formation of NO formation in premixed flames of C1-C3 alkanes and alcohols ($P = 0.101$ MPa, $\Phi = 1$ and 1.3). After that, **Watson et al. (2017)** studied the NO formation in rich premixed flames ($\Phi = 1.3$) of

C₁–C₄ alkanes and alcohols under 0.101 MPa. These two works confirm that alcohols produce less NO than alkane fuels at equivalent mixture compositions due to the slightly lower flame temperatures of the alcohol flames, and the tendency of the alcohols to produce lower concentrations of the CH radical due to inhibition of the formation of methyl groups. Recently, **De Persis et al. (2020)** investigated the NO formation in high pressure premixed flames of methane (P=0.1-0.7 MPa; Φ = 0.7, 1 and 1.2). This work allowed validating the new NO_x kinetic submechanism at high pressure, recently revised and validated in low pressure flames, jet stirred and plug-flow reactors under sub-atmospheric and atmospheric pressure conditions by **Lamoureux et al. (2016)**.

To conclude, most of the studies of NO_x formation are in flames (because of the relevant high temperatures in flames) and, to my knowledge, there is no study of the NO_x formation using a flow reactor. The lack of data in literature justified the investigation of the NO_x formation during the oxidation of CH₄, ethylene and N₂ in a flow reactor which presents the advantage of running under quite well defined operating conditions.

II.3 Bio-Oils

Bio-oils are a complex mixture of organic compounds. There are as many chemical compositions as studies on the subject. In order to describe as much possible bio-oils, the surrogate composition is composed of pyrrole and ethylene glycol. In the following part the state of the art about experimental oxidation studies on these bio-oil surrogates will be detailed.

II.3.1 Pyrrole

Pyrrole, along with pyridine, is an important component in many oil-based products and a predominant source of fuel nitrogen in coal, other low-rank fossil fuels and bio-oils. It is mainly produced from biomass from animal origins. The nitrogen atoms come indeed from the proteins present in the biomass of origin (Azargohar et al., 2013). These compounds could lead to the emissions of nitrogen oxides, which is a huge impact on human health and environment (World Health Organization, 2006).

II. State of the art on the molecules studied as part of the thesis

However, only a few research studies on the combustion of pyrrole have been reported as shown in [Table 18](#).

Table 18: Summary of Pyrrole oxidation studies.

Instrument	Experimental Conditions	Bath gas	Pyrrole	Reference
Shock tube	T= 1050–1450 K; P=0.304 MPa; $\Phi = \infty$	Ar	1.0%	(Lifshitz et al., 1989)
	T= 1200–1700 K; P=0.76-1.37 MPa; $\Phi = \infty$	Ar	700 & 5000 ppm	(Mackie et al., 1991)
	T= 1100–1800 K; P=0.2 – 0.56 MPa; $\Phi = 0.5 - 2.0$	Ar	0.5 –1.0%	(MacNamara and Simmie, 2003)
Burner	T= 500-1836 K; P= 0.003 MPa ; $\Phi = 0.55 & 1.84$	Ar	-	(Tian et al., 2007)
Flow reactor	T=700-1500 K; P= 0.1 MPa; $\phi = 0.045-1.18$	Air	100 ppm	(Lumbreras et al., 2001)
	T =1250-1700 K; P=0.0002 MPa; $\Phi = \infty$	-	-	(Hong et al., 2009)
	T=800–1400 K; P=0.101 MPa; $\Phi = 0.07-0.2$	N ₂	200 ppm	(Yamamoto et al., 2012)
	T= 973–1373 K; P=0.101 MPa; oxy-fuel conditions	-	-	(Wang et al., 2016)
	T= 500-871 K; P=1.91-3.58 MPa; $\Phi = 0.87-1.30$	Ar and H ₂ Ovapor	-	(Fedyeva et al., 2019)

In 2001, **Lumbreras et al.**, when studying pyrrole oxidation in a flow quartz reactor (700–1500 K, 0.1 MPa), revealed that the main oxidation intermediate was HCN. The addition of NO in the experiments did not significantly affect the experiments. The NO added was reduced in reburn-type reactions at high temperatures and low excess air ratios because of hydrocarbon radicals generated from the reaction, while it exhibited a minimum due to its conversion to NO₂ under lean conditions.

In 2003, **MacNamara and Simmie** investigated the oxidation of pyrrole in a shock tube, using argon as a diluent. Ignition delay times were measured at initial pyrrole concentrations of 0.5 to 1.0% over the reflected shock temperature range of

II. State of the art on the molecules studied as part of the thesis

1102–1805 K, for pressures of 190 to 560 kPa, and equivalence ratios ranging from 0.5 to 2.0. It was found that the final pressure is increased from 200 to 500 kPa, shorter ignition delay times are observed. Furthermore, the concentration of oxygen is increased, ignition delay times decrease; or simply that ignition delay times show a negative oxygen concentration dependence as shown in [Figure 33](#).

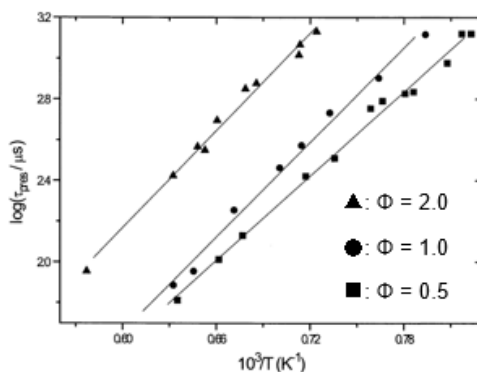


*Figure 33: Ignition delay times for 0.5% pyrrole, 350 kPa in a shock tube
Figure extracted from MacNamara and Simmie, 2003.*

After that, **Tian et al. (2007)** experimentally studied low-pressure premixed laminar pyrrole/O₂/Ar flames under lean ($\Phi = 0.55$) and rich ($\Phi = 1.84$) conditions with tunable synchrotron photoionization and molecular-beam mass spectrometry techniques. It was found that N₂, NO, and NO₂ are the major nitrogenous products, while hydrogen cyanide, isocyanic acid, and 2-propenenitrile are the most abundant nitrogen-containing intermediates in pyrrole flames. Moreover, concentrations of C₂H₂ and HCN in the rich flame are higher than in the lean flame, whereas HNCO is easily formed in the lean flame.

Yamamoto et al. (2012), when studying pyrrole oxidation in N₂ with the addition of water vapor (3 and 8% mol) using a flow quartz reactor (800–1400 K, 0.1 MPa) showed that HCN was transformed to N₂ or NO via NCO and nearly 90% of nitrogen in pyrrole finally was converted into N₂ or NO at the temperature of over 1400 K. There was no effect of the residence time on the reaction rate and the reaction rate largely depended on the reaction temperature as shown in [Figure 34](#).

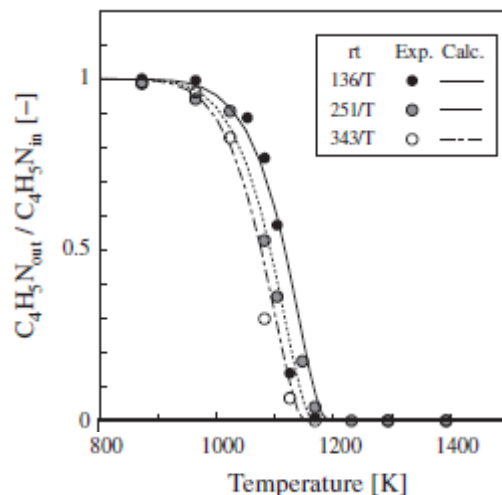


Figure 34: Comparison of experimental data with model predictions for pyrrole under different residence times (136/T, 251/T and 343/T s), with 8 vol% H₂O and 20,000 ppm O₂. Symbols denote experimental data and lines denote model predictions. Figure extracted from Yamamoto et al., 2012.

In 2016, **Wang et al.** conducted pyrrole and pyridine oxidation under oxy-fuel conditions in a flow quartz reactor (973–1373 K, 0.1 MPa). It was found that when the temperature is equal to or greater than 1073 K, neither HCN nor CO can be observed in O₂/N₂ atmosphere, while in O₂/CO₂ atmosphere, both HCN and CO can only be yielded. In addition, due to the increase of oxygen concentration, both NO and N₂O concentrations will be enlarged obviously.

More recently, **Fedyeva et al. (2019)** studied heterogeneous–homogeneous oxidation of pyrrole in water vapor at elevated pressure. It is shown that increasing the water vapor density, reduces the contribution of heterogeneous reactions and prevents the complete conversion of pyrrole due to the manifestation of “cage effect”.

Nitrogen-containing compounds are very important species from bio-oils, especially for their ability to form NO_x and nitrogen containing organic molecules like HCN. The combustion and pyrolysis of pyrrole were studied in many cases, but no experiment was carried out in jet-stirred reactor. The specificities of this kind of reactor could be used to obtain additional data in order to improve and develop detailed kinetic model for this category of molecules.

II.3.2 Ethylene glycol

In the present work, ethylene glycol is selected as a single-component surrogate for the bio-oils because of its similar chemical and physical properties and also because it is a small molecule obtained from the decomposition of simple sugars. For example, the mean values of density, viscosity, enthalpy of combustion, and C/H/O ratio of bio-oils and ethylene glycol are approximately equal. In the last few years, there has not been various research on combustion of ethylene glycol as shown in [Table 19](#).

Table 19: Summary of Ethylene Glycol oxidation studies.

Instrument	Experimental Conditions	Bath gas	Reference
Shock tube	T= 800–1500 K; P= 1.6 MPa; Φ = 1.0	Ar	(Kathrotia et al., 2017)
Flow reactor	T= 700–1200 K; P= 0.101 MPa; Φ = 1.0 & 2.0	Ar	(Kathrotia et al., 2017)

Ye et al. (2012), studied the kinetics and mechanisms for the unimolecular decomposition of ethylene glycol by high-level abinitio theories and variational RRKM calculations. It was found that the H₂O elimination reaction played a significant part in the decomposition process.

In 2017, **Kathrotia et al.** studied the kinetics of ethylene glycol oxidation in a shock tube (800-1500 K, 16 bar) and a flow reactor (700-1200 K, 1 atm). These new experiments supply an important database on the ignition delay times as well as quantitative species profiles of various major products and intermediates as shown in [Figure 35](#). The detailed kinetic model is first time tested against the experimental data and is found to reproduce the measurements with excellent agreement.

II. State of the art on the molecules studied as part of the thesis

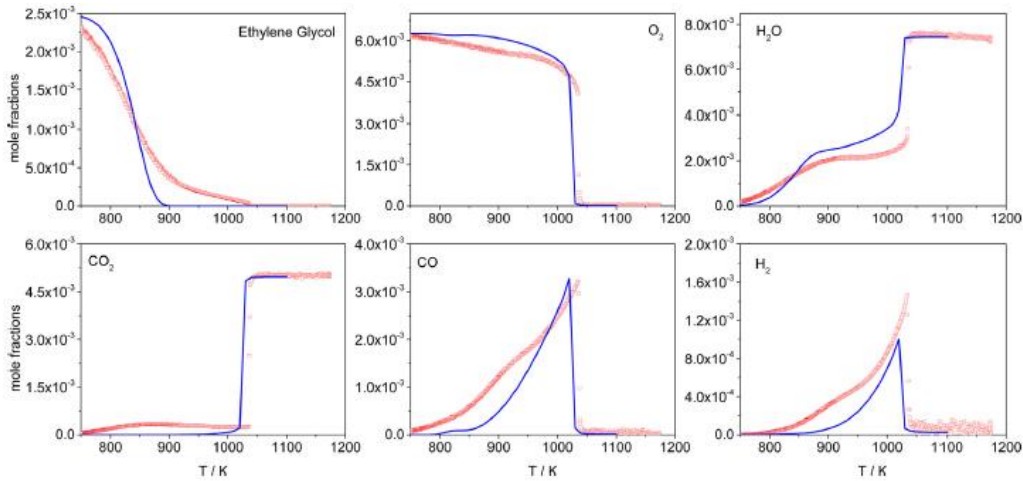


Figure 35: Mole fraction profiles of fuel, O_2 , and major products CO , CO_2 , H_2O and H_2 for $\Phi = 1$ in a flow reactor as a function of the respective oven temperatures. Red symbols represent experimental data and blue lines modeling results. Figure extracted from Kathrotia et al., 2017.

More recently, **Fernando et al. (2019)** developed a reduced reaction mechanism for describing the gasification chemistry of ethylene glycol. This mechanism was first validated by computing ignition delay times and laminar flame speeds of several relevant species and by comparing the calculated values against published experimental data.

The lack of data in literature justified the investigation of the oxidation and pyrolysis of glycol in a jet-stirred reactor. This lack of data is likely due to experimental difficulties linked to the nature of this type of compounds as it was experienced during my PhD.

II.4 Conclusion of the state of art

The surrogates of bio-oils studied in my PhD were defined by the previous works of Namysl (2019) within IMPROOF project framework. The surrogates of bio-oils studied were chosen in term of chemical families. Namysl (2019) studied many surrogates, which were sorted by five chemical families of bio-oils compounds; alcohols, aldehydes, carboxylic acids, furan and oxygenated aromatics. There were still two chemical families of bio-oils compounds, which had not been studied by Namysl (2019), these are nitrogen-containing compounds and diols. Therefore, pyrrole, ethylene and propylene glycols were studied during my PhD.

II. State of the art on the molecules studied as part of the thesis

This chapter reports the studies, which can be found in the literature for the surrogates used in my biogas and bio-oil studies. These are measurements of Laminar Burning Velocities (LBV), ignition delay times, species concentration profiles, etc. Different techniques and instruments were used to obtain these experimental results, such as burners, Constant-Volume Bomb (CVB), gas turbine, flow reactors, etc. There are already many results available in the literature for the combustion of biogas surrogates, but not so much concerning their oxidation. In addition, there is much less work concerning the bio-oils surrogates that I studied. Furthermore, the studies about glycols lack of data concerning the pathways of fuel consumption and pollutants formation. To our best knowledge, the oxidation and pyrolysis of propylene glycol are the first-ever studied.

My PhD aims thus at studying surrogates used in my biogas and bio-oils studies to determine their combustion behaviors, especially the kinetic aspects. My PhD focuses mostly on the experiments by using jet-stirred and flow reactors with various analysis techniques in order to detect a wide range of products. To better understand the oxidation of pyrrole, diols, methane, ammonia, hydrogen sulfide, hydrogen as well as that of their mixtures, this manuscript presents also the kinetic modelling studies.

III. EXPERIMENTAL SET-UPS AND METHODS

The main purpose of this PhD work was to investigate experimentally the oxidation of biofuels, molecules which surrogate a part of the biogas and bio-oils as described in the previous chapter. The experimental data were collected from the different reactors using various analysis techniques. These data allow a better understanding of the fuel reactivity and its decomposition and helping to identify the kinetic pathways controlling the reactivity.

III.1 Experimental set-ups

This chapter of the manuscript gives an overview of the experimental apparatus and the analysis techniques used during this PhD work. The experimental set-ups used for the oxidation study of biogas and bio-oils are slightly different due to the different physical properties of these biofuels (state of matter, viscosity, boiling point (see [Table 5](#) and [Table 6](#) in introduction section). Especially, the system of the evaporation and mixing chamber is adapted depending on the conditions and the fuels to be studied.

Bio-oils must be vaporized before mixing with the carrier gas and O₂, whereas biogas can be directly mixed with the bath gas and O₂. Analytical devices and techniques are also slightly different according to the composition of the samples to be analyzed and the type of information, which is desired.

Three different types of set-ups are described in this part. The first set-up consisted of a jet-stirred reactor fed with species in the gas phase under standard conditions, used to perform the experiments of biogas at temperatures up to 1200 K. The second type of set-up used a flow tube reactor located in an oven. Two tube geometries were used for experiments (see details hereafter). This type of set-up was also used to carry out the oxidation and pyrolysis of biogas at higher temperatures (up to 2073.15 K). The last type of set-up was used to investigate the experiments of bio-oils at low temperature in a jet-stirred reactor with the system of the evaporation-mixing chamber needed to evaporate the liquid bio-oils. The impact of the fuel-air equivalence ratio, ϕ (phi), was studied and was fixed to 0.5, 1 and 2 in order to cover a wide range of conditions (from fuel-lean to fuel-rich mixtures). The influence of the temperature was also studied by carrying out experiments over a temperature range from 650 K to 2073 K. Pressure was set constant in the range 0.107-0.127 MPa. Gas chromatography, online mass spectrophotometry, Fourier Transform InfraRed

spectroscopy (FTIR spectroscopy) methods and a NO_x analyzer (ThermoFisher) were used to identify and quantify the products.

III.1.1 Experimental set-up for the studies of biogas components in a JSR

The bibliographic study presented at the beginning of this manuscript shows that the biogas composition varies depending on its sources, but that most of the time biogas contains methane, carbon dioxide, water, ammonia and hydrogen sulfide. It also shows that the literature is scarce for ammonia and hydrogen sulfide oxidation, and also for the mutual interactions between methane and these two species. During my PhD work, experiments were performed to fill these gaps. Some experiments were also performed in order to study the mutual interaction of ammonia with methane and hydrogen.

Experiments were performed using three different setups. The first set-up uses a jet-stirred reactor (which will be described in the section III.4 about reactors). It is used to investigate the oxidation and pyrolysis of biogas. The JSR experimental apparatus is composed of three main parts: gas fuel storage and flow control system, jet-stirred reactor with heating system and pressure control, and sampling and analysis system. This set-up is presented in Figure 36.

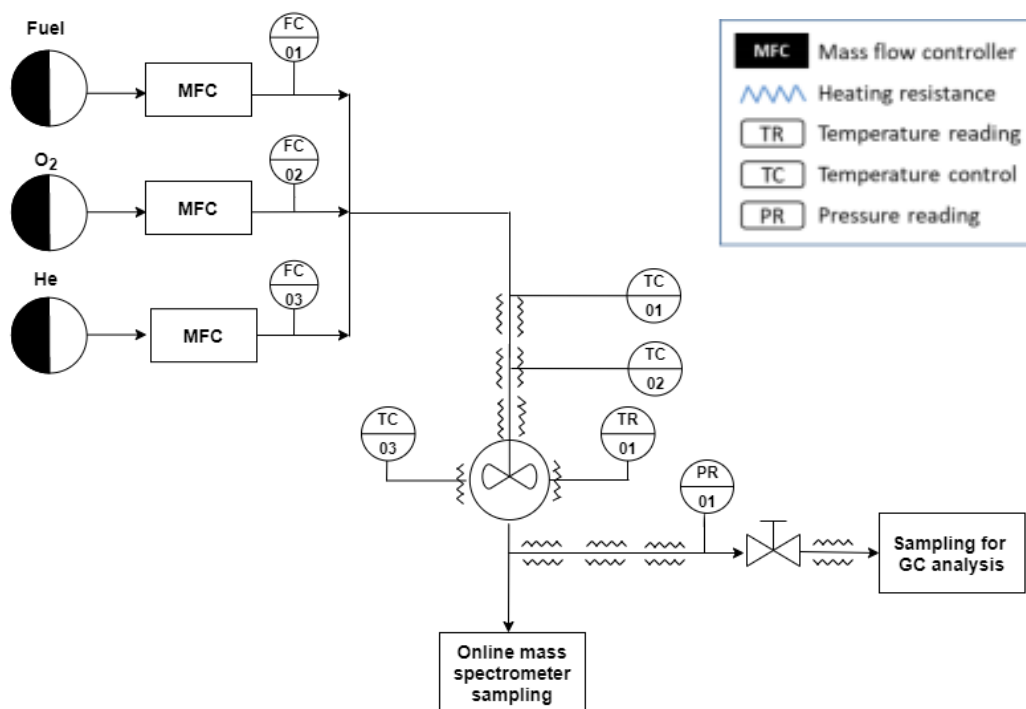


Figure 36: Experimental set-up using a JSR for the studies of biogas oxidation.

Figure 36 shows a schematic of the first setup used for the study of the oxidation of biogas. The heart of the setup is the reactor, here a JSR. The analytical methods used for this study are gas chromatography (several gas chromatographs were used to analyze the wide range of intermediates formed during the reaction) and online mass spectrometry.

III.1.2 Experimental set-up for the studies of biogas components in a FR

The second type of setups which was used for investigating the oxidation and pyrolysis of biogas includes a FR in an oven. Two tubes were used with two different ovens. One of them enables to reach temperatures up to 2073.15 K, which is particularly adapted to the studies of species with low reactivity, like ammonia. The experimental apparatus is composed of three main parts:

- Gas fuel storage and flow control system
- Alumina flow reactor with heating system and pressure control
- Sampling and analysis system.

This set-up is presented in Figure 37. The analytical methods used for this study are gas chromatography, NOx analyzer, online mass spectrometry and FTIR spectroscopy.

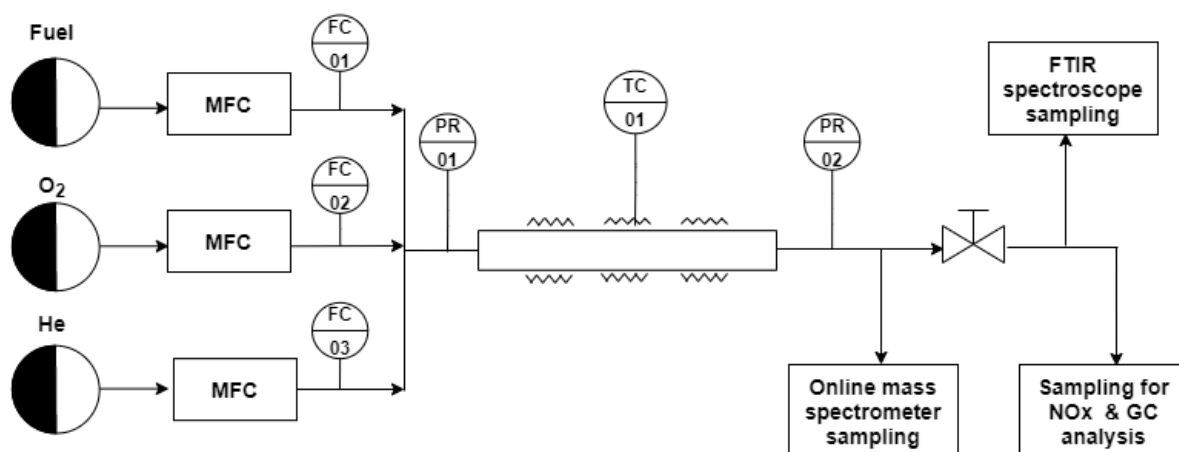


Figure 37: Experimental set-up coupled with a FR used for the studies of biogas oxidation.

III.1.3 Experimental set-up for the studies of bio-oil surrogates in a JSR

Figure 38 shows a schematic of the setup used for studying the oxidation of bio-oils. The experimental apparatus is composed of four main parts:

- Gas fuel storage and flow control system
- Evaporation and mixing system
- Fused silica jet-stirred reactor with heating system and pressure control
- Sampling and analysis system.

The analytical method used for this study is gas chromatography (several gas chromatographs were used to analyze the wide range of intermediates formed during the reaction). Analytical tools and methods are described in detail in section III.8 of this manuscript.

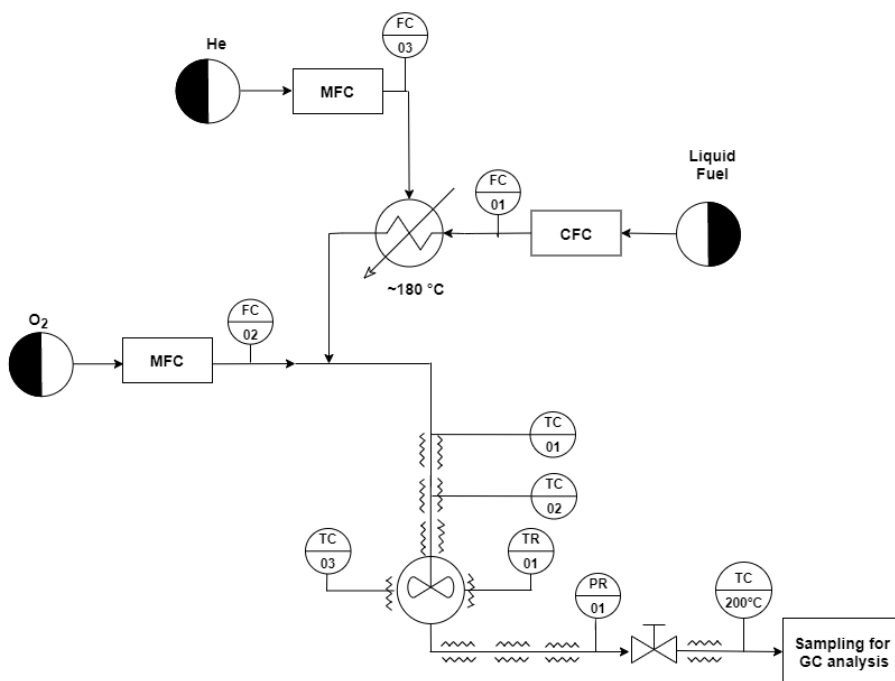


Figure 38: Experimental set-up coupled with a JSR used for the studies of bio-oils oxidation.

III.2 Liquid storage, flow control and evaporation system

III.2.1 Liquide storage and flow control

A liquid storage is used to store liquid fuels (pyrrole, diols). It is a stainless-steel tank pressurized with helium as shown in [Figure 39](#). The pressure in the tank is set around 5 bars in order to allow easy flow of liquid through the liquid flow controller. A CORI-FLOW meter and controller of Bronkhorst are used to measure the liquid flow rate exiting the tank and to send the information to a valve placed downstream. It is based on the Coriolis measuring principle, designed with integrated PID controller for fast and stable control of gas or liquid flow ranges between 0.1 and 5 g/h. The controller gives so an absolute value of the flow rate with a relative error around 1%.

The optical sensor measures the vibration deviates. The digital electronics then translates the measured vibrational value into a mass flow value and compares this to the set point from a PC. The integrated PID controller adjusts the flow rate if the measured value is different from the set point value in order to generate the correct output.

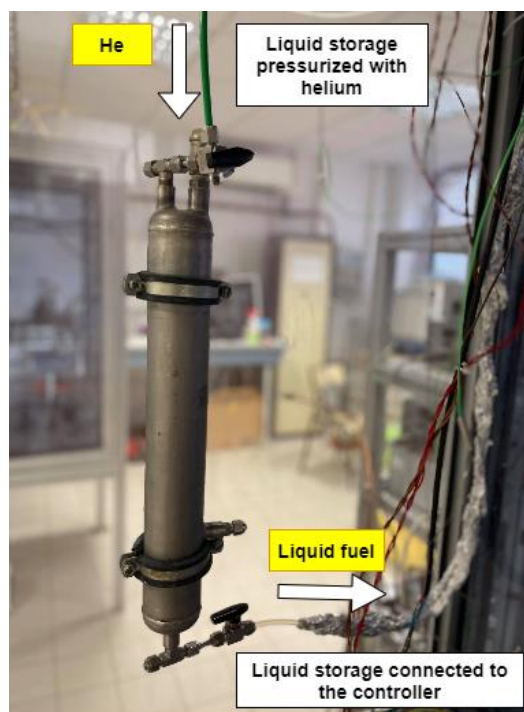


Figure 39: Liquid fuel storage.

Figure 40 shows a screenshot of the liquid flow regulation. The green line presents the actual flow rate which is stabilized around the set-point flowrate (red line). The yellow line is the regulation valve opening percentage.

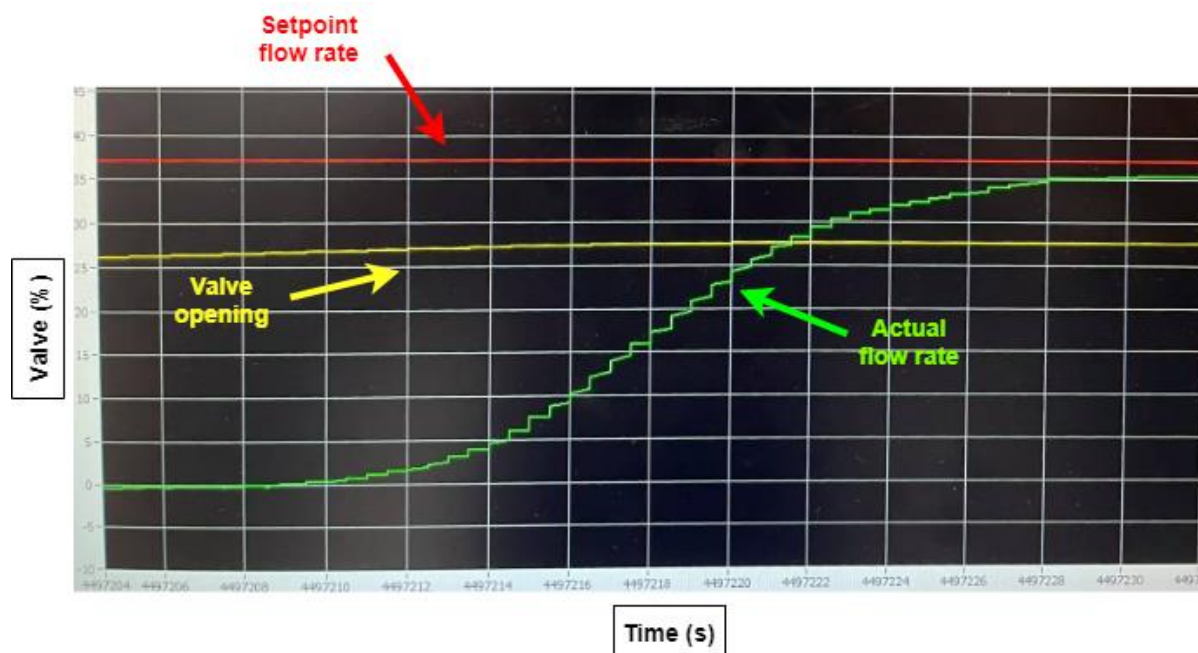


Figure 40: Liquid flow regulation display during the start of an experiment.

III.2.2 Evaporation and mixing system

The liquid fuel needs to be evaporated before mixing with oxygen. Therefore, the controlled evaporator mixer provided by Bronkhorst is used to produce precise vapor flow delivery to the entrance of the reactor. The temperature-controlled mixing device is used in combination with a liquid flow meter and a Mass Flow Controller (MFC) for carrier gas, together forming a Controlled Evaporation and Mixing (CEM) System (Figure 41).

The liquid drawn from a pressurized tank is measured by the liquid flow meter and led into mixing valve. A small pulse free flow of liquid is injected into the carrier gas stream (helium). This combination forms an aerosol and is then led into the heated section of the evaporator but that can be said up to 473 K to achieve total evaporation. The evaporator temperature selected should be very close to the boiling point of the liquid fuel to have a pure gas phase and to ensure that the fuel does not react in this part of the set-up if the temperature is too high to promote the reactivity.

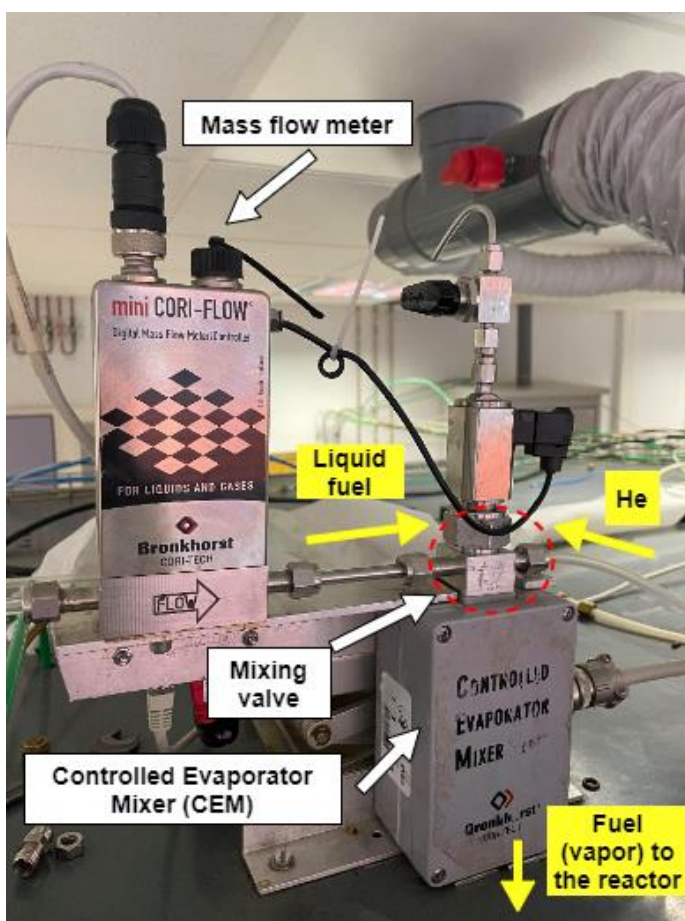


Figure 41: Picture of Controlled Evaporation and Mixing (CEM) System.

III.3 Gas inlet

The experiments of fuel oxidation were carried out under diluted conditions (> 90 % mol of carrier gas), using He and N₂ as a carrier gas. N₂ was only used as a carrier gas for the study of NO_x formation at high temperature. The dilution allows avoiding high temperature increases due to the exothermic reactions, which can prevent from working under isothermal conditions.

III.3.1 Mass Flow Controller (MFC)

The thermal Mass Flow Controllers provided by Bronkhorst were used to control the flow rates of the gases. They have a high accuracy to measure the gas flow rates with a relative error of 0.5%. Three kinds of MFC were selected corresponding to the used gases: fuel (methane), oxygen and bath gas (helium). The MFC calibrated for methane can be used for other fuels and that for helium can be used for nitrogen, but it is needed to take into account the conversion factors of the flow rate at 293 K under 1 atm. The MFCs are chosen depending on their maximal

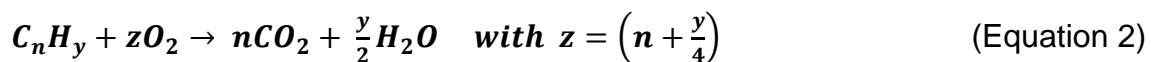
flow rate values. Table 20 shows the maximal flow rate for each flow meter and the conversion factors for each gas.

Table 20: Maximal flow rate depending on the gas used and conversion factor for each gas (source: Bronkhorst manual).

Gas	Maximal flow rate (NL/min)	Conversion factor (20 °C, 1 atm, ref=N ₂)
He	2	1.41
N ₂		1
Oxygen	0.2 - 2	0.98
CH ₄	0.005	0.76
H ₂ S		0.82
NH ₃		0.77
C ₂ H ₄		0.60

III.3.2 Determination of the inlet gas flow rates

The flow rate of each inlet species was calculated to control the experimental conditions. But first, it was needed to determine the inlet mole fraction of each compounds. The inlet mole fraction of fuel is fixed by the user and that of oxygen will be deduced from the stoichiometric combustion equation, whereas the fuel-air equivalence ratio had to be imposed. The stoichiometric combustion equation for a standard hydrocarbon in presence of oxygen is:



Examples of the stoichiometric combustion equations of methane, ammonia and pyrrole are shown in Equations 3-5, respectively.



The equivalence ratio is usually defined from the complete combustion of the fuel and the complete reaction products to consider are those, which are thermodynamically stable under the conditions of the study. This is straightforward for species only containing C and H atoms: CO₂ and H₂O are the final products. For nitrogen containing compounds, N₂ should be considered as well. But N₂ is not the only species that can be formed; there are also NO and NO₂ which have higher oxygen

contents than N_2 . Under the conditions of these studies, we observed the formation of N_2 along with that of NO , even at the highest temperatures. Thus, to ensure the complete combustion, especially when studying the oxidation of mixtures of ammonia and co-fuels like CH_4 and H_2 , NO or NO_2 was considered as “final product” to calculate the equivalence ratio. To be rigorous, the equivalence ratio considering N_2 as final product will be given as well.

Equation 6 is the formula of the fuel-air equivalence ratio (φ).

$$\varphi = \frac{x_{fuel}/x_{O_2}}{(x_{fuel}/x_{O_2})_{stoichio}} = \frac{x_{fuel}/x_{O_2}}{1/z} = \frac{x_{fuel} * z}{x_{O_2}} \quad (\text{Equation 6})$$

Normally, experiments will be investigated for four equivalence ratio conditions:

- ✓ $\varphi=1$: stoichiometric conditions
- ✓ $\varphi<1$: fuel-lean conditions
- ✓ $\varphi>1$: fuel-rich conditions
- ✓ $\varphi= \infty$: no presence of oxygen in the inlet mixture (pyrolysis)

As the inlet mole fraction of fuel x_{fuel} and φ has been imposed, thus the mole fraction of oxygen can be deduced with Equation 7.

$$x_{O_2} = x_{fuel} * z / \varphi \quad (\text{Equation 7})$$

The mole fraction of bath gas, which can be He or N_2 , is then calculated to complete the mixture. The mole fractions are then used in the process of the mass flow rate determination as explained below:

$$Q_m^i = F^{tot} * x_i * M_i$$

where $F^{tot} = \frac{P * Q_v^{tot}}{R * T}$ and $Q_v^{tot} = V_{reactor} / \tau$,

with:

Q_m^i : mass flow rate of gas (g/s),

F^{tot} : total mole flow rate (mol/s),

x_i : gas mole fraction (-),

M_i : gas molar mass (g/mol),

Q_v^{tot} : total volume flow rate (m^3/s),

$V_{reactor}$: reactor volume (m^3),

τ : residence time (s),

P: reactor pressure (Pa),

R: ideal gas constant ($8.314 J.K^{-1}.mol^{-1}$),

T: reactor temperature (K).

Examples of flow rate calculations are given in Appendix X.1.

III.4 Reactors

The experimental study of the oxidation and the pyrolysis of biogas components and bio-oils surrogates has been performed using three different reactor facilities, which are a JSR and two FR, FR1 and FR2. Figure 42 presents the three different reactors used for each fuel surrogate study.

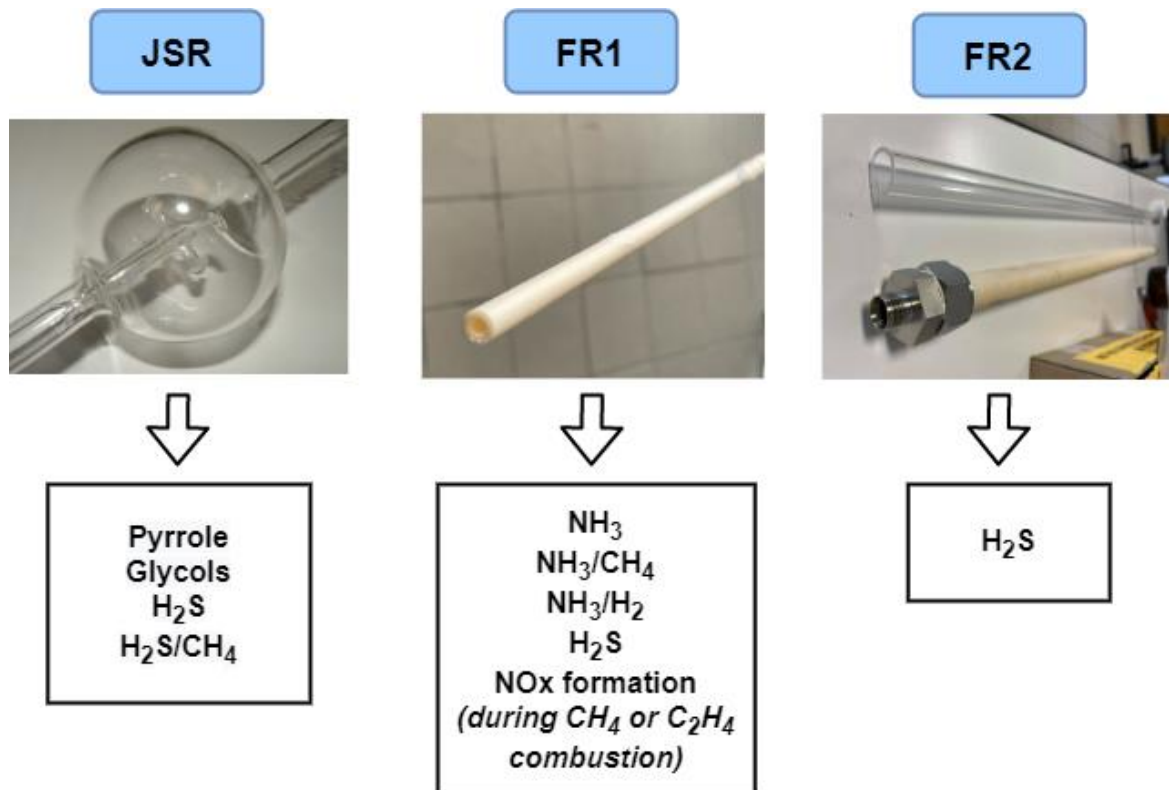


Figure 42: Reactors used for the studies of each fuel surrogate.

III.4.1 Jet-Stirred Reactor

The JSR consists of a fused silica sphere (volume of 92 cm³) equipped with four injection nozzles located at the center of the reactor creating high turbulence resulting in homogeneity in composition and temperature (Herbinet and Dayma, 2013; Herbinet et Battin-Leclerc, 2014). As a result, the JSR can be modeled as a perfectly stirred reactor. The reactor was heated using Inconel resistances, and the reaction temperature was measured with a K-type thermocouple positioned in a glass finger close to the center of the reactor (uncertainty of ±5 K). Figure 43 shows a picture of a jet-stirred reactor.



Figure 43: Picture of a jet-stirred reactor.

To ensure thermal homogeneity, the heated JSR is preceded by a quartz annular preheating zone, in which the temperature of the gas is increased up to the reactor temperature. The heating is ensured by resistances (Thermocoax) carefully rolled to fit the reactor and the preheating zone shapes, which allows flexibility and swiftness in the heating of each area. Temperatures are measured by several K-type thermocouples: one is located in a glass finger inside the inlet cross for the actual reaction temperature measurement, and two are located between the resistances and the external wall of the reactor for the temperature control. The resistance allows increasing the temperature up to 1273K. The JSR was used for the studies of the oxidation of bio-oil surrogates and hydrogen sulfide under 0.107MPa with a residence time of 2 s.

III.4.2 Flow Reactor (FR1)

The experiments of the combustion of biogas components at high temperatures up to 2073 K, were performed using an alumina FR1 located in an oven as shown in Figure 44.



Figure 44: Oven used to heat FR1 in high-temperature experiments.

The reactor is made of a recrystallized alumina tube with 4 mm of inside diameter and 100 cm of length. It is heated by an electric furnace (Carbolite Gero) that can reach 2073 K. The pressure is set constant around 0.12 MPa. Bath gas was either pure N₂ or He. The gas is mixed before being injected at the inlet of the reactor. The residence time is set between 0.025 and 1.5 s.

a) Calculation of the Peclet number (Pe)

The dimensionless Peclet number (Pe) is used to quantitatively describe the ratio of plug-flow to mixed-flow in a reactor with compound-flow pattern (Bingchen, 2007). A plug-flow reactor allows all the molecules flow at about the same speed: this is the image of the piston advancing inside the reactor with a constant velocity. A reactor can be considered as an ideal plug-flow reactor, if a Peclet number is larger than 100 (Villiermaux, 1993; Levenspiel, 1999).

The Pe number is defined by [Equation 8](#);

$$Pe = \frac{uL}{E_x} \quad (\text{Equation 8})$$

with u: velocity of the gases in FR1 (m.s⁻¹)

L: FR1 length (m)

E_x: coefficient of axial dispersion (m².s)

Under a laminar regime, for $Re \leq 2300$, there is a theoretical formula verified by the experimental results (Levenspiel, 1999), presented in [Equation 9](#):

$$\frac{E_x}{D} = 1 + \frac{1}{192} * \frac{(ud)^2}{D} \quad (\text{Equation 9})$$

with:

d: FR1 diameter (m)

D: molecular diffusion coefficient (cm².s⁻¹)

E_x: coefficient of axial dispersion (cm².s)

The calculation of the coefficient D under a large helium dilution condition is from the resolution of the Boltzmann equation as shown in [Equation 10](#);

$$D = \frac{0.00266T}{PM_{He}} \quad (\text{Equation 10})$$

with:

T: temperature (K)

P: pressure (bar)

M_{He} : molar mass of helium ($\text{g}\cdot\text{mol}^{-1}$)

D: molecular diffusion coefficient ($\text{cm}^2\cdot\text{s}^{-1}$)

Under the explored conditions, the flow in FR1 is laminar ($\text{Re} \leq 2300$). The Pe number calculated with the residence time of 0.025 s is between 440 and 852. Therefore, FR1 satisfies the plug-flow criterion.

Measurements in [Figure 45](#) have shown that the reactor is quasi-isothermal in the zone between 34 and 62 cm. These actual measured temperature profiles were used to run simulations in conditions close to the experimental ones.

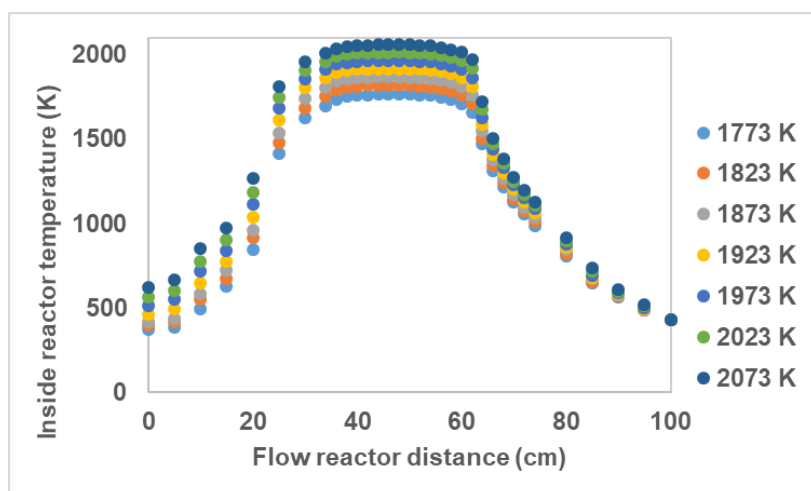


Figure 45: Temperature profiles measured as a function of the set temperature and the position in the reactor.

Note that the material of the tube is a crucial parameter to obtain reliable data. The first tests conducted with an alumina tube were not conclusive. Indeed, very strange results, showing some reactivity of ammonia in an unusual low temperature range, were obtained. They were totally incompatible with the literature and modeling results. They were likely due to reactions at the wall of the reactor or reactions with oxygen diffusing through the porosity of alumina. New tubes, made of recrystallized alumina, were purchased and tested. Recrystallized alumina is impervious and is a set of defect-free grains. This allowed performing experiments without observing the previously described strange phenomena.

III.4.3 Flow Reactor (FR2)

The flow reactor (FR2) was used to carry out studies under conditions closer to those used with the jet-stirred reactor (residence time of about 2s) but at higher temperatures (> 1200 K). During my PhD, FR2 was only used for the study of H_2S oxidation and pyrolysis because the temperature onset of H_2S during the pyrolysis in JSR is above 1200 K. To follow the whole H_2S reactivity, FR2 was thus needed.

The reactors used are a recrystallized alumina tubes and also a fused silica tubes with an internal diameter of 20 mm and an external diameter of 25 mm as shown in [Figure 46](#). The total length of the tubes is 600 mm. The two tubes were purchased from SCERAM. The alumina tube can be used up to a temperature of 2000 K.



Figure 46: Fused silica and alumina flow tubes (FR2).

An oven provided by Vecstar as shown in [Figure 47](#) is used to heat FR2. It has internal regulation, but the actual temperature profile is nevertheless measured by a type S thermocouple with a diameter of 1 mm. This thermocouple can withstand temperatures up to 1850 K.

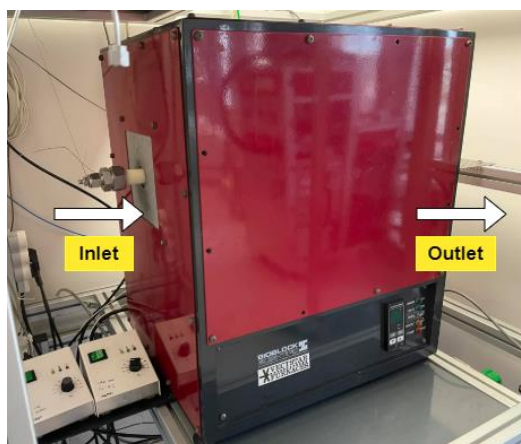


Figure 47 : Oven used during the experimental studies in a FR2.

The temperature profile measurements were carried out with a type S thermocouple. Temperature profiles of the reactor were measured by Vin (2019) for different furnace set temperatures, the results can be seen in Figure 48:

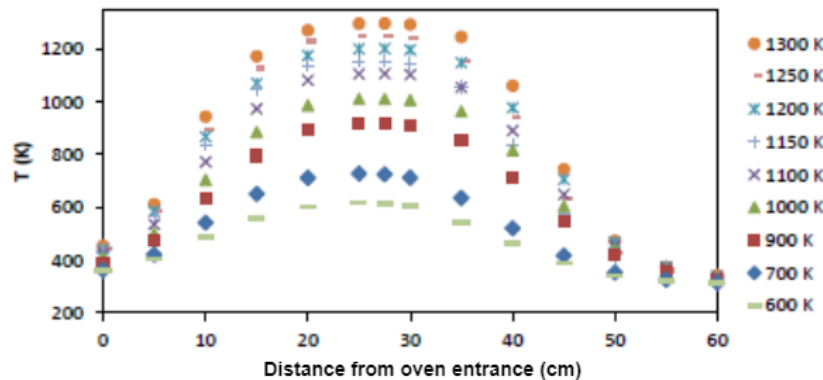


Figure 48: Temperature profiles measured as a function of the set point temperature and the position in the FR2 (source: Vin, 2019).

Figure 48 shows that the isothermal reaction zone is located between 20 and 35 cm with a uniform temperature profile (± 40 K). These actual temperature profiles are used to accurately characterize the temperature in the reactor during simulations. The pressure in the reactor during the pyrolysis and oxidation studies are all at 0.107 MPa. Under the explored conditions, the gas flow in FR2 is a laminar flow ($Re \leq 2300$) with the residence of about 2 s.

Vin (2019), investigated the experiments of the residence time distribution (RTD) by using FR2 to justify the flow pattern as an ideal plug-flow. According to the measurements of RTD (Vin,2019), FR2 is quite close to an ideal plug-flow reactor. Figure 49 presents the Pe numbers as a function of temperatures and residence times, respectively.

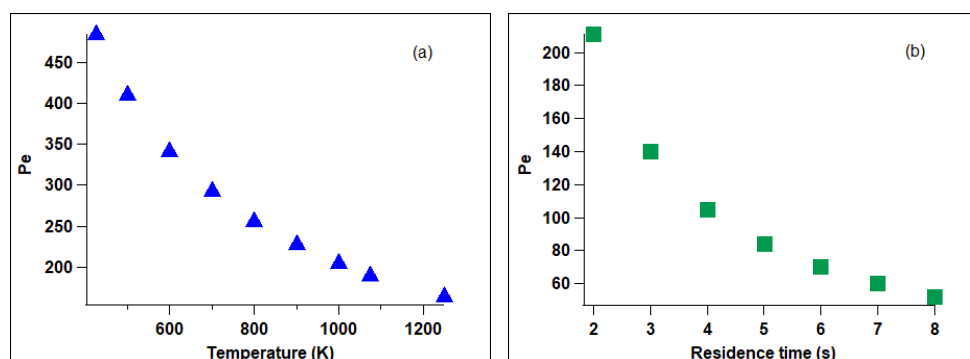


Figure 49: Pe number as a function of temperatures (a) and residence times (b) (source: Vin, 2019).

It can be observed that the hypothesis of plug-flow reactor is less valid when the residence time and the temperature increase. Under the explored conditions, FR2 is in the plug-flow criterion with the residence time of 2 s, corresponding to the Pe number of 211 see in [Figure 49b](#).

III.4.4 Reactor wall treatment

Undesirable catalytic effects of the reactor wall were observed using the fused silica JSR and FR1, especially for H₂S and NH₃ oxidation. The occurrence of wall catalytic effects has already been observed by other authors (Zhou et al., 2013; Egerton and Warren, 1951). To solve this problem, the three used types of reactor were treated with a solution of boric acid (boric acid in 50% water - 50% ethanol) to form an impervious layer of boric oxide (Zhou et al., 2013; Egerton and Warren, 1951). The tube was first filled with a saturated solution, then it was drained and dried with helium flowing through. The tube was then heated to ~ 393 K to eliminate the remaining solvent molecules. To obtain the impervious layer covering the wall, heating at 773 K was needed (the obtained layer is white and translucent before the heating, invisible after the heating, as mentioned in literature). The procedure was repeated twice for the fused silica jet-stirred reactor as the geometry is more complex than tubular ones. Several tests were made with coated and non-coated reactors to highlight possible catalytic effects. The comparison between coated and non-coated JSRs was investigated during the experiments of H₂S oxidation as shown in [Figure 50](#).

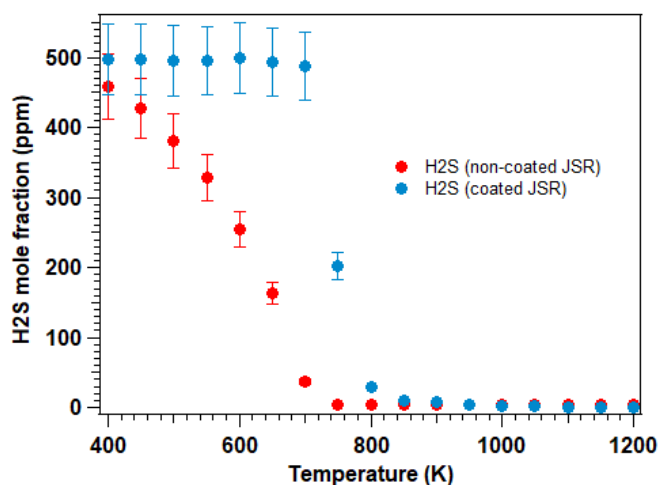


Figure 50: H₂S quantification during the H₂S oxidation using coated and non-coated JSRs. (500 ppm inlet H₂S, $\phi = 0.25$, 0.107MPa, $\tau = 2s$).

In [Figure 50](#), H₂S quantitation from non-coated (red symbols) and coated (blue symbols) JSRs is different, especially at low temperatures (400-800K). It was observed that, before coating the JSR, H₂S profile decreased slowly from 400 K to 800 K which means that H₂S was adsorbed on the JSR wall, catalyzing the reaction. Whereas, H₂S profile remains constant between 400K and 700K after coating.

III.5 Analytical methods

In order to detect a wide range of reaction products at the outlet of reactor, gas chromatography, online mass spectrophotometry, Fourier Transform InfraRed spectroscopy (FTIR spectroscopy) methods and NO_x analyzer (ThermoFisher) are used to identify and quantify the products.

III.5.1 Gas chromatography analysis

The gas at the outlet of the reactor is transferred by a heated line maintained at 420 K to the gas chromatographs (GCs) to analyze the wide range of products formed by the reactions, especially the carbon containing species. The connection between the heated transfer line and a gas chromatograph is performed by a 6-way sampling valve.

The first chromatograph, equipped with a Carbosphere packed column, a thermal conductivity detector (TCD) and a flame ionization detector (FID), is used for the quantification of light-weight compounds (also called permanent gases) like methane, ethylene, acetylene and ethane using helium as the carrier and reference gas. H₂ is also quantified using gas chromatography equipped with a Carbosphere packed column and a TCD providing a separation of the helium and H₂ peaks and the carrier and reference gas was argon.

The second chromatograph is fitted with a Q-Bond capillary column and a FID preceded by a methanizer and is used for the quantification of compounds containing from one carbon atom, like methane or carbon monoxide, up to species containing up to 6 carbon atoms. The methanizer (nickel catalyst for hydrogenation) allows the detection of species like CO, CO₂ and CH₂O with a better sensitivity and increases the sensitivity for species containing oxygenated functional groups in a general manner.

A third gas chromatograph equipped with a FID and a HP-5 capillary column is used for the quantification of the heaviest compounds (C_{5+}).

The fourth chromatograph is a gas chromatograph equipped with both type of capillary columns and coupled to a mass spectrometer quadrupole (GC-MS). This is an analytical method that combines the features of gas-chromatography and mass spectrometry as shown in [Figure 51](#). These two components, used together, allow a much finer degree of substance identification than either unit used separately does.



Figure 51: Picture of the GC-MS used for the analysis.

Two methods can be used to send the gas into these chromatographs:

- ✓ Using a heated line and a six-way sampling valve. In this case it is called online analysis
- ✓ With a trap at liquid nitrogen temperature followed by injection using an automatic liquid sampler and it is an offline analysis

The liquid nitrogen trap is used in case of condensation of outlet species. The liquid nitrogen condensates the outlet flows, only the heaviest fraction of the gases is sampled with this technique. Furthermore, some recombination products can be formed with the solvent used for the dilution of the liquefied sample. It is possible that condensation and physical adsorption occur on some surfaces in the manifolds (cold points, valve, gums). This could affect the quality of the results. [Table 21](#) summarizes the uncertainty sources and their quantifications related to these experiments.

Table 21: Uncertainty quantification of the experimental setup.

Uncertainty sources	Uncertainty bounds
Temperature in the reactor	±5K
Temperature in the transfer line	±7K
Impurity of the fuels and the gases	<1%
Flow rate of liquid fuel	±1%
Flow rate of gases	±0.5%
Residence time	±2%

The above table shows that the main uncertainties come from the product calibrations and especially that by the effective carbon number method.

Calibrations are performed by injecting gaseous and liquid external standards when available. So we can obtain a factor k between the mole fraction of the species and the area of the corresponding peak measured as defined in Equation 11.

$$x_i = k_i * A_i \quad (\text{Equation 11})$$

In Equation 11, A is the measured area on the chromatogram and x is the corresponding mole fraction. Higher is the mole fraction of the associated compound; larger is the area. For species, which could not be directly calibrated with a standard, the effective carbon number (ECN) method, relying on the properties of the FID with respect of the structure of the molecule, was used to obtain calibration coefficients. This method requires:

- ✓ the knowledge of the effective carbon number of the species.
- ✓ the determination of the calibration coefficient of at least one species, called the reference (ref).

To obtain the calibration coefficient for a species i , we use the Equation 12.

$$k_i = \frac{n_{ref}}{n_i} * k_{ref} \quad (\text{Equation 12})$$

where n is the effective carbon number and k the calibration coefficient defined by Equation 11.

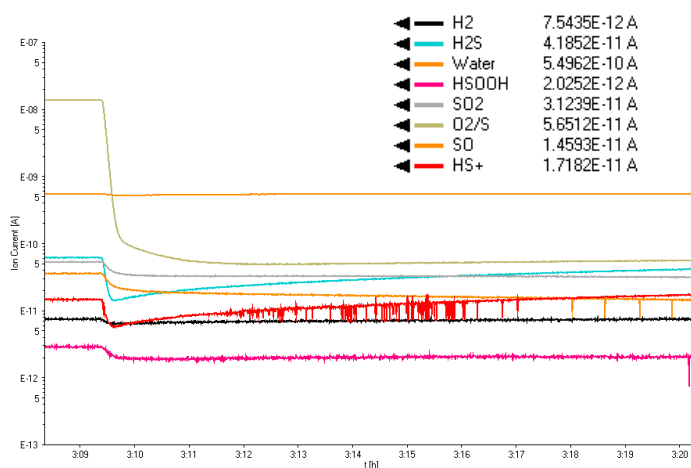
III.5.2 Online Mass Spectrometry (MS)

Mass spectrometry was used to detect H₂O, CH₄, CO₂ and O₂ and small species like nitrogen and sulfur containing species. The particularity of the mass spectrometer (Figure 52) is the sampling which is achieved through a capillary tube directly connecting the reactor and the analyzer. This sampling method enables the direct sampling of the gas phase with fast analysis of species. It can be used for two types of experiments:

- ✓ Species quantification as a function of the time in case of dynamic behavior (oscillations) in the jet-stirred reactor,
- ✓ Species quantification at the outlet of the tubular flow reactor. For example for the detection of ammonia, which is a species that is difficult to accurately detect by gas chromatography.



(a)



(b)

Figure 52: Picture of the online mass spectrometer (a) and MS display during the oxidation of neat H₂S (500 ppm inlet H₂S, phi=0.5, 0.107 MPa, $\tau = 2$ s) (b).

This technique requires the calibration of each species as there is no obvious relationship between their calibration factors (the ECN methods, which is valid for FIDs, does not apply here). It also requires a careful analysis of possible interferences as the ionization at 70 eV is high enough to allow the fragmentation of ions (as an example, water can produce ions at m/z 16, which is also the m/z for methane). Once these interferences are known, it is possible to perform signal deconvolution.

Mass spectrometry can be used for studying the oscillation phenomena and adsorption wall effect. Figure 53 shows how the phenomenon of water adsorption can be seen during the oxidation of diethyl ether (DEE).

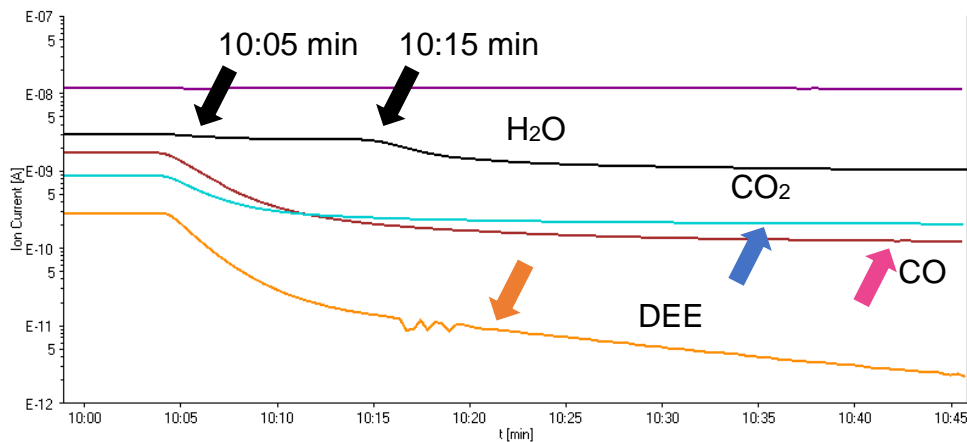


Figure 53: MS display of catalytic wall effect during the oxidation of diethyl ether (DEE).

In Figure 53, it can be noticed that after stopping gas flow (after 10:05 min), DEE, CO₂, CO signals decreased suddenly, but not H₂O. A decrease in two steps was observed for H₂O (one after 10:05 min like other species and the second one from 10:15 min). This probably means that there was some water absorbed on the reactor wall during the experiment.

III.5.3 NOx analyzer

A chemiluminescence NO_x analyzer (Fisher Scientific provided by Megatec SA) was adopted to measure NO and NO₂. Chemiluminescence is the emission of light (luminescence) as the result of a chemical reaction. Ozone is combined with NO to form nitrogen dioxide in an activated state ($\text{NO} + \text{O}_3 \rightarrow \text{NO}_2 + \text{O}_2$). The activated NO₂ luminesces broadband visible to infrared light as it reverts to a lower energy state. This apparatus is capable of measuring nitrogen oxides at concentrations ranging from 0 to 5000 ppm and 0-500 ppm for NO₂ with 0.1 ppm sensitivity, respectively. Two pumps were used for outlet and bypass channels, respectively. This technique required the calibration of the species with standards. Figure 54 presents the NO_x analyzer used during my PhD.



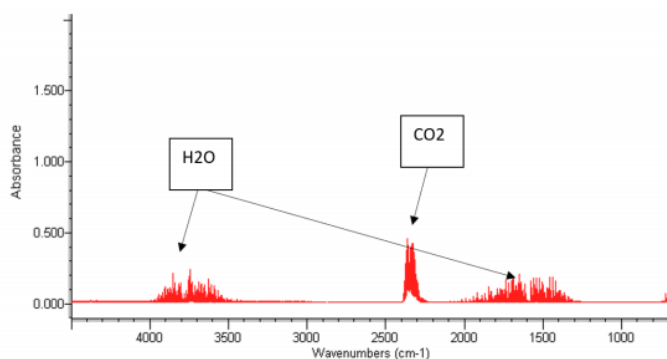
Figure 54: Picture of the NOx analyzer.

III.5.4 FTIR spectrometer

Fourier-Transform InfraRed spectroscopy (FTIR) is a technique used to measure how much light a sample absorbs at each wavelength. The FTIR spectrometer was mainly used to detect HCN (calibrated using a HCN diluted (1000 ppm in N₂) cylinder). It can also be used to detect NO and NO₂, H₂O and CO₂ as shown in Figure 55. Note that, theoretically, ammonia could also be detected using this apparatus, but tests were inconclusive as ammonia absorption was too intense and the signal was saturated. Other techniques were used for ammonia quantification. This technique requires the calibration of each species.



(a)



(b)

Figure 55: Picture of the FTIR spectrometer (a) and example of the FTIR spectrum (b).

Table 22 summarizes the uncertainty related to the analysis techniques. The uncertainty of the FTIR and NOx analyzer is $\pm 5\%$ because the product calibration with standards was performed. Relative uncertainties in mole fractions of calibrated species detected by on-line mass spectrometry are $\pm 10\%$ and $\pm 20\%$ for water.

Table 22: Uncertainty of the experimental methods.

Experimental methods	Uncertainty bounds
GC	
- Fuel calibration	±5%
- Product calibration by effective carbon number method	±10%
- Product calibration with standards	±5%
Online-MS	±10- 20%
FTIR	±5%
NOx analyzer	±5%

III.6 Conclusion of the experimental set-ups and methods

This chapter shows the overview of the experimental apparatus and the analysis techniques used during this PhD work. The experimental measurements in the different reactors using various analysis techniques are analyzed in the next chapters, with the raw data given in Appendix for the following reactions;

- The oxidation and pyrolysis of NH_3 , oxidation of NH_3/CH_4 , NH_3/H_2 .
- The oxidation and pyrolysis of neat hydrogen sulfide, oxidation of $\text{H}_2\text{S}/\text{CH}_4$.
- The formation of NO_x during the oxidation of N_2 , methane and ethylene in air.
- The oxidation and pyrolysis of pyrrole.
- The oxidation and pyrolysis of ethylene glycol.
- The oxidation and pyrolysis of propylene glycol.

IV. PYROLYSIS AND OXIDATION OF BIOGAS COMPONENTS

This chapter is dedicated to the experimental and kinetic studies to investigate biogas components. The objectives are to study their reactivity and to better understand their decomposition mechanism under oxidative and pyrolysis conditions. This chapter is divided in five parts. First, the study of neat ammonia (NH_3) oxidation will be presented. The second part describes the studies of the interaction of ammonia and methane. The third part presents the experimental results of the oxidation of ammonia doped with hydrogen (H_2). The study of hydrogen sulfide (H_2S) oxidation is presented in the fourth part. The last part presents the study of hydrogen sulfide-methane interaction. In each part, the experimental results are described and discussed. Those results will be compared with models developed by the CRECK group from Politecnico di Milano. The raw experimental data are given in Appendix.

These works led to the publication of three papers in international peer-reviewed journals and in a paper of the European Combustion Meeting:

- ✓ Stagni, A., Cavallotti, C., Arunthanayothin, S., Song, Y., Herbinet, O., Battin-Leclerc, F., & Faravelli, T. (2020). An experimental, theoretical and kinetic-modeling study of the gas-phase oxidation of ammonia. *Reaction Chemistry & Engineering* (5), 696-711.
- ✓ Arunthanayothin, S., Stagni, A., Song, Y., Herbinet, O., Faravelli, T., & Battin-Leclerc, F. (2020). Ammonia–methane interaction in jet-stirred and flow reactors: An experimental and kinetic modeling study. *Proceedings of the Combustion Institute* (38), 345-353.
- ✓ Stagni, A., Arunthanayothin, Y., Herbinet, O., Battin-Leclerc, F., & Faravelli, T. (2021). An experimental and kinetic-modeling study of H_2S combustion in ideal reactors, presented to the 10th European Combustion Meeting (ECM 2021).

IV.1 Ammonia pyrolysis and oxidation

This part presents the kinetic model and then the experimental and simulation results obtained during the pyrolysis and oxidation of ammonia. These data were obtained using the FR1 setup and analytical tools described in [Chapter III](#).

IV.1.2 Kinetic modeling

The development of the kinetic model was performed by the PoliMi team, our partner in the Improof European project. It was carried out by following a hierarchical and modular approach, as originally conceived in the CRECK kinetic framework (Ranzi et al., 2012). The core H_2/O_2 mechanism was adopted after the work of Metcalfe et al., 2013. The NO_x module, foundation of the whole NH_3 mechanism, was taken from the work of Song et al., 2018, on turn based on the works of Faravelli, Frassoldati et al., 2003. The major updates were performed on HONO/ HNO_2 chemistry, after the recent work of Chen et al., 2018. For all the species, thermodynamic properties were systematically updated using the database of Burcat and Ruscic, 2005. Ammonia sub-mechanism was added on top of the NO_x module, and the critical reactions are summarized in [Table 23](#). The reactions involving NH and NH_2 radicals were taken from Klippenstein et al., 2009 as well as NH_2OH chemistry. The only exception is represented by R7: in this case, the high-temperature estimation of Davidson et al., 1990 was adopted (~35% smaller), which (extrapolated) showed a better agreement with lower-temperature experimental data. As for NH_2 reactions with NO and NO_2 (R16-R19), both rate constants and branching ratios between the product channels were taken following the guidelines of Glarborg et al., 2018, while for $NH+NO$ (R26 and R27), the theoretical calculations of Haworth et al., 2003 were fitted in the 1000 K – 2600 K interval. For the higher N_2H_x chemistry, reactions were mainly taken from the review of Dean and Bozzelli (2000), including H-abstractions from N_2H_x compounds and N_2H_x dissociation. The complete kinetic mechanism is made up of 31 species and 203 reactions.

Table 23: List of critical reactions in the NH_3 oxidation mechanism. Reaction rate expression is modified Arrhenius $k = AT^\beta \exp[-E_{\text{act}}/(RT)]$. Units are cm^3 , cal, mol, K, s.

ID	Reaction	A	β	E_a	Notes	Reference
R1	$\text{NH}_3 \leftrightarrow \text{NH}_2 + \text{H}$	7.230E+29	-	110862.4	0.1 atm	Stagni et al., 2020a
		3.497E+30	5.316	111163.3	1 atm	
		1.975E+31	5.224	111887.8	10 atm	
		2.689E+31	5.155	112778.7	100 atm	
			4.920			
R2	$\text{NH}_3 + \text{H} \leftrightarrow \text{NH}_2 + \text{H}_2$	1.963E+04	2.854	8520.2		Stagni et al., 2020a
R3	$\text{NH}_3 + \text{OH} \leftrightarrow \text{NH}_2 + \text{H}_2\text{O}$	1.559E+05	2.372	118.9		Stagni et al., 2020a
R4	$\text{NH}_3 + \text{O} \leftrightarrow \text{NH}_2 + \text{OH}$	4.430E+02	3.180	6739.9		Stagni et al., 2020a
R5	$\text{NH}_3 + \text{HO}_2 \leftrightarrow \text{NH}_2 + \text{H}_2\text{O}_2$	1.173E+00	3.839	17260.0		Stagni et al., 2020a
R6	$\text{NH}_3 + \text{O}_2 \leftrightarrow \text{NH}_2 + \text{HO}_2$	1.415E+10	1.285	55224.0		Davidson et al., 1990
R7	$\text{NH}_2 + \text{NH} \leftrightarrow \text{N}_2\text{H}_2 + \text{H}$	1.500E+15	-	0.0		Klippenstein et al., 2009
R8	$\text{NH}_2 + \text{NH} \leftrightarrow \text{NH}_3 + \text{N}$	9.600E+05	2.460	107.0		Klippenstein et al., 2009
R9	$\text{NH} + \text{NH} \leftrightarrow \text{NH}_2 + \text{N}$	5.700E-01	3.880	342.0		Klippenstein et al., 2009
R10	$\text{NH} + \text{NH} \rightarrow \text{N}_2 + \text{H}_2$	6.260E+12	-	-160.9		Klippenstein et al., 2009
R11	$\text{NH} + \text{NH} \rightarrow \text{N}_2 + \text{H} + \text{H}$	5.634E+13	-	-160.9		Klippenstein et al., 2009
R12	$\text{NH}_2 + \text{NH}_2 \leftrightarrow \text{NH}_3 + \text{NH}$	5.640E+00	3.530	550.0		Klippenstein et al., 2011
R13	$\text{NH}_2 + \text{O}_2 \leftrightarrow \text{HNO} + \text{OH}$	2.900E-02	3.764	18185.0		Klippenstein et al., 2011
R14	$\text{NH}_2 + \text{O}_2 \leftrightarrow \text{H}_2\text{NO} + \text{O}$	2.600E+11	0.487	29050.0		Baulch et al., 2005
R15	$\text{NH}_2 + \text{HO}_2 \leftrightarrow \text{OH} + \text{H}_2\text{NO}$	1.566E+13	0.000	0.0		Song et al., 2002
R16	$\text{NH}_2 + \text{NO} \leftrightarrow \text{N}_2 + \text{H}_2\text{O}$	2.600E+19	-	870.0		Song et al., 2002
R17	$\text{NH}_2 + \text{NO} \leftrightarrow \text{NNH} + \text{OH}$	4.300E+10	0.294	-866.0		Glarborg et al., 2018
R18	$\text{NH}_2 + \text{NO}_2 \leftrightarrow \text{H}_2\text{NO} + \text{NO}$	8.600E+11	0.110	-1186.0		Glarborg et al., 2018
R19	$\text{NH}_2 + \text{NO}_2 \leftrightarrow \text{N}_2\text{O} + \text{H}_2\text{O}$	2.200E+11	0.110	-1186.0		Glarborg et al., 2018
R20	$\text{NH}_2 + \text{H} \leftrightarrow \text{NH} + \text{H}_2$	4.000E+13	0.000	3650.0		Davidson et al., 1990
R21	$\text{NH}_2 + \text{OH} \leftrightarrow \text{NH} + \text{H}_2\text{O}$	9.600E+06	1.970	670.0		Mousavipour et al., 2009
R22	$\text{NH}_2 + \text{O} \leftrightarrow \text{NH} + \text{OH}$	7.000E+12	0.000	0.000		Dean and Bozzelli, 2000
	duplicate	3.300E+08	1.500	5076.8		Dean and Bozzelli, 2000
R23	$\text{NH}_2 + \text{O} \leftrightarrow \text{HNO} + \text{H}$	1.500E+15	-	836.7		Sumathi et al., 1998
	duplicate	7.730E+13	-	646.4		Sumathi et al., 1998
			0.277			
R24	$\text{NH} + \text{O}_2 \leftrightarrow \text{HNO} + \text{O}$	4.050E+11	0.090	10670.0		Talipov et al., 2009
R25	$\text{NH} + \text{O}_2 \leftrightarrow \text{NO} + \text{OH}$	2.010E+15	-	5670.0		Talipov et al., 2009
			1.380			

ID	Reaction	A	β	E_a	Notes	Reference
R26	$\text{NH} + \text{NO} \leftrightarrow \text{N}_2\text{O} + \text{H}$	5.328E+12	0.026	-2893.9		Burcat and Ruscic, 2005
R27	$\text{NH} + \text{NO} \leftrightarrow \text{N}_2 + \text{OH}$	3.635E+10	0.361	-2844.3		Burcat and Ruscic, 2005
R28	$\text{HNO} \leftrightarrow \text{H} + \text{NO}$	2.104E+20	-	48651.0	0.1 atm	Stagni et al., 2020a
		1.568E+21	3.151	48707.0	1 atm	
		1.060E+22	3.113	48978.0	10 atm	
		4.976E+22	3.059	49471.0	100 atm	
		2.963	-	-	-	
R29	$\text{HNO} + \text{O}_2 \leftrightarrow \text{NO} + \text{HO}_2$	2.000E+13	0.000	14896.0		Dean and Bozzelli, 2000
R30	$\text{H}_2\text{NO} + \text{H} \leftrightarrow \text{HNO} + \text{H}_2$	4.800E+08	1.500	1559.8		Dean and Bozzelli, 2000
R31	$\text{H}_2\text{NO} + \text{H} \leftrightarrow \text{NH}_2 + \text{OH}$	4.000E+13	0.000	0.000		Dean and Bozzelli, 2000
R32	$\text{H}_2\text{NO} + \text{O} \leftrightarrow \text{HNO} + \text{OH}$	3.300E+08	1.500	486.8		Dean and Bozzelli, 2000
R33	$\text{H}_2\text{NO} + \text{OH} \leftrightarrow \text{HNO} + \text{H}_2\text{O}$	2.400E+06	2.000	1192.2		Dean and Bozzelli, 2000
R34	$\text{H}_2\text{NO} + \text{NO}_2 \leftrightarrow \text{HNO} + \text{HONO}$	6.000E+11	0.000	2000.0		Garborg et al., 2000
R35	$\text{H}_2\text{NO} + \text{NH}_2 \leftrightarrow \text{HNO} + \text{NH}_3$	1.800E+06	1.940	-580.0		Dean and Bozzelli, 2000
R36	$\text{H}_2\text{NO} + \text{O}_2 \leftrightarrow \text{HNO} + \text{HO}_2$	2.300E+02	2.994	16500.0		Garborg et al., 2018; Song et al., 2016
R37	$\text{H}_2\text{NO} + \text{HO}_2 \leftrightarrow \text{HNO} + \text{H}_2\text{O}_2$	3.360E+05	2.000	-1434.0	estimated	Stagni et al., 2020a

This model has been validated on previous experimental results of literature concerning IDTs and LBVs (Stagni et al., 2020a), as well as on results obtained at LRGP before the start on my PhD about the oxidation of ammonia (500 ppm) in JSR under 0.107 MPa. The model provides a good agreement for the profiles of NH_3 and NO over the temperature range of 600 to 1200 K, as shown in Figure 56.

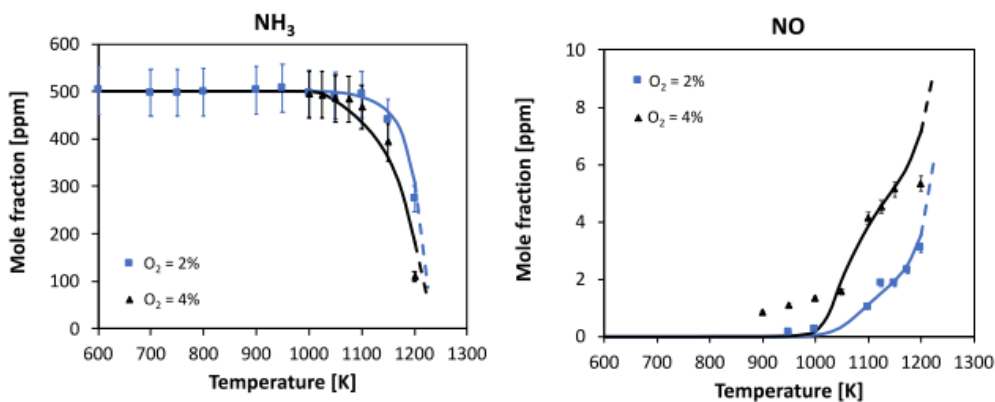


Figure 56: Oxidation of 500 ppm of NH_3 with 2% and 4% of O_2 in a JSR, $P = 0.107$ MPa. $\tau = 1.5$ s. Experimental data obtained before my PhD. by Song Y. (symbols). Lines are computed data.

IV.1.2 Experimental results

Ammonia pyrolysis

Experiments for the pyrolysis of ammonia were carried out in an alumina tubular flow reactor operated at steady state under dilute conditions using helium as a bath gas. The reaction was studied at temperatures ranging from 1373 K to 1873 K, a residence time of about 250 ms and a pressure of 850 Torr. The inlet mole fraction of ammonia is 1000 ppm. The products of the reaction were quantified by gas chromatography. The experimental results (symbols) and the simulated data (lines) are compared in [Figure 57](#).

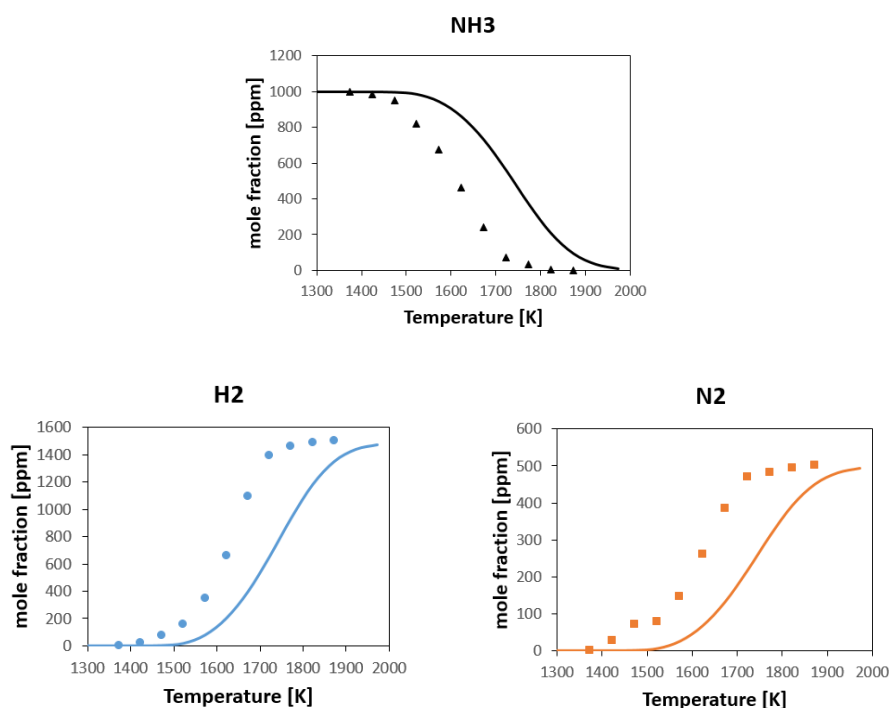


Figure 57: Mole fractions of NH₃, N₂ and H₂ as a function of temperature (FR1 data, P= 0.113 MPa, residence time of about 250 ms).

[Figure 57](#) shows the mole fractions of species as a function of the temperature. The two detected reaction products are nitrogen and hydrogen. There is a shift (~ 50 K) between the experimental data and data computed using a model developed by Politecnico di Milano. Ammonia is fully consumed at 1800 K. The formation of H₂ and N₂ could be observed from 1400 K and they are gradually produced with the increase of temperature.

Ammonia oxidation

Ammonia oxidation was performed in a FR at temperatures above 1300 K. In this work, the equivalence ratio is defined by considering the following stoichiometric equation: $2\text{NH}_3 + 1.5\text{O}_2 \rightarrow \text{N}_2 + 3\text{H}_2\text{O}$. Experiments were carried out by injecting 1000 ppm NH_3 with 2000 ppm O_2 ($\Phi = 0.375$), with a flow rate regulated in such a way to obtain a fixed residence time in the reactive zone, equal to about 50 ms. Figure 58 shows the results for the major species. Ammonia conversion is observed from about $T = 1400$ K, and is complete above 1500 K. In this temperature interval, H_2 is formed as an intermediate product, with an observed peak of about 50 ppm. N_2 and NO are the two major nitrogenated products, with the NO yield progressively increasing with temperature.

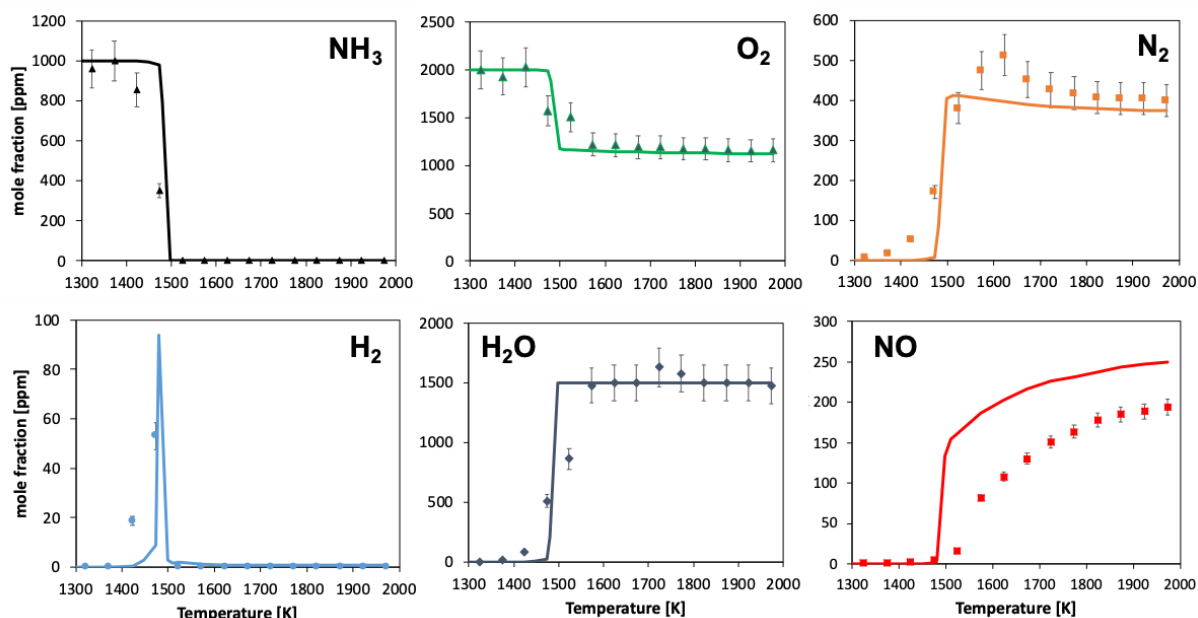


Figure 58: Oxidation of 1000 ppm NH_3 with 2000 ppm O_2 in a FR ($\phi=0.375$). Experimental and modeling results. $P = 950$ torr. Average τ in the reactive zone is 50 ms.

The kinetic model predicts the ignition temperature reasonably well, and consequently NH_3 , O_2 and H_2O profiles. However, the predicted consumption rate of ammonia and product formation are more abrupt than what was experimentally observed. The location and intensity of H_2 peak are satisfactorily caught by the model. The onset of NO formation is well reproduced in terms of temperature. However, the predicted NO/N_2 ratio is higher than the measured one: the shape of both profiles is

well caught, but an overestimation of the NO mole fraction (about 25%) is observed at high temperature.

Kinetic analysis

The reaction flux analysis in FR at 1523 K is presented in Figure 59. It shows the routes leading to NO and N₂ formation at intermediate temperatures. The formation of N₂H₂ via NH₂+NH opens a new branching route through NNH, since overall, an H atom is released in the conversion from NH₂ to N₂. NO is released as final product through HNO formation via NH₂+O.

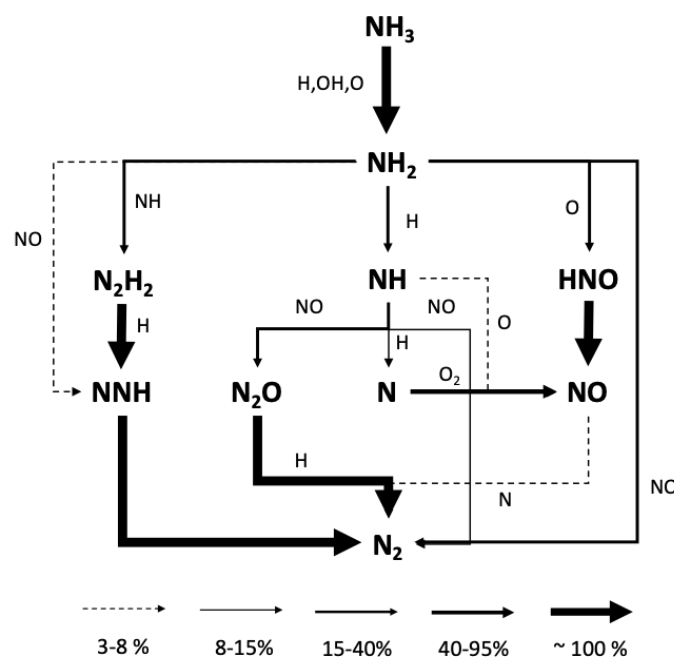


Figure 59: Reaction flux analysis in FR at $T = 1523$ K and $x = 55$ cm. Arrow thickness is proportional to the reaction flux.

The competition between the paths to NO and N₂ becomes more apparent in the sensitivity analysis shown in Figure 60, performed right after the reactivity onset, at a reactor length where NH₃ is almost fully consumed, and the reactions driving NO/N₂ selectivity can be distinguished. It can be observed that under such conditions, the path via HNO (R23 and R28) controls NO formation more than the path via N (thermal NO_x). On the other side, the major antagonists to NO selectivity are its reactions with NH and NH₂, respectively (R27 and R16), directly converting into N₂. Moreover, a higher formation of NH₂ (R3), precursor to the formation of both NO and N₂, enhances the formation of N₂ while having an antagonistic effect on NO. This can

be attributed to NH formation via R20, on turn reacting again with NO and providing N₂.

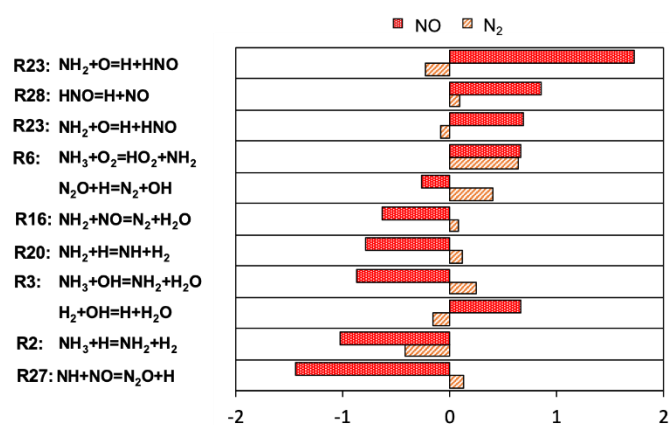


Figure 60: Sensitivity coefficients to NO and N₂ mole fractions in FR case at T = 1523 K – x = 58.5 cm (~100% ammonia conversion).

IV.1.3 Conclusion

In the recent year, NH₃ combustion has gained attention, which has made available a significant amount of experimental data characterizing its reactivity in a wide range of operating conditions. However, a comprehensive understanding of its kinetic behavior is still an open challenge. In this work, this topic was addressed through a combined experimental and modelling approach able to shed light on the kinetic behavior of ammonia at high temperature.

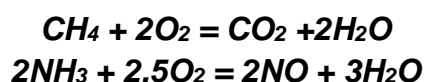
New experimental data were collected in a flow reactor at atmospheric pressure, in such a way to cover the whole range of temperatures (1300 – 2000 K). In order to interpret these results, a kinetic analysis was performed to evaluate some of the most critical steps in the pyrolysis and oxidation mechanisms. Especially, the rate constants for ammonia decomposition, H-abstractions and the dissociation of the HNO intermediate were evaluated and included in a comprehensive kinetic model, built up following a first-principles approach, and incorporating the state-of-the-art kinetic rates. It was found out in the analysis of flow reactor experiments that decelerating effect of the reaction NH₂+O=HNO+H promotes instead NO formation at high temperature.

IV.2 Oxidation of methane doped with ammonia

This part presents the influence of the addition of ammonia on the oxidation of methane investigated both experimentally and numerically. Experiments were carried out at atmospheric pressure, using a fused silica jet stirred reactor, and a recrystallized alumina tubular reactor.

IV.2.1 Experimental results

In this work, the equivalence ratio (Φ) was defined considering CO_2 , water and NO as final combustion products from methane and ammonia oxidation.



NO was considered rather than N_2 since high amounts of NO were formed under the conditions of this study. If N_2 is the final product, the equivalence ratio will be 0.988 and 0.85 for JSR and FR1 cases, respectively.

a) Jet-Stirred Reactor

JSR experiments were performed over the temperature range 600-1200 K, at a residence time of 1.5 s, a pressure of 106.7 kPa, with inlet methane and ammonia mole fractions of 10000 and 500 ppm, respectively, and at three equivalence ratios (0.5, 1 and 2). Two particular phenomena were observed during experiments, making the oxidation study of methane/ammonia mixtures tricky. The first was the occurrence of oscillation regimes under specific conditions (at the highest temperatures for the lean and stoichiometric mixtures). Mole fractions were not constant in time, which was not compatible with the diagnostics used in this study. For this reason, the temperature range is limited for some conditions in the results displayed hereafter. This phenomenon has been previously reported in literature for the oxidation of neat methane (Lubrano Lavadera et al., 2018), and its kinetic foundations were explained in Stagni et al., 2019. The second phenomenon was the occurrence of wall reactions strongly enhancing the ammonia consumption, although the reactor was made of fused silica. This problem was solved by treating the surface of the JSR before each experiment by flowing all gases but ammonia under reactive conditions.

Figure 61 shows the mole fractions of both reactants and main products. The temperature of the reactivity onset is very sensitive to the equivalence ratio: it is about 1000 K for the lean condition, 1075 K for the stoichiometric ones, and 1150 K in rich mixtures, according to the temperature dependence of the methane and ammonia mole fractions shown in Figure 61a-b. Figure 61a also displays CH₄ mole fractions in the case of the oxidation of neat methane for comparison. Mole fractions are comparable to those of methane when doped with ammonia for the rich conditions, whereas the reactivity onset is anticipated (~100 K) by ammonia addition under lean conditions, and conversion is slightly enhanced in stoichiometric conditions.

The main carbon containing products are carbon monoxide, carbon dioxide, ethylene, and ethane (Figure 61). Under lean conditions, carbon monoxide mole fractions peak at 1025 K. Above this temperature, a decrease of the CO mole fraction is observed with a simultaneous increase of that of CO₂. The mole fractions of ethylene and ethane remain low (less than 500 ppm). Larger equivalence ratios favor the formation of unburnt species.

Only two nitrogen-containing species were detected during this study: nitric oxide (NO) and nitrogen dioxide (NO₂), but more N-containing species are formed in significant amounts because the N-atom balance is not closed. This is likely due to the formation of N₂, which was expected, but its detection was not possible because of interference in GC analyses. NO and NO₂ mole fractions are displayed in Figure 61. Under lean conditions, the mole fractions of these last products increase simultaneously to ammonia depletion. NO₂ mole fraction already peaks at 1025 K and afterward decreases whereas that of NO continue to increase. Note that NO behaves closely to CO₂ whereas NO₂ behaves closely to CO.

Under stoichiometric conditions, oscillation behavior was detected above 1025 K. Beyond this temperature, data for ammonia are not accurate because oscillations are not compatible with the CRDS spectrum acquisition time of ammonia (about 30 min) and the in-situ sampling. Data recorded with the NO_x analyzer and by GC, with a sampling strategy based on the injection of a defined volume accumulated on the larger time scale, can be considered as time averages. Oscillations seem to have a minor impact on species like methane, carbon monoxide and carbon dioxide.

This is because the mole fractions of these species are larger compared to those of nitric oxide and nitrogen dioxide.

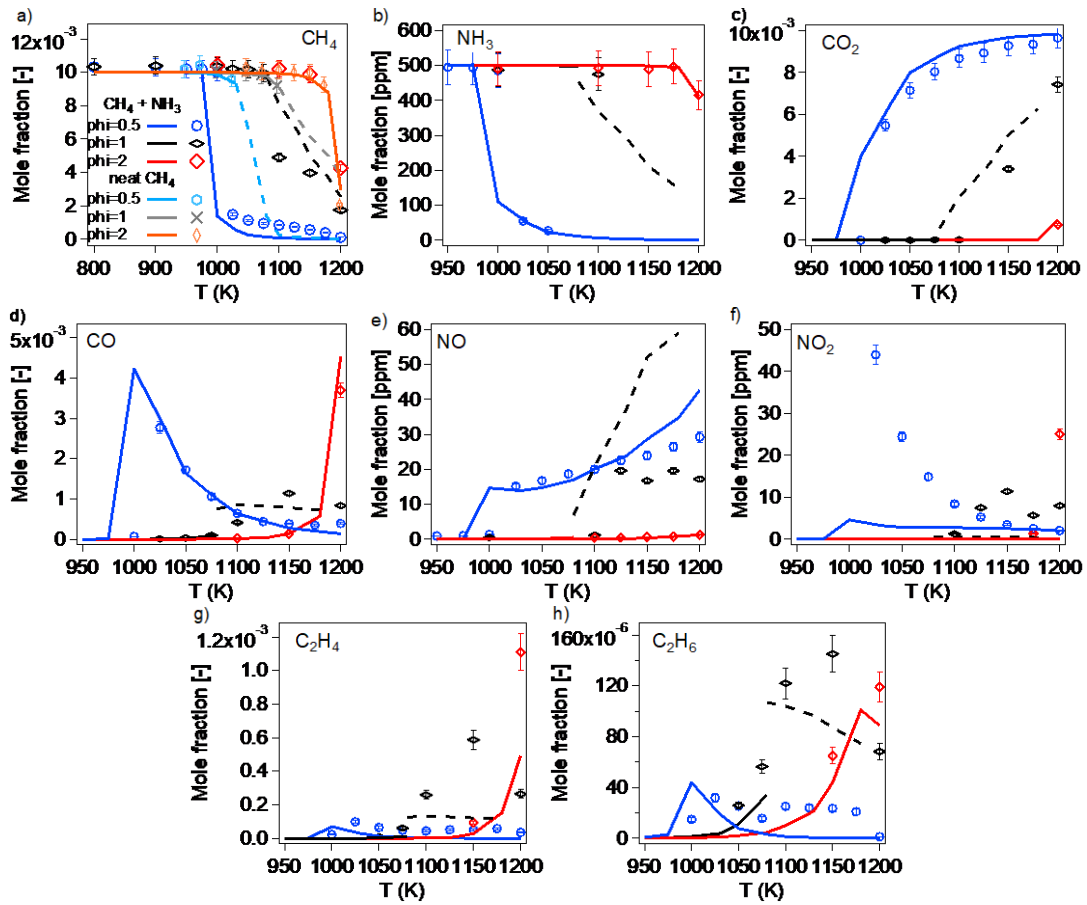


Figure 61: Mole fractions of reactants and main reaction products at different temperatures and equivalence ratios in the JSR. Symbols: experiments. Lines: data computed with the model (dashed lines are averaged mole fractions due to oscillation regime).

b) Flow reactor

FR experiments were performed over a temperature range significantly higher than in the JSR thanks the use of a recrystallized alumina tube and an oven heating up to temperatures as high as ~2000 K. The two fuels, the oxidizer, and 11 reaction products were followed. Reaction products can be divided as follow:

- species specific to methane oxidation: CO, CO₂, C₂H₂, C₂H₄, C₂H₆ and C₃H₆,
- species specific to ammonia oxidation: N₂, NO and NO₂,
- species common to both fuels: water and HCN.

Note that HCN is the only cross-product whose formation was observed during these high temperature experiments. Mole fraction profiles are displayed in Figure 62. C-, N-, H- and O-atom balances were calculated for each temperature and are all in the range of 0.99 ± 0.05 .

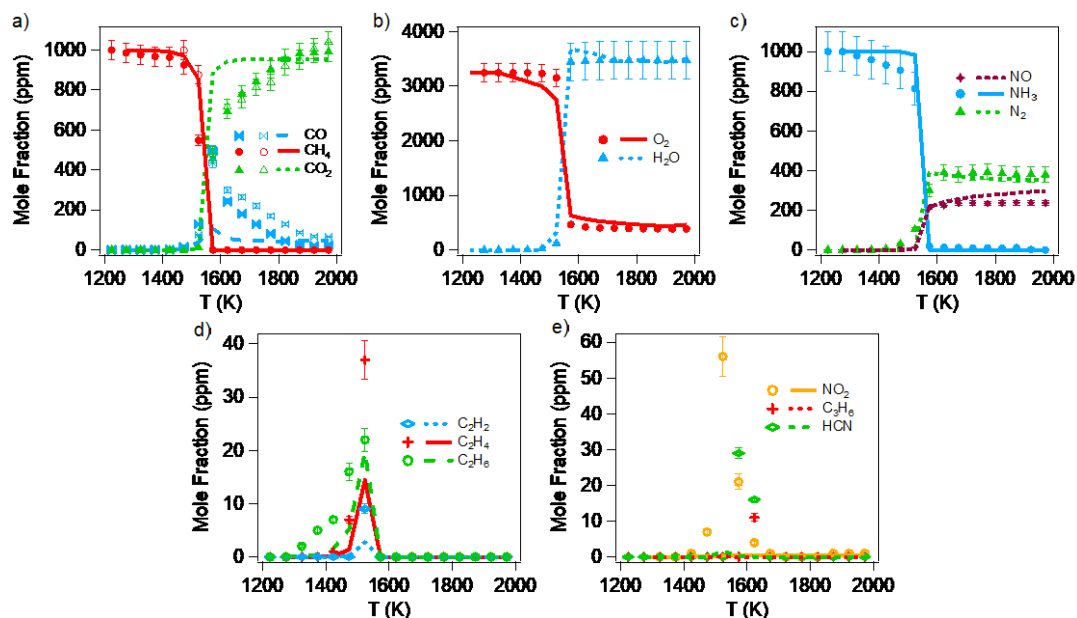


Figure 62: Mole fractions of the fuels and main reaction products recorded during the oxidation of methane and ammonia in the flow tube reactor ($\Phi=1$). Symbols: experiments (close symbols in panel a) are for methane-ammonia co-oxidation, open symbols are for neat methane oxidation). Lines: data computed with the model.

The consumption of methane and ammonia becomes significant starting from ~ 1500 K and they are already totally consumed at ~ 1600 K. The two main products from the oxidation of methane are CO and CO₂. CO peaks at 1573 K and is then progressively converted to CO₂ when the temperature increases. Ammonia is mainly converted to NO and N₂, and NO/N₂ ratio slightly increases with temperature. Note that under these conditions, equilibrium calculations predict the formation of N₂ quasi exclusively. Small amounts of NO₂ were also observed on a very narrow range (between 1550 and 1600 K). A part of O₂ remains not consumed even at the highest temperatures because of the formation of N₂ from NH₃ (the NH₃/O₂ inlet ratio was calculated considering only NO as product to be sure to have enough oxygen for fully consuming methane). Other reaction products (C₂ species, C₃H₆ and HCN) are produced in small amounts and over a narrow temperature range as for NO₂ (Figure 62e).

IV.2.2 Kinetic modeling

The kinetic model describing ammonia and methane oxidation and their mutual interaction was performed by following a hierarchical methodology, i.e., the founding principle of the CRECK framework (Ranzi et al., 2012). The mechanism relied on a core C₀-C₂ module developed by Metcalfe et al., 2013, on top of which the C₃ mechanism of Burke et al., 2015 was added. Thermodynamic properties were taken from the database of Burcat and Ruscic, 2005. NO_x submechanism leveraged the recent work of Song et al., 2019. A full description of the mechanism construction and its wide-range validation can be found in the paper by Stagni et al., 2020a. The complete mechanism consists of 157 species and 2444 reactions.

Comparison between experimental and simulated results

The experimental data and model results were compared in [Figure 61](#) and [Figure 62](#). The kinetic model well predicts the temperature of the reactivity onset for both reactors as it can be seen for methane and ammonia in [Figure 61](#) and [Figure 62](#). The temperature dependence of the conversion of both fuels is also well predicted, although the residual presence of methane after T = 1025 K is underestimated. In the JSR, at $\phi = 1$, where oscillation behavior was found above 1025 K, the mole fractions of methane (GC detection) reasonably agree with averaged computed mole fractions (dashed lines in [Figure 61](#)). The model predicts the anticipated reactivity of methane in presence of ammonia under lean conditions.

As far as reaction products in JSR are concerned, mole fractions of carbon monoxide and of carbon dioxide are well predicted by the model at all equivalence ratios (even for the stoichiometric case for which oscillating computed mole fractions were averaged). Mole fractions of ethane and NO are also reproduced fairly well by the model. Discrepancies are observed for nitrogen dioxide for which the model underestimates the formation, especially under lean conditions. This issue was also previously observed by Song et al., 2019 in the CH₄ oxidation doped with NO. For the rich case, the signal detected for NO₂ under these high temperature conditions is likely due to an interference with that of HCN, which is a typical high temperature product under rich conditions (whereas NO₂ is usually produced at low-temperature oxidation), as already observed in work of Song et al., 2019.

In the FR, the agreement is also rather satisfactory for the main reaction products such as H_2O , NO and N_2 . Surprisingly, the model predicts a more abrupt increase of CO_2 and decrease of CO mole fractions than in the experiments. This trend is also observed when studying the oxidation of neat methane (open symbols in [Figure 62a](#)), indicating that it is not due to the presence of ammonia in the feed of the reactor. According to a kinetic analysis performed at 1600 K, the second most sensitive reaction is $\text{CO} + \text{OH} = \text{CO}_2 + \text{H}$ (after the branching reaction $\text{H} + \text{O}_2 = \text{OH} + \text{O}$) the kinetic parameters of which are relatively well known. With the current mechanism there is no way to explain this deviation, as well as the pre-reaction of NH_3 before ignition (which was also observed in Mendiara and Glarborg (2009) with different inlet mixtures). The model predicts negligible amounts of NO_2 , C_3H_6 and HCN compared to the experiment.

Kinetic analysis

Rate-of-production and sensitivity analyses were performed to highlight the chemistry involved during the co-oxidation of methane and ammonia, and their mutual interactions. [Figure 63](#) presents a rate analysis for fuel consumption ([Figure 63a](#)) and a sensitivity analysis for methane mole fraction ([Figure 63b](#)) performed under JSR conditions (944 K, $\varphi = 0.5$, corresponding to conversions of 18 and 9% of methane and ammonia, respectively). [Figure 64](#) displays a rate analysis for fuel consumption ([Figure 64b](#)) and a sensitivity analysis for methane mole fraction ([Figure 64a](#)) performed under FR conditions (~ 1560 K, $\varphi = 1$, and an abscissa of 46 cm (length from the tube inlet) corresponding to methane and ammonia conversions of ~ 50 and $\sim 20\%$, respectively).

At low temperature and under JSR conditions, the analysis shows that the consumption of methane starts with the classic H-atom abstraction reaction, $\text{CH}_4 + \text{OH} = \text{CH}_3 + \text{H}_2\text{O}$. The main consumption route of CH_3 is $\text{CH}_3 + \text{NO}_2 = \text{CH}_3\text{O} + \text{NO}$ (as in the case of the oxidation of methane doped with NO and NO_2 (Song et al., 2019)), NO_2 coming from the reaction $\text{NO} + \text{HO}_2 = \text{NO}_2 + \text{OH}$. Minor channels are $\text{CH}_3 + \text{HO}_2 = \text{CH}_3\text{O} + \text{OH}$ and the recombination reaction forming ethane. Afterwards, the reaction series leading to CO_2 , via CH_3O , CH_2O , CHO , CO , is not directly affected by the presence of ammonia. The central role of the HO_2 radicals in converting CH_3 to CH_3O is noteworthy, through both direct reaction with CH_3 and indirectly by

regenerating NO_2 from NO . The main sources of HO_2 radicals are the reactions $\text{HCO} + \text{O}_2 = \text{CO} + \text{HO}_2$ and $\text{H} + \text{O}_2 (+\text{M}) = \text{HO}_2 (+\text{M})$.

In these conditions, ammonia is mainly consumed by H-abstraction by HO_2 , which is present in relevant amounts at low temperatures. The high amounts of HO_2 also cause the termination of NH_2 radical, such that the reverse reaction prevails over the forward H-abstraction, and acts as a termination. This effect had already been noticed by Stagni et al., 2020a in the oxidation of pure ammonia, although in this setup it does not affect reactivity to a significant extent (Figure 63b) because of the presence of methane in higher amounts. NH_2 holds a key role in modifying the reactivity of pure methane: it reacts with NO and NO_2 , and each of these two paths owns a branching and a terminating channel.

The sensitivity analysis (Figure 63b), carried out at different Φ for the same CH_4 conversion (1%), highlights the importance of H_2NO , formed by both branching channels and by NH_2 reaction with HO_2 . H_2NO is then further oxidized to HNO and finally to NO (chemistry of H_2NO is one of the biggest challenges in ammonia kinetics (Glarborg et al., 2018; Stagni et al., 2020a)). The interplay between NO_2 and NO is also evident in the sensitivity analysis, since NO_2 formation via $\text{NO} + \text{HO}_2$ enhances reactivity, and vice versa for its disappearance via its reaction with H . Indeed, NO_2 is the key molecule in sensitizing methane chemistry: the formation of the reactive methoxy radical (CH_3O) triggers the oxidation process of methane, as already shown in Song et al., 2019. Therefore, the two reactions $\text{CH}_3 + \text{NO}_2 = \text{CH}_3\text{O} + \text{NO}$ and $\text{NO} + \text{HO}_2 = \text{NO}_2 + \text{OH}$ act as a catalytic cycle enhancing the consumption of methane. Conversely, with a richer mixture, the importance of ammonia chemistry becomes less and less important, and the lower amount of HO_2 stops the catalytic cycle. Thus, with increasing Φ , the usual CH_4 oxidation mechanism prevails, and sensitivity analysis shows that H-abstraction reactions and methyl conversion to methoxy govern the system reactivity.

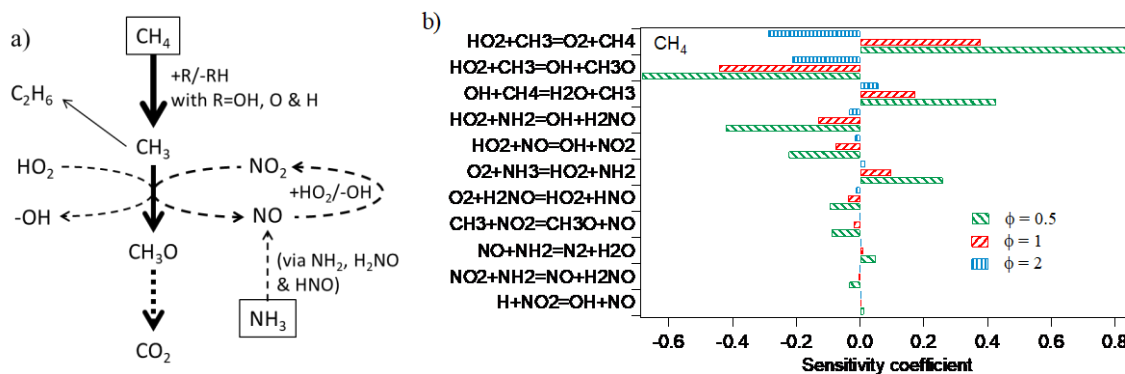


Figure 63: a) Consumption pathways of methane and ammonia, and b) sensitivity analysis for methane mole fraction at variable Φ for $\sim 1\%$ CH₄ conversion. Sensitivity coefficients are normalized with respect to the value of H+O₂=O+OH (not included).

Under FR conditions, there are fewer direct interactions between methane and nitrogen species. Methane is still mainly consumed through H-abstractions by H, O and OH radicals. CH₃ radicals mainly react with O-atoms to CH₂O+H, i.e., bypassing CH₃O chemistry, crucial at lower temperatures. The second most important CH₃ reaction is the termination to ethane, and the third one is its interaction with NH forming CH₂NH+H. However, this does not have a significant impact on reactivity (Figure 64a). Formaldehyde reacts following the usual sequence to give CO₂. CH₂NH chemistry is not discussed here, as it is not determining. The sensitivity diagram in Figure 64a shows that the reactivity is mainly governed by the chemistry of methane, whereas the impact of ammonia is minor, and limited to i) H-abstraction on ammonia itself, slowing down the reactivity since it subtracts active radicals for branching, and ii) N₂H₂ formation from NH₂ and NH, with consequent release of a H radical. Therefore, the oxidation paths of the two fuels are mostly governed by their independent interactions with the radical pool (H, O, OH).

As far as ammonia specific chemistry is concerned, the intermediate HNO plays a minor role under these high temperature conditions. The NH₂ radical mainly gives NH. It also reacts back to ammonia and leads to N₂H₂ by recombination. N₂H₂ is converted into N₂, one of the major reaction products, through NNH. The NH radical mainly reacts with CH₃ yielding CH₂NH, while its second most important consumption route is to produce N₂H₂. It also yields N₂ via N₂O and NO, another major reaction product, via N. N₂O mostly acts as an intermediate species rather than as a final product, due to the high temperatures involved, causing its quick decomposition to N₂

and O. Anyway, the main NO formation pathway is still through HNO, which is formed from NH₂, although it is a minor consumption pathway for this last species.

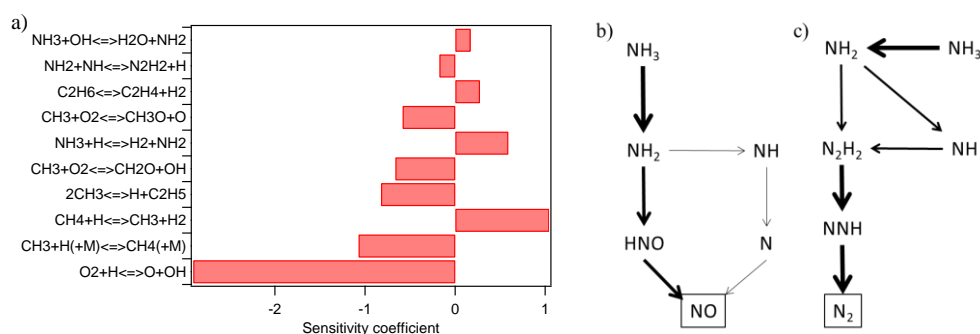


Figure 64: a) Sensitivity diagram for methane under the FR conditions. b) and c) Formation routes to NO and N₂ (T = 1560 K, φ=1, x = 46 cm (length from the tube inlet)). The arrow thickness is proportional to the reaction flux.

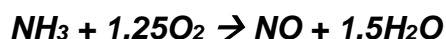
IV.2.3 Conclusion

In this part, the co-oxidation of methane and ammonia was studied to investigate their mutual interactions. Experiments were carried out in jet-stirred and flow tube reactors working up to ~2000 K. Comparison of experimental data with simulations using a novel detailed kinetic model showed a satisfactory agreement for the reactivity and for the mole fractions of most reaction products.

The kinetic analysis of the system shed light on the underlying causes of the NH₃ promoting effect, and on the major role played by NO in anticipating methane reactivity at low temperature. It was observed that even as an intermediate species in the ammonia oxidation path, it affects methane oxidation to a major extent, shifting the reactivity onset by up to ~100 K, especially in leaner conditions. This effect is not present at higher temperatures where the reactivity is mainly governed by fuel H-abstractions by OH, O and H. In this case, as soon as methane reacts, the radical pool necessary to trigger ammonia oxidation becomes available, such that the reactivity onset of the two fuels occurs at the same temperature and is slightly anticipated with respect to pure CH₄ mostly because of the higher amount of fuel.

IV.3 Ammonia doped with hydrogen oxidation

The experimental and modelling results obtained during the oxidation of ammonia doped with hydrogen are presented in this part. These data were obtained using the FR setup and the analytical tools described in Chapter III. The experiments on the oxidation of ammonia/hydrogen mixtures have been carried out under atmospheric pressure (0.128MPa) with helium as carrier gas, at temperatures ranging from 873 to 1773 K and at a residence time of about 0.05 s. The consumption of ammonia, hydrogen, oxygen and the mole fraction of products have been measured as a function of the reactor temperature for several mixtures composed of 1000 ppm of ammonia and of variable amounts of hydrogen over the range 0-2000 ppm (Table 24). The fuel-air equivalence ratio was always set constant to one using the following stoichiometric equations:



NO was considered rather than N₂ since high amounts of NO were formed under the conditions of this study. If N₂ is the final product, the equivalence ratio will vary between 0.75 and 0.86 (instead of one), as shown in Table 24.

Table 24: Summary of the conditions investigated in this study.

Set	$x_{\text{NH}_3}^{\text{inlet}}$ (ppm)	$x_{\text{H}_2}^{\text{inlet}}$ (ppm)	H ₂ composition in NH ₃ /H ₂ mixture	Φ (NO: final product)	Φ (N ₂ : final product)
1	1000	0	0%	1	0.75
2		111	10%		0.76
3		266	21%		0.77
4		538	35%		0.79
5		1000	50%		0.82
6		2003	66.7%		0.86

Species were sampled at the outlet of the reactor and analyzed online using mass spectrometry and a dedicated analyzer for NO_x. The first diagnostic was used for the detection of ammonia, hydrogen, oxygen, water, nitrogen, and NO. The calibration was performed by injecting standards except for water, which was calibrated considering the combustion complete at the highest temperatures. The second diagnostic was used for the detection of NO and confirmed that no NO₂ was observed under the conditions of this study).

IV.3.1 Experimental results

In this section, the experimental results obtained during my PhD are compared to simulation data using the kinetic model which was already discussed in the section about neat ammonia oxidation (part IV.1). Figure 66 compares the simulated mole fractions of reactants and main products with the oxidation data in FR, being obtained over the temperature range 873-1773 K. Six species were quantified in the present study: ammonia, hydrogen, oxygen, nitrogen, nitric oxide (NO) and water. The effect of the progressive addition of hydrogen on the reactivity of ammonia and the formation of reaction products was observed. As shown in Figure 66, the more hydrogen in the feed, the more reactive the system. The ammonia profiles obtained for the different inlet H₂ mole fractions conditions are similar, but significantly shifted towards lower temperatures when adding hydrogen in the feed. The shift is about 450 K from the neat ammonia case to the case with 2000 ppm of hydrogen addition. The evolution of the temperature at mid conversion as a function of the percentage of H₂ in the NH₃/H₂ mixture is quasi linear as shown in Figure 65.

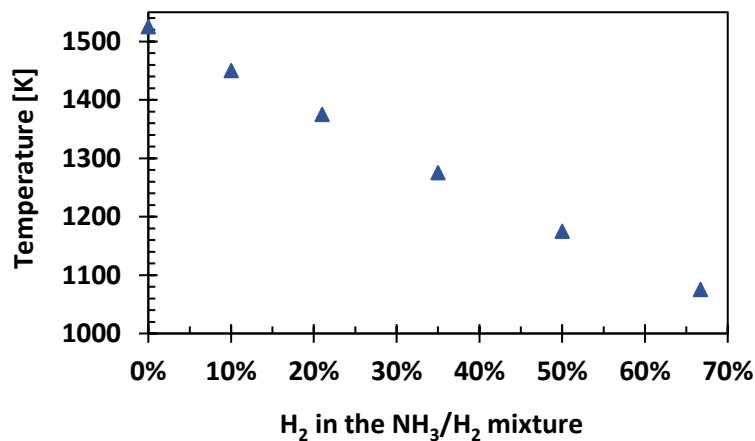


Figure 65: Evolution of the temperature at mid conversion as a function of the percentage of H₂ in the NH₃/H₂.

Interestingly, H₂ consumption profiles are different from those for ammonia. For a given amounts of H₂ in the feed, the onset for the reactivity for both fuels is the same, showing that there is a mutual interaction between the two species. But then ammonia consumption rate is faster than that of hydrogen when the temperature increases. Another interesting point, when comparing the profile for 1000 ppm neat H₂ and 1000

ppm H₂ with 1000 ppm NH₃, is that the profile for H₂ is different and that for the mixture case exhibits a slower consumption rate of H₂. It seems that the interaction with ammonia mitigates the reactivity of H₂, whereas H₂ enhances that of ammonia.

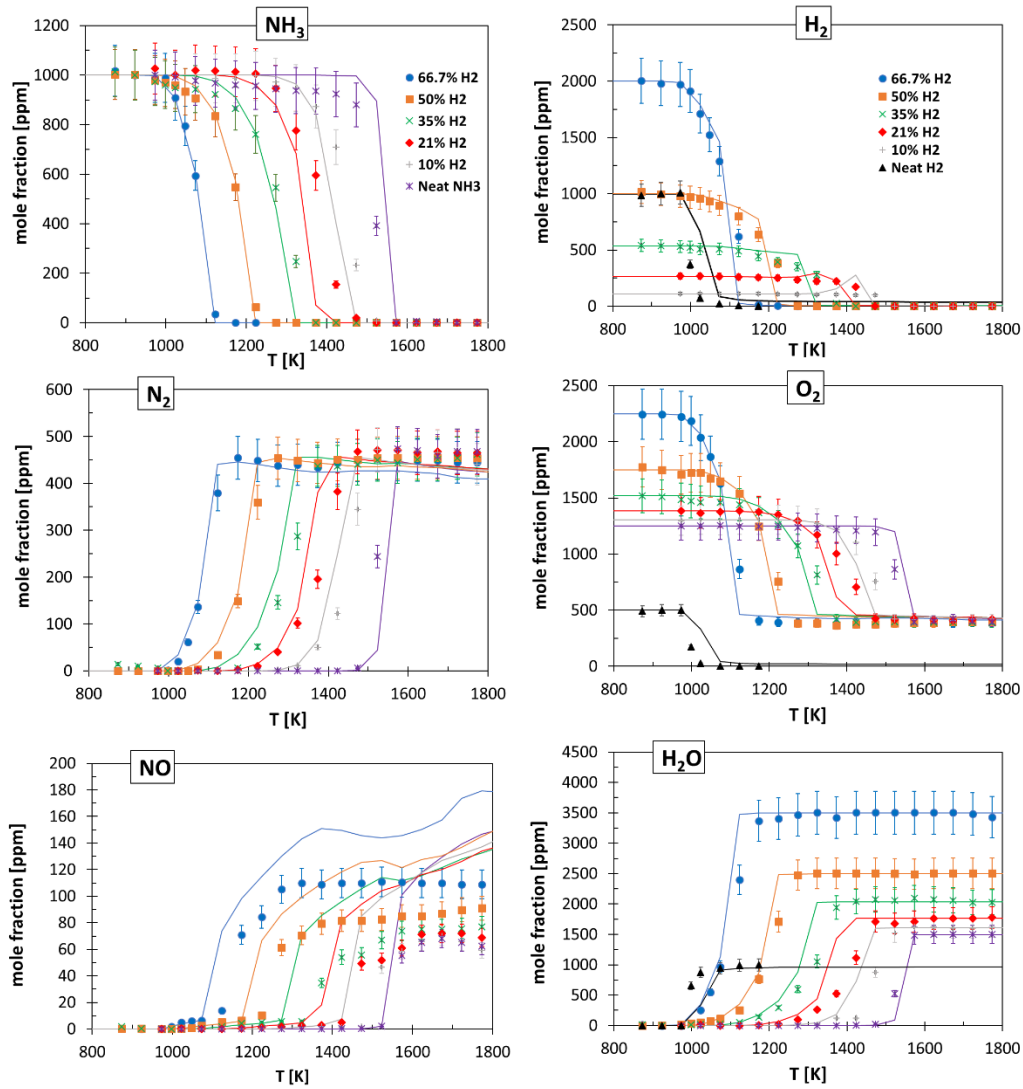


Figure 66: Effect of progressive addition of H₂ to the oxidation of 1000 ppm NH₃ in a FR. Symbols: experiments. Lines: data computed with the model. P = 0.128MPa. The average residence time in the reactive zone is 50 ms.

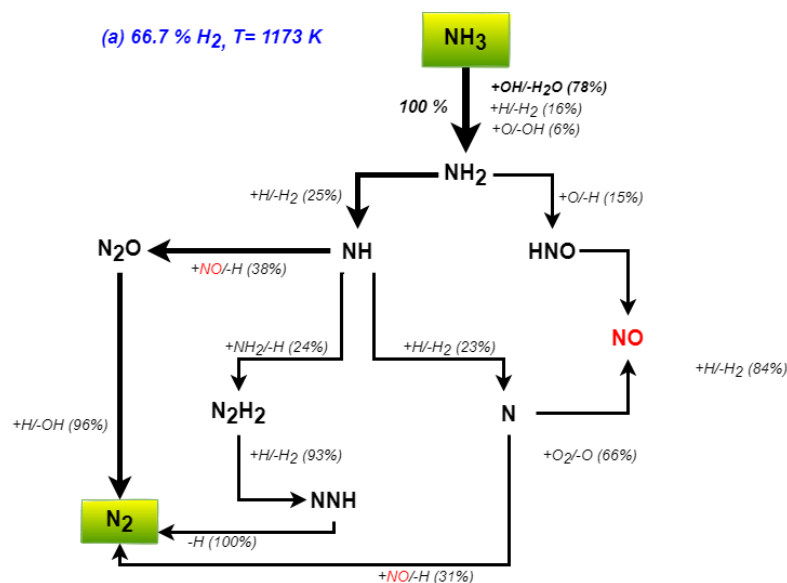
The addition of hydrogen has also an effect on the formation of reaction products which is anticipated with increasing amount of H₂ in the feed. This is to be associated to the higher reactivity of the system. As for neat ammonia, important amounts of N₂ are observed concomitantly to the consumption of ammonia, whereas mole fractions of NO start to increase in a significant way once ammonia is fully consumed (this can be explained by the reburning of NO by reaction with NH₃ at the

lower temperatures which cannot occur anymore at higher temperatures once NH_3 is fully consumed). The addition of hydrogen also plays a role on the ratio between NO and N_2 . While the addition of H_2 has a very limited effect up to 35% of H_2 in the feed, the final mole fraction of NO (which is quasi constant at the highest temperature) jumps slightly for the 50% case and still more for the 66.7% case.

Computed data from the kinetic model shows a satisfactory agreement for fuels conversion and reaction products but less for NO profiles.

IV.3.2 Kinetic analysis

The kinetic mechanism was used to investigate the rate of consumption of fuels and the sensitivity coefficients to NH_3 mole fraction. Figure 67 presents a rate analysis for NH_3 and H_2 carried out in the FR for 1000 ppm NH_3 oxidation under 0.128 MPa at temperatures of 1073 K, 1173 K, and 1573 K corresponding to H_2 composition of 66.7% (Figure 67a), 35% (Figure 67b) and 0% (Figure 67c), respectively.



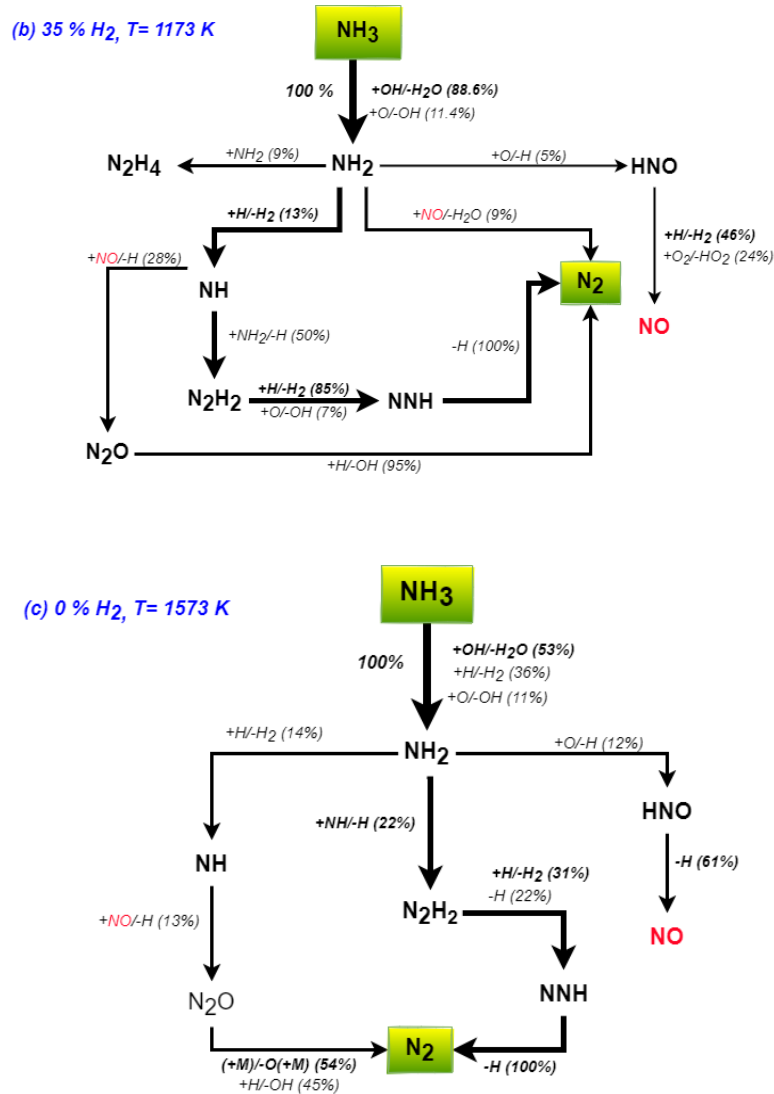


Figure 67: Reaction flux analysis in FR at temperatures of 1073 K, 1173 K, and 1573 K corresponding to H₂ composition of 66.7% (a), 35% (b) and 0% (c), respectively.

The addition of hydrogen has an effect on the consumption of NH₃ to NH₂ (especially via NH₃+OH=NH₂+H₂O) which is more important when increasing the amount of H₂ in the feed. With the presence of H₂ (Figure 67a-b), NH₂ is mainly consumed to yield NH by H-abstraction (NH₂+H=NH+H₂). Whereas, without H₂ in the mixture (Figure 67c), NH₂ is mainly consumed by NH radicals to form N₂H₂. However, the NH₃ consumption pathway cannot clearly show the effect of H₂ on the oxidation of NH₃.

Figure 68 presents sensitivity analysis of ammonia at temperatures of 1073 K, 1173 K, and 1573 K corresponding to H₂ composition of 66.7% (Figure 68a), 35% (Figure 68b) and 0% (Figure 68c), respectively. In the presence of H₂, the reaction O₂+H=O+OH is the most sensitive reaction increasing the reactivity whereas without

H_2 , the reaction $H+O_2(+M)=HO_2(+M)$ becomes the most sensitive reaction. Moreover, $H+O_2(+M)=HO_2(+M)$ is an inhibiting reaction for NH_3 reactivity in case of presence of H_2 .

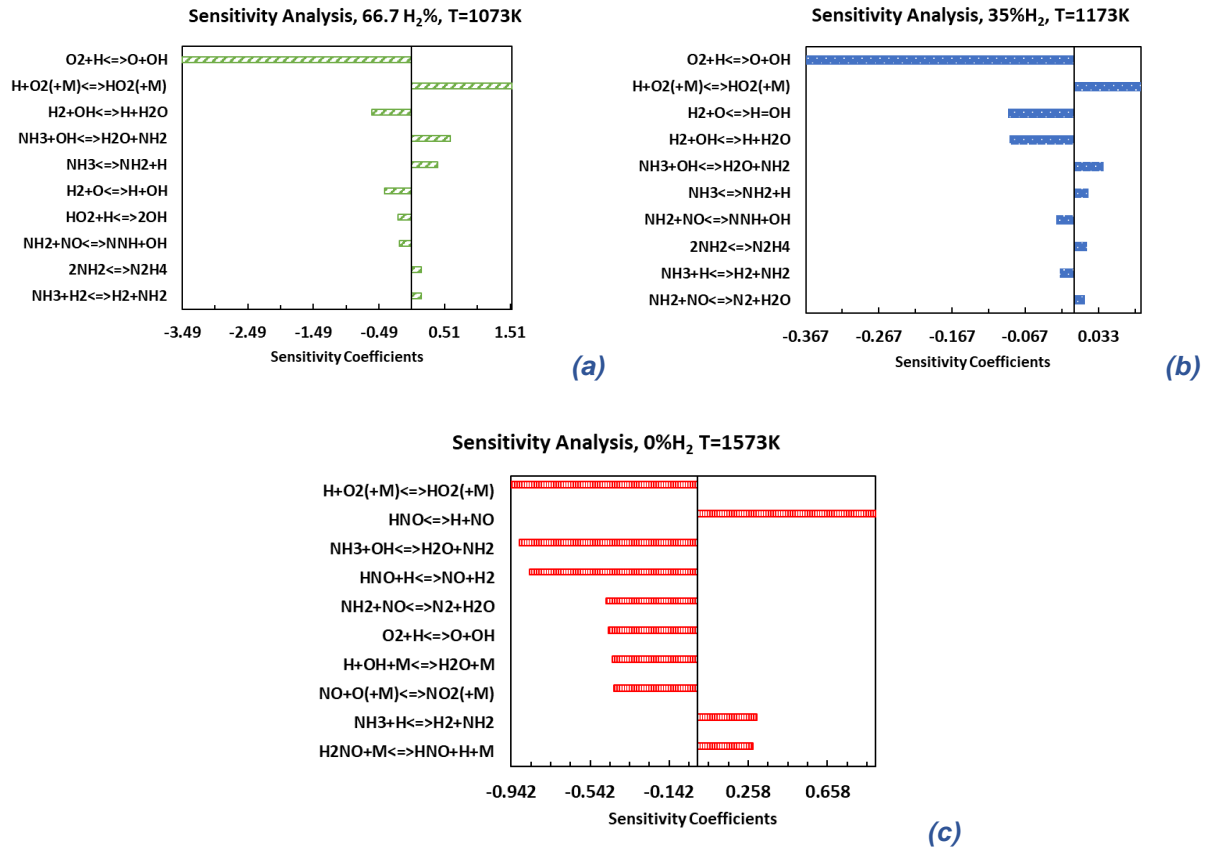


Figure 68: Sensitivity coefficients to NH_3 mole fractions in FR1 case at temperatures of 1073 K, 1173 K, and 1573 K corresponding to H_2 composition of 66.7% (a), 35% (b) and 0% (c), respectively.

IV.3.3 Conclusion

In this part, the co-oxidation of ammonia and hydrogen was studied to investigate their mutual interactions in a FR. These experiments were difficult to be carried out due to catalytic effects on the reactor wall. The comparison of experimental data with simulations using the novel detailed kinetic model of Milano shows a satisfactory agreement for the reactivity and for the mole fractions of most reaction products. The kinetic analysis of the system shed light on the effect of H_2 addition, which enhances the NH_3 consumption. The kinetic model needs to be further developed because there is still a significant deviation between experiments and simulation for NO profiles.

IV.4 Neat hydrogen sulfide pyrolysis and oxidation

This section of the [chapter IV](#) is aimed at describing the experimental and modelling results about the reaction of neat H₂S. First, neat hydrogen sulfide pyrolysis will be described. Neat H₂S oxidation will be then presented. The experiments were carried out in the JSR, and in the two flow reactors (FR1 and FR2) with helium as bath gas under atmospheric pressure with 500 and 800 ppm of inlet mole fraction of hydrogen sulfide. The use of all three reactors allowed to explore the kinetic behavior of H₂S at low temperatures and high residence times and vice versa. Several tests were made with coated and non-coated reactors to highlight possible catalytic effects. These tests show that the coating is necessary to prevent H₂S from reacting at the wall. Performing experiments with different devices working under different configurations was crucial as it gave more confidence in the obtained experimental data as far as potential surface effects are concerned. In the last part, a detailed analysis of reaction products is presented and the results are interpreted with a comprehensive kinetic model developed in Milano.

IV.4.1 Kinetic modeling

In the next section, the kinetic mechanism developed by the team of Prof. T. Faravelli at Politecnico di Milano was used to investigate the rate of consumption of H₂S and the sensitivity coefficients to H₂S mole fraction for H₂S pyrolysis and oxidation in JSR. The kinetic modeling of H₂S pyrolysis and oxidation was performed through a hierarchical and modular methodology, as implemented in the CRECK kinetic framework. The relevant reactions composing the model are summarized in [Table 25](#). Concerning the oxidation model, the oxidation reactions of the SH radical with O₂ were adopted after the work of Zhou et al. (2009) on the related branching ratio, with SH+O₂ =SO₂+H reaction updated after the recent estimation of Song et al. (2017). H-abstractions were taken from the most updated sources, where theoretical estimations were performed: reaction with HO₂ was kept from the same previous reference (Zhou et al. (2009)). Regarding sulfur-containing species, abstractions by SO were taken from the estimations of Zhou et al. (2013), as included in their oxidation model.

Table 25: List of key reactions in the H_2S pyrolysis and oxidation mechanism. Reaction rate expression is modified Arrhenius $k = AT^\beta \exp[-E_a/(RT)]$. Units are cm^3 , cal, mol, K, s.

Reaction	A	β	E_a	Notes	Ref
$H_2S + M = H_2 + S + M$	5.10×10^{13}	0.000	56350		Karan et al. (1999)
$SH + O_2 = HSO + O$	2.30×10^6	1.816	20008		
$SH + O_2 = S + HO_2$	4.70×10^6	2.017	36913		Zhou et al. (2009)
$SH + O_2 = HSO + OH$	7.50×10^4	2.100	16384		
$SH + O_2 = SO_2 + H$	1.50×10^5	2.123	11020		Song et al., (2017)
$SH + HO_2 = H_2S + O_2$	3.80×10^4	2.775	-1530		Zhou (2009)
$SH + HO_2 = HSO + OH$	2.46×10^8	1.477	-2169		
$H_2S + O = SH + OH$	1.86×10^5	2.644	2032		Wang et al. (2005)
$H_2S + H = SH + H_2$	7.26×10^8	1.538	1068		Cavallotti et al., (2019)
$H_2S + OH = SH + H_2O$	1.30×10^8	1.846	-1150		
$SH + H_2O_2 = H_2S + HO_2$	5.60×10^4	2.823	7668	$E_{act} - 1000$	Zhou (2009)
$SH + H_2O_2 = HSOH + OH$	9.49×10^3	2.800	9829		
$H_2S + SO = SH + HOS$	5.38×10^3	3.200	26824		Zhou et al. (2013)
$H_2S + SO = SH + HSO$	1.00×10^{13}	0.000	36500		
$H_2S + S = SH + SH$	5.87×10^{23}	-2.516	13617	$A \times 0.9$	Shiina et al. (1996)
$S + O_2 = SO + O$	5.43×10^5	2.100	-1451		Lu et al. (2003)
$SO + O_2 = SO_2 + O$	8.91×10^6	1.400	3712		Garland (1998)
$SH + S = S_2 + H$	3.31×10^{12}	0.500	-29		Zhou (2009)
$SH + O = SO + H$	2.40×10^{11}	0.700	-1027		Sendt and Haynes (2007)
$S_2 + O = S + SO$	1.32×10^{13}	0.000	17		

IV.4.2 Experimental results

In the next section, the experimental results are compared to the simulation data calculated using the kinetic. The results about H₂S pyrolysis in three different reactors are first presented, then those about H₂S oxidation are displayed. In this work, the equivalence ratio (ϕ) was defined considering the following global reaction: **$H_2S + 1.5 O_2 = SO_2 + H_2O$** .

a) Hydrogen sulfide pyrolysis

The only reaction product detected during the pyrolysis of hydrogen sulfide is hydrogen. On-line mass-spectrometry (MS) was used for the quantification of H₂S and H₂. Sampling was achieved through a capillary tube directly connecting the reactor outlet and the analyzer. H₂ was also quantified using gas chromatography to validate the mass spectrometry detection method. GC and MS data are in excellent agreement as shown in [Figure 72](#).

No S containing species could be detected, likely because they condensed at the outlet of the reactors. Solid sulfur, a yellow solid was nevertheless observed at the outlet when dismantling FR2 and cleaning it with solvents (see picture in [Figure 69](#)).



Figure 69: Solid sulfur found at the outlet of FR2.

In the JSR, hydrogen sulfide pyrolysis was performed at a residence time of about 2 s and at temperatures ranging from 500 to 1200 K with an initial fuel mole fraction of 500 ppm. The mole fraction profiles of H₂S and H₂ are shown in [Figure 70](#). The consumption of H₂S and the formation of H₂ were only observed at high temperatures, from ~1000 K. A conversion of about 10% was reached at 1200 K, which is the maximum operating temperature for the JSR.

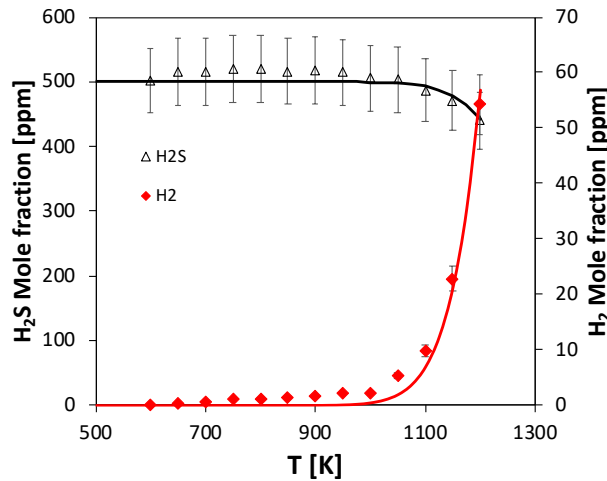


Figure 70: Pyrolysis of 500 ppm H₂S in the JSR. $P = 0.107\text{MPa}$. $\tau = 2\text{ s}$. Symbols are for experiments and lines for data computed with the model.

To extend the range of temperatures, FR2 was used for the experiment at higher temperatures, up to 1600K, to follow the H₂S reactivity under 0.107 MPa with a residence time around 2 s. As shown in Figure 71, H₂S consumption becomes significant from ~1323 K and the reactant was quasi totally consumed from ~1523 K.

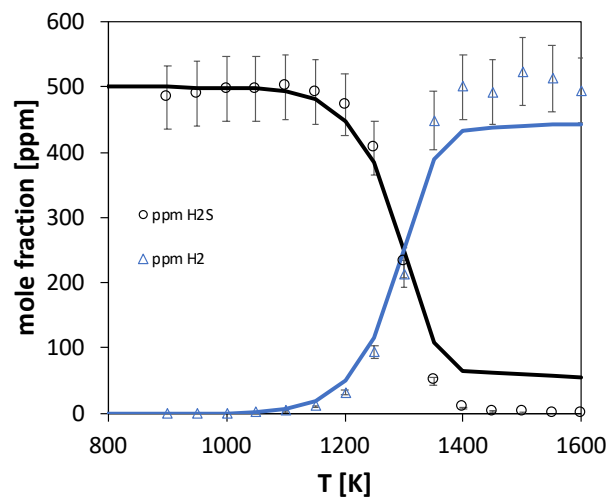


Figure 71: Pyrolysis data in FR2 ($P = 0.107\text{MPa}$, $\tau \sim 2\text{ s}$, $x_{fuel}^{in} = 500\text{ ppm}$). Symbols are for experiments and lines for data computed with the model.

Figure 72 presents the results of H₂S pyrolysis conducted in FR1 under 0.123 MPa but at a smaller residence time of about 0.25 s. The reactivity profile of H₂S is similar to that observed in FR2 operated at about 2 s of residence time, but shifted towards higher temperatures as a result of the shorter residence time.

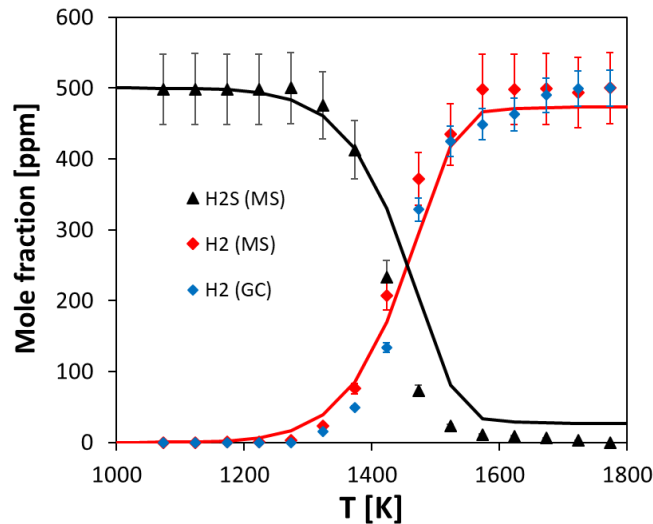


Figure 72: Pyrolysis of 500 ppm H₂S in FR1. $P = 0.123$ MPa. $\tau = 0.25$ s. Symbols are for experiments and lines for data computed with the model.

b) Hydrogen sulfide oxidation

The three reactor facilities have been also used to perform H₂S oxidation experiments. As expected, the reactivity is enhanced compared to pyrolysis. Reaction products detected during the oxidation experiments are sulfur dioxide (SO₂), water and hydrogen (H₂). On-line mass-spectrometry (MS) was used for the quantification of H₂S, H₂, H₂O, SO₂ and O₂. This technique required the calibration of each species using gaseous standards. Water was calibrated considering the reaction complete at the highest temperature.

JSR data

In the JSR, H₂S oxidation experiments were carried out with two different inlet mole fractions of fuel (500 and 800 ppm) and two different equivalence ratios, (0.25 and 0.5), at 0.107 MPa with a residence time of 2 s. Figure 73 displays the data obtained, using the coated JSR. The reactivity is only very little affected by the different conditions, with a significant conversion observed in the range 700 - 800 K. Only one intermediate species was observed during these experiments: H₂. It was formed simultaneously from the fuel decay and its mole fraction peaked at about 850 K. The two other product species were SO₂ and H₂O, which exhibited typical profiles of final combustion products with a plateau at the highest temperatures.

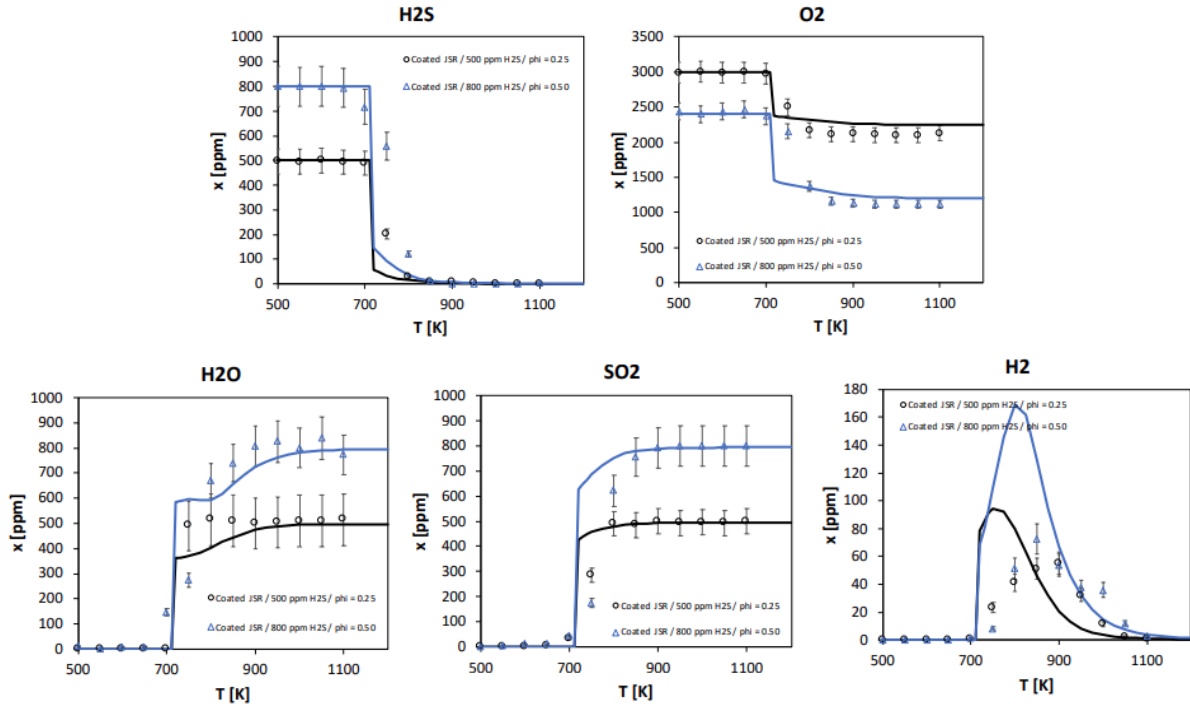


Figure 73: JSR oxidation data ($P = 800$ Torr, $\tau = 2$ s) for two cases, $x_{fuel}^{in} = 500$ ppm / $\phi = 0.25$, and $x_{fuel}^{in} = 800$ ppm / $\phi = 0.50$. The reactor wall was treated to minimize catalytic effects. Symbols are for experiments and lines for data computed with the model.

The effect of the equivalence ratio was investigated for 500 ppm of inlet mole fraction of H_2S . The experiments were performed by varying the amount of oxygen (3000, 20400 and 40800 ppm corresponding to equivalence ratios of 0.25, 0.0367 and 0.0184). The two cases with large amount of oxygen (20400 and 40800 ppm O_2) were studied for comparison with data for the CH_4 - H_2S mutual interaction oxidation study presented later. In addition, the use of the JSR allowed to explore the reactivity at low temperatures, with very high oxygen amounts. Figure 74 also shows the related experimental and modeling predictions.

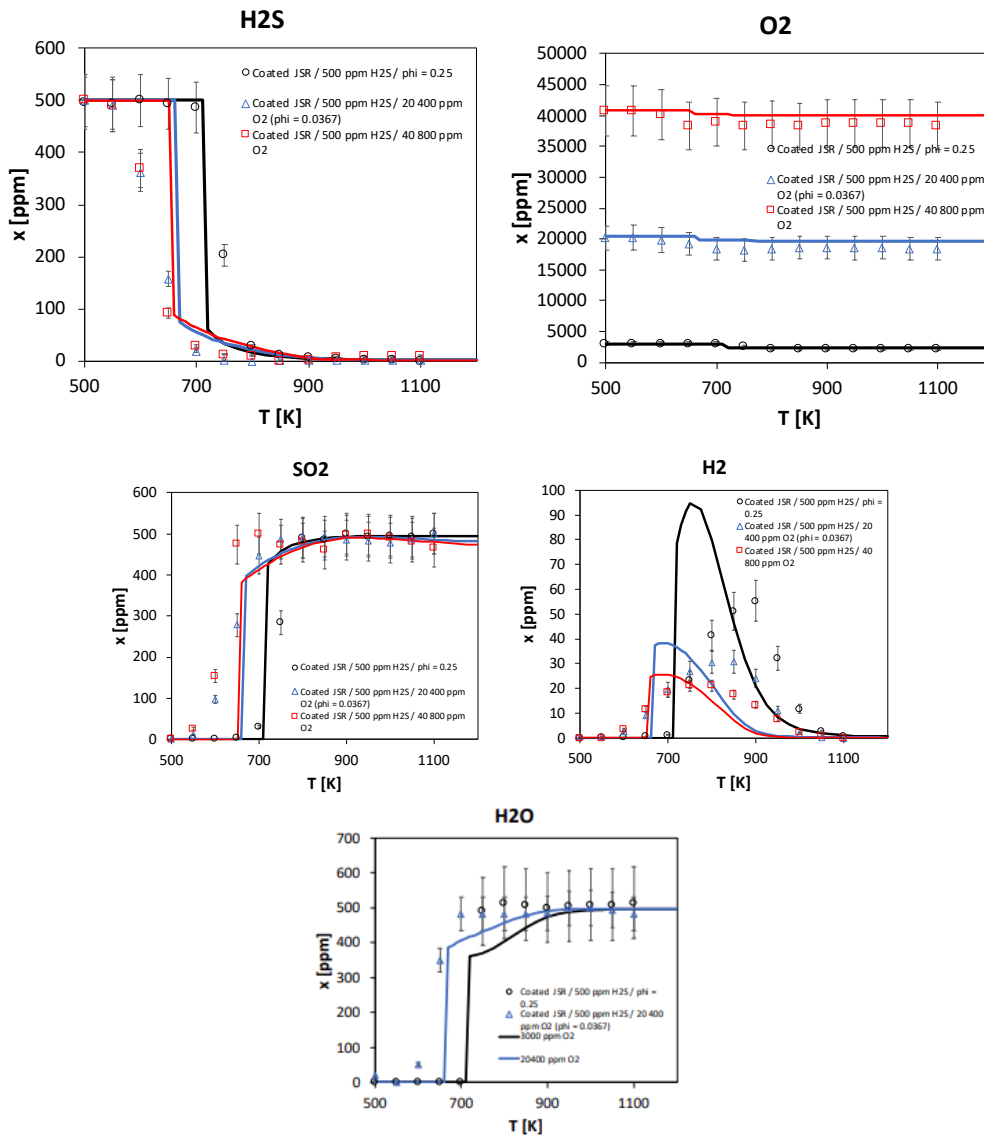


Figure 74: Oxidation of 500 ppm H_2S with 3000, 20400 and 40800 ppm O_2 in JSR. $P = 0.107$ MPa. $\tau = 2$ s. Symbols are for experiments and lines for data computed with the model.

The reactivity is only very little affected by the different conditions, with a significant conversion observed in the range 700-800 K. Only one intermediate species is again observed during these experiments: H_2 , which is formed simultaneously from the fuel decay and whose mole fraction peaks at about 850 K. The two other product species are SO_2 and H_2O , which exhibit typical profiles of final combustion products with a plateau at the highest temperatures. As for pyrolysis, no S containing intermediate species is observed in these experiments.

The equivalence ratio influences the reactivity, the leanest case being the most reactive and the richest case being the least reactive. In the leanest conditions, H₂S conversion starts as early as at ~600 K, while the model overestimates the reactivity onset by ~50 K. However, the increasing reactivity of the mixture with higher oxygen amounts is coherently reproduced. In addition, the H₂ peak is overestimated, especially for lower oxygen amounts.

The two leanest cases have similar reactivity. As far as products are concerned, the shift in reactivity directly affects the profiles of water and SO₂. Hydrogen mole fractions are also affected by the shift in the reactivity in two ways. At $\varphi = 0.25$, the mole fraction increase is observed at a higher temperature (~ 700 K to be compared to 600 K for $\varphi = 0.0367$) and the mole fraction at the peak is larger (55 ppm to be compared to 31 ppm for $\varphi = 0.0367$) and also observed at a high temperature (~ 900 K to be compared to 850 K for $\varphi = 0.0367$).

FR1 data

Figure 75 displays the profiles of the main species at intermediate temperatures, as sampled in FR1. Two conditions were tested: $\tau \sim 0.1$ s – $\varphi = 0.25$ and $\tau \sim 0.25$ s – $\varphi = 0.1$. A satisfactory agreement can be observed between model predictions and experiment data points for all the species. The fuel decay is observed at lower temperature for the leanest conditions and longest residence time (923 K to be compared to 1023 K). The H₂ mole fraction profiles have similar shape with both having a maximum around 100 ppm, but being shifted by 100 K as for the fuel mole fraction profiles. SO₂ and water have profiles of final combustion products. The water profiles were not so accurate for the leanest conditions with no obvious reason. This could be due to the large amount of O₂, which is the only parameter being very different between the two sets of experiments.

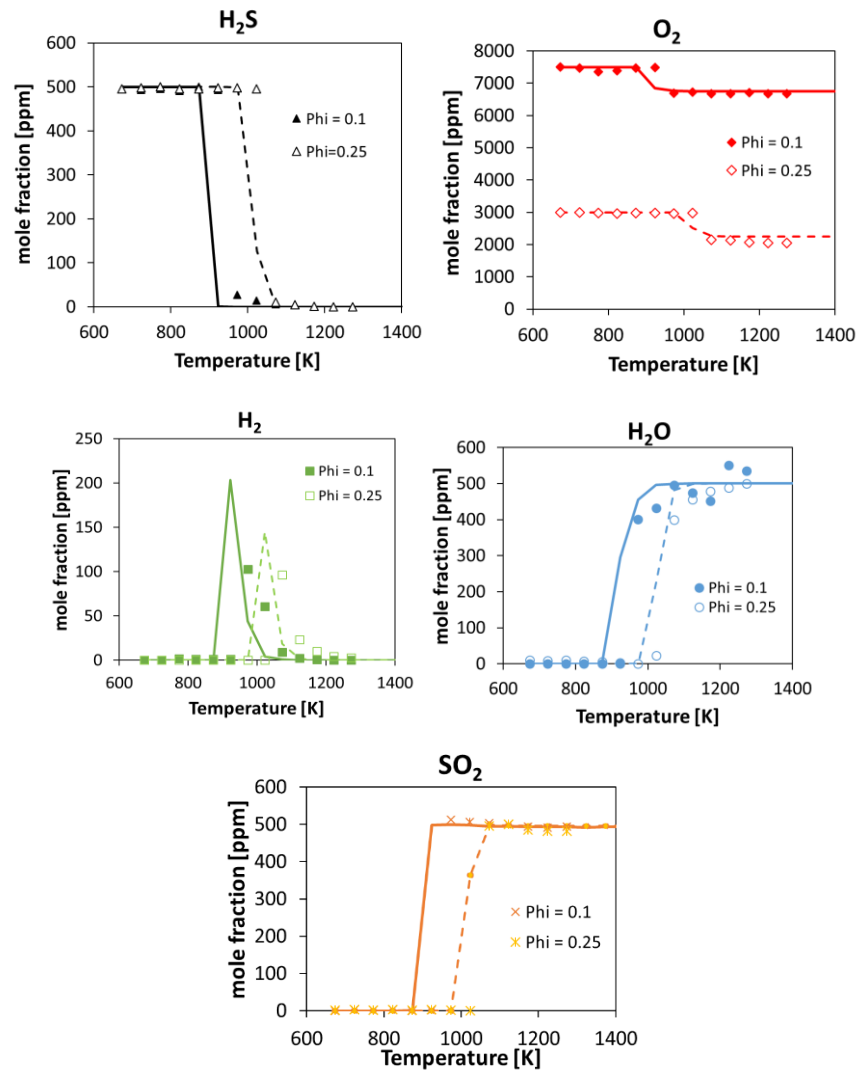


Figure 75: Oxidation of 500 ppm H₂S in FR1. $P = 0.127$ MPa. Symbols are for experiments and lines for data computed with the model. Solid lines: $\tau = 0.25$ s, $\Phi = 0.1$. Dashed lines: $\tau = 0.1$ s, $\Phi = 0.25$.

FR2 data

Comparable trends can be observed for the longer residence times used in FR2, as shown in Figure 76. Four configurations were tested with coated and non-coated alumina tubes and coated and non-coated fused silica tubes. As far as non-coated tubes are concerned, both sets of data looked similar with a slightly higher reactivity in the uncoated alumina tube compared to the fused silica one. Data obtained with the two-coated tubes were in excellent agreement and the reactivity is lower than that observed with the non-coated tubes. Given these observations, there is probably a wall catalytic effect with the non-coated alumina and fused silica tubes.

As in the JSR, SO₂ and water have typical profiles of final combustion products whereas H₂ mole fraction profile peaks at about 850 K.

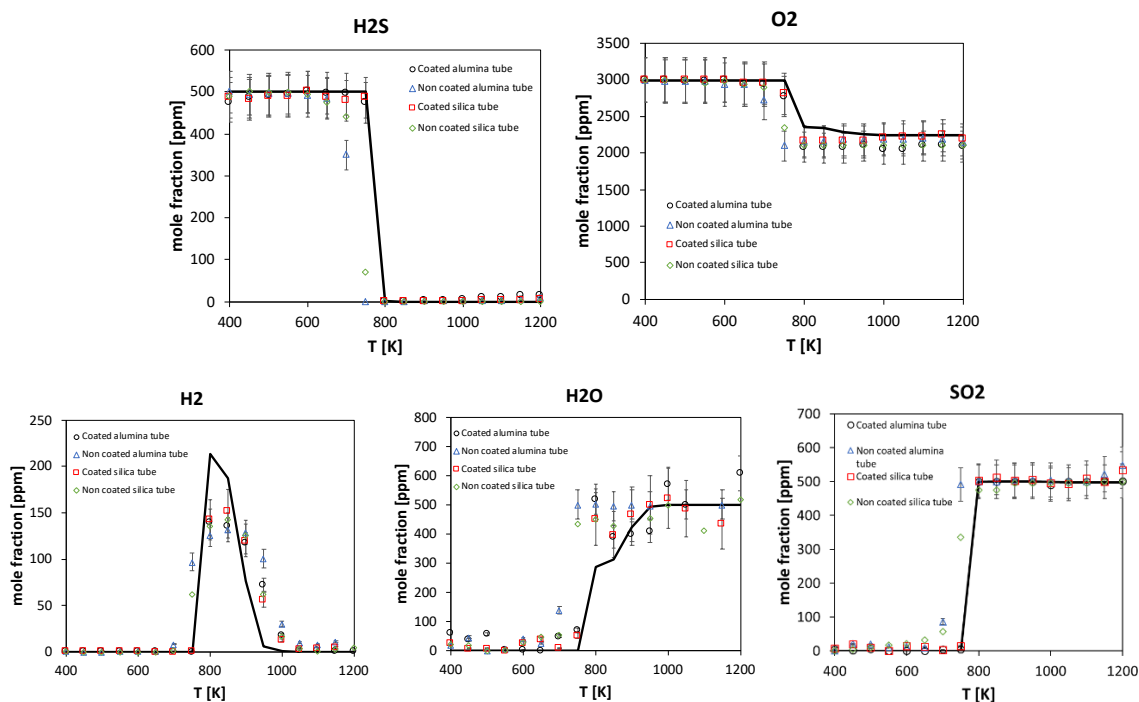


Figure 76: Oxidation of 500 ppm H₂S in 0.3% O₂ (FR2). $P = 0.107$ MPa, $\tau = 2$ s, $\Phi = 0.25$. Symbols are for experiments and lines for data computed with the model.

The reactivity profiles obtained in FR2 are similar to that in the JSR with the main difference being in the slope in the fuel decay, which is more abrupt in FR2 (over 50 K window, whereas the fuel decay occurs over a 100 K window in JSR). This more abrupt evolution is also observed for O₂, SO₂ and water. The temperature windows for H₂ mole fraction profiles are similar, but the shape of the profiles are different and larger mole fractions of H₂ were obtained in FR2 (152 ppm at 850 K to be compared with 55 ppm at 900 K in the JSR).

IV.4.3 Kinetic analysis

Figure 77 shows flux analysis performed at 1200 K and 725 K for neat hydrogen sulfide pyrolysis (Figure 77a) and oxidation (Figure 77b), respectively, in JSR. Under pyrolysis condition (Figure 77a), H₂S is mainly consumed by H-abstraction forming SH radicals. This channel contributes to 57 % of H₂S consumption. H₂S is also consumed (38 %) yielding solid sulfur via H₂S(+M)=H₂(+M)+S reaction. S and SH are subsequently converted to S₂.

At 725 K, $\phi = 0.25$, corresponding to 89.8 % fuel conversion; H_2S is almost entirely consumed by H-abstraction reactions to form SH as shown in Figure 77b. The main abstracting radical are OH, O and H. The SH radical is mainly consumed by another SH radical to form solid sulfur and yield H_2S back. This channel contributes to 45 % of SH consumption. Solid sulfur was found on the walls of the reactor but could not be quantified. The SH radical is also consumed (25 %) by the O atoms to form SO. Finally, SO is oxidized to SO_2 .

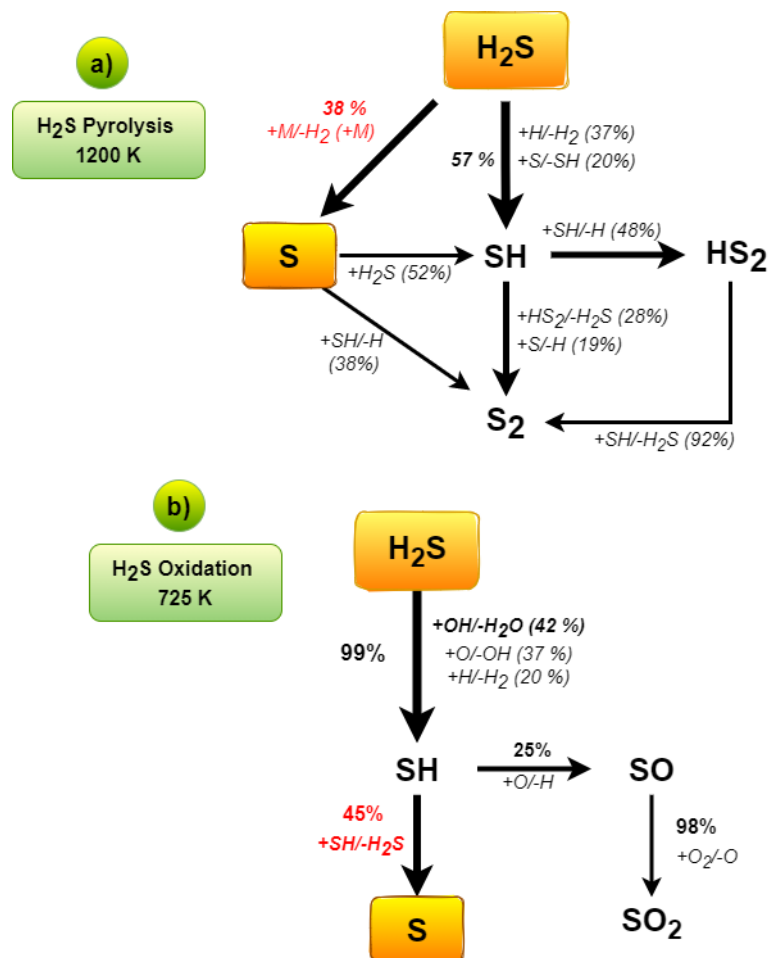


Figure 77 : Consumption pathway of H_2S under pyrolysis (a) and oxidative (b) conditions at 1200 K and 725 K, respectively, in JSR, $P= 0.107$ MPa, 500 ppm H_2S , 3000 ppm O_2 , $\tau = 2$ s .

In order to identify the reaction pathways governing the system reactivity, a sensitivity analysis to H_2S mole fraction was performed in representative conditions for both pyrolysis and oxidation. Figure 78 presents the sensitivity coefficients to H_2S mole fraction for H_2S pyrolysis at 1200 K in JSR.

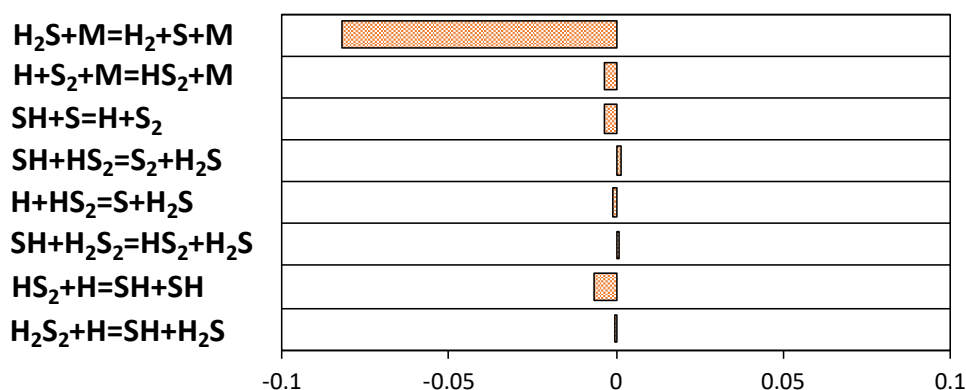


Figure 78: Sensitivity coefficients to H_2S mole fraction for H_2S pyrolysis in JSR. $T = 1200\text{ K}$, $P = 0.107\text{ MPa}$, $500\text{ ppm } H_2S$, $\tau = 2\text{ s}$.

Figure 78 indicates that the third-body thermal decomposition of H_2S : $H_2S + M \rightleftharpoons H_2 + S + M$ drives the whole system reactivity. It is worth pointing out that theoretical data for such a reaction are very limited and related to close-to-atmospheric pressures. Theoretical studies for a wider range of pressures as started by Song et al. (2016), might be necessary to improve accuracy.

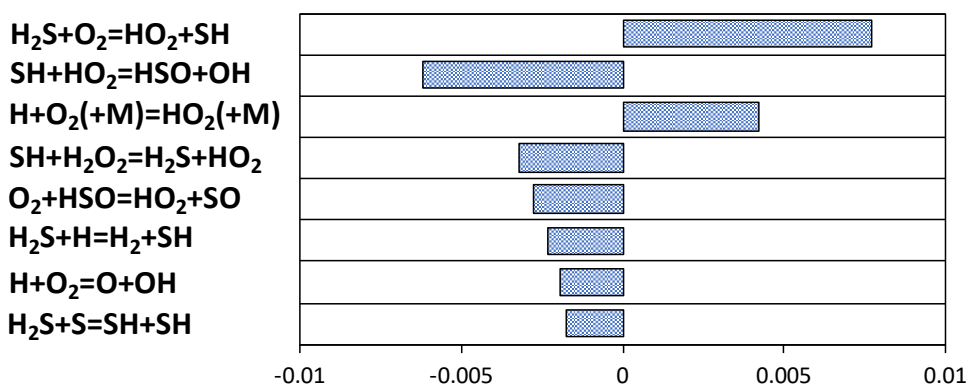


Figure 79: Sensitivity coefficients to H_2S mole fraction for H_2S oxidation in JSR. $T = 675\text{ K}$, $P = 0.107\text{ MPa}$, $500\text{ ppm } H_2S$, $40800\text{ ppm } O_2$, $\tau = 2\text{ s}$.

Regarding H_2S oxidation, sensitivity coefficients to H_2S mole fraction in JSR are displayed in Figure 79. In particular, the antagonistic effect of H-abstraction by O_2 slows down the system; $H_2S + O_2 \rightleftharpoons SH + HO_2$. The key role of HO_2 is comparable to what is observed under low temperature conditions with different fuels in previous studies (Stagni et al., 2020a). HO_2 is involved in two competitive pathways because of its reaction with the SH radical. The termination route, returning two stable molecules (fuel and oxidizer), slows down the reactivity. Conversely, the propagation

route provides two reactive radicals; HSO and OH, therefore promoting the system reactivity. Thus, an accurate, temperature-dependent estimation of the branching ratio of the reaction between SH and HO₂ becomes essential to obtain an accurate prediction of the fuel reactivity in the low temperature range, where HO₂ is stable enough to be present in significant amounts. The third step involves instead the H-abstraction of H₂S by HO₂ itself; SH + H₂O₂ ⇌ H₂S + HO₂. This is particularly critical because it consumes HO₂, thus subtracting it from the termination pathway SH + HO₂ ⇌ H₂S + O₂, returning again the stable fuel and oxygen.

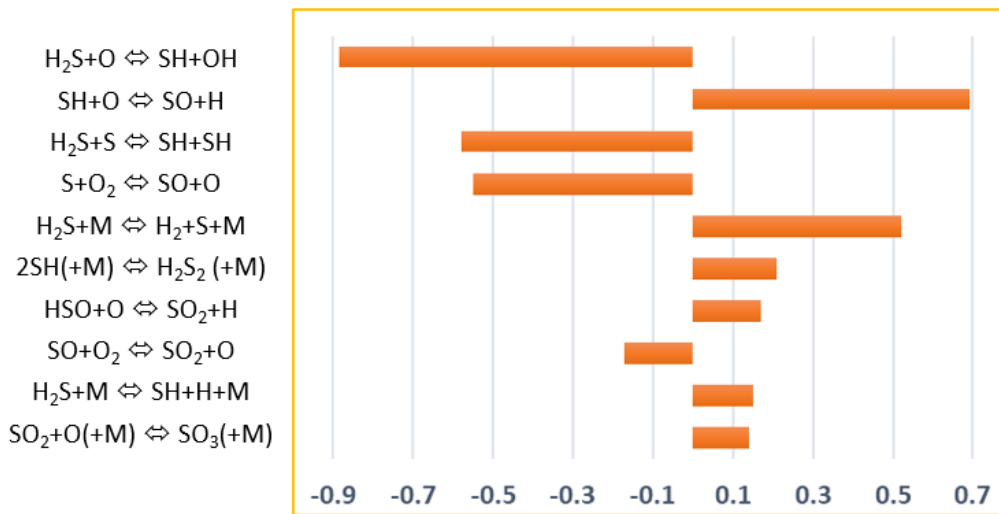


Figure 80: Sensitivity (of fuel mole fraction to reactions) analysis of H₂S oxidation to rate constants at T=725 K in JSR, P= 0.107 MPa, 500 ppm H₂S, 3000 ppm O₂, τ = 2 s.

For H₂S oxidation with the lower oxidizer (3000 ppm O₂), sensitivity coefficients to H₂S mole fraction in JSR was shown in Figure 80. The kinetic analysis shows that the H-abstraction by O drives the whole process; H₂S + O ⇌ SH + OH which is different to H₂S oxidation with 40800 ppm O₂ (system was driven by H-abstraction by O₂). In addition, H₂S is sensitive to the branching fraction for the SH + SH reaction. The formation of H₂S + S promotes the rate of oxidation due to the consecutive chain branching reactions of S and SO with O₂.

IV.4.3 Conclusion

In this work, a combined experimental and kinetic modeling study on neat H₂S combustion was performed using a JSR and two FR under atmospheric pressure. Surface effects promoting an early oxidation in all the reactors were identified. Therefore, an established coating procedure via boric acid was first implemented. Then, by leveraging the different available configurations, a wide range of working conditions was explored, in terms of i) temperature, ii) residence time, and iii) composition. Thanks to online mass-spectrometry and gas chromatography, three products have been quantified.

The experimental work was not easy to handle because H₂S is very toxic. It has been referred to as the “knock down gas” because inhalation of high concentrations can cause immediate loss of consciousness and death (Belly et al., 2005). However, prolonged exposure to lower concentrations, such as 10-500 ppm, can cause various respiratory symptoms that range from rhinitis to acute respiratory failure (Doujaiji and Al-Tawfiq, 2010). Moreover, H₂S can be easily adsorbed on the reactor wall, which caused surface effects. Thus, it was needed to repeat the experiments many times to ensure the results and to use different devices for being more confident. H₂S study also shew that reactor use history is also of importance. Indeed, the FR1 was used afterwards for the experiments of the oxidation of NH₃/H₂. The experimental results were too inconsistent with the computed data, which shed light on possible wall effects due to previous experiments with H₂S. Therefore, it was decided to use a new FR1 alumina tube to repeat the second experiment of NH₃/H₂ oxidation. It was observed that the two sets of results were somehow different, especially H₂ and NO profiles as shown in [Figure 81](#) below. This confirms that S compounds can enhance reactor surface effects and that reactor use history is of importance for data accuracy.

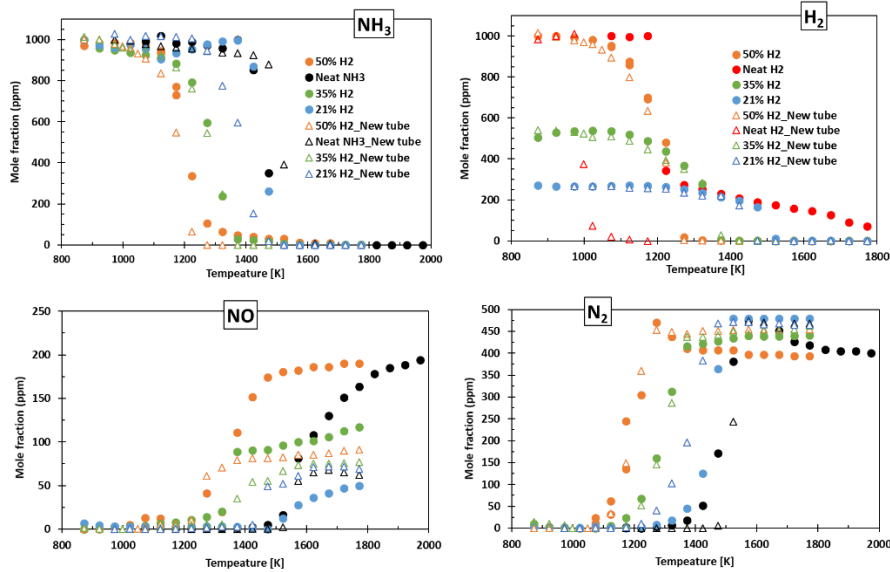


Figure 81: Comparison of experimental results of NH_3/H_2 oxidation using the FR1 after H_2S experiments (full symbols) and the new FR1 (hollow symbols). NO was detected by the MS for the first experiments and by the NO_x analyzer for the second experiment (new FR1).

Finally, the kinetic model needs to be further improved because it gives not enough accurate data, in particular for H_2 profile predictions. It tends to overestimate the consumption of H_2S under oxidation conditions, especially in the JSR. Moreover, the model predicts that H_2S is not totally consumed during pyrolysis in FR1 and FR2 from 1400 K to 1800 K, whereas the experimental results display a full consumption.

IV.5 Methane doped with hydrogen sulfide oxidation

In this part, the results of experiments showing the effects of H_2S addition on methane oxidation are presented. The experiments were performed using the JSR setup under atmospheric pressure (0.107 MPa) with helium as carrier gas and at temperatures ranging from 450 to 1200 K and at a residence time of about 2.0 s. The consumption of methane, hydrogen sulfide and the mole fraction of products have been measured as a function of the reaction temperature for a mixture of 20 000 ppm of methane and 500 ppm of hydrogen sulfide (Table 26). The fuel-air equivalence ratio is calculated according to the two following stoichiometric equations:

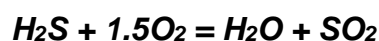
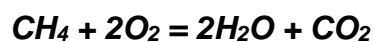


Table 26: Summary of conditions investigated in this study.

Set	$x_{CH_4}^{inlet}$ (ppm)	$x_{H_2S}^{inlet}$ (ppm)	$x_{O_2}^{inlet}$ (ppm)	ϕ
1	20,000	500	81,600	0.5
2			40,800	1
3			20,400	2

Species were sampled at the outlet of the reactor and analyzed online using mass spectrometry and gas chromatography. The first diagnostic was used for the detection of hydrogen sulfide, sulfur dioxide, water, and hydrogen. Hydrocarbon species and oxygen were quantified by gas chromatography coupled with a FID detector.

IV.5.1 Experimental results

The experimental results obtained during my PhD are compared to simulation data using the kinetic model of Mulvihill et al. (2019). This model is based on the model of Gersen et al. (2017) with the 17 reaction rate adjustments proposed by Mathieu et al. (2017).

Figure 82 compares the mole fractions of reactants and main products obtained by model predictions with the experimental oxidation data in a JSR. Eleven species were detected in the present study: methane, hydrogen sulfide, oxygen, hydrogen, sulfur dioxide (SO₂), CO₂, CO, C₂H₂, C₂H₄, C₂H₆ and water.

As shown in Figure 82, the onset temperatures of the reactivity of the two fuels are similar and are between 950-1100K. Compared to the neat H₂S case (Figure 73), H₂S reactivity seems mitigated by the much larger amount of methane present in the feed. The more oxygen, the more reactive the mixture. The computed data show that the onset temperatures of the reactivity of hydrogen sulfide are lower than those of methane (950-1000 K). No oscillation was observed, whereas oscillations were observed in previous work about neat methane oxidation, see part IV.2.1 (Figure 61).

The main products from the oxidation of methane are H₂O, CO and CO₂. CO peaks at 950 K and is then progressively converted to CO₂ when the temperature increases. Hydrogen sulfide is mainly converted to SO₂ and H₂. Logically some oxygen remains not consumed even at the highest temperatures for fuel lean condition. Other

reaction products (C_2H_2 , C_2H_4 , C_2H_6) are produced in small amounts compared to CH_4 inlet mole fraction. Interestingly, the formation of ethane (C_2H_6) is anticipated at low temperature, which is evidence of an interaction between methane and hydrogen sulfide. Given that H_2S is not consumed in a significant way in the low temperature region where C_2H_6 mole fraction is increasing, we can assume that methane is attacked by S containing species (e.g., SH radicals) yielding CH_3 radicals (the source for C_2H_6) and yielding H_2S back.

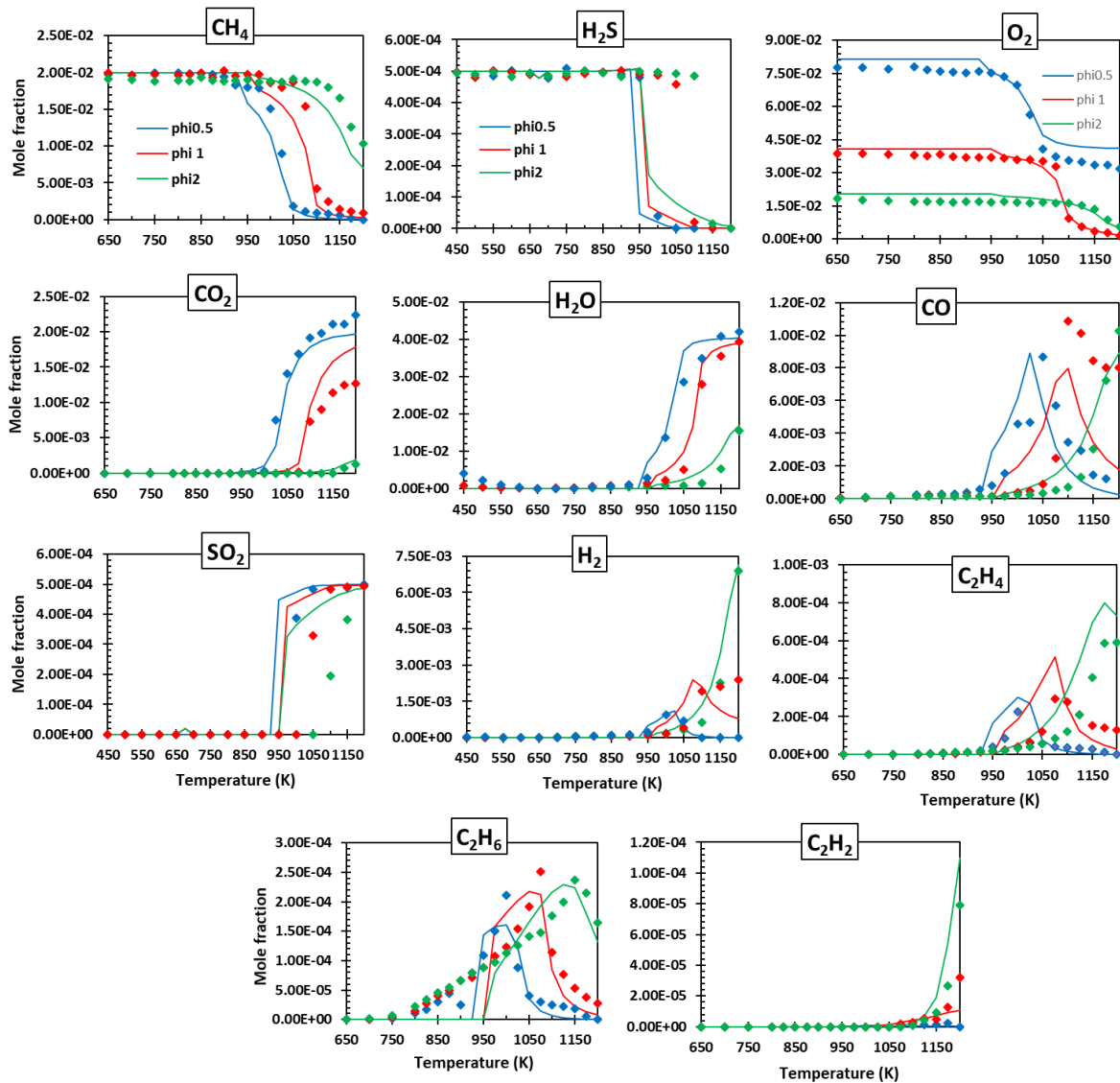


Figure 82: Oxidation of 20 000 ppm CH_4 with 500 ppm H_2S in a JSR under 0.107MPa. Symbols: experiments. Lines: data computed with the model.

The kinetic model well predicts the temperature of the reactivity onset for methane but less for hydrogen sulfide. The model predicts the anticipated reactivity of

hydrogen sulfide in presence of methane under stoichiometric and rich conditions, with a significant shift of about 100 K. The temperature of the consumption of oxygen is also well predicted. Moreover, the mole fractions of carbon dioxide, carbon monoxide, water and C_2H_x are also reproduced fairly well by the model but less for ethane. The model predicts also the anticipated formation of sulfur dioxide under stoichiometric and rich conditions, with the significant shift of about 100 K. Given the above observations, it seems that modeling efforts are required to better account for the mutual interaction between methane and H_2S .

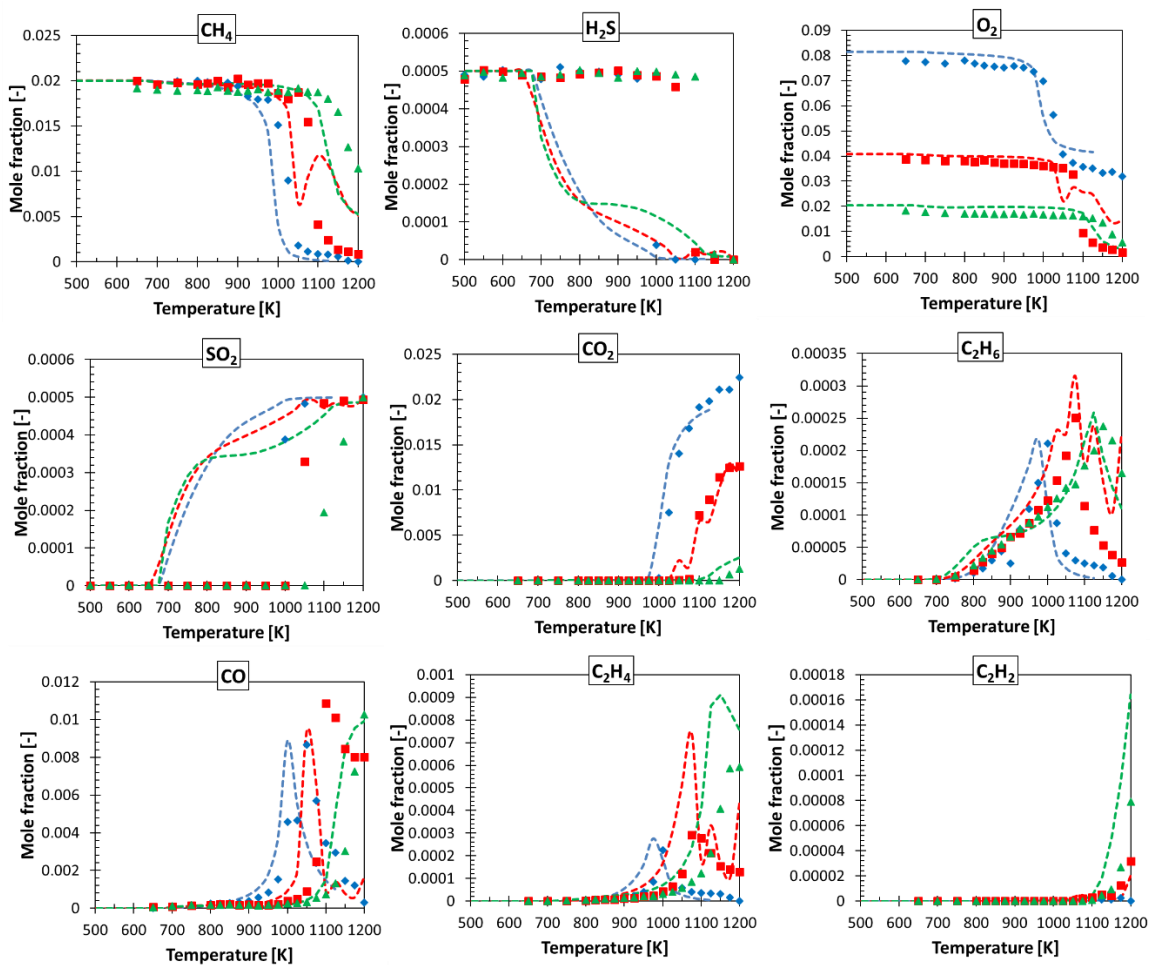


Figure 83: Oxidation of 20 000 ppm CH_4 with 500 ppm H_2S in a JSR under 0.107MPa. Symbols: experiments. Lines: data computed with the model.

Figure 83 shows the comparison between the experimental data and simulation data from the model developed in Milano as described previously. It is observed that this model predicts the reactivity onset of H_2S at very low temperature compared to the experimental reactivity onset (apparition onset shifted by ~ 350 K). However, both

models predict a reactivity too important for H₂S, indicating that it is necessary to revisit the kinetic constants of some reactions of H₂S.

Figure 84 displays the profiles of CH₄ with two different mixtures; neat CH₄ and methane doped with H₂S. As shown in Figure 84, H₂S addition very little affects methane reactivity (due to the much larger inlet fraction than that of H₂S), but it clearly enhances the production of ethane (apparition onset shifted by ~200 K). However, methane addition on H₂S oxidation inhibits the consumption of H₂S (reactivity onset shifted by ~450 K).

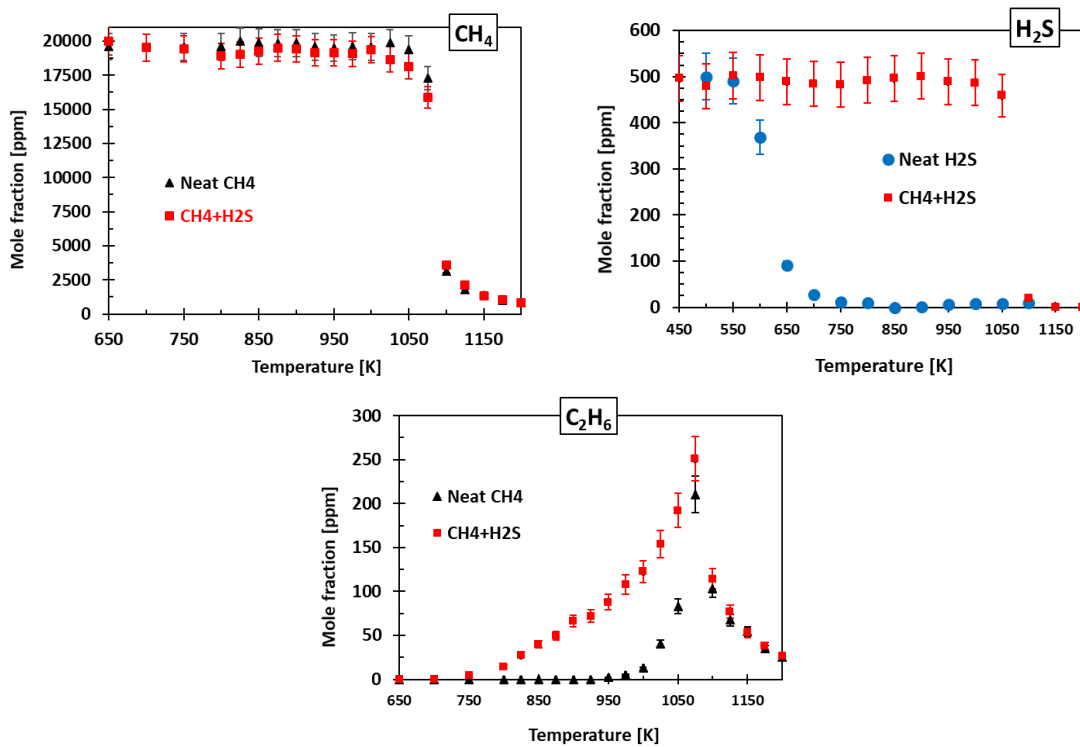


Figure 84: Effect of addition of 500 ppm H₂S to the oxidation of 20 000 ppm CH₄ in JSR, O₂ inlet mole fraction: 40 800 ppm. Black symbols: neat CH₄. Blue symbols: neat H₂S. Red symbols: CH₄/H₂S.

IV.5.2 Kinetic analysis

The kinetic mechanism was used to investigate the consumption pathways of fuels and the sensitivity coefficients to CH₄ and H₂S mole fraction. Figure 85 presents a consumption pathway for 2% CH₄ doped with 0.05% H₂S oxidation under 0.107 MPa at 975 K (which is the reactivity onset of CH₄), under stoichiometric condition.

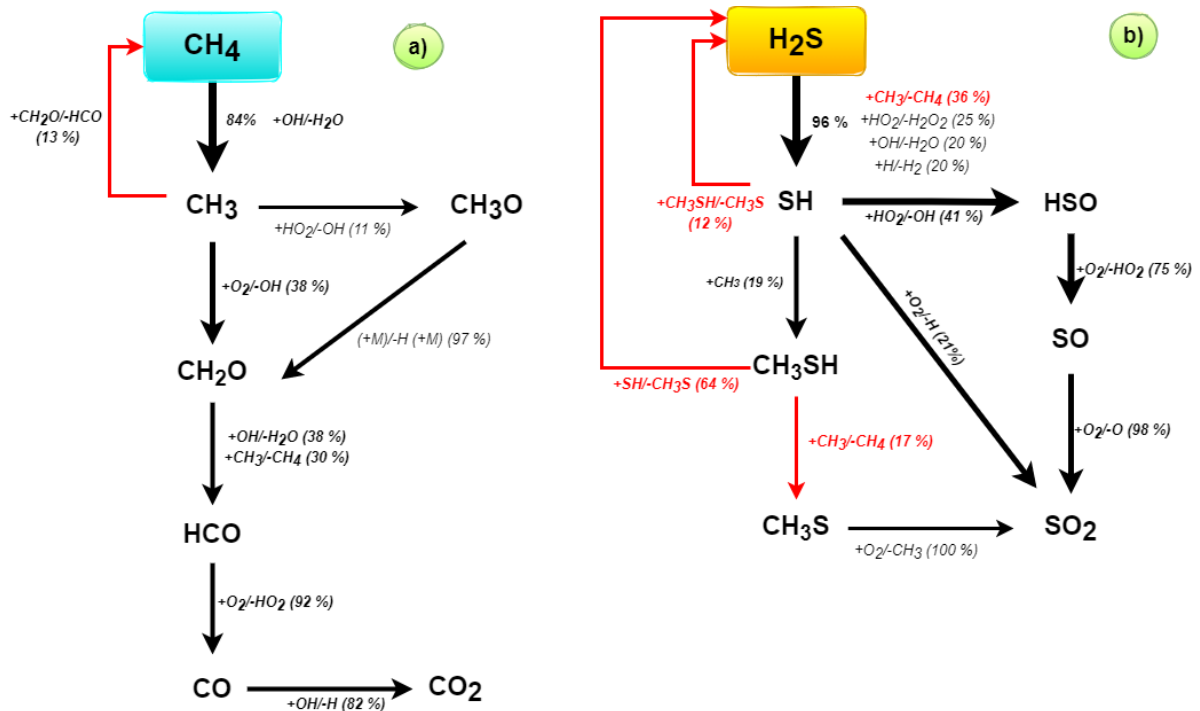


Figure 85: Consumption pathways of methane (a) and hydrogen sulfide (b) under 0.107MPa, stoichiometric condition (975K).

The analysis (Figure 85a) shows that methane is largely consumed (84%) by the classic H-atom abstraction reaction by OH radical to form the CH₃ radical (CH₄+OH=CH₃+H₂O) that is slightly converted back to methane through the reaction CH₃+CH₂O=HCO+CH₄. No interaction between CH and S radicals is observed in CH₄ consumption pathways. On the other hand, the interaction between CH and S radicals is observed in H₂S consumption pathway. The main consumption routes of H₂S (Figure 85b) are H-abstractions by CH₃, HO₂, OH, and H to yield SH. This channel contributes to 96% of H₂S consumption. The role of the CH₃ radicals in converting H₂S to SH is noteworthy, especially as methane inlet mole fraction is much larger than that of H₂S. SH radical is then slightly converted back to H₂S through the CH₃SH radical which is formed by CH₃ and SH radicals. CH₃SH reacts with CH₃, forming CH₃S and

yielding CH_4 back. CH_3S is then consumed to form the final product, SO_2 . The consumption pathway of H_2S allows to shed light on the major role played by CH_3 radicals in inhibiting H_2S reactivity.

Figure 86 presents sensitivity analysis of methane (Figure 86a) and hydrogen sulfide (Figure 86b) at temperatures of 950 K, 975 K, and 1100 K corresponding to fuel lean, stoichiometric and rich conditions, respectively. The reaction $\text{CH}_3+\text{O}_2=\text{CH}_2\text{O}+\text{OH}$ is the most sensitive increasing the reactivity of both fuels. Moreover, $\text{CH}_4+\text{O}_2=\text{CH}_3+\text{HO}_2$ is an inhibiting reaction for CH_4 and H_2S reactivity. Under these conditions, the reaction proceeds backward, consuming CH_3 and HO_2 and, thus, decreasing the number of species in the radical pool.

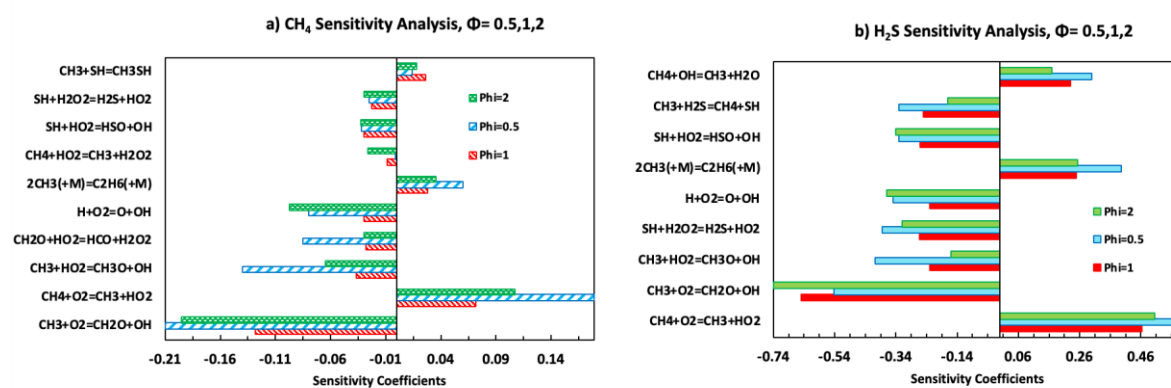


Figure 86: Sensitivity coefficients to CH_4 (a) and H_2S (b) mole fractions in JSR at temperatures of 950 K, 975 K, and 1100 K corresponding to fuel lean, stoichiometric and rich conditions, respectively.

IV.5.3 Conclusion

In this work, the co-oxidation of methane and hydrogen sulfide was studied to investigate their mutual interactions in combustion processes. Experiments were performed in a jet-stirred reactor working up to ~ 1200 K, under 0.107 MPa. Comparison of experimental data with simulations using a detailed kinetic model from the literature showed a satisfactory agreement for the reactivity and for the mole fractions of most reaction products, except at the lowest temperature (see C_2H_6 profile as an example). Moreover, the significant shifts between the experimental and computed data for H_2S and SO_2 need to be solved. The problem of these shifts may come from the experimental part or from the kinetic mechanism.

V. NO_x FORMATION AT HIGH TEMPERATURES

NO_x are common pollutants mainly resulting from high temperature combustion reactions. They are harmful to health and the environment. As a result, the regulation and limitation of this type of emissions are becoming essential in the current context and require the understanding of the mechanisms of formation of the species involved. The objectives of this chapter are to study the formation of NO_x during the oxidation of synthetic air, methane and ethylene in air, which is a more common condition than oxy-combustion for industrial processes. The experimental data obtained helped to develop and validate kinetic models in the gas phase. Simulation using the CRECK kinetic mechanism presented here before were performed with Chemkin to better understand the formation pathways of NO_x.

This chapter is divided into three parts. First, the study of the formation of NO_x from dry synthetic air and then from humid synthetic air will be presented. The second part describes the study of the formation of NO_x during the oxidation of methane. The last part presents the study of the formation of NO_x during the oxidation of ethylene. In each part, the experimental results are described and discussed. Those results will be compared with a kinetic simulation. The experimental conditions are summarized in [Table 27](#).

Table 27: Summary of experimental conditions used in the NO_x formation study.

Set	Fuel	T (K)	P (MPa)	τ (s)	ϕ	x_{fuel}^{inlet}	$x_{O_2}^{inlet}$	$x_{H_2O}^{inlet}$	$x_{N_2}^{inlet}$
1	Dry air	1273-	~0.12	0.04	–	-	20.9%	-	79.1%
2	Humid air	2073			-	-	20.9%	1%	78.1%
3	Methane	1073- 2073			~0.01	0.1%	20.9%	-	79.0%
4	Ethylene	973- 2073			0.5	0.05%	0.3%	-	99.65%
5					1		0.15%	-	99.80%
6					2		0.075%	-	99.88%

V.1 Study of the formation of NO_x from synthetic air

This part presents the comparison of the experimental and modelling results obtained during the flowing of synthetic dry and humid air (1mol % H₂O) at high temperatures. The experiments were carried out in FR1 over the temperature range of 1273 – 2073 K, under 0.12 MPa with a residence time of about 0.04 s.

The objective was to study the formation of NO_x (NO, N₂O and NO₂) and the method of analysis used was the online mass spectrometry. The second experiment was carried out by adding water (1 % H₂O on a mole basis) in order to study the influence of this compound on the results. Indeed, water is often added in small proportion in this type of experiments (Abian et al, 2015) (in reality there is between 0.1 and 5% of water vapor in the ambient air (MeteoFrance, 2021)) and water could have an effect on reaction kinetics or prevent the adsorption of certain species at the reactor wall.

[Figure 87](#) displays the comparison of the experimental and simulated NO formation during the flowing at high temperatures of synthetic dry (simulated as 79.1% N₂ and 20.9% O₂ on a mole basis) and humid air (1% H₂O on a mole basis). Neither NO₂ nor N₂O were observed. As shown in [Figure 87](#), the NO profiles in both experiments are similar and both lead to a final NO mole fraction (at 2073 K) of around 120 ppm. On the other hand, the results of the simulations (dry air) are different and underestimated (80 ppm at 2073 K). Adding water enhances the formation of NO with a two times larger concentration than that measured when burning dry air (340 ppm at 2073 K). However, the difference between the experimental and computed data can be explained by multiple factors mainly coming from the different uncertainties. It would be better to repeat these two experiments and to use the NO_x analyzer (it was under repair at the time of these experiments) to verify these results. A more in-depth study by varying the percentage of water (experimentally quite complicated due to the condensation before entering the reactor) could help to further study the impact of the presence of water on the formation of NO. It is interesting to note that the presence of water can also interfere with the mass spectrometer measurements. If verified, efforts will be needed to improve the NO/water chemistry in detailed kinetic models.

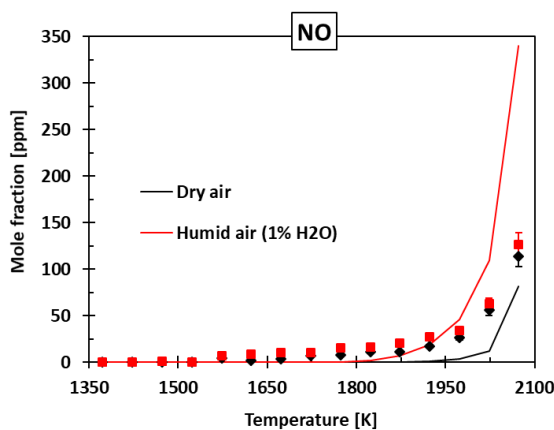


Figure 87: NO mole fraction profiles in synthetic dry and humid air (1% H₂O on a mole basis) under 0.12 MPa, $\tau = 0.04$ s. Symbols: experiments. Lines: data computed with the model.

V.2 Study of the NO_x formation during the oxidation of CH₄ (in air)

The experiments of methane oxidation were carried out by keeping the previous synthetic air (without water) and adding 1000 ppm of methane. The objective of these experiments was to study the influence of a carbon containing compound on the formation of NO. Indeed, the presence of carbon atoms could allow the formation of new nitrogenous radicals and imply new reactions in the process of formation of NO_x (Asthana et al., 2008). The experiments were performed in the same reactor (FR1) but the temperature range was widened due to the reactivity of methane (1073-2073 K). The pressure was set constant at 0.12 MPa with the residence time of about 0.04 s. These experiments were repeated three times using different analytical systems in order to be able to best quantify the different species. The equivalence ratio was defined by considering the following stoichiometric equation: $\text{CH}_4 + 2\text{O}_2 \rightarrow \text{CO}_2 + 2\text{H}_2\text{O}$.

Figure 88 shows the comparison of the experimental and simulated results obtained during the oxidation of 1000 ppm of methane in air. As shown in Figure 88, four products were detected (CO, CO₂, H₂O and NO). Neither NO₂ nor N₂O were observed. CO is the only intermediate product. The results show a good agreement between the experimental and simulation results, especially for CO₂ profiles. Methane is consumed at 1223 K to form CO and CO₂ formation begins at this temperature.

While water is formed at higher temperature (1273 K). CH₄ is totally consumed at 1373 K, above this temperature; CO₂ and water remain quasi constant at 1000 and 2000 ppm, respectively. CO peaks at 1323 K (700 ppm) and is then completely consumed at 1473 K. The NO formation occurs at very high temperature (from 1923 K). At 2073 K, NO was formed around 110 ppm, whereas the simulation overestimated NO formation by a factor of five (709 ppm).

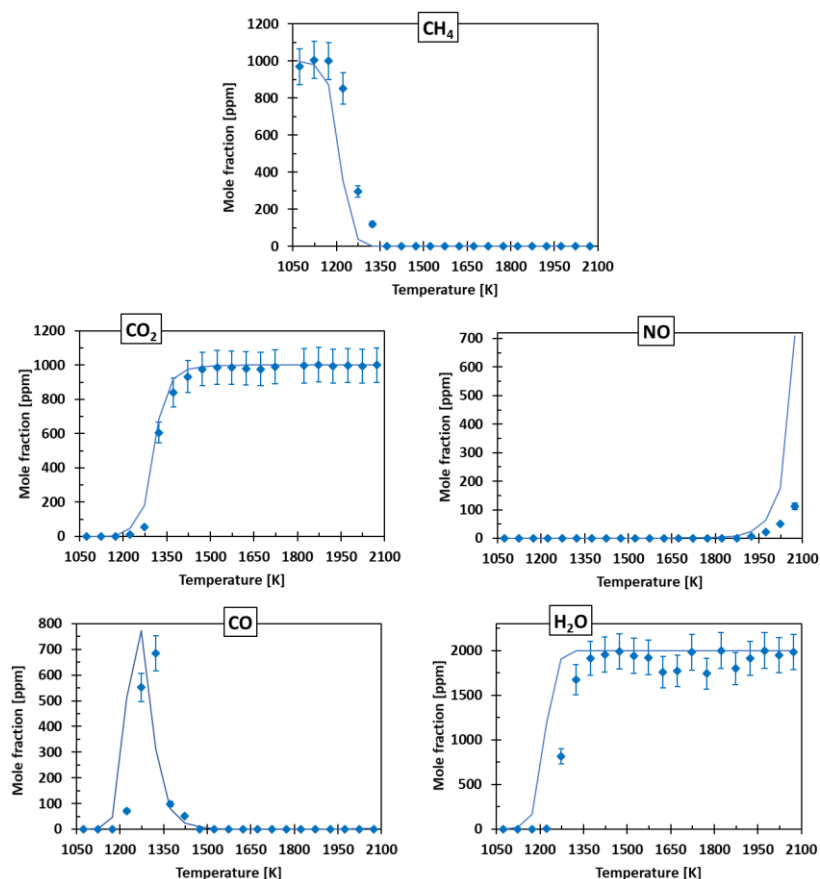


Figure 88: Oxidation of 1000-ppm methane in FR1 under 0.12 MPa and $\tau = 0.04$ s. Comparison between experimental (symbols) and predicted (lines) mole fraction profiles of fuel, intermediate and product species.

The formation of prompt NO is favored by a high fuel/oxygen ratio, which is not the case in the present study. This was observed in a previous unpublished study in our laboratory by Yu Song and co-workers (Figure 89). In their study, NO concentrations were the largest for the rich and stoichiometric conditions and were much lower for the lean condition ($\varphi = 0.4$). In our study, because of the very low equivalence ratio ($\varphi = \sim 0.01$), the radical pool concentration is very low and the NO

formation reactions by the prompt mechanism are very disadvantaged. Therefore, one way to decrease the formation of prompt NO is to decrease the equivalence ratio.

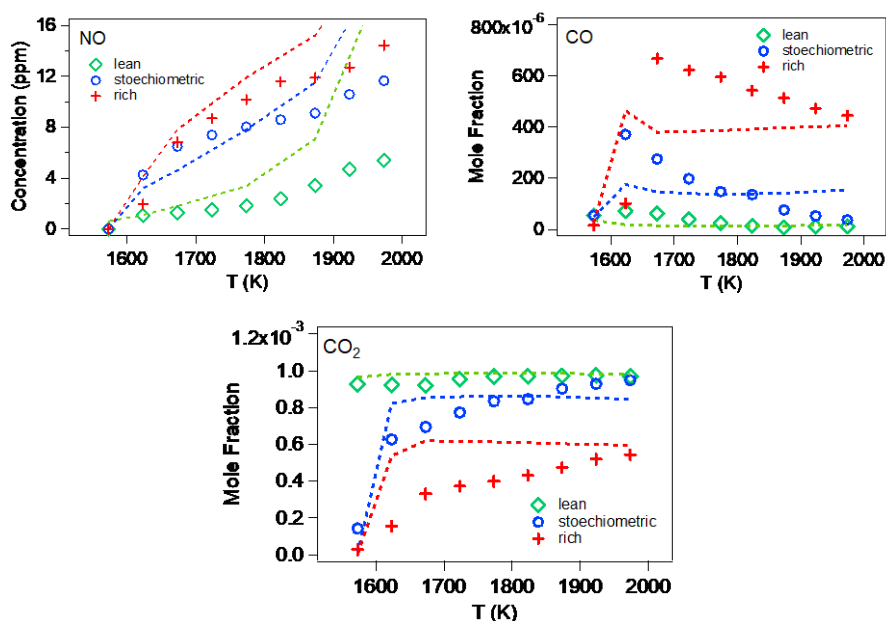


Figure 89: Oxidation of methane in N₂ enriched air in FR1 by Song and co-workers (private communication). 1000 ppm of methane, $\phi = 0.4, 1.0$ and 1.25 (dilution in N₂), $P = 0.12$ MPa and $\tau = 0.03$ s.

As shown in Figure 87 and Figure 88, the NO mole fraction profiles in the three experiments (oxidation of synthetic dry air, humid air and air doped with methane) are similar with the same NO quantity at 2073 K (~120 ppm). Whereas the simulation shows that the addition of CH₄ and water favors the NO formation by factors of five and three, respectively, compared to the experimental results.

To better understand this difference, the NO formation pathways and sensitivity analysis were studied. Figure 90 presents the NO formation pathways during the oxidation of dry air (a), humid air (b) and dry air + CH₄ (c), in FR1 at 2023 K. As shown in Figure 90, thermal NO is mainly formed via $N_2 + O \rightleftharpoons N + NO$ and $O_2 + N \rightleftharpoons O + NO$ for the three cases. NO is also formed via the reaction intermediate N₂O with the O• radicals in case of the presence of water and methane in air. What we can learn from these rate of production analyses is that water and methane have little influence on the formation of thermal NO.

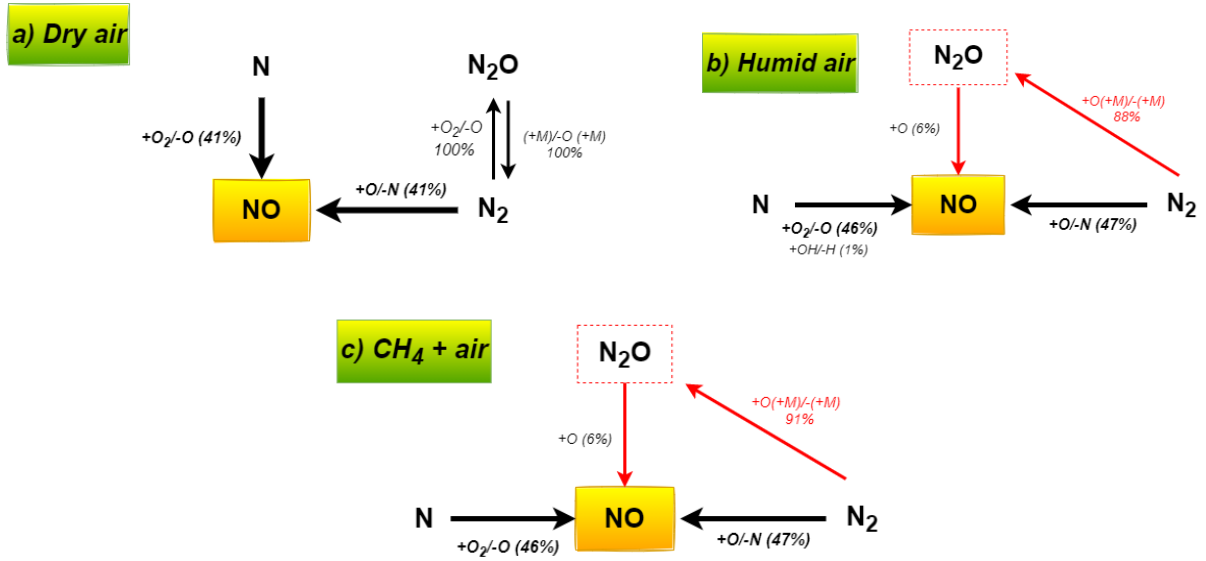


Figure 90: NO formation pathways during the oxidation of N₂ [dry air (a) and humid air (b)] and N₂ [dry air] + CH₄ (c), in FR1 at 2023 K. x = 50 cm (length from the tube inlet).

Figure 91 displays the sensitivity analysis of NO formation during the three experiments at 2023 K. It can be observed for the three cases that the path via N• radicals, (thermal NO) controls NO formation. Moreover, the NO formation via N₂O becomes more apparent in the sensitivity analysis in case of CH₄ and water addition.

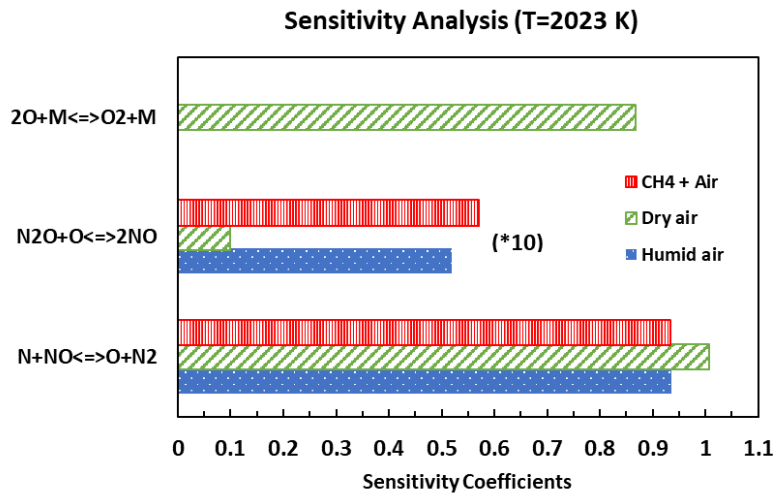


Figure 91: Sensitivity coefficients to NO mole fraction in FR during the oxidation of dry air (green), humid air (blue) and air doped with CH₄ (red) at 2023 K. x = 50 cm (length from the tube inlet).

V.3 Study of the NO_x formation during the oxidation of C₂H₄

The experiments of 500-ppm ethylene oxidation were carried out in FR1 using N₂ as a carrier gas, over the temperature range of 973-2073 K. The pressure was set constant at 0.123 MPa with a residence time of about 0.04 s and three different equivalence ratios ($\varphi = 0.5$ and 1). The equivalence ratio was defined by considering the following stoichiometric equation: **$C_2H_4 + 3O_2 = 2CO_2 + 2H_2O$** .

Figure 92 shows the comparison of the experimental and simulated results obtained during the oxidation of 500 ppm of ethylene. As shown in Figure 92, three products were detected (CO₂, H₂O and NO). Neither NO₂ nor N₂O were observed. Note that, neither GC-TCD nor MS can detect CO because the retention time of CO is the same as that of CO₂ (using GC-TCD) and the molar mass of CO (28 g/mol) is the same as that of N₂ and ethylene (using MS). This experiment needs to be repeated using the GC-FID-Methanizer in order to detect CO. The results show a fair agreement between the experimental and simulation results but less for the profiles of ethylene and NO. The temperature of the reactivity onset is very sensitive to the equivalence ratio: it is about 1023 K for the lean condition and 1123 K for the stoichiometric ones. As shown in Figure 92, the more oxygen, the more formed NO. The NO is formed at high temperatures (from 1573 K). At 2073 K, NO was formed around 11 ppm for the lean condition and 6 ppm for the stoichiometric ones. However, the simulation for the learner conditions ($\varphi = 0.5$ and 1) overestimated at 2073 K, four times higher for the NO mole fraction (~ 40 ppm) compared to the experimental results.

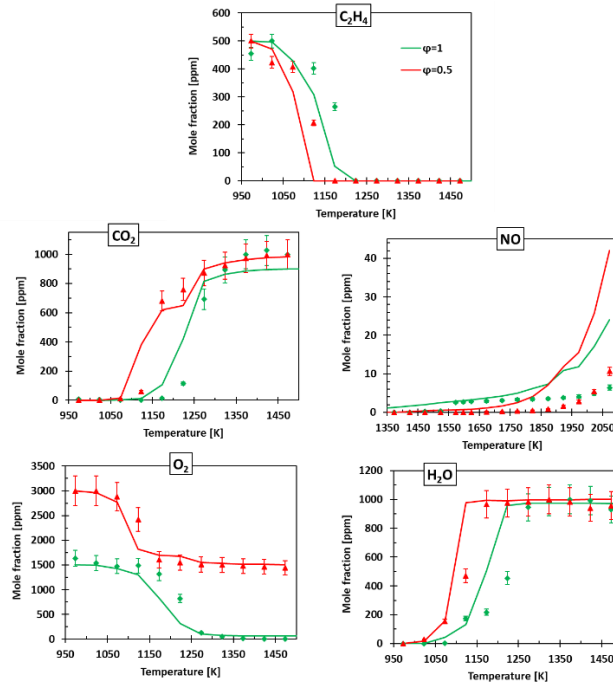


Figure 92: Oxidation of 500-ppm ethylene in FR1 under 0.123 MPa and $\tau = 0.04$ s. Comparison between experimental (symbols) and predicted (lines) mole fraction profiles of reactants and product species.

To highlight reactions that have a significant effect on the mole fraction of NO, formation pathways and sensitivity analyses were therefore performed at 1273 K, under stoichiometric condition. Figure 93 shows that C_2H_4 reactivity is a key parameter in the formation of prompt NO, as it leads to the formation of CH radicals.

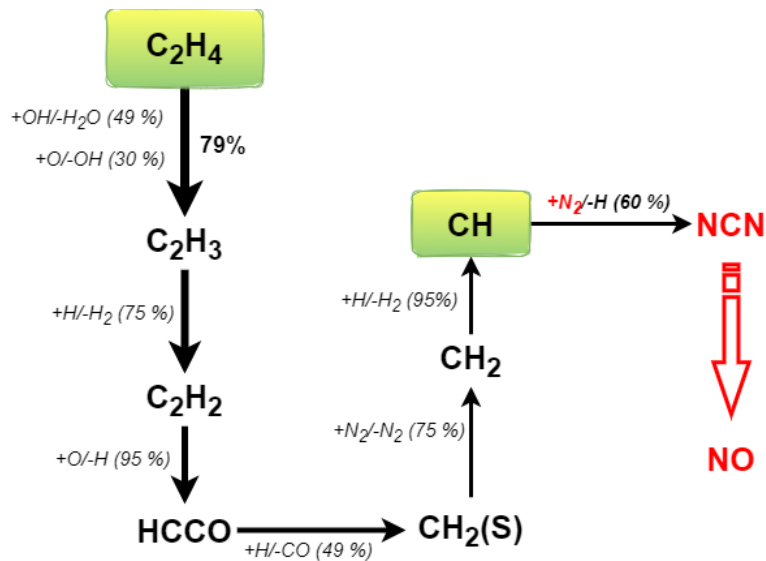


Figure 93: Formation pathways of prompt NO during the oxidation of ethylene for $\phi = 1$ at 1273 K. The size of the arrows is proportional to the percentages.

The sensitivity analysis (1273 K, $\phi=1$) in Figure 94, shows that the reaction of $\text{CH}_2+\text{H}=\text{CH}+\text{H}_2$ is the most sensitive reaction to the formation of prompt NO. Moreover, the reaction of CH radical ($\text{CH}+\text{O}_2=\text{HCO}+\text{O}$) is also sensitive to NO formation, increasing the reactivity. The sensitivity analysis confirms that the reaction of CH_2 and CH radicals drive the prompt NO formation pathways.

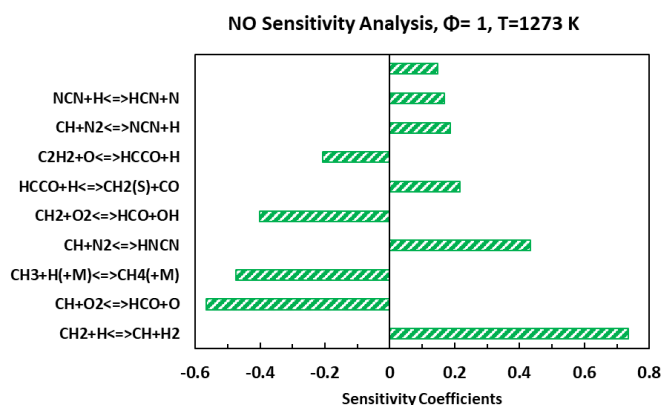


Figure 94: Sensitivity analysis of NO during the oxidation of ethylene for $\phi = 1$ at 1273 K.

V.4 Conclusion

Four tentative experimental studies were performed in flow reactor up to very high temperatures (above 2000 K) in order to better understand the formation of thermal NO, those are preliminary work of great interest because of the unusual used conditions, but still requiring further investigation. These studies included experiments in dry synthetic air at temperatures up to 2073 K and investigation of the influence of the addition of water, and methane. In the future, it would be interesting to perform further experiments varying the water and methane composition (for example by using the concentrations of water vapor in the air) in order to study their influence more precisely. Moreover, the oxidation of 500 ppm of ethylene using N_2 as carrier gas was also studied under these conditions studied to observe the formation of NO. The deviation observed between experimental and simulated results should be further investigated. Indeed, some phenomena could have been neglected (e.g. adsorption) but it is also possible that some kinetic data or experimental measurements are imprecise due to the complexity of having perfect control of the temperature. In addition, the uncertainties related to the fact of using such high temperatures should be more assessed.

VI. PYROLYSIS AND OXIDATION OF BIO-OIL SURROGATES

This chapter is dedicated to the experimental and kinetic studies performed on bio-oil surrogates. The aims are to study their reactivity and to better understand their decomposition mechanism under oxidative and pyrolysis conditions. This chapter is divided into three parts. First, the study of neat pyrrole pyrolysis and oxidation will be presented. The second part describes the experimental and kinetic modelling studies of ethylene glycol pyrolysis and oxidation. The last part presents the experimental results of the oxidation of propylene glycol. In each part, the experimental results are described and discussed. The results of pyrrole oxidation will be compared to a model developed by the CRECK group from Politecnico di Milano. The results of ethylene glycol will be compared to a model developed during my PhD. This kinetic model is composed of an ethylene glycol subset by Kathrotia et al. (2017) and an ethylbenzene kinetic subset adopted from Husson et al. (2011).

This work led to the publication of a paper about pyrrole gas phase kinetics:

- ✓ Pelucchi, M., Arunthanayothin, S., Song, Y., Herbinet, O., Stagni, A., Carstensen, H-H., Faravelli, T., Battin-Leclerc, F., 2021. Pyrolysis and Combustion Chemistry of Pyrrole, a Reference Component for Bio-oil Surrogates: Jet-Stirred Reactor Experiments and Kinetic Modeling. *Energy & Fuels* 35 (9), 7265-7284.

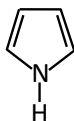
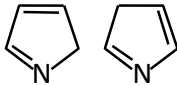
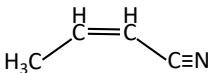
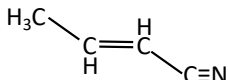
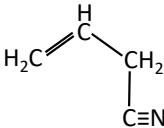
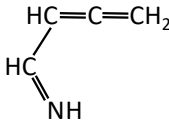
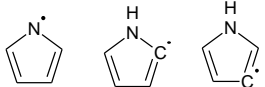
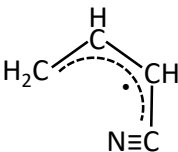
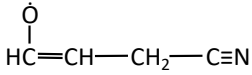
VI.1 Pyrrole pyrolysis and oxidation

This part of the [chapter V](#) describes the experimental and theoretical results of the pyrrole study. First, a kinetic model developed by the team of Prof. T. Faravelli at Politecnico di Milano is presented. Next, the experimental results are presented and compared to the simulation data calculated using the kinetic. In the last part, a detailed kinetic analysis is presented.

VI.1.1 Kinetic modeling

The kinetic model of pyrrole pyrolysis and oxidation consists of 189 chemical species and 2888 reactions. Specifically, the pyrrole pyrolysis and oxidation subset contain 33 species and 456 reactions. The structures and the names of the chemical species involved in this kinetic model are displayed in [Table 28](#).

Table 28: Nomenclature of relevant species in pyrrole pyrolysis and oxidation.

Species Name	Brute Formula	Representation	Model name
Pyrrole	C ₄ H ₅ N		C ₄ H ₅ N
Pyrrolenine	C ₄ H ₅ N		PYRLNE
Cis-crotonitrile	C ₄ H ₅ N		C-C ₃ H ₅ CN
Trans-crotonitrile	C ₄ H ₅ N		T-C ₃ H ₅ CN
Allyl cyanide	C ₄ H ₅ N		A-C ₃ H ₅ CN
Allenic Imine	C ₄ H ₅ N		HNCPROP
Pyrlyl radical	C ₄ H ₄ N		PYRLYL
Cyano propen-2-yl radical	C ₄ H ₄ N	$\text{H}_3\text{C}-\text{CH}=\dot{\text{C}}-\text{C}\equiv\text{N}$	C ₃ H ₄ CN
Cyano propen-4-yl radical	C ₄ H ₄ N	$\text{H}\dot{\text{C}}=\text{CH}-\text{CH}_2-\text{C}\equiv\text{N}$	C-C ₃ H ₄ CN
Cyano allyl radical	C ₄ H ₄ N		A-C ₃ H ₄ CN
Allyloxy cyanide	C ₄ H ₄ NO		C ₄ H ₄ NO
Acetonitrile	C ₂ H ₃ N	$\text{H}_3\text{C}-\text{C}\equiv\text{N}$	CH ₃ CN
Cyano methyl radical	C ₂ H ₂ N	$\text{H}_2\dot{\text{C}}-\text{C}\equiv\text{N}$	CH ₂ CN
Acrylonitrile radical	C ₃ H ₃ N	$\text{H}_2\text{C}=\text{CH}-\dot{\text{C}}\equiv\text{N}$	CH ₂ CHCN
Acrylonitrile	C ₃ H ₂ N	$\text{H}\dot{\text{C}}=\text{CH}-\text{C}\equiv\text{N}$	CHCHCN
Cyanoacetylene	C ₃ HN	$\text{HC}\equiv\text{C}-\text{C}\equiv\text{N}$	C ₃ HN
Butanedinitrile	C ₄ H ₄ N ₂	$\text{N}\equiv\text{C}-\text{CH}_2-\text{CH}_2-\text{C}\equiv\text{N}$	C ₄ H ₄ N ₂
Butanedinitrile radical	C ₄ H ₃ N ₂	$\text{N}\equiv\text{C}-\text{CH}_2-\dot{\text{C}}\text{H}-\text{C}\equiv\text{N}$	C ₄ H ₃ N ₂
Fumaronitrile	C ₄ H ₂ N ₂	$\text{N}\equiv\text{C}-\text{CH}=\text{CH}-\text{C}\equiv\text{N}$	C ₄ H ₂ N ₂
Propionitrile	C ₃ H ₅ N	$\text{H}_3\text{C}-\text{CH}_2-\text{C}\equiv\text{N}$	C ₂ H ₅ CN
Propionitrile primary radical	C ₃ H ₄ N	$\text{H}_2\dot{\text{C}}-\text{CH}_2-\text{C}\equiv\text{N}$	CH ₂ CH ₂ CN
Propionitrile secondary radical	C ₃ H ₄ N	$\text{H}_3\text{C}-\dot{\text{C}}\text{H}-\text{C}\equiv\text{N}$	CH ₃ CHCN
Formimidoyl	CH ₂ N	$\text{HN}=\dot{\text{C}}\text{H}$	CH ₂ N

Species Name	Brute Formula	Representation	Model name
Cyanomethylene radical	C ₂ HN	H \dot{C} -C \equiv N	HCCN
Cyanomethylidyne	C ₂ N	\dot{C} =C \equiv N	C ₂ N
2-Butynedinitrile	C ₄ N ₂	N \equiv C-C \equiv C-C \equiv N	C ₄ N ₂
Carbonyl cyanide	C ₂ NO	\dot{N} =C=C=O	NCCO
Formyl cyanide	C ₂ HNO	H(C=O)-C \equiv N	OCHCN
Hydroxy acetonitrile radical	C ₂ H ₂ NO	\dot{O} -CH ₂ -C \equiv N	OCH ₂ CN
Cyano radical	CN	$\dot{C}\equiv$ N	CN
Hydrogen cyanide	CHN	HC \equiv N	HCN
Isocyanic acid	CHNO	HN=C=O	HNCO
Isocyanate radical	CNO	N=C=O	NCO

The kinetic model was built on the CRECK core mechanism composed of a hydrogen subset by Kéromnés et al. (2013), C₁–C₂ from Metcalfe et al. (2013) and C₃ and molecular growth pathways from Burke et al. (2015) and Ranzi et al. (2012) and Ranzi et al. (2014) recently updated by Bagheri et al. (2020). A NO_x kinetic subset is adopted from Song et al. (2019) with small updates concerning acetonitrile (CH₃CN) from the recent study by Alzueta et al. (2021).

Thermodynamic properties of relevant species have been taken from Song et al. (2019), Martoprawiro et al. (1999), Doughty and Mackie (1992), Burcat and Ruscic (2005). Important reactions in the pyrrole pyrolysis and oxidation subset are shown in [Table 29](#), with references of selected rate coefficients and notes on minor modifications.

Table 29: Rate coefficients for relevant reactions in the following discussion on pyrrole pyrolysis and oxidation.

Reaction	A	n	Ea	Ref	Notes
$C_4H_5N \leftrightarrow PYRLNE$	3.16E+13	0.005	46300		
$C_4H_5N \leftrightarrow HNCPROP$	1.10E+14	0.000	77162		
$PYRLNE \leftrightarrow aC_3H_5CN$	5.24E+15	0.000	75710		Ax2
$PYRLNE \leftrightarrow cC_3H_5CN$	1.65E+15	0.000	70050		A/2
$PYRLNE \leftrightarrow HNCPROP$	2.51E+15	0.000	79474		
$HNCPROP \leftrightarrow HCN + C_3H_4-p$	5.50E+12	0.000	37740	(Martoprawiro et al., 1999)	A/2, E _a =+1500 cal/mol
$PYRLNE \leftrightarrow \dot{H} + c\dot{C}_3H_4CN$	2.04E+17	0.000	86746		Ax2
$aC_3H_5CN \leftrightarrow tC_3H_5CN$	7.00E+14	0.000	61969		
$aC_3H_5CN \leftrightarrow cC_3H_5CN$	7.20E+14	0.000	58863		
$cC_3H_5CN \leftrightarrow tC_3H_5CN$	1.40E+14	0.000	57573		
$aC_3H_5CN \leftrightarrow \dot{C}_2H_3 + \dot{C}H_2CN$	3.40E+15	0.000	82640	(Pelucchi et al., 2021)	
$aC_3H_5CN + \dot{H} \leftrightarrow C_2H_4 + \dot{C}H_2CN$	1.00E+13	0.000	3010	(Doughty & Mackie, 1992)	Ax2
$tC_3H_5CN + \dot{H} \leftrightarrow HCN + \dot{C}_3H_5-s$	6.00E+12	0.000	4000		
$\dot{H} + C_4H_5N \leftrightarrow H_2 + PYRLYL$	1.00E+06	2.000	2825		
$\dot{C}H_3 + C_4H_5N \leftrightarrow CH_4 + PYRLYL$	4.50E+04	2.000	3778		
$\dot{C}H_2CN + C_4H_5N \leftrightarrow CH_3CN + PYRLYL$	1.35E+04	2.000	12460	(Pelucchi et al., 2021)	
$\dot{O}H + C_4H_5N \leftrightarrow H_2O + PYRLYL$	9.00E+08	1.000	-695		
$H\dot{O}_2 + C_4H_5N \leftrightarrow H_2O_2 + PYRLYL$	3.60E+06	2.000	14440		
$O_2 + C_4H_5N \leftrightarrow H\dot{O}_2 + PYRLYL$	8.00E+13	0.000	37150		
$\dot{O} + C_4H_5N \leftrightarrow \dot{O}H + PYRLYL$	1.10E+06	2.000	1404		
$\dot{H} + aC_3H_5CN \leftrightarrow H_2 + a\dot{C}_3H_4CN$	1.90E+02	3.500	1627		
$\dot{C}H_3 + aC_3H_5CN \leftrightarrow CH_4 + a\dot{C}_3H_4CN$	7.14E+00	3.500	7642		
$\dot{C}H_2CN + aC_3H_5CN \leftrightarrow CH_3CN + a\dot{C}_3H_4CN$	2.00E+11	0.000	12000	(Doughty & Mackie, 1992)	A/2
$\dot{O}H + aC_3H_5CN \leftrightarrow H_2O + a\dot{C}_3H_4CN$	7.70E+05	2.200	-437		
$H\dot{O}_2 + aC_3H_5CN \leftrightarrow H_2O_2 + a\dot{C}_3H_4CN$	7.82E-01	3.970	11702		
$O_2 + aC_3H_5CN \leftrightarrow H\dot{O}_2 + a\dot{C}_3H_4CN$	5.00E+13	0.000	37190	(Pelucchi et al., 2021)	
$\dot{O} + aC_3H_5CN \leftrightarrow \dot{O}H + a\dot{C}_3H_4CN$	1.75E+11	0.700	5884		
$\dot{H} + tC_3H_5CN \leftrightarrow H_2 + a\dot{C}_3H_4CN$	3.64E+05	2.455	4361		
$\dot{C}H_3 + tC_3H_5CN \leftrightarrow CH_4 + a\dot{C}_3H_4CN$	2.21E+00	3.500	5675		
$\dot{C}H_2CN + aC_3H_5CN \leftrightarrow CH_3CN + a\dot{C}_3H_4CN$	5.00E+12	0.000	10989	(Doughty & Mackie, 1992)	A/2
$\dot{O}H + tC_3H_5CN \leftrightarrow H_2O + a\dot{C}_3H_4CN$	4.46E+06	2.072	1051		
$H\dot{O}_2 + tC_3H_5CN \leftrightarrow H_2O_2 + a\dot{C}_3H_4CN$	3.07E-02	4.403	13547		
$O_2 + tC_3H_5CN \leftrightarrow H\dot{O}_2 + a\dot{C}_3H_4CN$	1.20E+20	-1.67	46191	(Pelucchi et al., 2021)	
$\dot{O} + tC_3H_5CN \leftrightarrow \dot{O}H + a\dot{C}_3H_4CN$	5.24E+11	0.700	5884		
$\dot{H} + tC_3H_5CN \leftrightarrow H_2 + \dot{C}_3H_4CN$	2.25E+07	1.930	12950		
$\dot{C}H_3 + tC_3H_5CN \leftrightarrow CH_4 + \dot{C}_3H_4CN$	4.85E+02	2.947	15148		
$\dot{C}H_2CN + tC_3H_5CN \leftrightarrow CH_3CN + \dot{C}_3H_4CN$	5.00E+12	0.00	12000	(Doughty & Mackie, 1992)	A/2
$\dot{O}H + tC_3H_5CN \leftrightarrow H_2O + \dot{C}_3H_4CN$	1.11E+04	2.745	2216		
$H\dot{O}_2 + tC_3H_5CN \leftrightarrow H_2O_2 + \dot{C}_3H_4CN$	2.15E+05	2.000	20243	(Pelucchi et al., 2021)	
$O_2 + tC_3H_5CN \leftrightarrow H\dot{O}_2 + \dot{C}_3H_4CN$	2.11E+13	0.000	57623		
$\dot{O} + tC_3H_5CN \leftrightarrow \dot{O}H + \dot{C}_3H_4CN$	1.08E+07	2.000	8782		
$a\dot{C}_3H_4CN \leftrightarrow c\dot{C}_3H_4CN$	5.00E+13	0.000	51983	(Doughty & Mackie, 1992)	

Reaction	A	n	E _a	Ref	Notes
PYRLEYL ↔ cC ₃ H ₄ CN	1.50E+13	0.000	38987	(Martoprawiro et al., 1999)	
Ĉ ₃ H ₄ CN ↔ ĈH ₃ +C ₃ HN	6.00E+14	0.000	42000	(Doughty & Mackie, 1992)	
cĈ ₃ H ₄ CN ↔ C ₂ H ₂ +Ĉ ₂ CN	1.07E+15	-0.560	36320	(Pelucchi et al., 2021)	
Ĥ+C ₃ HN ↔ C ₂ H ₂ +ĈN	1.00E+14	0.000	2000		
aĈ ₃ H ₄ CN+HÖ ₂ ↔ C ₄ H ₄ NÖ+ÖH	1.95E+18	-1.060	7852		
cĈ ₃ H ₄ CN+O ₂ ↔ C ₄ H ₄ NÖ+Ö	2.30E+20	-2.650	6489		
C ₄ H ₄ NÖ ↔ C ₂ H ₃ CHO+ĈN	1.50E+13	0.000	33000	(Ranzi et al., 2001)	C-C β-scission
C ₄ H ₄ NÖ → C ₂ H ₂ +CH ₂ O+ĈN	1.50E+13	0.000	33000		
Ĉ ₂ CN+Ĉ ₂ CN ↔ C ₄ H ₄ N ₂	2.30E+13	0.000	0.000	(Sendt et al., 1999)	High pressure limit
CH ₃ CN(+M) ↔ Ĉ ₂ CN+H(+M)	9.20E+12	0.850	95770		
Ĉ ₂ CN+C ₄ H ₄ N ₂ ↔ CH ₃ CN+Ĉ ₄ H ₃ N ₂	3.50E+12	0.000	5000	(Doughty & Mackie, 1992)	
NO+Ö(+M) ↔ NO ₂ (+M)	1.30E+15	-0.750	0.000	(Allen et al., 1997)	
Ö+C ₃ HN ↔ CO+HĈ-CN	7.40E+08	1.280	2472	(Pelucchi et al., 2021)	
O ₂ +HĈ-CN ↔ CO ₂ +HCN	1.10E+12	0.000	0.000	(Alzueta et al., 2021)	
ÖH+CH ₃ CN ↔ H ₂ O+Ĉ ₂ CN	2.00E+07	2.000	5000	(Pelucchi et al., 2021)	
Ĉ ₂ CN+Ö ↔ Ĥ+OCHCN	3.00E+11	0.640	0.000	(Alzueta et al., 2021)	
OCHCN ↔ HCN+CO	3.50E+14	0.000	66300	(Chang & Yu, 1995)	
ÖH+HCN ↔ Ĥ+HNCO	1.71E+11	0.000	8744	(Miller & Melius, 1988)	
ÖH+HCN ↔ H ₂ O+ĈN	1.45E+13	0.000	10900	(Wang et al., 2002)	
ÖH+HNCO ↔ H ₂ O+ĤNCO	3.50E+06	1.500	3600	(Wooldridge et al., 1996)	
O ₂ +ĤNCO ↔ CO ₂ +NO	2.00E+12	0.000	20000	(Miller & Bowman, 1991)	
C ₂ N ₂ +M ↔ ĈN+ĈN+M	1.60E+34	-4.32	130000	(Natarajan et al., 1986)	
C ₂ N ₂ +Ĥ ↔ HCN+ĈN	3.10E+14	0.000	7860	(Sendt et al., 1999)	
HĈCO+NO ↔ HCN+CO ₂	2.23E+14	-0.750	400	(Carl et al., 2002)	

^a Rate coefficients refer to an Arrhenius expression of the rate constants as $k = AT^n \exp(-E_a/RT)$. Units are cal, mol, K, cm, and s.

The simulation results from this model were compared to the experimental data of Mackie et al. (1991) as shown in [Figure 95](#). They investigated the pyrolysis of pyrrole in a single pulse shock tube over the temperature range 1200-1700 K, total

pressures of 7.5-13.5 atm and nominal mixture compositions of pyrrole of 5000 and 700 ppm.

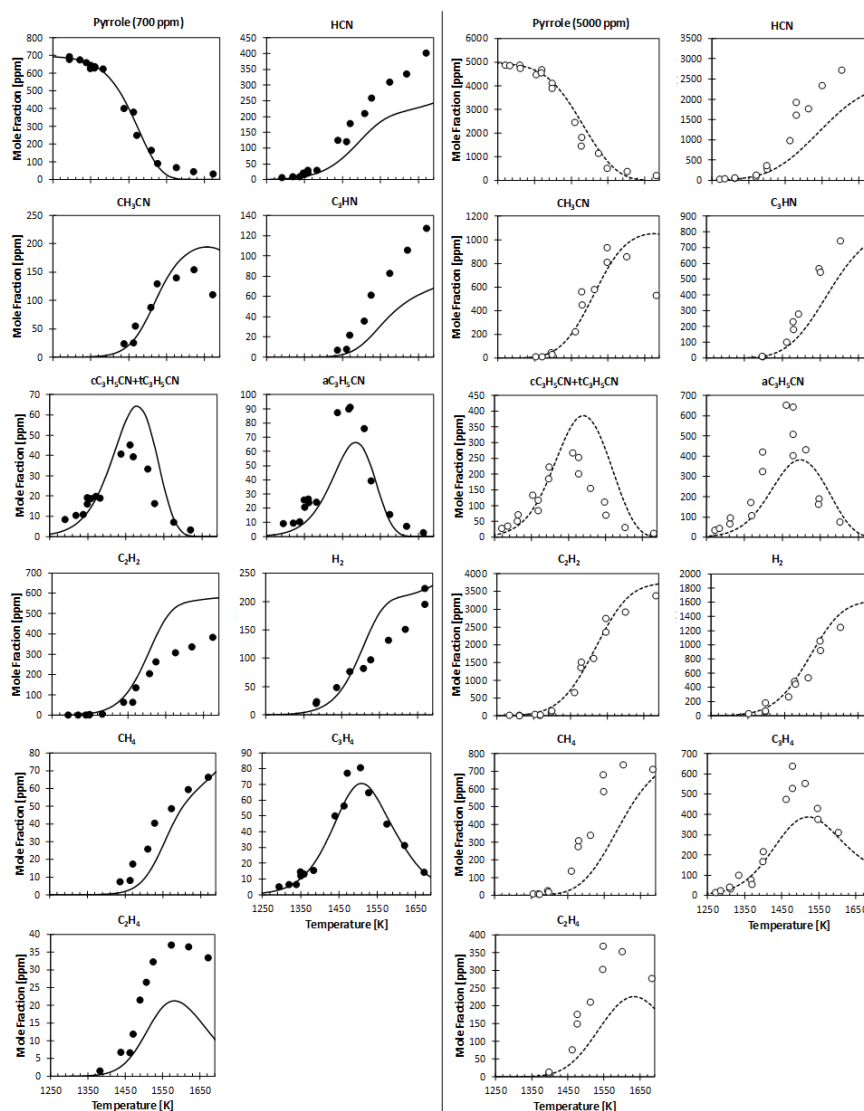


Figure 95: Pyrolysis of pyrrole (700 ppm left panel, 5000 ppm right panel in argon) in a single pulse shock tube at $p=13$ atm and $\tau = 550 \mu\text{s}$. Comparison between experimental (symbols) (Mackie et al., 1991) and predicted (lines) (Pelucchi et al., 2021) mole fraction profiles of intermediate and product species.

Figure 95 compares model results with the single-pulse shock tube data by Mackie et al. (1991). Fuel conversion profiles, as well as the temperature dependence of product mole fraction, are well captured by the model for both the 700 ppm and 5000 ppm cases.

VI.1.2 Experimental results

In the next section, the experimental results obtained during my PhD are compared to simulation data using this kinetic model. The results of pyrrole pyrolysis are first presented, then those of pyrrole oxidation are shown. In this work, the equivalence ratio is defined by considering the following stoichiometric equation:

$$\mathbf{C_4H_5N + 6.25O_2 = 4CO_2 + 2.5H_2O + NO_2.}$$

Experiments for the pyrolysis and oxidation of pyrrole were performed in the fused silica Jet-Stirred Reactor (JSR). The reaction was studied at temperatures ranging from 700 K to 1200 K, a residence time of about 2 s and a pressure of 0.107MPa. The inlet mole fraction of pyrrole is 10000 ppm. Experiments were performed under diluted conditions using helium as a bath gas. Before mixing with helium and oxygen, pyrrole was first vaporized in a vaporization chamber maintained 393 K. Although the boiling point of pyrrole is ~403 K, the temperature of the evaporator was set at a lower temperature to avoid the foaming and clogging of this part of the apparatus. It happened several times and the evaporator had to be cleaned by acid solution; this operation was quite complex due to the small diameter of the tube inside the evaporator.

The outlet gas leaving the reactor was then transported by a short-heated line (393 K) to a Fourier-transform infrared spectroscopy and gas chromatographs (GC). FTIR and GC analyses were performed in separated experiments. The calibration was performed for the fuel by injecting synthetic gas mixtures of pyrrole and helium. Other species detected with the FID were calibrated using the effective carbon number (ECN) method. Moreover, Fourier-transform infrared spectroscopy was also used to quantify CO, CO₂ and HCN. FTIR calibrations were performed using gaseous standards provided by Messer and Air Liquide. Experimental conditions are summarized in [Table 30](#). NO₂ was considered as the final product under the conditions of this study. If N₂ is the final product, the equivalence ratio will be lower than that calculated using NO₂, as shown in [Table 30](#).

Table 30: Summary of experimental conditions used in the present pyrrole study.

Set	T (K)	P (MPa)	τ (s)	$x_{pyrrole}^{inlet}$	φ (NO ₂ : final product)	φ (N ₂ : final product)
1	925-1200			0.93%	∞	∞
2	700-1200	0.107	2	1.05%	0.5	0.42
3	700-1200			1.05%	1	0.84
4	700-1200			1.05%	2	1.68

a) Pyrrole pyrolysis data

Figure 96 compares the experimental data with model predictions in JSR, under 0.107 MPa, $\tau=2.0$ s in the temperature range $T=900$ -1200 K. The conversion of pyrrole becomes significant from ~ 1050 K. Good agreement is observed for pyrrole conversion, especially concerning the temperature of onset of reactivity. Pyrrole consumption is slightly underestimated for temperatures above 1100 K. Reaction products detected are hydrocarbons and N-containing species. Hydrocarbons are methane, acetylene, ethylene, ethane, propene, allene, propyne, a C₄H_x species which could not be clearly identified (but highly unsaturated), benzene and toluene. N-containing species are hydrogen cyanide (HCN), acetonitrile (CH₃CN), 2-propenenitrile (also called acrylonitrile, CH₂CHCN), and three isomers for butene-nitrile (but-3-enitrile, (2E)-but-2-enenitrile⁸ and (2Z)-but-2-enenitrile⁹, also named allyl cyanide, trans-crotonitrile and cis-crotonitrile, respectively; see Table 28 for the structures of the species). The mass spectra for the three isomers are similar and the peak attribution could not be performed with certainty. Mole fractions of most of species increase over the studied temperature range. The few species for which a maximum in mole fraction is observed are allene, propyne, propene and all N-containing species except HCN.

⁸ (2E)-but-2-enenitrile (C₄H₅N): trans-2-Butenenitrile, trans conveys that they are on opposing sides.

⁹ (2Z)-but-2-enenitrile (C₄H₅N): cis-2-Butenenitrile, cis indicates that the functional groups (substituents) are on the same side of some plane

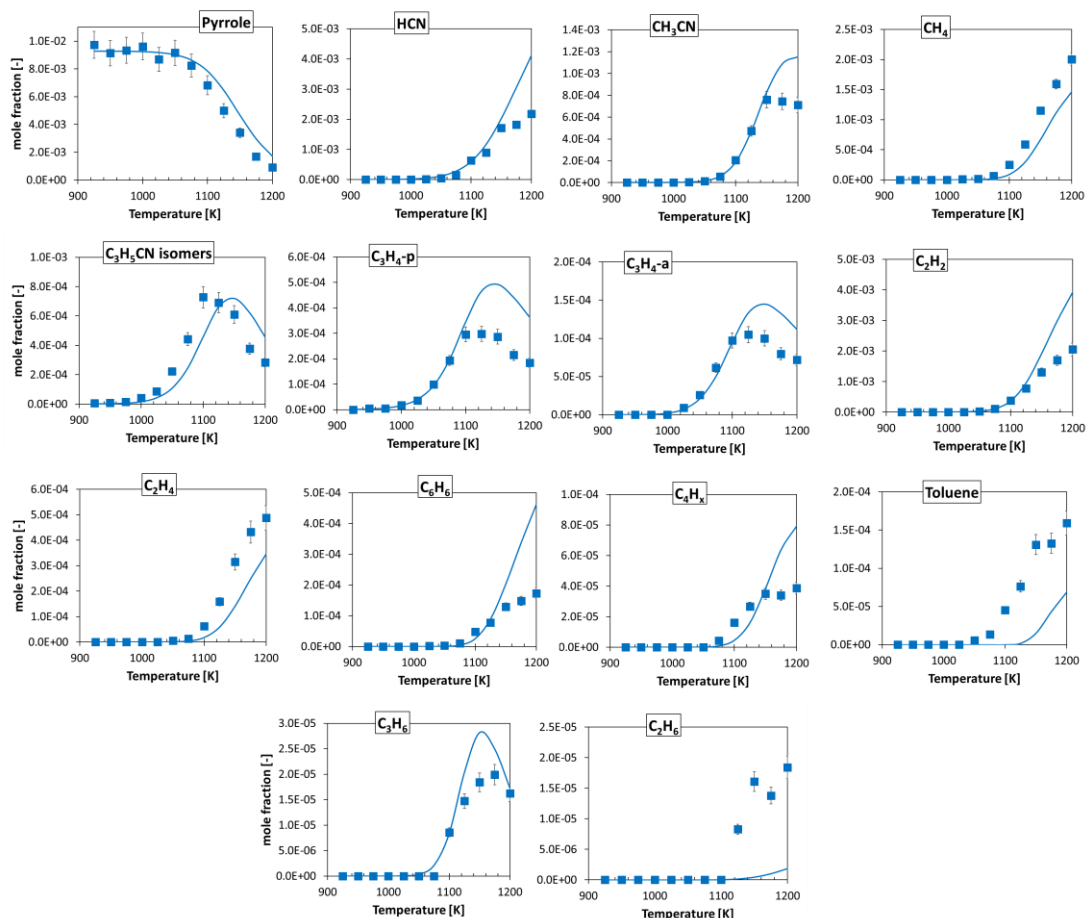


Figure 96: Pyrolysis of ~10000 ppm pyrrole in the JSR under $P=0.107$ MPa and $\tau = 2$ s. Comparison between experimental (symbols) and predicted (lines) mole fraction profiles of fuel, intermediate and product species

c) Pyrrole oxidation data

Experimental measurements and model predictions for the oxidation of pyrrole in the JSR are compared in Figure 97 for three equivalence ratios, $\phi = 0.5, 1.0,$ and 2.0 covering from lean to rich conditions. Fuel consumption is correctly predicted by the model for the $\phi = 1.0$ case. For the leanest case ($\phi = 0.5$), the model strongly under predicts the fuel reactivity, despite correctly capturing the onset of conversion. In the richest case ($\phi = 2.0$), the model over predicts pyrrole consumption for $T < 1050$ K and slightly under predicts the complete conversion at higher temperatures.

Reaction products detected are the same as those detected during pyrolysis (except for toluene, only observed for pyrolysis). In addition, small oxygenated compounds, such as carbon monoxide and carbon dioxide were detected. The reactivity is enhanced compared to pyrolysis, with a significant pyrrole conversion

observed from ~850 K. The equivalence ratio has an effect on the reactivity, the leanest case being the most reactive and the richest case being the least reactive.

At mid conversion, the three pyrrole mole fraction profiles ($\phi = 0.5, 1.0, \text{ and } 2.0$) are shifted by about 50 K. All reaction products detected are the intermediates, their mole fractions going through a maximum, except for CO_2 which is an end product. For the rich case, the default of O_2 leads to higher mole fractions of intermediates and significant mole fractions of CO are still observed at 1200 K which is the highest temperature considered in this study. Some of the intermediates observed under pyrolysis and rich conditions are not detected (e.g., ethane, propene, allene, propyne...), for the stoichiometric and lean mixtures.

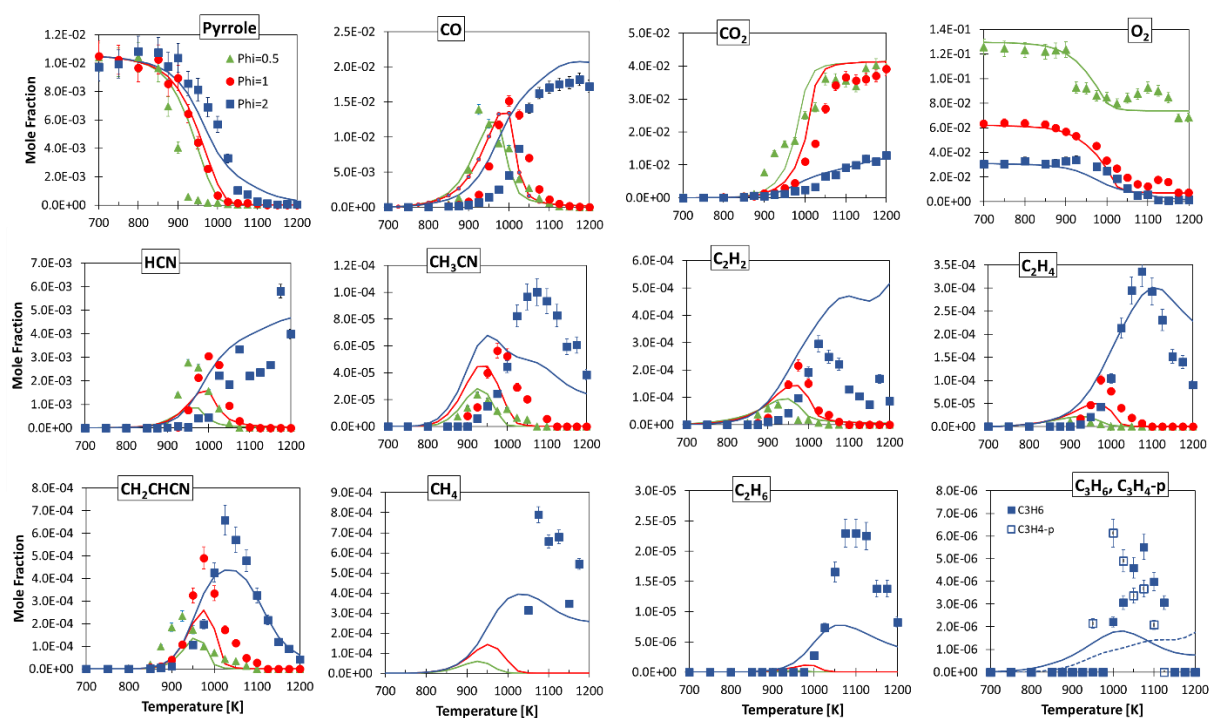


Figure 97 : Mole fraction of species from pyrrole (10000 ppm at the inlet) oxidation in JSR as a function of temperature (0.107 MPa, $\tau = 2\text{s}$, $\Phi = 0.5, 1 \text{ and } 2$). Symbols are experimental data and lines simulations

As already mentioned earlier, the fouling in the evaporation chamber occurred and it had to be cleaned several times. This is likely due to the condensation of some heavy aromatic species (possibly containing N-atoms). For oxidation experiments, the carbon atom balance is satisfactory over the whole range of temperatures, usually lying in between 0.8 and 1 except in the range 850-1000 K where it falls to ~0.8 (see

Table 31. In general, the carbon atom balance is slightly better for the lean and stoichiometric mixtures than for the rich ones. H and O atom balances are not significant because water, one of the main reaction products, was not quantified during this study. This is also the case of the N-atom balance. One or several N containing species were not detected during these oxidation experiments because the N atomic balance is only satisfactory up to 875 K, then it decreases in a monotonous way to zero for the lean and stoichiometric case, and to ~0.4 for the rich case. The potential presence of some species such as N₂, NH₃, NO, NO₂ and N₂O was then further investigated. If present, N₂ could be detected using gas chromatography with the TCD detector. This species was not observed during oxidation, nor during pyrolysis of pyrrole. If present, NH₃, NO, NO₂ and N₂O could be detected using the FTIR spectroscopy tool as they have very characteristics absorption structures in the wavenumber range investigated. None of these species could be identified in recorded spectra during oxidation experiments, even in traces. . Due to the high number of light species present, MS could not be used. The non-detection of the light N-containing species suggests that the loss of N-atoms is likely due the condensation of heavy species.

Table 31: C-, H-, N- and O-atom balances for oxidation experiments.

T (K)	C			H*			O*			N		
	$\varphi=0.5$	$\varphi=1$	$\varphi=2$									
700	1.04	1.05	0.97	1.04	1.05	0.97	1.01	1.01	0.98	1.04	1.05	0.97
750	1.01	1.03	1.00	1.01	1.02	0.99	0.99	1.02	0.98	1.01	1.02	0.99
800	1.05	0.97	1.08	1.04	0.97	1.08	0.99	1.02	1.06	1.04	0.97	1.08
850	0.99	1.04	1.08	0.97	1.03	1.07	0.98	1.01	0.98	0.97	1.03	1.08
875	0.77	0.88	1.00	0.71	0.86	0.98	1.00	0.97	1.02	0.71	0.86	0.98
900	0.76	0.96	1.06	0.43	0.90	1.04	1.07	0.94	1.07	0.44	0.90	1.04
925	0.81	0.74	0.90	0.12	0.66	0.86	0.91	0.89	1.12	0.23	0.66	0.87
950	0.83	0.72	0.90	0.12	0.51	0.84	0.92	-	-	0.33	0.56	0.84
975	0.75	0.78	0.85	0.09	0.38	0.74	0.86	0.89	1.02	0.28	0.53	0.77
1000	0.90	0.84	0.82	0.06	0.19	0.66	0.91	0.83	0.95	0.18	0.41	0.68
1025	0.82	0.85	0.77	0.03	0.11	0.50	0.87	0.80	0.84	0.09	0.31	0.64
1050	0.98	0.91	0.76	0.01	0.05	0.29	0.97	0.80	0.78	0.03	0.12	0.37
1075	0.93	0.95	0.84	0.00	0.03	0.34	0.99	0.79	0.65	0.00	0.05	0.48
1100	0.91	0.96	0.81	0.00	0.01	0.23	1.03	0.79	0.74	0.00	0.01	0.30
1125	0.86	0.90	0.82	0.01	0.00	0.20	0.99	0.85	0.64	0.01	0.00	0.28
1150	0.99	0.91	0.85	0.00	0.00	0.14	0.99	0.83	0.69	0.00	0.00	0.29
1175	1.01	0.93	0.92	0.00	0.00	0.24	0.87	0.71	0.69	0.00	0.00	0.60
1200	0.99	0.98	0.87	0.00	0.00	0.13	0.86	0.74	0.73	0.00	0.00	0.41

* H and O atom balances are not significant because water was not quantified.

VI.1.3 Kinetic analysis

In the next section, the kinetic mechanism was used to investigate the rate of production of pyrrole and the sensitivity coefficients to pyrrole mole fraction for pyrrole oxidation in JSR.

Rate of production of pyrrole

A rate of production analysis during pyrrole oxidation at 950 K under stoichiometric condition was shown in [Figure 98](#). Pyrrole is consumed through H-abstraction reactions by $\dot{\text{O}}\text{H}$, $\ddot{\text{O}}$, $\dot{\text{H}}$ and $\text{H}\dot{\text{O}}_2$ to form pyrlyl radical, that is largely converted back to pyrrole through the backward reaction $\text{C}_4\text{H}_5\text{N} + \text{O}_2 \leftrightarrow \text{PYRLYL} + \text{H}\dot{\text{O}}_2$. This reaction is highly endothermic ($E_a = 46.9$ kcal/mol) and most likely proceeds in the backward direction at conditions where $\text{H}\dot{\text{O}}_2$ concentration is high (e.g., $T < 1000$ K). 41% of pyrlyl is consumed, while its decomposition to $\text{c}\dot{\text{C}}_3\text{H}_4\text{CN}$ accounts for 57%. At such low temperatures, $\text{c}\dot{\text{C}}_3\text{H}_4\text{CN}$ is isomerized to $\text{a}\dot{\text{C}}_3\text{H}_4\text{CN}$ (cyano allyl radical), which decomposes it to acetylene and $\dot{\text{C}}\text{H}_2\text{CN}$. $\text{a}\dot{\text{C}}_3\text{H}_4\text{CN}$ reacts with $\text{H}\dot{\text{O}}_2$, forming $\dot{\text{O}}\text{H}$ and a cyano alkoxy radical ($\text{C}_4\text{H}_4\text{N}\dot{\text{O}}$) that decomposes then through β -scission to form cyano radical ($\dot{\text{C}}\text{N}$) and unsaturated products such as acrolein ($\text{C}_2\text{H}_3\text{CHO}$), or acetylene and formaldehyde.

To a lower extent, $\text{a}\dot{\text{C}}_3\text{H}_4\text{CN}$ also reacts with $\text{H}\dot{\text{O}}_2$, releasing O_2 and forming allyl cyanide, activating the isomerization reactions to $\text{C}_3\text{H}_5\text{CN}$ isomers, which are then consumed through H-abstraction reactions by $\ddot{\text{O}}$ to form $\dot{\text{C}}_3\text{H}_4\text{CN}$ that decomposes to methyl radical and cyanoacetylene through β -scission. The rate coefficients for these pathways were estimated based on analogy with allyl radical ($\dot{\text{C}}_3\text{H}_5\text{-a}$)/ $\text{H}\dot{\text{O}}_2$ kinetics.

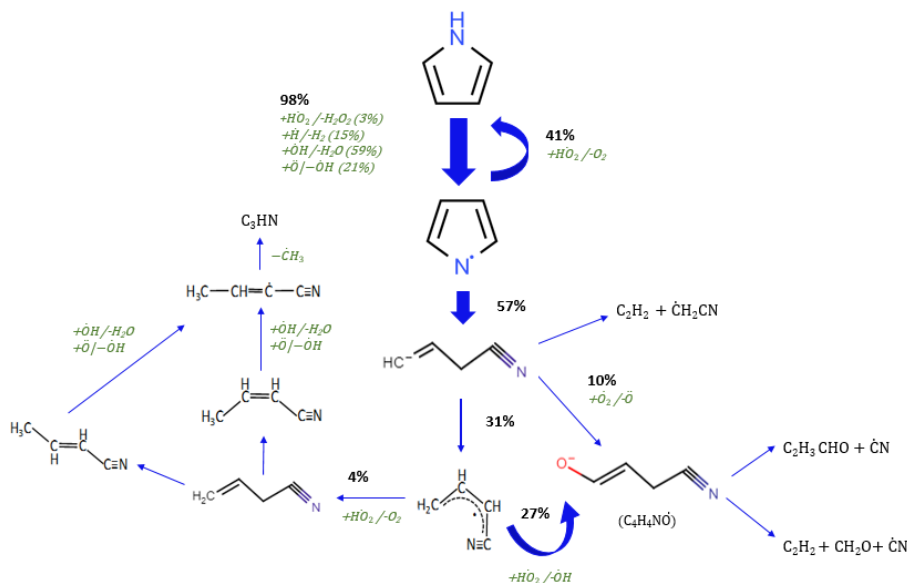


Figure 98 : rate of production analysis at $T=950\text{ K}$, for pyrrole oxidation JSR at $\phi=1.0$, $p=0.107\text{ MPa}$ and $\tau = 2.0\text{ s}$. Arrow's width qualitatively represents the importance of each reactive flux.

A sensitivity analysis of rate constants to fuel consumption at 950 K for the three mixtures is performed in order to investigate possible reasons for model shortcomings in predicting the effect of equivalence ratio. A sensitivity analysis is shown in Figure 99. Sensitivity coefficients have been normalized over that of the most sensitive reaction, $\dot{\text{H}} + \text{O}_2 \rightleftharpoons \ddot{\text{O}} + \dot{\text{O}}\text{H}$.

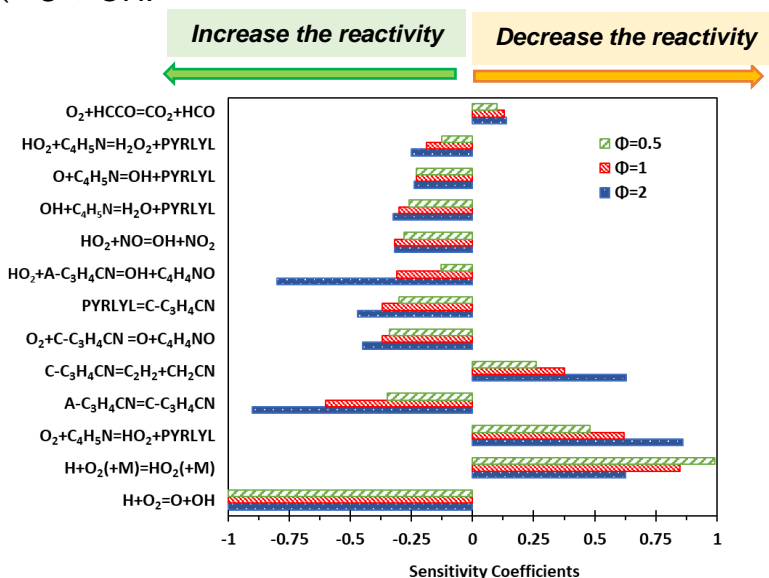


Figure 99 : Sensitivity analysis of fuel consumption to model rate constants at $T=950\text{ K}$ for the $\phi = 0.5$, 1.0 and 2.0 mixtures. Sensitivity coefficients are normalized over that of $\dot{\text{H}} + \text{O}_2 \leftrightarrow \ddot{\text{O}} + \dot{\text{O}}\text{H}$. A negative sensitivity coefficient stands for a reaction increasing reactivity (i.e., contributing to fuel consumption) and vice versa.

The competition between the branching reaction $\dot{H} + O_2 \leftrightarrow \ddot{O} + \dot{OH}$ increasing system reactivity and the third body recombination $\dot{H} + O_2 (+M) \leftrightarrow H\dot{O}_2 (+M)$ decreasing system reactivity, increases for leaner mixtures ($\phi = 0.5$). Pyrrole consumption through H-abstraction by O_2 is the most sensitive reaction ($C_4H_5N + O_2 \leftrightarrow PYRLYL + H\dot{O}_2$). As already highlighted in the above discussion, this reaction proceeds backward consuming pyrlyl and $H\dot{O}_2$ thus decreasing fuel consumption. In addition to partly restoring the concentration of fuel, the produced O_2 is then converted through the recombination reaction $\dot{H} + O_2 (+M) \leftrightarrow H\dot{O}_2 (+M)$ or $O_2 + H\dot{C}O \leftrightarrow H\dot{O}_2 + CO$ forming once again $H\dot{O}_2$.

Reactions belonging to the pyrrole subset such as $C_4H_5N + H\dot{O}_2 \leftrightarrow PYRLYL + H_2O_2$ and $a\dot{C}_3H_4CN + H\dot{O}_2 \leftrightarrow \dot{OH} + \dot{C}_4H_4NO$ increase the reactivity because $H\dot{O}_2$ is converted into radicals that are more reactive. $H\dot{O}_2$ is also consumed by NO forming \dot{OH} and NO_2 for which we adopted the value of Howard et al. (1980), as already discussed in Song et al. (2019).

The isomerization of pyrlyl radical to the vinylic radical ($pyrlyl \leftrightarrow c\dot{C}_3H_4CN$) clearly favors pyrrole conversion. The \dot{C}_4H_4N isomers chemistry ($c\dot{C}_3H_4CN \leftrightarrow a\dot{C}_3H_4CN$) and the oxidation ($O_2 + c\dot{C}_3H_4CN \leftrightarrow \ddot{O} + \dot{C}_4H_4NO$) reactions increase reactivity with the decomposition reaction ($c\dot{C}_3H_4CN \leftrightarrow C_2H_2 + \dot{C}H_2CN$) consuming $c\dot{C}_3H_4CN$. The oxidation of $a\dot{C}_3H_4CN$ ($a\dot{C}_3H_4CN + H\dot{O}_2 \leftrightarrow \dot{OH} + \dot{C}_4H_4NO$) also contributes to increase the overall reactivity, releasing two reactive radicals.

VI.1.4 Conclusion

The pyrolysis and oxidation of pyrrole were carried out in an atmospheric pressure jet-stirred reactor significantly extending the validation targets available for pyrrole kinetic model validation purposes. A preliminary model, based on previous research efforts and on analogy with kinetic subsets already implemented in the CRECK kinetic framework is presented, showing general good agreement. To the author's knowledge, these experimental data of pyrrole in JSR are the first work in the literature. The kinetic model study allows inclusion of pyrrole as a representative nitrogen-containing component in more complex surrogate models for pyrolysis bio-oils (Pelucchi et al., 2019b). Experimental data on pyrrole combustion at higher

pressure would be useful to extend the confidence of the proposed model at conditions closer to that of actual combustion devices (e.g., gas turbines).

In addition, this detailed kinetic should be further developed because the results of fuel products, especially the hydrocarbons (e.g., C_2H_2 , CH_4 , and C_2H_6) are not very satisfactory with significant shifts between experimental and computed data. On the other hand, many experimental data were found in the literature especially that performed in tubular flow reactors and shock tubes, but less in JSR. The experimental data in JSR allow developing the kinetic models with the longest residence times.

Moreover, as shown in the part above, C_2H_2 and other unsaturated hydrocarbons¹⁰ are produced in large quantities, posing some concerns about the fact that using bio-oil leads to not only the nitrogen oxides formation but also the particulate matter formation.

VI.2 Ethylene glycol pyrolysis and oxidation

This part of the chapter VI present experimental and numerical results about the pyrolysis and oxidation of EG in a JSR under atmospheric pressure. The experimental results were interpreted using a newly developed detailed kinetic model. The kinetic model describing EG pyrolysis and oxidation is adopted from Kathrotia et al. (2017). A particularity of ethylene glycol gas phase chemistry is the existence of several molecular reactions for the decomposition of the fuel. Two of them are water elimination leading to acetaldehyde. Others lead to H_2 and glycolaldehyde, to methanol and formaldehyde, and to ethylene and hydrogen peroxide. In the mechanism of Kathrotia et al. (2017), acetaldehyde is considered to be the only direct decomposition product of EG. They cannot distinguish and confirm if ethenol or acetaldehyde is the major product of EG decomposition in the water elimination reactions. They assume that, due to the energy barriers, ethenol may quickly

¹⁰ Unsaturated hydrocarbons that have double or triple covalent bonds between adjacent carbon atoms.

isomerized/tautomerized to acetaldehyde and therefore the equilibrium concentration may not show any ethenol.

VI.2.1 Experimental results

In the next section, the experimental results obtained during my PhD are compared to simulation data using the kinetic model. The results of ethylene glycol pyrolysis are first presented, then those of ethylene glycol oxidation are shown. In this work, the equivalence ratio is defined by considering the following stoichiometric equation: $C_2H_6O_2 + 2.5O_2 = 2CO_2 + 3H_2O$.

Experiments were carried out for pyrolysis and for oxidation under fuel-rich, stoichiometric and fuel lean conditions. Different sets experiments with EG were obtained using a JSR working close to atmospheric pressure (0.107MPa), with helium as carrier gas, at a temperature ranging from 600 to 1100 K and at a residence time of about 2 s. The initial fuel mole fraction is 1%. The used experimental conditions are summarized in [Table 32](#).

Table 32: Summary of JSR Experimental Conditions Used in the Present Study.

set	T (K)	P (MPa)	τ (s)	ϕ	Inlet mole fraction (%)		
					EG	O ₂	He
1	650 - 1100			∞	1.00	0.00	99.00
2	600 - 1075			0.5	1.00	5.00	94.00
3	600 - 1075	0.107	2	1	1.00	2.50	96.50
4	600 - 1075			2	1.00	1.25	97.75

The temperature of the evaporator (473 K) was set above the boiling temperature of ethylene glycol (470 K) to avoid the fuel condensation. To avoid condensation, the reactants and reaction products leaving the reactors were transported by a heated transfer line maintained at 393 K toward two gas chromatographs (GCs). Moreover, due to the condensation of outlet heavy species (e.g., ethylene glycol, formic acid) in transfer line to GCs, a trap maintained at liquid nitrogen temperature was used. The trap was connected to the outlet of the reactor and the outlet flow was condensed due to the low temperature during a period of 15 minutes. Afterward, the sample was mixed with an internal standard (n-octane) and a solvent (ethanol), allowing for the dilution of the liquefied sample. It is possible that condensation and physical adsorption occur on some surfaces in the manifolds (cold

points, valve, gums) and could affect the quality of the results. The sample was then injected to the gas chromatography-mass spectrometer (GC-MS) with an automatic liquid sampler.

a) Ethylene glycol pyrolysis data

Figure 100 compares the mole fractions of reactant and main products predicted using the model with the pyrolysis data in a JSR, being performed over the temperature range 650-1100 K, at a residence time of 2 s, a pressure of 0.107 MPa, with an inlet EG mole fraction of 10000 ppm.

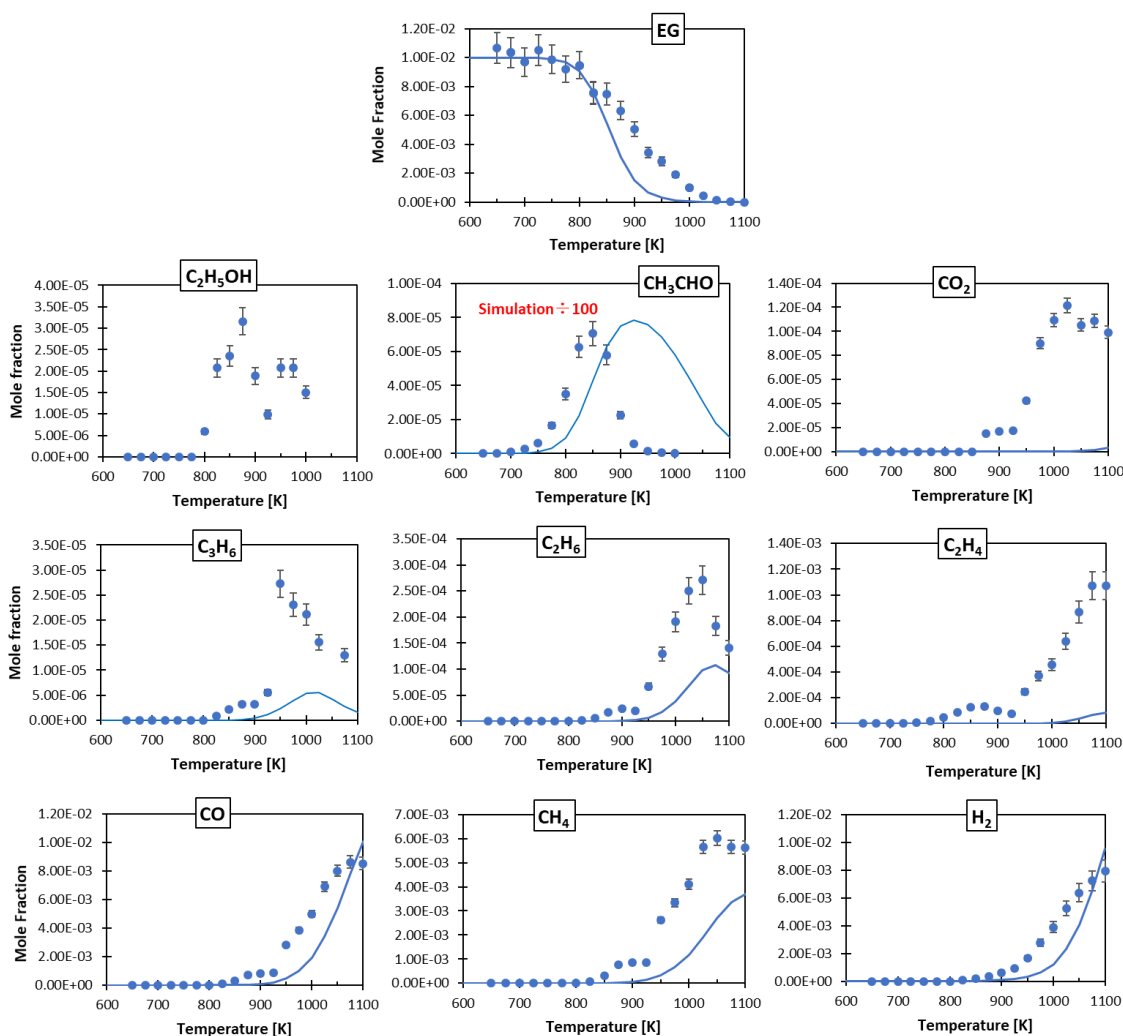


Figure 100: Mole fractions of reactants and main reaction products during the pyrolysis of EG over the temperature range 650-1100 K in the JSR ($P = 0.107$ MPa and $\tau = 2$ s). Symbols: experiments. Lines: data computed with the model.

The temperature of the reactivity onset of EG is about 800 K. Satisfactory agreement is observed for EG conversion despite a slight underestimation for $T > 850$ K. Carbon monoxide, hydrogen and methane, the major experimental products, are formed from 875 K, with their mole fractions being reasonably predicted despite a shift of 100 K between the experimental and computed data for CH_4 at 950-1100 K. The mole fractions of acetaldehyde, carbon dioxide, ethane and ethylene, formed in lower amounts, are strongly underestimated, except for acetaldehyde (the simulation over-predicted its formation by a factor of 100). The mole fractions of ethanol and propene remain low (less than 70 ppm) and their productions are underestimated. There is a significant shift between the experimental and computed data for acetaldehyde (50 K) profile. Acetaldehyde is formed at lower temperatures in experiments than in the simulation.

b) Ethylene glycol oxidation data

The comparison of model predictions and experimental measurements for the oxidation of EG for three equivalence ratios $\varphi=0.5$, 1.0 and 2.0, are displayed in [Figure 101](#). Shifts between the experimental and computed data are observed for EG conversion. The simulated fuel consumption profiles are very little influenced by the equivalence ratio and the three conversion curves are almost superimposed. EG consumption is rather correctly predicted by the model for $\varphi=2.0$ case, through a shift of 25 K between the experimental and computed data is observed. For the leanest cases ($\varphi=0.5$ and 1), the fuel consumption is slightly over-predicted. Oxygen consumption is well predicted for $T < 900$ K for three equivalence ratios.

Major products (such as CO, CO_2 and methane) formation is correctly predicted for $\varphi=2.0$. The model over-predicts acetaldehyde formation by a factor of about 25, while the experimental data shows very low quantities of acetaldehyde (i.e. 25-30 ppm). Not only is its over-prediction observed but also a temperature significant shift between the experimental and computed data. Ethane productions is strongly over-predicted, especially for $\varphi=1.0$ and 2. Whereas acetone is strongly under-predicted. Ethylene and propene formations are well predicted for $\varphi=0.5$ and 2. Under stoichiometric condition, ethylene and propene are strongly over-predicted while they are detected in much lower quantities in the experimental measurements. With the current mechanism there is no way to explain this deviation.

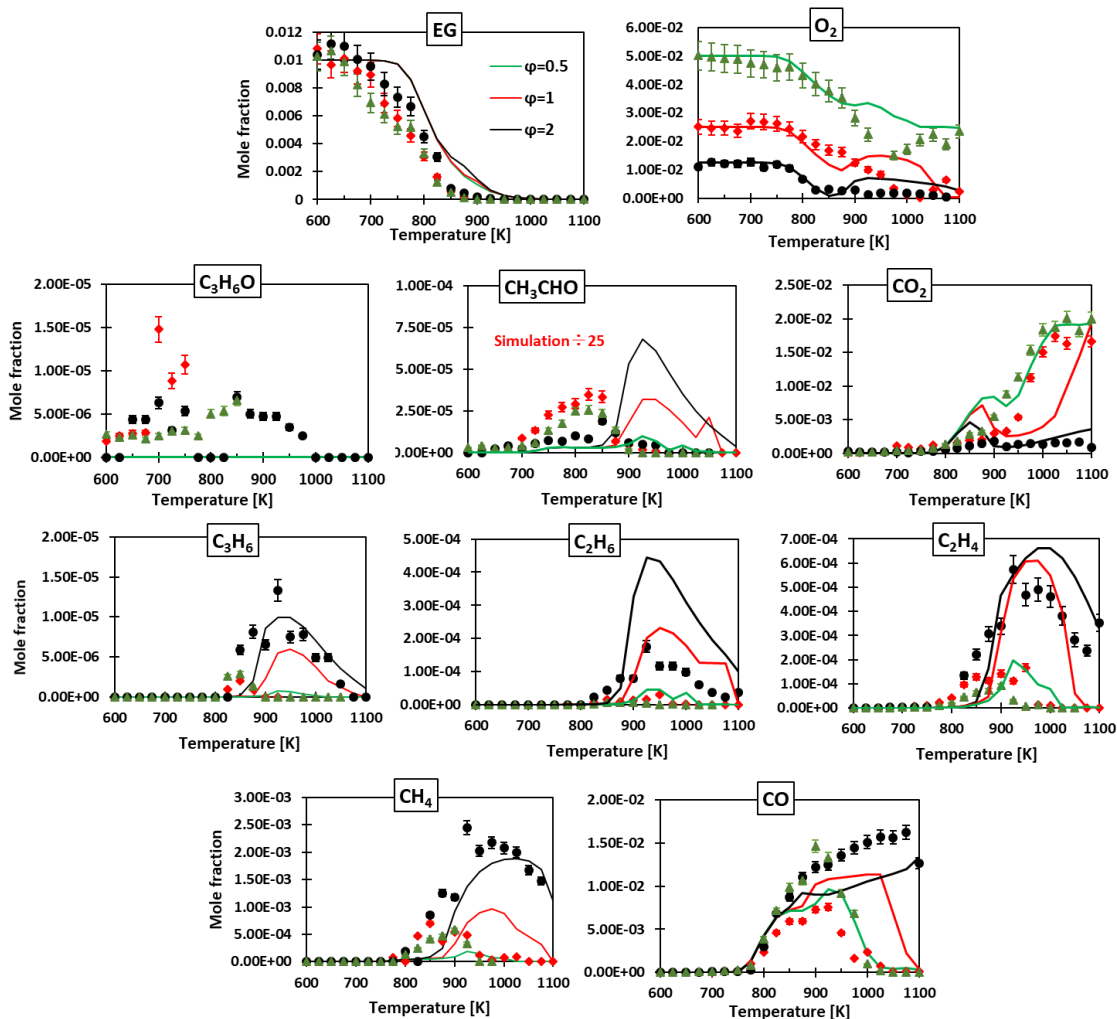


Figure 101: Mole fractions of reactants and main reaction products during the oxidation of 10000 ppm EG in the JSR ($\phi = 0.5, 1$ and $2, P = 0.107$ MPa and $\tau = 2$ s) over the temperature range 600-1100 K. Symbols: experiments. Lines: data computed with the model.

In order to verify the performance of the technique analysis, the carbon balance and the selectivity analysis are therefore performed. Table 33 displays the carbon balances for the four EG experiments ($\Phi = \infty, 0.5, 1$, and 2). It can be observed that, from 875 to 1025 K, the carbon balance for the EG pyrolysis is below to 80%. The carbon balance of the oxidation experiments is below 80% from 725 to 925 K, which means that some species were not detected in these temperature ranges. For the carbon balance slightly higher than 100%, this is due to uncertainties in species mole fractions.

Table 33: Carbon balance of the experimental results of EG.

T (K)	Pyrolysis	Phi=1	Phi=0.5	Phi=2
600	-	109%	104%	105%
625	-	97%	108%	113%
650	107%	102%	100%	111%
675	104%	94%	84%	102%
700	97%	96%	72%	97%
725	106%	74%	65%	84%
750	99%	64%	56%	75%
775	92%	61%	60%	70%
800	96%	54%	60%	64%
825	78%	65%	60%	70%
850	80%	70%	72%	65%
875	74%	66%	75%	77%
900	61%	78%	105%	82%
925	44%	76%	112%	88%
950	60%	92%	102%	91%
975	61%	78%	111%	97%
1000	63%	98%	97%	98%
1025	77%	91%	94%	101%
1050	84%	82%	101%	98%
1075	85%	-	91%	99%
1100	83%	88%	100%	72%

Figure 102 presents the selectivity analysis performed at three different temperatures (800 K for $\phi=2$, 775 K for $\phi = 0.5$ and 1, and 900K for $\phi = \infty$) with ~50 % of fuel conversion. This helps to highlight the main products for each condition.

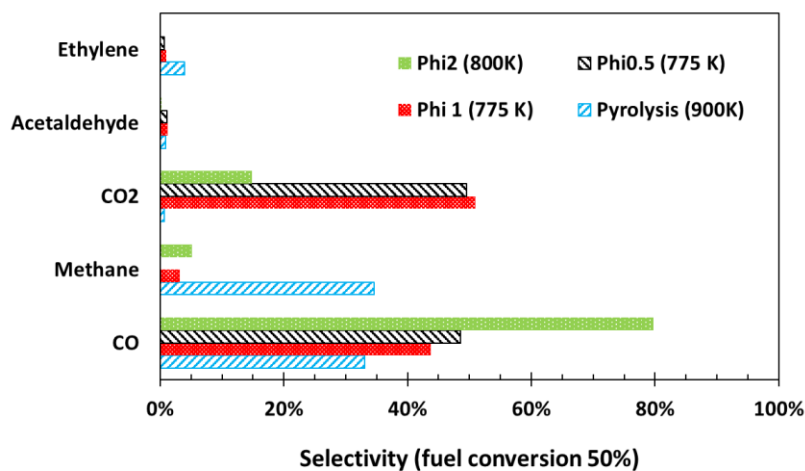


Figure 102: Reaction product selectivity analysis for EG pyrolysis and oxidation (800 K for $\phi=2$, 775 K for $\phi = 0.5$ and 1, and 900K for $\phi = \infty$). ~50 % of fuel conversion.

As shown in [Figure 102](#), the equivalence ratio has effect on the product distribution, especially for CO, CO₂ and methane. Methane formation is negligible under fuel-rich condition. Whereas, CO₂ formation is favored under fuel-lean conditions. The selectivity analysis also shows that acetaldehyde and ethylene are the most important intermediates at these temperatures.

VI.2.2 Conclusion

In this work, the pyrolysis and the oxidation of 1% ethylene glycol were experimentally investigated in a jet-stirred reactor under atmospheric pressure. Comparison of the experimental results with simulations using a literature kinetic model showed a reasonable agreement for the reactivity and for the mole fractions of major reaction products. To the authors knowledge this EG experimental work is the first one performed in a JSR in the literature. The scarcity of literature data for this fuel with simple structure could seem surprising. It is likely due to experimental difficulties specific to this class of compounds, as it was experienced in the present study. Thus, these new experiments provide an original database on the species profiles of various major products and intermediates. Moreover, the oxidation chemistry of ethylene glycol should be further investigated because simulations for minor products, especially acetaldehyde and hydrocarbons indicate significant deviations between experimental and computed data. The problem of the overestimation of acetaldehyde production (100 times more than experimental data for pyrolysis). It will require a much deeper investigation of the specific chemistry involved in the gas phase kinetics of EG. The acetaldehyde over prediction is probably due to the inaccuracy of the rate constants of EG decomposition to acetaldehyde and the lack of complementary reactions of ethenol which must be completed in the kinetic model. Thus, complementary experimental data and theoretical studies are needed to improve these rate constants and provide more knowledge on the role of ethenol in EG oxidation.

VI.3 Propylene glycol pyrolysis and oxidation

This part of the [chapter VI](#) investigates only experimentally the pyrolysis and oxidation of propylene glycol (PG) in a JSR under quasi atmospheric pressure (0.107MPa). Two sets of experiments with PG were performed similarly to those of EG (experiments were carried out for pyrolysis and for oxidation under stoichiometric condition), using the same JSR with helium as carrier gas. The PG pyrolysis and oxidation experiments were performed at temperatures ranging from 600 to 1200 K and at a residence time of about 2 s. The initial fuel mole fraction is 0.01. The used experimental conditions are summarized in [Table 34](#).

Table 34: Summary of JSR Experimental Conditions Used in the Present Study.

set	T (K)	P (MPa)	τ (s)	ϕ	Inlet mole fraction (%)		
					PG	O ₂	He
1	650 - 1200	0.107	2	∞	1.00	0.00	99.00
2	600 - 1200			1	1.00	4.00	95.00

The temperature of the evaporator (473 K) was set above the boiling temperature of PG (461 K) to avoid the fuel condensation. The analytic tools used for the quantification of fuel consumption and product formation are the same as those used for EG experiments ([section VI.2](#)). As for ethylene glycol, experimental difficulties have been experienced despite the simple structure of this fuel (mainly condensation and adsorption problem in GC transfer lines).

VI.3.1 Experimental results

In the next section, the experimental results of PG obtained during my PhD are presented. The results of PG pyrolysis are compared with PG oxidation in [Figure 103](#). In this work, the equivalence ratio is defined by considering the following stoichiometric equation: $C_3H_8O_2 + 4O_2 = 3CO_2 + 4H_2O$.

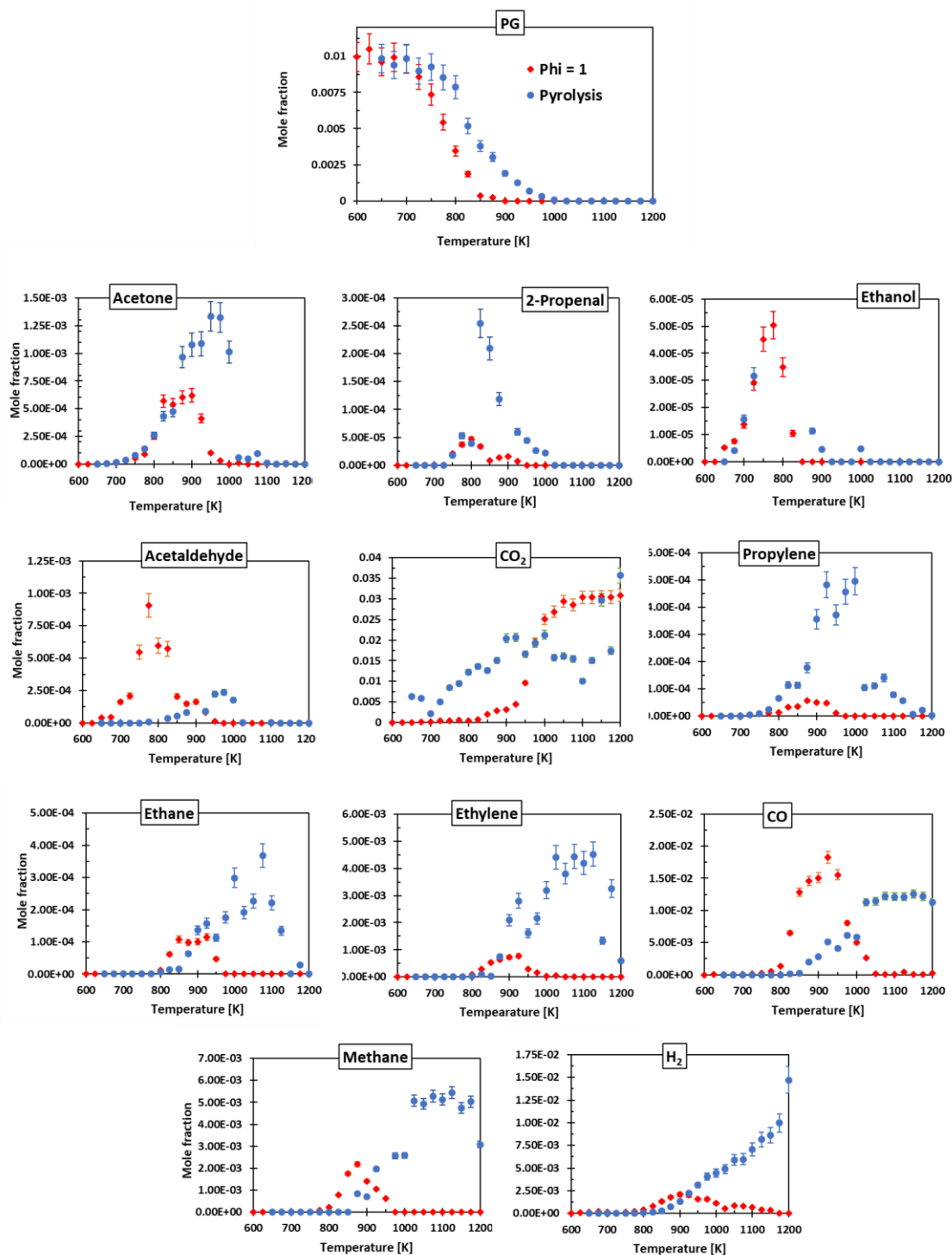


Figure 103: Mole fractions of reactants and main reaction products during the pyrolysis and oxidation of PG over the temperature range 600-1200 K in the JSR ($P = 0.107$ MPa and $\tau = 2$ s). Blue symbols: pyrolysis experiments. Red symbols: oxidation experiments.

The main products detected during the pyrolysis of PG are oxygen, carbon monoxide, methane, ethylene, and hydrogen. The conversion of PG becomes significant from ~775 K and fuel is totally consumed at ~1025 K. The major experimental products, are formed from 875 K, except O₂ and C₃H₆, which are formed at 750 K. Only CO mole fractions, increase over the studied temperature range. The most species for which a maximum in mole fraction is observed are methane, acetaldehyde, ethane, ethylene, ethanol, acetone, and propene. The formation of ethanol remains low (less than 30 ppm).

Reaction products detected during the oxidation experiments are the same as those detected during pyrolysis but with the higher amount of oxygenated species ([Figure 104](#)). The presence of oxygen enhances the fuel reactivity and the formation of oxygenated compounds, like carbon monoxide and carbon dioxide, acetaldehyde, acetone and ethanol. The mole fractions of CO₂ during oxidation is 100 times more significant than that during pyrolysis, as well as CO, which is formed in two times higher amount than that during pyrolysis. The presence of oxygen has a strong effect on products and slightly for fuel reactivity. The fuel reactivity is enhanced with significant propylene glycol conversions observed from ~725 K and fuel is totally consumed at ~875 K. The consumption of O₂ begins from 825 K which is after that of PG, because fuel decomposition reaction is dominant at low temperature (<825 K). The conversion of oxygen is not total, O₂ remained constant from 1000 K (~1000 ppm). There is only one end product detected which is CO₂, every product is intermediates with their mole fractions going through a maximum. C₂H₅OH, CH₃CHO and C₃H₆O species are formed earlier (at ~725 K) than the other products which are the products from PG decomposition reactions.

The carbon balance of the experimental results of PG ($\phi=1$ and ∞) is displayed in [Table 35](#). The carbon balance for PG oxidation is globally better than that of PG pyrolysis. Some species were not detected in the temperature ranges of 750-900K for the oxidation case and 825-1000 K for the pyrolysis because in these temperature ranges, the carbon balance is below to 80%. Due to uncertainties in species mole fractions, the carbon balance can be slightly higher than 100%.

Table 35: Carbon balance of the experimental results of PG.

T (K)	Pyrolysis	Phi = 1
650	99%	96%
675	94%	100%
700	99%	99%
725	91%	88%
750	94%	77%
775	89%	60%
800	84%	45%
825	63%	54%
850	48%	69%
875	59%	79%
900	60%	78%
925	73%	90%
950	52%	89%
975	68%	93%
1000	69%	100%
1025	87%	99%
1050	83%	99%
1075	93%	95%
1100	88%	101%
1125	91%	103%
1150	68%	102%
1175	80%	102%
1200	53%	104%

The reaction product selectivity analysis for PG pyrolysis (775 K) and oxidation ($\phi=1$, 825 K) is presented in [Figure 104](#). At these temperatures, PG conversion is about 50%. Main PG pyrolysis products are acetone, 2-propenal and ethanol. The presence of O_2 in the PG experiment (oxidation) promotes the formation of acetaldehyde, CO_2 and CO (PG oxidation products) but hardly affects the formation of H_2 .

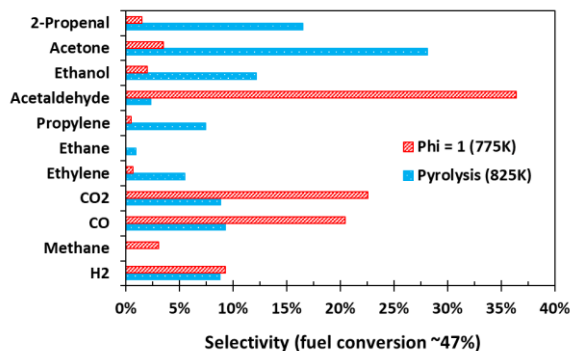


Figure 104: Reaction product selectivity analysis for PG pyrolysis and oxidation (775 K for $\phi = \infty$ and 825 K for $\phi = 1$). ~50 % of fuel conversion.

VI.3.2 Comparison of PG and EG experimental results

a) Pyrolysis data

PG and EG molecules are similar with the same functional groups (diol) containing two hydroxyl groups (-OH groups) but different with the number of carbon. The comparison of the experimental results of the pyrolysis of EG and PG is presented in Figure 105.

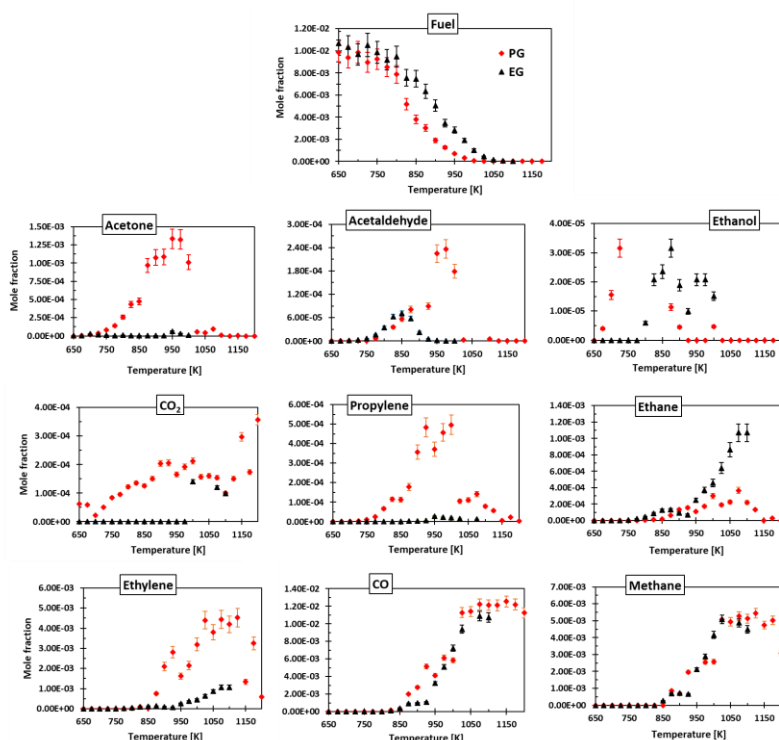


Figure 105: Mole fractions of reactants and main reaction products during the pyrolysis of PG and EG over the temperature range 600-1200 K in the JSR ($x_{fuel}^{inlet} = P = 0.107$ MPa and $\tau = 2$ s). Red symbols: PG experiments. Black symbols: EG experiments.

As shown in [Figure 105](#) PG is more reactive than EG. The temperatures of reactivity onset of PG and EG are ~775 K and 825 K, respectively. Reaction products detected during the PG and EG pyrolysis are methane, carbon dioxide, carbon monoxide, ethylene, ethane, propene, acetone and acetaldehyde. However, during PG pyrolysis more acetone, acetaldehyde, propylene and ethylene are formed than during EG pyrolysis. The CO and methane profiles during the pyrolysis of the two fuels are quite similar. During the pyrolysis of PG, ethanol is produced at a lower temperature (675 K) than the case of EG (800 K). However the maximum ethanol produced for two cases is quite the same (~ 30 ppm).

b) Oxidation data

The comparison of the experimental results of PG and EG oxidation ($\phi=1$) is displayed in [Figure 106](#). The experiments with the two fuels were performed under the same conditions ($x_{fuel}^{inlet} = 1\%$, $P = 0.107$ MPa, $\tau = 2$ s). [Figure 106](#) shows that PG and EG have similar temperatures of reactivity onset, but EG seems to be a little more reactive than PG. EG consumption begins at 675 K, meanwhile, PG is consumed from 725K. O_2 during PG oxidation is not totally consumed whereas, in the case of EG, O_2 is totally consumed.

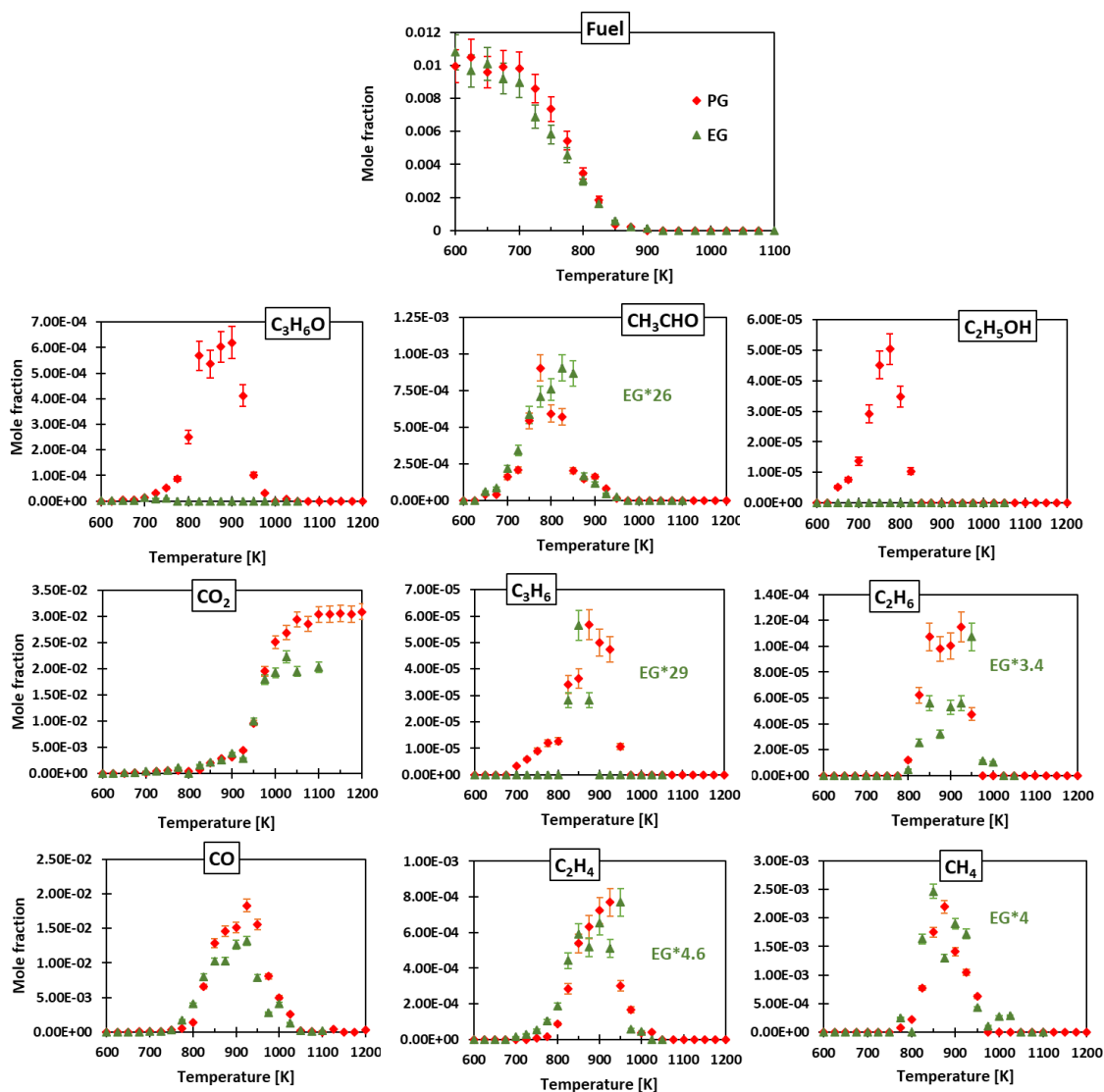


Figure 106: Mole fractions of reactants and main reaction products during the oxidation ($\varphi=1$) of PG and EG over the temperature range 600-1200 K in the JSR ($x_{fuel}^{inlet} = 1\%$, $P = 0.107$ MPa and $\tau = 2$ s). Red symbols: PG experiments. Green symbols: EG experiments.

Reaction products detected during the PG oxidation experiments are rather the same as those detected during EG oxidation, they are methane, carbon dioxide, carbon monoxide, ethylene, ethane, propene, acetone and acetaldehyde. Moreover, the quantities of reaction products during the PG oxidation are higher than that of EG because PG molecule is bigger than EG which gives more fragments.

The mole fractions of CH₄ during PG oxidation are about four times higher than during EG oxidation, as well as ethylene and ethane. In addition, propene and acetaldehyde mole fractions during PG oxidation are 29 and 26 higher, respectively, than mole fractions of these species detected during EG oxidation. Ethanol during PG

oxidation is also detected with a maximum of 50 ppm whereas in case of EG, there is no ethanol detection.

VI.3.3 Conclusion

In this work, the pyrolysis and oxidation (stoichiometric condition) of 1% propylene glycol were experimentally investigated in a jet-stirred reactor at quasi atmospheric pressure (0.107 MPa). To the author's knowledge, this PG experimental work is the first one performed in the literature. This could be linked to experimental difficulties due to the nature of this class of compounds. These new experiments provide an important database on the species profiles of various major products and intermediates. Comparison of the PG experimental results with EG results showed a different reactivity of these two fuels, which allow to better understand PG behavior. It can also help to investigate the kinetic modelling of PG oxidation that has never been studied in the literature before. The structure of PG is similar to that of EG but a little more complicated, which can make it hard for kinetic modeling study. To develop an accurate kinetic model, it is required a much deeper investigation of the specific chemistry involved in the gas phase kinetics of propylene glycol. As for ethylene glycol, concerted molecular pathways should play a great role (which is deduced from the large amount of acetone observed during the propylene glycol experiments).

VII. CONCLUSION AND PERSPECTIVES

The conclusion of the work presented in this work is divided into five parts. A first section is dedicated to the synthesis of the performances of the analytical techniques. The second part summarizes the study of the oxidation of biogas. Then, the study of the NO_x formation is synthesized in the third section. The fourth part is about the study of the oxidation of bio-oils. While the last part presents my perspectives. [Table 36](#) summarizes all the experiments with the conditions performed during my thesis.

Table 36: Experiments performed during my thesis.

Reactants	Experiments	x_{fuel}^{inlet} (ppm)	T (K)	P(MPa)	τ (s)	ϕ	Reactors
Study of the oxidation of biogas components							
Neat NH ₃	Pyrolysis	1,000	1373-1873	0.113	0.25	∞	FR1
	Oxidation	1,000	1073-1973	0.127	0.05	0.375	FR1
NH ₃ +CH ₄	Oxidation	1,000 (both fuels)	1223-1973	0.127	0.025	1	FR1
		NH ₃ :500 CH ₄ : 12,000	500-1200	0.107	1.5	0.5,1,2	JSR
NH ₃ +H ₂	Oxidation	NH ₃ : 1,000 H ₂ : 0-2003	873-1773	0.127	0.05	1	FR1
Neat H ₂ S	Pyrolysis	500	600-1200	0.107	2	∞	JSR
		500	973-1923	0.123	0.25		FR1
		500	900-1600	0.107	2		FR2
	Oxidation	500	400-1200	0.107	2	0.009-0.25	JSR
		500	673-1423	0.127	0.1, 0.25	0.1, 0.25	FR1
		500	400-1200	0.107	2	0.25	FR2
H ₂ S+CH ₄	Oxidation	H ₂ S: 500 CH ₄ : 20,000	650-1200	0.107	2	0.5,1, 2	JSR
Study of the NO_x formation							
N ₂	Oxidation	791,000	1373-2073	0.120	0.04	3.78	FR1
CH ₄		1,000	1050-2073	0.120	0.04	0.01	
C ₂ H ₄		500	973-1473	0.123	0.04	0.5, 1, 2	
Study of the oxidation of bio-oil surrogates							
Pyrrole	Pyrolysis	10,000	950-1200	0.107	2	∞	JSR
	Oxidation		700-1200			0.5,1, 2	
EG	Pyrolysis		650-1100			∞	
	Oxidation		600-1100			0.5,1, 2	
PG	Pyrolysis		650-1100			∞	
	Oxidation		600-1200			1	

a) Performances of the analytical techniques

This thesis aims at developing an experimental database for low to high temperature reactions during biogas and bio-oil combustion, with specific monitoring of the formation of reaction products and intermediates, in order to:

- ✓ better understand the chemical reactions involved,
- ✓ develop and validate detailed kinetic models capable of reproducing the combustion of fuels.

The low-temperature oxidation (< 1200 K) of the fuel surrogates was carried out in a JSR, working with homogeneous temperature and composition and at steady state (except for a few conditions for which transient behavior was observed). Where the high-temperature (< 2000 K) oxidation was investigated in a FR, the temperature profile along the tube needs to be considered for the simulations dedicated to the development of kinetic models. The species leaving the reactor were analyzed using four different complementary analytical techniques, making it possible both to check the consistency of the results and to detect a wider range of compounds:

- ✓ Gas chromatography: separation method allowing the analysis of a wide range of compounds, especially those containing carbon atoms when the detector is a flame ionization one.
- ✓ NO_x analyzer: specific method allowing the analysis of NO_x species such as NO and NO₂, based on chemiluminescence.
- ✓ Online mass spectrometry: analytical technique used to measure the mass-to-charge ratio of ions.
- ✓ Fourier-transform Infrared spectroscopy: technique used to measure how much light a sample absorbs at each wavelength over a given range, mainly used to detect HCN, NO_x, H₂O and CO₂.

The mole fraction profiles of many species could be compared between the different analytical techniques and testify to the good reproducibility of the results. One of the analytical techniques used to detect the heavy species is gas chromatography coupled to a quadrupole mass spectrometer (GC-MS) with liquid automatic sampler; this was used in case of vapor condensation during the oxidation of bio-oil, but required an additional step in the analytical methodology: the trapping of the gas at the outlet of the reactor at liquid nitrogen temperature.

However, each analytical technique has certain limitations to its use. There are superimposed signals of molecules, which have the same molecular weight when using MS, and MS cannot be used during the oxidation of bio-oils due to too many products formed. Moreover, isomer molecules can often not be separated by using GC, but this problem can be solved by using two-dimensional gas chromatography (2D-GC). This is a type of multidimensional gas chromatography; the compounds are separated in a two-dimensional space and characterized by two retention times, one for each dimension (thanks the use of two columns). In addition, this device was installed in my lab at the end of my PhD, and this technique will be used further to detect more species during oxidation studies. As already mentioned, the C atom balances for the oxidation of EG and PG are not quite good (<50%), likely because of species not detected, so this technique will help to improve the balance of C atoms. It is also difficult to quantify H₂O because of its low volatility, in particular during the oxidation of bio-oil. MS cannot partly solve this problem even if water desorption can still cause perturbations; it will be good if we can have some other robust techniques to routinely detect water.

b) Study of the oxidation of biogas components

This thesis allowed studying the oxidation of numerous components of biogas and surrogates of bio-oils. The chemistry of ammonia was first studied with the case of the oxidation of neat ammonia, methane doped with ammonia, and ammonia co-firing with H₂. Then, the oxidation of neat H₂S and of methane doped with H₂S were investigated. Some pyrolysis experiments have also been performed to better understand the gas phase chemistry of these systems. During this work, the formation of NO_x at high temperatures during ethylene and methane oxidation in air was also investigated. However, the experiments about the oxidation of ammonia and hydrogen sulfide were the trickiest to carry out. These mixtures have the peculiarity of easily adsorbing at the walls, requiring performing multiple tests, as well as taking specific precautions to obtain reliable data.

The study of the pyrolysis and oxidation of neat ammonia in the FR1 at very high temperatures provides a better understanding of the chemical reactions involved. Although current models are relatively efficient in predicting the reactivity of ammonia and their main stable products during oxidation, but less for ammonia pyrolysis. The

equivalence ratio has also an important influence on the oxidation reactivity; the poor mixture favors reactions with oxygen, leading to an accelerated ammonia reactivity. A new field of investigations could consist in highlighting the effect of the pressure on the gas-phase kinetics of ammonia as kinetic constants of many reactions are far from the high-pressure limit around the atmospheric pressure.

In order to assess the influence of the presence of methane and hydrogen on ammonia, the oxidation of ammonia doped with H₂ or CH₄ was studied using the FR1. [Figure 107](#) compares NH₃ reactivity for three different mixtures: neat NH₃, NH₃/CH₄ mixture and NH₃/H₂ mixture. As shown in [Figure 107](#), the presence of methane almost does not affect NH₃ reactivity onset (~1450-1500K). On the other hand, NH₃ promotes methane reactivity at low temperature with a major role played by NO. It affects methane oxidation increasing the temperature of the reactivity onset by up to ~100 K, especially in the leanest conditions in JSR. The presence of H₂ on ammonia favors the reactivity of ammonia and the temperature of its reactivity onset is shifted to ~1100 K. The addition of H₂ also enhances the NO formation, the more H₂ addition, the more NO production.

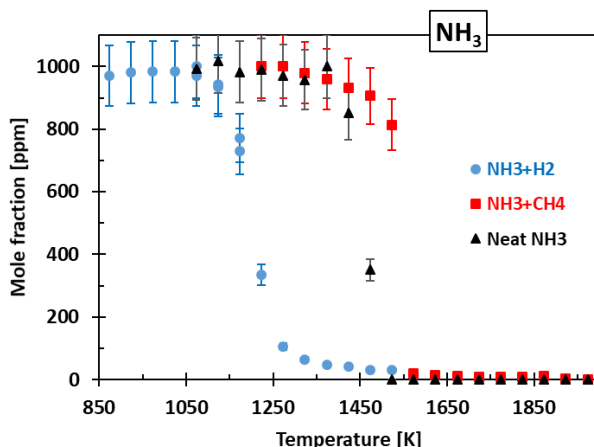


Figure 107: Effect of addition of 1000 ppm H₂ and CH₄ to the oxidation of 1000 ppm NH₃ in FR. Symbols: experiments.

The oxidation of neat hydrogen sulfide in the three different reactors was studied in order to explore H₂S reactivity at lower temperatures and higher residence times and vice versa. Several tests were made with coated and non-coated reactors to highlight possible catalytic effects. The comparison between the experimental results and computed data is generally quite satisfactory but less for H₂ profiles. The influence of H₂S addition on methane oxidation in JSR was studied to better

understand the interaction between these two fuels. The results show that H₂S addition very little affects methane reactivity, but it rather enhances the production of ethane.

90% of my thesis relates to the experimental study. Even though I not so much study the modeling part, but I can clearly see how experiments and kinetic modeling are dependent on each other. Without kinetic model, it is hard to identify and point out the inconsistencies in the experiments (catalytic effects for example). Contrariwise, without experiment, it is impossible to test and validate the theory of kinetic chemistry.

c) Study of the formation of NO_x

The study of the formation of NO is receiving attention because of its toxic effects as atmospheric pollutants generated from the combustion of fossil fuels. The kinetic mechanisms for reactions involving nitrogen compounds have been extensively studied. To my knowledge, the experiments of the formation of thermal NO were performed only in flame. Therefore, the experiment carried out during my thesis will be the first experiments using the flow reactor at high temperature (up to 2073 K).

The study of the formation of NO was performed under 0.12 MPa, 1350-2073 K, in FR1 using three different fuels; N₂, methane and ethylene. Two different experiments of the oxidation of N₂ (without and with 1% of H₂O in the feed) were carried out to better understand the effect of water on the formation of thermal NO. NO was detected by the online mass spectrometry. No influence of H₂O on the formation of NO was observed. NO formation during these two experiments has the same maximum of ~120 ppm at 2073 K, whereas the simulation over-predicted the formation of NO by a factor of 3 (340 ppm) in case of the presence of 1% of H₂O. The thermal NO was formed ~100 ppm during the oxidation of methane in air, whereas no prompt NO was observed because of too low amount of methane in the feed (0.1%). However, the formation of prompt NO was noticed during the oxidation of ethylene (0.05%) but only in the case of fuel-rich and stoichiometric conditions. These experiments need to be repeated to better observe CO and NO formation by using the GC-Methanizer and the NO_x analyzer, respectively.

d) Study of the oxidation of bio-oil surrogates

The pyrolysis and oxidation of pyrrole in JSR allowed validating the pyrrole kinetic mechanism in the CRECK kinetic framework, showing general good agreement

but less for the hydrocarbons. The significant formation of unsaturated hydrocarbons poses some concerns about the use of bio-oil, which leads not only to the formation of nitrogen oxides, but also to the formation of PAHs and particles.

The pyrolysis and the oxidation of 1% ethylene glycol were experimentally and modelling using the kinetic model of Kathrotia et al. (2017). The comparison between the experimental results and computed data showed a good agreement for the fuel reactivity but less for the products, some reactions are likely still missing in the model (probably some molecular pathways). In addition, due to the condensation problem, some products could not be detected by our analytical techniques, which is why the carbon atom balance is not as good (<50%) as usual. In the literature, there are few experimental and kinetic studies about this molecule; therefore, more investigations with various devices are probably needed to obtain a complete picture of the gas phase chemistry of this type of species. Moreover, the lack of information on the ethenol chemistry is likely responsible of the overestimation of acetaldehyde.

An experimental study about propylene glycol was performed to compare its reactivity with that of EG. The structures of these two molecules are quite simple but in fact, their chemistry appeared to be much more complicated than it could be expected. To my knowledge, this PG experimental work is the first one reported in the literature. The development of a kinetic model will require a much deeper investigation of the specific chemistry involved in the gas phase kinetics of PG using advanced quantum mechanics calculations to explore potential energy surfaces of these specific systems.

e) Perspectives

General perspectives

Bio-oils have been considered as promising fuels to replace fossil fuels due to their convenience in storage or transport compared to gaseous products and their lower formation of NO_x and SO_x compared to petroleum-based fuel. However, bio-oils have a very complicated composition containing many different compounds and must be upgraded prior to use due to their high viscosity, high oxygen content, high corrosiveness, and flame instability due to their high water content. Moreover, the heating values of bio-oils are only about half that of petroleum-based heating oil by weight. Co-firing of natural gas and bio-oils could be the option to minimize the issues

with bio-oil combustion, especially for flame quality. However, this application may be difficult for the industry due to the handling requirements for both gaseous and liquid fuels.

Biogas is also one of the renewable energy solutions, also known as renewable natural gas. It is renewable in the sense that humans and animals will keep producing wastes which is the source of biogas. Biogas allows removing the abundant supply of food waste from the environment and prevents methane emissions, nitrogen pollution and runoff into water resources. However, Biogas production is affected by weather conditions. The optimum temperature for the bacteria necessary for the digestion of waste is around 37°C. In cold climates, digesters need thermal energy to maintain a constant supply of biogas. Moreover, due to its NH₃ and H₂S content, biogas poses some concerns about higher NO_x and SO_x emissions than natural gas.

Biogas can be upgraded to biomethane by removing CO₂ and other contaminants present in the biogas, which can solve the problem of NO_x and SO_x emissions. In addition, biomethane can provide as much heat of combustion as natural gas (PCI of around 36 MJ/m³). Therefore, biomethane is a better option than biogas to replace natural gas. However, the high production costs are still an obstacle for the industries. The price of biomethane is around € 90 / MWh (IEA, 2017), which is around 4 times higher than that of natural gas production (~ 23 € / MWh).

Co-firing ammonia and hydrogen plays an important role in the decarbonization of the energy sector. However, the more the H₂ percentage increases, the more NO_x emissions increase. Moreover, hydrogen production today is almost entirely from natural gas and coal, which means that the production of H₂ promotes the emission of CO₂.

Electrification has received recent interest as a low-carbon emission technology, especially for mobility and industry. However, electric vehicle technology faces many challenges; lack of charging station and the current high cost. Moreover, electrification has its limits for the industrial processes, as many processes require high temperatures (above 1273 K), making it difficult to replace fuels. In the future, the development of the low-carbon technologies dependent on many factors regarding infrastructure, technology development, and political framework conditions. However,

to meet the climate targets, alternative fuels should be studied and developed in parallel.

Scientific perspectives

A next challenge in the experimental study of biofuels is investigate a mixture of more than two species as a more realistic surrogate of a real biofuel. This has rarely been performed up to now due to the limitations in analytical techniques. Advanced analytical techniques should enable the identification and quantification of the numerous expected intermediates formed from a multi-component mixture. Studying mixtures will highlight possible interactions between species, as it is the case in actual processes using conventional fuels and biofuels.

The difficulty during my PhD was to deal with the catalytic effect on the reactor wall. We know some methods to prevent this problem by coating the reactor wall, however we cannot be fully sure for the efficiency of coating, even if a significant reactivity shift was observed after applying the coating procedure. As already discussed above, after using the coated FR1 for the oxidation of H_2S , the experimental results of the oxidation of NH_3/H_2 were odd, which mean that coating is not efficient for a long-term use and that the reactor use history can have an impact on the reliability of the data recorded after. It would be better if we can investigate what happen inside the reactor wall by using the theoretical knowledge and by finding an experimental methodology proving that there is no wall effect occurrence.

The agreement of experimental and computed data obtained during the oxidation and pyrolysis of NH_3 is quite satisfying, even if improvements can still be made. As an example, it would be better if the shift of 100 K between experimental and simulation data during NH_3 pyrolysis could be justified and resolved. The overall agreement of experimental and computed data obtained during the oxidation of NH_3 is also good but the formation and consumption pathways of NO need to be improved (problem of overestimation by the model).

H_2S model reproduces well the experimental results obtained during the oxidation of H_2S , but H_2 formation was overestimated especially when using JSR. H_2 was detected by the online-MS, to improve these profiles; the GC-Carbosphere can be used to confirm the experimental data. There is not only the problem of catalytic wall effect when performing experiments with H_2S , this toxic reactant can also cause

problems for the analysis techniques, such as the GC-Methaniser (H_2S can damage the nickel catalyst in the methaniser). Some other techniques could be envisaged to detect these species with better accuracy. As an example SO_2 could be detected using specific tools based on light absorption or electrochemical cells as in safety detectors. Nevertheless, it must be checked that these detectors are really specific to the species to be detected and not sensitive to other species.

The difference of NO profiles between the experimental and simulated data during the study of the NO formation needs to be solved, especially in the presence of water. This could be due to a third body effect in some sensitive reactions (the collision efficiency factor is the largest for water, but the value used in models could be uncertain). In a more general way, these collision efficiency factors have been rarely measured and some measurements would likely benefit to the refinement of models. During the oxidation of N_2 and CH_4 , NO was detected by the online-MS. There might be the interference signals of NO using the MS. Repeating this experiment by using the NO_x analyzer might help improving the results. With the low amount of CH_4 in feed during the oxidation, it cannot shed light on the formation of prompt NO. Increasing the amount of methane or working under the very fuel-rich condition might help point out the formation of prompt NO_x .

As shown in [chapter VI](#), C_2H_2 and other unsaturated hydrocarbons are produced in large quantities during the oxidation of pyrrole, EG and PG, posing some concerns about the fact that using bio-oil leads to, not only the nitrogen oxides formation, but also to particulate matter formation. Moreover, due to their high viscosity, the experiments with bio-oils were not easy to carry out: the foaming and clogging of the evaporator happened several times. In addition, atom balances were not closed showing that some species were likely not detected. Thus, new sampling techniques should be proposed to detect a maximum of intermediates during gas phase kinetic studies. As an example, a more direct sampling strategy and analysis (e.g., sampling cone creating a molecular beam with mass spectrometry analysis (Fristrom, 1975; Hsu and Tung, 1992; Horn et al., 2006; Benedikt et al., 2009)) could be used instead of a heated transfer line. The trapping at liquid nitrogen temperature with further injection under liquid state is also an option, which is already used, and which could be improved. But the sample needs to be processed before being injecting

and this technique is therefore less direct than a sampling of the gas phase through a molecular beam.

To finish with perspectives, all data recorded during this study were at quasi atmospheric pressures. These studies should be repeated at higher pressures, especially for small systems as ammonia and hydrogen sulfide given that many reaction kinetic constants are far from their high pressure limits. Indeed, whatever the process of energy conversion used (e.g., internal combustion engines, gas turbines), it is likely that the operating pressure will be far above the atmosphere (< 10 atm) for thermodynamic efficiency purposes. The improvements of these energy conversion processes will require the development of detailed kinetic models well accounting for the pressure effect.

VIII. COMMUNICATIONS AND PUBLICATIONS DURING THE THESIS

a) Publications in peer reviewed journals

- ✓ Stagni, A., Cavallotti, C., Arunthanayothin, S., Song, Y., Herbinet, O., Battin-Leclerc, F., & Faravelli, T. (2020). An experimental, theoretical and kinetic-modeling study of the gas-phase oxidation of ammonia. *Reaction Chemistry & Engineering* (5), 696-711.
- ✓ Arunthanayothin, S., Stagni, A., Song, Y., Herbinet, O., Faravelli, T., & Battin-Leclerc, F. (2020). Ammonia–methane interaction in jet-stirred and flow reactors: An experimental and kinetic modeling study. *Proceedings of the Combustion Institute* (38), 345-353.
- ✓ Pelucchi, M., Arunthanayothin, S., Song, Y., Herbinet, O., Stagni, A., Carstensen, H-H., Faravelli, T., Battin-Leclerc, F., 2021. Pyrolysis and Combustion Chemistry of Pyrrole, a Reference Component for Bio-oil Surrogates: Jet-Stirred Reactor Experiments and Kinetic Modeling. *Energy & Fuels* 35 (9), 7265-7284.

b) Publication in congress proceeding

- ✓ Stagni, A., Arunthanayothin, Y., Herbinet, O., Battin-Leclerc, F., & Faravelli, T. (2021). An experimental and kinetic-modeling study of H₂S combustion in ideal reactors, was submitted to the 10th European Combustion Meeting (ECM 2021)

c) Oral communications

- ✓ Arunthanayothin, S., Song, Y., Herbinet, O., Battin-Leclerc, An experimental study of the gas-phase oxidation of ammonia. **“Workshop on combustion kinetics with to Tohoku University”**, Nancy (France), 29 September 2019.
- ✓ Stagni, A., Arunthanayothin, Y., Herbinet, O., Battin-Leclerc, F., & Faravelli, T. (2020). Experimental study and modeling of the kinetics of the oxidation of H₂S in a jet-stirred reactor and in flow reactors. **Conference “Les journées François LACAS”**, videoconference, 19 January 2021.
- ✓ Arunthanayothin, S., Stagni, A., Song, Y., Herbinet, O., Faravelli, T., & Battin-Leclerc, F. (2020). Ammonia–methane interaction in jet-stirred and flow reactors: An experimental and kinetic modeling study. **Symposium: “38th**

International Symposium on Combustion», videoconference, 24-29 January 2021.

d) Poster communications

- ✓ Arunthanayothin, S., Song, Y., Herbinet, O., Battin-Leclerc, An experimental study of the gas-phase oxidation of ammonia. **2nd Quadmarts Network Workshop**, Nancy (France), 20-22 May 2019.
- ✓ Stagni, A., Cavallotti, C., Arunthanayothin, S., Song, Y., Herbinet, O., Battin-Leclerc, F., & Faravelli, T. Ammonia–methane interaction in jet-stirred and flow reactors: An experimental and kinetic modeling study. **Conference: “Fuels, Processes, and Combustion Physics in the Energy Transformation”**, Bad Honnef (Germany), 8-12 March 2020.

IX. REFERENCES

- Abdel-Shafy, H.I., Mansour, M.S.M., 2016.** A review on polycyclic aromatic hydrocarbons: Source, environmental impact, effect on human health and remediation. *Egyptian Journal of Petroleum* 25, 7-123. <https://doi.org/10.1016/j.ejpe.2015.03.011>
- Alzueta, M. U., Guerrero, M., Millera, Á., Marshall, P., Glarborg, P., 2021.** Experimental and kinetic modeling study of oxidation of acetonitrile. *Proc. Combust. Inst.* 38 (1), 575-583. <https://doi.org/10.1016/j.proci.2020.07.043>
- Appels, L., Baeyens, J., Degreève, J., Dewil, R., 2008.** Principles and potential of the anaerobic digestion of waste-activated sludge. *Progress in Energy and Combustion Science* 34, 755– 781. <https://doi.org/10.1016/j.pecs.2008.06.002>
- Arunthanayothin, S., Stagni, A., Song, Y., Herbinet, O., Faravelli, T., & Battin-Leclerc, F., 2020.** Ammonia–methane interaction in jet-stirred and flow reactors: An experimental and kinetic modeling study. *Proceedings of the Combustion Institute* 38, 345-353. <https://doi.org/10.1016/j.proci.2020.07.061>
- Aung K.T., Hassan M.I., Faeth G.M., 1997.** Flame stretch interactions of laminar premixed hydrogen/air flames at normal temperature and pressure. *Combust Flame* 109, 1-24.
- Azargohar, R., Jacobson, K.L., Powell, E.E., Dalai, A.K., 2013.** Evaluation of properties of fast pyrolysis products obtained, from Canadian waste biomass. *J. Anal. Appl. Pyrolysis* 104, 330–340. <https://doi.org/10.1016/j.jaap.2013.06.016>
- Bagheri, G., Ranzi, E., Pelucchi, M., Parente, A., Frassoldati, A., Faravelli, T., 2020.** Comprehensive kinetic study of combustion technologies for low environmental impact: MILD and OXY-fuel combustion of methane. *Combust. Flame*, 212, 142–155. <https://doi.org/10.1016/j.combustflame.2019.10.014>
- Barbas, M., Costa, M., Vranckx, S., Fernandes, R., 2015.** Experimental and kinetic modeling study of CO and NO formation under oxy-fuel conditions. Presented at the Proceedings of the 8th World Conference on Experimental Heat Transfer, Fluid Mechanics and Thermodynamics, pp. 16–20.
- Basu, P., 2018.** Chapter 12: Production of Synthetic Fuels and Chemicals from Biomass. *Biomass Gasification. Pyrolysis and Torrefaction (Third Edition)*, 415-443. <https://doi.org/10.1016/B978-0-12-812992-0.00012-1>
- Belley, R., Bernard, N., Côté, M., Paquet, F., Poitras J., 2005.** Hyperbaric oxygen therapy in the management of two cases of hydrogen sulfide toxicity from liquid manure. *CJEM*. 7(4):257-61.
- Benedikt, J., Ellerweg, D., von Keudell, A., 2009.** Molecular beam sampling system with very high beam-to-background ratio: The rotating skimmer concept. *Review of Scientific Instruments*, 80(5), 055107. <https://doi.org/10.1063/1.3133804>
- Benés, M., Pozo, G., Abián, M., Millera, Á., Bilbao, R., & Alzueta, M. U., 2021.** Experimental Study of the Pyrolysis of NH₃ under Flow Reactor Conditions. *Energy & Fuels*, 35(9), 7193–7200. <https://doi.org/10.1021/acs.energyfuels.0c03387>

- Berg, P. A.,** Smith, G. P., Jeffries, J. B., & Crosley, D. R., **1998.** Nitric oxide formation and reburn in low-pressure methane flames. *Symposium (International) on Combustion*, 27(1), 1377–1384. [https://doi.org/10.1016/S0082-0784\(98\)80543-2](https://doi.org/10.1016/S0082-0784(98)80543-2)
- Bingchen, Z., 2007.** Chemical reaction engineering. (in Chinese) 4rd ed. Beijing: Chemical Industry Press
- Bongartz, D. and Ghoniem, A.F., 2015.** Chemical kinetics mechanism for oxy-fuel combustion of mixtures of hydrogen sulfide and methane. *Combustion and Flame*, 162(3), 544–553. <https://doi.org/10.1016/j.combustflame.2014.08.019>
- Bridgwater, A.V.,** Czernik, S., Piskorz, J., **2001.** An overview of fast pyrolysis. In: Bridgwater, A.V. (Ed.), *Progress in Thermochemical Biomass Conversion*. Blackwell Science, 977–997.
- Brook, J.R.,** Dann, T.F., Burnett, R.T., **1997.** The relationship among TSP, PM10, PM2.5, and inorganic constituents of atmospheric particulate matter at multiple Canadian locations. *J Air Waste Manag Assoc* 47, 2–19. <https://doi.org/10.1080/10473289.1997.10464407>
- Burcat, A. and Ruscic, B., 2005.** Third Millennium Ideal Gas and Condensed Phase Thermochemical Database for Combustion (with Update from Active Thermochemical Tables); Argonne National Laboratory (ANL): Argonne, IL, ANL-05/20, <https://doi.org/10.2172/925269>
- Burke, S. M.,** Burke, U., Mc Donagh, R., Mathieu, O., Osorio, I., Keesee, C., Morones, A., Petersen, E. L., Wang, W., DeVerter, T. A., Oehlschlaeger, M. A., Rhodes, B., Hanson, R. K., Davidson, D. F., Weber, B. W., Sung, C.-J., Santner, J., Ju, Y., Haas, F. M., Dryer, F. L., Volkov, E. N., Nilsson, E. J.K., Konnov, A. A., Alrefae, M., Khaled, F., Farooq, A., Dirrenberger, P., Glaude, P.-A., Battin-Leclerc, F.; Curran, H. J., **2015.** An experimental and modeling study of propene oxidation. Part 2: Ignition delay time and flame speed measurements, *Combustion and Flame* 162 (2), 296-314. <https://doi.org/10.1016/j.combustflame.2014.07.032>.
- Cavallotti, C.,** Pelucchi, M., Georgievskii, Y., Klippenstein, S.J., **2019.** EStokTP: Electronic Structure to Temperature- and Pressure-Dependent Rate Constants- A Code for Automatically Predicting the Thermal Kinetics of Reactions. *J Chem Theory Comput* 15, 1122–45.
- Cedigaz, (2019).** Global Biomethane Market: Green Gas Goes Global, www.cedigaz.org/global-biomethane-market-green-gas-goes-global/.
- CERFACS, 2020.** From IMPROOF Project: <https://improof.cerfacs.fr>
- Chen, X.,** Fuller, M. E., Goldsmith, C. F., **2018.** Decomposition Kinetics for HONO and HNO₂. *Reaction Chemistry & Engineering*. <https://doi.org/10.1039/C8RE00201K>
- Chin, H.S.,** Karan, K., Mehrotra, A.K., Behie, L.A., **2001.** The fate of methane in a Claus plant reaction furnace. *The Canadian Journal of Chemical Engineering* 79, 482–490.

- Clavin, P., 1985.** Dynamic behavior of premixed flame fronts in laminar and turbulent flows. *Progress in Energy and Combustion Science* 11, 1–59. [https://doi.org/10.1016/0360-1285\(85\)90012-7](https://doi.org/10.1016/0360-1285(85)90012-7)
- Colom-Díaz, J. M., Abián, M., Ballester, M. Y., Millera, Á., Bilbao, R., Alzueta, M. U., 2019b.** H₂S conversion in a tubular flow reactor: Experiments and kinetic modeling. *Proceedings of the Combustion Institute*, 37, 727-734. <https://doi.org/10.1016/j.proci.2018.05.005>
- Colom-Díaz, J. M., Abian, M., Millera, Á., Bilbao, R., Alzueta, M. U., 2019b.** Influence of pressure on H₂S oxidation. Experiments and kinetic modeling. *Fuel*, 258, 116145. <https://doi.org/10.1016/j.fuel.2019.116145>
- Colom-Díaz, J. M., Leciñena, M., Peláez, A., Abián, M., Millera, Á., Bilbao, R., & Alzueta, M. U., 2020.** Study of the conversion of CH₄/H₂S mixtures at different pressures. *Fuel*, 262, 116484. <https://doi.org/10.1016/j.fuel.2019.116484>
- Colom-Díaz, J. M., Alzueta, M. U., Zeng, Z., Altarawneh M., Dlugogorski, B.Z., 2021.** Oxidation of H₂S and CH₃SH in a jet-stirred reactor: Experiments and kinetic modeling. *Fuel* 283. <https://doi.org/10.1016/j.fuel.2020.119258>
- Dahoe, A.E., K. Hanjalic, K., B. Scarlett, B., 2002.** Determination of the laminar burning velocity and the Markstein length of powder–air flames. *Powder Technology* 122, 222-238. [https://doi.org/10.1016/S0032-5910\(01\)00419-3](https://doi.org/10.1016/S0032-5910(01)00419-3)
- Dahoe, A.E., 2005.** Laminar burning velocities of hydrogen–air mixtures from closed vessel gas explosions. *Journal of Loss Prevention in the Process Industries*, 18(3), 152–166. <https://doi.org/10.1016/j.jlp.2005.03.007>
- Dai, L., Gersen, S., Glarborg, P., Levinsky, H., Mokhov, A., 2020.** Experimental and numerical analysis of the autoignition behavior of NH₃ and NH₃/H₂ mixtures at high pressure, *Combustion and Flame* 215, 134-144. <https://doi.org/10.1016/j.combustflame.2020.01.023>
- Davidson, D. F., Kohse-Höinghaus, K., Chang, A. Y., Hanson, R. K., 1990.** A pyrolysis mechanism for ammonia. *International Journal of Chemical Kinetics*, 22(5), 513–535. <https://doi.org/10.1002/kin.550220508>
- Dean A.M. and Bozzelli J.W., 2000.** *Combustion Chemistry of Nitrogen*. In: Gardiner W.C. (eds) *Gas-Phase Combustion Chemistry*. Springer, New York, NY. https://doi.org/10.1007/978-1-4612-1310-9_2
- De Persis, S., Pillier, L., Idir, M., Molet, J., Lamoureux, N., & Desgroux, P., 2019.** NO formation in high pressure premixed flames: Experimental results and validation of a new revised reaction mechanism. *Fuel*, 260, 116331. <https://doi.org/10.1016/j.fuel.2019.116331>
- DigitalRefining, 2006.** Refinery CO₂ challenges. <https://www.digitalrefining.com>
- Dirrenberger, P., Le Gall, H., Bounaceur, R., Herbinet, O., Glaude, P.A., Konnov, A., Battin-Leclerc, F., 2011.** Measurements of Laminar Flame Velocity for Components of Natural Gas. *Energy & Fuels* 25 (9), 3875-3884. <https://doi.org.bases-doc.univ-lorraine.fr/10.1021/ef200707h>

- DOE EIA., 2012.** Crude oil distillation and the definition of refinery capacity.
- Doughty, A. and Mackie, J. C., 1992.** Kinetics of pyrolysis of the isomeric butenenitriles and kinetic modeling. *J. Phys. Chem.* , 96 (1), 272–281. <https://doi.org/10.1021/j100180a052>
- Doujaji, B. and Al-Tawfiq, J.A., 2010.** Hydrogen sulfide exposure in an adult male. *Ann Saudi Med* 30(1): 76-80. DOI:10.4103/0256-4947.59379.
- Dyakov, I.V., Konnov, A.A., De Ruyck, J., Bosschaart, K.J., Brock, E.C.M., de Goey, L.P.H., 2001.** Measurement of adiabatic burning velocity in methane-oxygen-nitrogen mixtures. *Combust. Sci. Technol.*, 172, 81.
- Egerton, S.A., Warren, D.R., 1951.** Kinetics of the hydrogen/oxygen reaction. The explosion region in boric acid-coated vessels. *Proc. R. Soc. London. Ser. A* 204, 465–476. <https://doi.org/10.1098/rspa.1951.0003>
- Ensys Energy, 2016.** Supplemental Marine Fuel Availability Study. MARPOL Annex VI Global Sulphur Cap Supply-Demand Assessment, Final Report, 15 July 2016. https://globalmaritimehub.com/wpcontent/uploads/attach_786.pdf
- European Commission, 2019.** Report from the Commission to the European parliament, the council, the European economic and social committee and the committee of the regions, Renewable Energy Progress Report.
- Fagernäs, L., 1995.** Chemical and physical characterization of biomass-based pyrolysis oils: Literature review. Technical Research Centre of Finland Espoo.
- Faravelli, T., Frassoldati, A., Ranzi, E., 2003.** Kinetic modeling of the interactions between NO and hydrocarbons in the oxidation of hydrocarbons at low temperatures, *Combustion and Flame*, 132 (1–2), 188-207. [https://doi.org/10.1016/S0010-2180\(02\)00437-6](https://doi.org/10.1016/S0010-2180(02)00437-6).
- Fedyeva, O. N., Artamonov, D. O., & Vostrikov, A. A., 2019.** Heterogeneous–homogeneous oxidation of pyrrole in water vapor at elevated pressure. *Combustion and Flame*, 210, 183-192. <https://doi.org/10.1016/j.combustflame.2019.08.029>
- Fenimore, C.P., 1971.** Formation of nitric oxide in premixed hydrocarbon flames, *Symposium (International) on Combustion* 13 (1), 373-380, [https://doi.org/10.1016/S0082-0784\(71\)80040-1](https://doi.org/10.1016/S0082-0784(71)80040-1).
- Fernando, N., Braun-Unkhoff, M., & Riedel, U., 2019.** Modeling Study of the Entrained Flow Gasification of Ethylene Glycol, a Surrogate Fuel for a Pyrolysis Oil. *Energy & Fuels*, 33(10), 9818-9827.
- Flockenhaus, C., 1969.** Rates of flame propagation of hydrogen sulphide/air mixtures. *Gaswaerme International*, vol. 18, no. 4.
- Frassoldati, A., Faravelli, T., Ranzi, E., 2003.** Kinetic modeling of the interactions between NO and hydrocarbons at high temperature. *Combustion and Flame*, 135(1-2), 97–112. [https://doi.org/10.1016/S0010-2180\(03\)00152-4](https://doi.org/10.1016/S0010-2180(03)00152-4)

- Frenklach, M.,** Lee, J.H., White, J.N. Gardiner, W.C., **1981.** Oxidation of hydrogen sulfide, *Combustion and Flame* 41, 1-16. [https://doi.org/10.1016/0010-2180\(81\)90035-3](https://doi.org/10.1016/0010-2180(81)90035-3)
- Engineeringtoolbox,** **2020.** Fuels-Higher and Lower Calorific Values. https://www.engineeringtoolbox.com/fuels-higher-calorific-values-d_169.html
- Garland, N.L.,** **1998.** Temperature dependence of the reaction: SO+ O₂. *Chem Phys Lett* 1998;290:385–90.
- Garo, A.,** Hilaire, C., Puechberty, D., **1992.** Experimental Study of Methane-Oxygen Flames Doped with Nitrogen Oxide or Ammonia. Comparison with Modeling. *Combustion Science and Technology* 86, 87–103. <https://doi.org/10.1080/00102209208947189>
- Gasnot, L.,** Desgroux, P., Pauwels, J., Sochet, L., **1999.** Detailed analysis of low-pressure premixed flames of CH₄ + O₂ + N₂: a study of prompt-NO. *Combustion and Flame*, 117(1-2), 291–306. [https://doi.org/10.1016/S0010-2180\(98\)00078-9](https://doi.org/10.1016/S0010-2180(98)00078-9)
- Gersen, S.,** van Essen, M., Darneveil, H., Hashemi, H., Rasmussen, C.T., Christensen, J.M., Glarborg, P., Levinsky, H., **2017.** Experimental and Modeling Investigation of the Effect of H₂S Addition to Methane on the Ignition and Oxidation at High Pressures. *Energy & Fuels*.
- Glarborg, P.,** Miller, J. A., Ruscic, B., Klippenstein, S. J., **2018.** Modeling nitrogen chemistry in combustion. *Progress in Energy and Combustion Science*, 67, 31–68. <https://doi.org/10.1016/j.pecs.2018.01.002>
- Goldmann, A., Dinkelacker, F.,** **2018.** Approximation of laminar flame characteristics on premixed ammonia/hydrogen/nitrogen/air mixtures at elevated temperatures and pressures, *Fuel* 224, 366-378. <https://doi.org/10.1016/j.fuel.2018.03.030>
- Grcar, J.F.,** Glarborg, P., Bell, J.B., Day, M.S., Loren, A., Jensen, A.D., **2005.** Effects of mixing on ammonia oxidation in combustion environments at intermediate temperatures. *Proceedings of the Combustion Institute* 30, 1193–1200.
- Han, X.,** Wang, Z., Costa, M., Sun, Z., He, Y., Cen, K., **2019.** Experimental and kinetic modeling study of laminar burning velocities of NH₃/air, NH₃/H₂/air, NH₃/CO/air and NH₃/CH₄/air premixed flames. *Combustion and Flame* 206, 214-226. <https://doi.org/10.1016/j.combustflame.2019.05.003>
- Han, X.,** Wang, Z., He, Y., Liu, Zhu, Y., Konnov, A.A., **2020.** The temperature dependence of the laminar burning velocity and superadiabatic flame temperature phenomenon for NH₃/air flames. *Combustion and Flame* 217, 314-320. <https://doi.org/10.1016/j.combustflame.2020.04.013>
- Haworth, N. L.,** Mackie, J. C., Bacskay, G. B., **2003.** An Ab Initio Quantum Chemical and Kinetic Study of the NNH + O Reaction Potential Energy Surface: How Important Is This Route to NO in Combustion? *The Journal of Physical Chemistry A*, 107(35), 6792–6803. <https://doi.org/10.1021/jp034421p>
- Hayakawa, A.,** Goto, T., Mimoto, R., Arakawa, Y., Kudo, T., Kobayashi, H., **2015.** Laminar burning velocity and Markstein length of ammonia/air premixed flames

- at various pressures, Fuel 159, 98–106.
<https://doi.org/10.1016/j.fuel.2015.06.070>
- Hayhurst, A. N. and Vince, I. M., 1977.** Production of “prompt” nitric oxide and decomposition of hydrocarbons in flames. *Nature*, 266(5602), 524–525.
<https://doi.org/10.1038/266524a0>
- He, X., Shu, B., Nascimento, D., Moshammer, K., Costa, M., Fernandes, R.X., 2019.** Auto-ignition kinetics of ammonia and ammonia/hydrogen mixtures at intermediate temperatures and high pressures, *Combustion and Flame* 206, 2019, 189-200. <https://doi.org/10.1016/j.combustflame.2019.04.050>
- Heard, D. E., Jeffries, J. B., Smith, G. P., & Crosley, D. R. 1992.** LIF measurements in methane/air flames of radicals important in prompt-NO formation. *Combustion and Flame*, 88(2), 137–148. [https://doi.org/10.1016/0010-2180\(92\)90048-T](https://doi.org/10.1016/0010-2180(92)90048-T)
- Herbinet, O., Dayma, G., 2013.** Jet-stirred reactors, *Clean. Combust.* Springer, London, 183–210. https://doi.org/10.1007/978-1-4471-5307-8_8
- Herbinet, O., Battin-Leclerc, F., 2014.** Progress in understanding low-temperature organic compound oxidation using a jet-stirred reactor, *Int. J. Chem. Kinet.* 46, 619–639. <https://doi.org/10.1002/kin.20871>
- Henshaw, P.F., D’Andrea, T., Mann, K.R.C., Ting, D.S.K., 2005.** Premixed ammonia-methane-air combustion. *Combustion Science and Technology* 177, 2151–2170.
<https://doi.org/10.1080/00102200500240695>
- Hong, X., Zhang, L., Zhang, T., Qi, F., 2009.** An Experimental and Theoretical Study of Pyrrole Pyrolysis with Tunable Synchrotron VUV Photoionization and Molecular-Beam Mass Spectrometry. *J. Phys. Chem. A* 113, 5397–5405.
<https://doi.org/10.1021/jp9002966>
- Horn, R., Ihmann, K., Ihmann, J., Jentoft, F. C., Geske, M., Taha, A., ... Schlögl, R., 2006.** Molecular beam mass spectrometer equipped with a catalytic wall reactor for in situ studies in high temperature catalysis research. *Review of Scientific Instruments*, 77(5), 054102. <https://doi.org/10.1063/1.2200872>
- Howard, C.J., 1980.** Kinetic study of the equilibrium $\text{HO}_2 + \text{NO}$. *Journal of the American Chemical Society* 102, 6937-6941.
- Howstuffworks, 2020.** How will population growth affect energy?
<https://science.howstuffworks.com/environmental/energy/population-growth-affect-energy.htm>
- Hsu, W. L., and Tung, D. M., 1992.** Application of molecular beam mass spectrometry to chemical vapor deposition studies. *Review of Scientific Instruments*, 63(9), 4138–4148. <https://doi.org/10.1063/1.1143225>
- Hughes, K.J., Tomlin, A.S., Dupont, V.A., Pourkashanian, M., 2002.** Experimental and modelling study of sulfur and nitrogen doped premixed methane flames at low pressure. *Faraday discussions* 119, 337–352.

- Ichikawa, A.,** Hayakawa, A., Kitagawa, Y., Somarathne, K.D. K. A., Kudo, T., Kobayashi, H., **2015**. Laminar burning velocity and Markstein length of ammonia/hydrogen/air premixed flames at elevated pressures, *International Journal of Hydrogen Energy* 40, 9570-9578. <https://doi.org/10.1016/j.ijhydene.2015.04.024>
- IEA, 2017**. World Energy Outlook (WEO) 2017
- IEA, 2019a**. WEO 2019-Presentation <https://www.iea.org/media/presentations/>
- IEA, 2019b**. CO₂ Emissions from Fuel Combustion 2019 Edition
- IPCC, 2019**. Climate change and land. Geneva (Switzerland): Intergovernmental panel on climate change (IPCC).
- Flockenhaus, C., 1969**. Rates of flame propagation of hydrogen sulphide/air mixtures, *Gaswaerme International* 18 (4).
- Fristrom, R. M., 1975**. Flame sampling for mass spectrometry. *International Journal of Mass Spectrometry and Ion Physics*, 16(1-2), 15–32. [https://doi.org/10.1016/0020-7381\(75\)85011-X](https://doi.org/10.1016/0020-7381(75)85011-X)
- Jabbour, T., Clodic, D.F., 2004**. Burning velocity and refrigerant flammability classification, *ashrae transactions*, Atlanta 110 522–533.
- Jerzak, W.,** Kuźnia, M., Szajding, A., **2016**. Experimental Studies and the Chemical Kinetics Modelling of Oxidation of Hydrogen Sulfide Contained in Biogas. *Procedia Engineering* 157, 222–229. <https://doi.org/10.1016/j.proeng.2016.08.360>
- JRC, 2017**. Supply chain of renewable energy technologies in Europe.
- Karan, K.,** Mehrotra, A. K., Behie, L. A., **1999**. On reaction kinetics for the thermal decomposition of hydrogen sulfide. *AIChE Journal*, 45(2), 383–389. <https://doi.org/10.1002/aic.690450217>
- Kathrotia, T.,** Naumann, C., Oßwald, P., Köhler, M., & Riedel, U., **2017**. Kinetics of Ethylene Glycol: The first validated reaction scheme and first measurements of ignition delay times and speciation data. *Combustion and Flame*, 179, 172-184. <https://doi.org/10.1016/j.combustflame.2017.01.018>
- Kéromnès, A.,** Metcalfe, W. K., Heufer, K. A., Donohoe, N., Das, A. K., Sung, C.-J., Herzler, J., Naumann, C., Griebel, P., Mathieu, O., Krejci, M. C., Petersen, E. L., Pitz, W. J., Curran, H. J., **2013**. An experimental and detailed chemical kinetic modeling study of hydrogen and syngas mixture oxidation at elevated pressures. *Combust. Flame*, 160 (6), 995–1011. <https://doi.org/10.1016/j.combustflame.2013.01.001>
- Klassen, M. S.,** THOMSEN, D. D., REISEL, J. R., & LAURENDEAU, N. M., **1995**. Laser-Induced Fluorescence Measurements of Nitric Oxide Formation in High-Pressure Premixed Methane Flames. *Combustion Science and Technology*, 110-111(1), 229–247. <https://doi.org/10.1080/00102209508951925>
- Klippenstein, S. J.,** Harding, L. B., Ruscic, B., Sivaramakrishnan, R., Srinivasan, N. K., Su, M.-C., Michael, J. V., **2009**. Thermal Decomposition of NH₂OH and

- Subsequent Reactions: Ab Initio Transition State Theory and Reflected Shock Tube Experiments. *The Journal of Physical Chemistry A*, 113(38), 10241–10259. <https://doi.org/10.1021/jp905454k>
- Kobayashi, H.**, Hayakawa, A., Somarathne, K.D. K.A., Okafor, E.C., **2019**. Science and technology of ammonia combustion, *Proc. Combust. Inst.* 37, 109–133.
- Konnov, A.A.**, Dyakov, I.V., De Ruyck, J., **2006**. Probe sampling measurements of NO in CH₄+O₂+N₂ flames doped with NH₃. *Combustion Science and Technology* 178, 1143–1164. <https://doi.org/10.1080/00102200500296788>
- Kumar, P. and Meyer, T.R.**, **2013**. Experimental and modeling study of chemical-kinetics mechanisms for H₂–NH₃–air mixtures in laminar premixed jet flames, *Fuel* 108, 166–176. <https://doi.org/10.1016/j.fuel.2012.06.103>
- Lamoureux, N.**, Merhubi, H. E., Pillier, L., de Persis, S., Desgroux, P., **2016**. Modeling of NO formation in low pressure premixed flames. *Combustion and Flame*, 163, 557–575. <https://doi.org/10.1016/j.combustflame.2015.11.007>
- Lamoureux, N.**, El-Bakali, A., Gasnot, L., Pauwels, J. F., & Desgroux, P., **2008**. Prompt-NO formation in methane/oxygen/nitrogen flames seeded with oxygenated volatile organic compounds: Methyl ethyl ketone or ethyl acetate. *Combustion and Flame*, 153(1-2), 186–201. <https://doi.org/10.1016/j.combustflame.2007.07.011>
- Lamoureux, N.**, Desgroux, P., El Bakali, A., Pauwels, J. F., **2010**. Experimental and numerical study of the role of NCN in prompt-NO formation in low-pressure CH₄–O₂–N₂ and C₂H₂–O₂–N₂ flames. *Combustion and Flame*, 157(10), 1929–1941. <https://doi.org/10.1016/j.combustflame.2010.03.013>
- Lee, J.H.**, Lee, S.I., Kwon, O.C., **2010**. Effects of ammonia substitution on hydrogen/air flame propagation and emissions, *International Journal of Hydrogen Energy* 35, 11332–11341. <https://doi.org/10.1016/j.ijhydene.2010.07.104>
- Lee, J.H.**, Kim, J.H., Park, J.H., Kwon, O.C., **2010**. Studies on properties of laminar premixed hydrogen-added ammonia/air flames for hydrogen production, *International Journal of Hydrogen Energy* 35, 1054–1064. <https://doi.org/10.1016/j.ijhydene.2009.11.071>
- Levenspiel, O.**, **1999**. Chemical reaction engineering, in: *Chemical Reaction Engineering*. John Wiley & Sons. Inc, New York, pp. 293–320
- Lhuillier, C.**, Brequigny, P., Lamoureux, N., Contino, F., Mounaïm-Rousselle, C., **2020**. Experimental investigation on laminar burning velocities of ammonia/hydrogen/air mixtures at elevated temperatures, *Fuel* 263, 116653. <https://doi.org/10.1016/j.fuel.2019.116653>
- Lhuillier, C.**, Brequigny, P., Contino, F., & Mounaïm-Rousselle, C., **2021**. Experimental investigation on ammonia combustion behavior in a spark-ignition engine by means of laminar and turbulent expanding flames. *Proceedings of the Combustion Institute*. <https://doi.org/10.1016/j.proci.2020.08.058>

- Li, B., He, Y., Li, Z., Konnov, A.A., 2013.** Measurements of NO concentration in NH₃ doped CH₄ + air flames using saturated laser-induced fluorescence and probe sampling. *Combustion and Flame* 160, 40–46. <https://doi.org/10.1016/j.combustflame.2012.10.003>
- Li, J., Huang, H., Kobayashi, N., He, Z., Nagai, Y., 2014.** Study on using hydrogen and ammonia as fuels: Combustion characteristics and NO_x formation, *International Journal of Energy Research* 38, 1214-1223. <https://doi.org/10.1002/er.3141>
- Li, X. Q., Brown, D. G., Zhang, W. X., 2007.** Stabilization of biosolids with nanoscale zero-valent iron (nZVI), *Journal of Nanoparticle Research* 9 (2), 233–243.
- Li, Y., Guo, Q., Dai, Z., Dong, Y., Yu, G., Wang, F., 2017.** Study of oxidation for gas mixture of H₂S and CH₄ in a non-premixed flame under oxygen deficient condition. *Applied Thermal Engineering* 117, 659–667. <https://doi.org/10.1016/j.applthermaleng.2016.10.168>
- Lifshitz, A., Tamburu, C., Suslensky, A., 1989.** Isomerization and decomposition of pyrrole at elevated temperatures: studies with a single-pulse shock tube. *J. Phys. Chem.* 93, 5802–5808. <https://doi.org/10.1021/j100352a030>
- Lindsey, R. and Dahlman, L., 2020.** Climate Change: Global Temperature [online]. Available at: <https://www.climate.gov/news-features/understanding-climate> [Accessed 15 August 2021]
- Lu, C-W., Wu, Y-J., Lee, Y-P., Zhu, R.S., Lin, M-C., 2003.** Experiments and calculations on rate coefficients for pyrolysis of SO₂ and the reaction O+ SO at high temperatures. *J Phys Chem A* 107, 11020–9.
- Lubrano Lavadera, M., Song, Y., Sabia, P., Herbinet, O., Pelucchi, M., Stagni, A., Faravelli, T., Battin-Leclerc, F, de Joannon, M., 2018.** Oscillatory Behavior in Methane Combustion: Influence of the Operating Parameters. *Energy & Fuels*. <https://doi.org/10.1021/acs.energyfuels.8b00967>
- Lumbreras, M., ALZUETA, M.U., MILLERA, A., BILBAO, R., 2001.** A Study of Pyrrole Oxidation Under Flow Reactor Conditions. *Combustion Science and Technology* 172, 123–139. <https://doi.org/10.1080/00102200108945397>
- Ma, S., Zhang, L., Zhu, L., Zhu, X., 2018.** Preparation of multipurpose bio-oil from rice husk by pyrolysis and fractional condensation. *J Anal Appl Pyrolysis*;131:113–9.
- Mackie, J., Colket, M., Nelson, P., Esler, M., 1991.** Shock-Tube Pyrolysis of Pyrrole and Kinetic Modeling. *Int. J. Chem. Kinet.* 23, 733–760. <https://doi.org/10.1002/kin.550230807>
- MacNamara, J.P., Simmie, J.M., 2003.** The high temperature oxidation of pyrrole and pyridine; ignition delay times measured behind reflected shock waves. *Combustion and Flame* 133, 231–239. [https://doi.org/10.1016/S0010-2180\(03\)00002-6](https://doi.org/10.1016/S0010-2180(03)00002-6)
- Manna, M.V., Sabia, P., Ragucci, R., Joannon, M., 2020.** Oxidation and pyrolysis of ammonia mixtures in model reactors, *Fuel* 264, 0016-2361, <https://doi.org/10.1016/j.fuel.2019.116768>

- Manna, M. V.,** Sabia, P., Ragucci, R., & de Joannon, M., **2021.** Ammonia oxidation regimes and transitional behaviors in a Jet Stirred Flow Reactor. *Combustion and Flame*, 228, 388–400. <https://doi.org/10.1016/j.combustflame.2021.02.014>
- Marrodán, L.,** Song, Y., Herbinet, O., Alzueta, M.U., Fittschen, C., Ju, Y., Battin-Leclerc, F., **2019.** First detection of a key intermediate in the oxidation of fuel+NO systems: HONO. *Chemical Physics Letters* 719, 22-26. <https://doi.org/10.1016/j.cplett.2019.01.038>
- Martoprawiro, M.,** Bacskay, G. B., Mackie, J. C., **1999.** Ab initio quantum chemical and kinetic modeling study of the pyrolysis kinetics of pyrrole. *J. Phys. Chem. A* 103 (20), 3923–3934.
- Mathieu, O.,** Petersen, E.L., **2015.** Experimental and modeling study on the high-temperature oxidation of Ammonia and related NOx chemistry, *Combustion and Flame* 162, 554-570, <https://doi.org/10.1016/j.combustflame.2014.08.022>
- Mathieu, O.,** Mulvihill, C., Petersen, E. L., **2017.** Shock-tube water time-histories and ignition delay time measurements for H₂S near atmospheric pressure. *Proceedings of the Combustion Institute*, 36(3), 4019–4027. <https://doi.org/10.1016/j.proci.2016.06.027>
- Mei, B.,** Zhang, X., Ma, S., Cui, M., Guo, H., Cao, Z., Li, Y., **2019.** Experimental and kinetic modeling investigation on the laminar flame propagation of ammonia under oxygen enrichment and elevated pressure conditions. *Combustion and Flame* 210, 236-246. <https://doi.org/10.1016/j.combustflame.2019.08.033>
- Mendiara, T. and Glarborg, P.,** **2009.** Ammonia chemistry in oxy-fuel combustion of methane, *Combustion and Flame* 156, 1937-1949. <https://doi.org/10.1016/j.combustflame.2009.07.006>
- Metcalf, W. K.,** Burke, S. M., Ahmed, S. S., & Curran, H. J., **2013.** A Hierarchical and Comparative Kinetic Modeling Study of C1– C2 Hydrocarbon and Oxygenated Fuels. *International Journal of Chemical Kinetics*, 45(10), 638–675. <https://doi.org/10.1002/kin.20802>
- Minowa, T.,** Murakami, M., Dote, Y., Ogi, T., Yokoyama, S., **1995.** Oil production from garbage by thermochemical liquefaction. *Biomass and Bioenergy* 8(2), 117–20.
- Moskaleva, L. V. and Lin, M. C.,** **2000.** The spin-conserved reaction CH+N₂→H+NCN: A major pathway to prompt no studied by quantum/statistical theory calculations and kinetic modeling of rate constant. *Proceedings of the Combustion Institute*, 28(2), 2393–2401. [https://doi.org/10.1016/S0082-0784\(00\)80652-9](https://doi.org/10.1016/S0082-0784(00)80652-9)
- Mulvihill, C. R.,** Keese, C. L., Sikes, T., Teixeira, R. S., Mathieu, O., & Petersen, E. L., **2019.** Ignition delay times, laminar flame speeds, and species time-histories in the H₂S/CH₄ system at atmospheric pressure. *Proceedings of the Combustion Institute*, 37(1), 735-742 <https://doi.org/10.1016/j.proci.2018.06.034>
- Namysl, S.,** **2019.** Experimental study of the formation of pollutants during the combustion of bio-oil surrogate molecules. Doctoral thesis, University of Lorraine. www.theses.fr

- Namysl, S.**, Pelucchi, M., Herbinet, O., Frassoldati, A., Faravelli, T., Battin-Leclerc, F., **2019**. A first evaluation of butanoic and pentanoic acid oxidation kinetics. *Chemical Engineering Journal* 373, 973-984. <https://doi.org/10.1016/j.cej.2019.05.090>
- Namysl, S.**, Pelucchi, M., Maffei, L.P., Herbinet, O., Stagni, A., Faravelli, T., Battin-Leclerc, F., **2020**. Experimental and modeling study of benzaldehyde oxidation. *Combustion and Flame* 211, 124-132. <https://doi.org/10.1016/j.combustflame.2019.09.024>
- NIST Chemistry WebBook**, **2020**. SRD 69, Thermophysical Properties of Fluid Systems, National Institute of Standard and Technology. <https://webbook.nist.gov/chemistry/fluid/>
- NRDC**, **2016**. Natural Resources Defense Council: Global warming 101. <https://www.nrdc.org/stories/global-warming-101>
- Okafor, E.C.**, Naito, Y., Colson, S., Ichikawa, A., Kudo, T., Hayakawa, A., Kobayashi, H., **2018**. Experimental and numerical study of the laminar burning velocity of CH₄-NH₃-air premixed flames, *Combustion and Flame* 187, 185-198. <https://doi.org/10.1016/j.combustflame.2017.09.002>
- Okafor, E.C.**, Somarathne, K.D. K.A., Ratthan, R., Hayakawa, A., Kudo, T., Kurata, O., Iki, N., Tsujimura, T., Furutani, H., Kobayashi, H., **2020**. Control of NO_x and other emissions in micro gas turbine combustors fuelled with mixtures of methane and ammonia, *Combustion and Flame* 211, 406-416, <https://doi.org/10.1016/j.combustflame.2019.10.012>
- Pahl, R.**, Holtappels, K., **2005**. Explosions Limits of H₂S/CO₂/Air and H₂S/N₂/Air. *Chemical Engineering Technology* 28, 746-749, <https://doi.org/10.1002/ceat.200500066>
- Pelucchi, M.**, Namysl, S., Ranzi, E., Frassoldati, A., Herbinet, O., Battin-Leclerc, F., Faravelli, T., **2019a**. An experimental and kinetic modelling study of n-C₄C₆ aldehydes oxidation in a jet-stirred reactor. *Proceedings of the Combustion Institute* 37, 389-397. <https://doi.org/10.1016/j.proci.2018.07.087>
- Pelucchi, M.**, Cavallotti, C., Cuoci, A., Faravelli, T., Frassoldati, A., & Ranzi, E., **2019b**. Detailed kinetics of substituted phenolic species in pyrolysis bio-oils. *Reaction Chemistry & Engineering*. <https://doi.org/10.1039/C8RE00198G>
- Pelucchi, M.**, Arunthanayothin, S., Song, Y., Herbinet, O., Stagni, A., Carstensen, H.-H., Faravelli, T., Battin-Leclerc, F., **2021**. Pyrolysis and Combustion Chemistry of Pyrrole, a Reference Component for Bio-oil Surrogates: Jet-Stirred Reactor Experiments and Kinetic Modeling. *Energy & Fuels* 35 (9), 7265-7284. <https://doi.org/10.1021/acs.energyfuels.0c03874>
- Pfahl, U.J.**, Ross, M.C, Shepherd, J.E., Pasamehmetoglu, K.O., Unal, C., **2000**. Flammability limits, ignition energy, and flame speeds in H₂-CH₄-NH₃-N₂O₂-N₂ mixtures, *Combustion and Flame* 123, 140-158. [https://doi.org/10.1016/S0010-2180\(00\)00152-8](https://doi.org/10.1016/S0010-2180(00)00152-8)
- Pillier, L.**, El Bakali, A., Mercier, X., Rida, A., Pauwels, J.-F., & Desgroux, P., **2005**. Influence of C₂ and C₃ compounds of natural gas on NO formation: an

- experimental study based on LIF/CRDS coupling. Proceedings of the Combustion Institute, 30(1), 1183–1191. <https://doi.org/10.1016/j.proci.2004.08.057>
- Pochet, M.,** Dias, V., Moreau, B., Foucher, F., Jeanmart, H., Contino, F., **2019.** Experimental and numerical study, under LTC conditions, of ammonia ignition delay with and without hydrogen addition. Proceedings of the Combustion Institute, 37(1), 621-629. <https://doi.org/10.1016/j.proci.2018.05.138>
- Rachel-Tang, D. Y.,** Islam, A., Taufiq-Yap, Y. H. , **2017.** Bio-oil production via catalytic solvolysis of biomass. RSC Advances 7 (13), 7820–7830. <https://doi.org/10.1039/C6RA27824H>
- Rahinov, I.,** Goldman, A., Cheskis, S., **2006.** Absorption spectroscopy diagnostics of amidogen in ammonia-doped methane/air flames. Combustion and Flame 145, 105–116. <https://doi.org/10.1016/j.combustflame.2005.11.004>
- Ranzi, E.,** Dente, M., Goldaniga, A., Bozzano, G., Faravelli, T., **2001.** Lumping procedures in detailed kinetic modeling of gasification, pyrolysis, partial oxidation and combustion of hydrocarbon mixtures. Progress in Energy and Combustion Science 27 (1), 99-139, [https://doi.org/10.1016/S0360-1285\(00\)00013-7](https://doi.org/10.1016/S0360-1285(00)00013-7)
- Ranzi, E.,** Frassoldati, A., Grana, R., Cuoci, A., Faravelli, T., Kelley, A. P., & Law, C. K., **2012.** Hierarchical and comparative kinetic modeling of laminar flame speeds of hydrocarbon and oxygenated fuels. Progress in Energy and Combustion Science, 38(4), 468–501. <https://doi.org/10.1016/j.pecs.2012.03.004>
- Ranzi, E.,** Frassoldati, A., Stagni, A., Pelucchi, M., Cuoci, A., Faravelli, T., **2014.** Reduced kinetic schemes of complex reaction systems: Fossil and biomass-derived transportation fuels. Int. J. Chem. Kinet. 46 (9), 512–542.
- Reiter, A.J., Kong, S.C., 2011.** Combustion and emissions characteristics of compression-ignition engine using dual ammonia-diesel fuel, Fuel 90, 87–97.
- Ronney, P.D., 1988.** Effect of Chemistry and Transport Properties on Near-Limit Flames at Microgravity, Combustion Science and Technology, 59:1-3, 123-141, <https://doi.org/10.1080/00102208808947092>
- Ross, A.B.,** Biller, P., Kubacki, M.L., Li, H., Lea-langton, A., Jones, J.M., **2010.** Hydrothermal processing of microalgae using alkali and organic acids. Fuel, 89(9): 2234–43.
- RTE-france, 2021.** CO₂ Emissions per kWh of Electricity Generated in France. <https://www.rte-france.com/en/eco2mix/co2-emissions>
- Sabia, P., & de Joannon, M., 2020.** On H₂–O₂ oxidation in several bath gases. International Journal of Hydrogen Energy. <https://doi.org/10.1016/j.ijhydene.2020.01.134>.
- Sabia, P.,** Lubrano Lavadera, M., Giudicianni, P., Sorrentino, G., Ragucci, R., & de Joannon, M., **2015.** CO₂ and H₂O effect on propane auto-ignition delay times under mild combustion operative conditions. Combustion and Flame, 162(3), 533–543. <https://doi.org/10.1016/j.combustflame.2014.08.009>

- Sabia, P.**, Manna, M. V., Ragucci, R., & de Joannon, M., **2020**. Mutual inhibition effect of hydrogen and ammonia in oxidation processes and the role of ammonia as “strong” collider in third-molecular reactions. *International Journal of Hydrogen Energy*. <https://doi.org/10.1016/j.ijhydene.2020.08.218>
- Selim, H.**, Al Shoaibi, A., Gupta, A.K., **2011**. Effect of H₂S in methane/air flames on sulfur chemistry and products speciation. *Applied Energy* 88, 2593–2600. <https://doi.org/10.1016/j.apenergy.2011.02.032>
- Selim, H.**, Al Shoaibi, A., Gupta, A., **2012**. Fate of sulfur with H₂S injection in methane/air flames. *Applied energy* 92, 57–64.
- Sendt, K. and Haynes, B.S.**, **2007**. Quantum chemical and RRKM calculations of reactions in the H/S/O system. *Proc Combust Inst* 31, 257–65.
- Shiina, H.**, Oya, M., Yamashita, K., Miyoshi, A., Matsui, H., **1996**. Kinetic studies on the pyrolysis of H₂S. *J Phys Chem* 100, 2136–40.
- Shope, R.**, **1991**. Global climate change and infectious diseases. *Environmental Health Perspectives*, 96, 171-174.
- Song, Y.**, Hashemi, H., Munkholt Christensen, J., Zou, C., Marshall, P., Glarborg, P., **2016**. Ammonia oxidation at high pressure and intermediate temperatures, *Fuel* 181, 358-365, <https://doi.org/10.1016/j.fuel.2016.04.100>
- Song, Y.**, Hashemi, H., Christensen, J. M., Zou, C., Haynes, B. S., Marshall, P., & Glarborg, P., **2017**. An Exploratory Flow Reactor Study of H₂S Oxidation at 30-100 Bar. *International Journal of Chemical Kinetics*, 49(1), 37–52. <https://doi.org/10.1002/kin.21055>
- Song, Y.**, Marrodán, L., Vin, N., Herbinet, O., Assaf, E., Fittschen, C., Stagni, A., Faravelli, T., Alzueta, M., Battin-Leclerc, F., **2019**. The sensitizing effects of NO₂ and NO on methane low temperature oxidation in a jet stirred reactor. *Proc. Combust. Inst.* 37 (1), 667–675. <https://doi.org/10.1016/j.proci.2018.06.115>
- Stagni, A.**, Cavallotti, C., Arunthanayothin, S., Song, Y., Herbinet, O., Battin-Leclerc, F., Faravelli, T., **2020a**. An experimental, theoretical and kinetic-modeling study of the gas-phase oxidation of ammonia. *Reaction Chemistry & Engineering*, 5, 696-711. <https://doi.org/10.1039%2FC9RE00429G>
- Stagni, A.**, Song, Y., Vandewalle, L. A., Van Geem, K. M., Marin, G. B., Herbinet, O., Battin-Leclerc, F., Faravelli, T., **2020b**. The role of chemistry in the oscillating combustion of hydrocarbons: an experimental and theoretical study. *Chemical Engineering Journal*, 123401. <https://doi.org/10.1016/j.cej.2019.123401>
- Sullivan, N.**, Jensen, A., Glarborg, P., Day, M.S., Grcar, J.F., Bell, J.B., Pope, C.J., Kee, R.J., **2002**. Ammonia conversion and NO_x formation in laminar coflowing nonpremixed methane-air flames. *Combustion and Flame* 131, 285–298. [https://doi.org/10.1016/S0010-2180\(02\)00413-3](https://doi.org/10.1016/S0010-2180(02)00413-3)
- Takizawa, K.**, Takahashi, A., Tokuhashi, K., Kondo, S., Sekiya, A., **2008**. Burning velocity measurements of nitrogen-containing compounds, *J. Hazard. Mater.* 155, 144–152. <https://doi.org/10.1016/j.jhazmat.2007.11.089>

- Tian, Z.,** Li, Y., Zhang, T., Zhu, A., Cui, Z., & Qi, F., **2007**. An experimental study of low-pressure premixed pyrrole/oxygen/argon flames with tunable synchrotron photoionization. *Combustion and flame*, 151(1-2), 347-365. <https://doi.org/10.1016/j.combustflame.2007.06.008>
- Tian, Z.,** Li, Y., Zhang, L., Glarborg, P., Qi, F., **2009**. An experimental and kinetic modeling study of premixed NH₃/CH₄/O₂/Ar flames at low pressure. *Combustion and Flame* 156, 1413–1426. <https://doi.org/10.1016/j.combustflame.2009.03.005>
- United Nation, 2019**. Department of Economic and Social Affairs, Population Division, 2020. World Population Prospects 2019: Highlights.
- Verplanken, B.,** Marks, E., Dobromir, A. I., **2020**. On the nature of eco-anxiety: How constructive or unconstructive is habitual worry about global warming? *Journal of Environmental Psychology*, 101528. <https://doi.org/10.1016/j.jenvp.2020.101528>
- Villermaux, J., 1993**. Génie de la réaction chimique, in: Génie de La Réaction Chimique. Tec&Doc, Paris, pp. 190193. <https://www.techniques-ingenieur.fr/base-documentaire/procedes-chimie-bio-agro-th2/reacteurs-chimiques-42330210/reacteurs-chimiques-j4010/>.
- Vin, N., 2019**. Kinetic study of the gas phase pyrolysis of organic molecules containing heteroatoms representative of toxic compounds present in polluted soils. Doctoral thesis, University of Lorraine. www.theses.fr
- Wang, C.,** Zhang, G., Wang, Z., Li, Q.S., Zhang, Y., **2005**. Direct ab initio dynamics study of the hydrogen abstraction reaction: H₂S+ O → HS+ OH. *J Mol Struct THEOCHEM* 731, 187–92.
- Wang, C.A.,** Du, Y.B., Jin, X., Che, D.F., **2016**. Pyridine and pyrrole oxidation under oxy-fuel conditions. *Energy Sources Part a-Recovery Utilization and Environmental Effects* 38, 975–981. <https://doi.org/10.1080/15567036.2013.824521>
- Watson, G. M. G.,** Versailles, P., Bergthorson, J. M., **2016**. NO formation in premixed flames of C₁–C₃ alkanes and alcohols. *Combustion and Flame*, 169, 242–260. <https://doi.org/10.1016/j.combustflame.2016.04.015>
- Watson, G. M. G.,** Versailles, P., & Bergthorson, J. M., **2017**. NO formation in rich premixed flames of C₁–C₄ alkanes and alcohols. *Proceedings of the Combustion Institute*, 36(1), 627–635. <https://doi.org/10.1016/j.proci.2016.06.108>
- Williams, B. A. and Fleming, J. W., 1994**. Comparative species concentrations in CH₄/O₂/Ar flames doped with N₂O, NO, and NO₂. *Combustion and Flame*, 98(1-2), 93–106. [https://doi.org/10.1016/0010-2180\(94\)90200-3](https://doi.org/10.1016/0010-2180(94)90200-3)
- Williams, B.A., Fleming, J.W., 1997**. Radical species profiles in low-pressure methane flames containing fuel nitrogen compounds. *Combustion and Flame* 110, 1–13. [https://doi.org/10.1016/S0010-2180\(97\)00063-1](https://doi.org/10.1016/S0010-2180(97)00063-1)

- Williams, B. A., & Fleming, J. W., 2007.** Experimental and modeling study of NO formation in 10torr methane and propane flames: Evidence for additional prompt-NO precursors. *Proceedings of the Combustion Institute*, 31(1), 1109–1117. <https://doi.org/10.1016/j.proci.2006.07.246>
- World Health Organization (Ed.), 2006.** Air quality guidelines: global update 2005: particulate matter, ozone, nitrogen dioxide, and sulfur dioxide. World Health Organization, Copenhagen, Denmark.
- Xiao, H., Valera-Medina, A., Bowen, P.J., 2017.** Study on premixed combustion characteristics of co-firing ammonia/methane fuels, *Energy* 140, 125–135.
- Xiu, S., Shahbazi, A., 2012.** Bio-oil production and upgrading research: A review. *Renewable and Sustainable Energy Reviews* 16, 4406–4414. <http://dx.doi.org/10.1016/j.rser.2012.04.028>
- Yamamoto, T., Kuwahara, T., Nakaso, K., Yamamoto, T., 2012.** Kinetic study of fuel NO formation from pyrrole type nitrogen. *Fuel* 93, 213–220. <https://doi.org/10.1016/j.fuel.2011.09.032>
- Yan, W. L., Herzing, A. A., Kiely, C. J., Zhang, W., 2010.** Nanoscale zero-valent iron (nZVI): aspects of the core-shell structure and reactions with inorganic species in water,” *Journal of Contaminant Hydrology* 118 (3-4), 96–104.
- Zakaznov, V.F., Kursheva, L.A. & Fedina, Z.I., 1988.** Determination of normal flame velocity and critical diameter of flame extinction in ammonia-air mixture. *Combust Explos Shock Waves* 14, 710–713. <https://doi.org/10.1007/BF00786097>
- Zeldovich, Y., 1946.** *Acta Physicochim.* URSS 21, 577.
- Zhou, C., Sendt, K., Haynes, B.S., 2009.** Computational study of the reaction SH + O₂. *J Phys Chem A* 113, 2975–81.
- Zhou C., 2009.** Kinetic study of the oxidation of hydrogen sulfide. University of Sydney; School of Chemical and Biomolecular Engineering.
- Zhou, C., Sendt, K., Haynes, B.S., 2013.** Experimental and kinetic modelling study of H₂S oxidation, *Proceedings of the Combustion Institute* 34, 625-632. <https://doi.org/10.1016/j.proci.2012.05.083>

X. APPENDIX

X.1 Example of a calculation sheet for the determination of the initial conditions

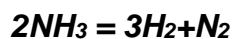
$$V_{FR1} = 3.77 \text{ cm}^3$$

T_{reactor} (K)	P (Pa)	τ (s)	Q (m ³ /s)	F (mol/s)	x_{N_2}	x_{O_2}	x_{CH_4}
1423.15	119990.132	0.04	9.43E-05	1.27E-03	0.79	0.209	0.001
1473.15	119990.132	0.04	9.43E-05	1.21E-03	0.79	0.209	0.001
1523.15	119990.132	0.04	9.43E-05	1.16E-03	0.79	0.209	0.001
1573.15	119990.132	0.04	9.43E-05	1.11E-03	0.79	0.209	0.001
1623.15	119990.132	0.04	9.43E-05	1.07E-03	0.79	0.209	0.001
1673.15	119990.132	0.04	9.43E-05	1.03E-03	0.79	0.209	0.001
1723.15	119990.132	0.04	9.43E-05	9.91E-04	0.79	0.209	0.001
1773.15	119990.132	0.04	9.43E-05	9.56E-04	0.79	0.209	0.001
1823.15	119990.132	0.04	9.43E-05	9.23E-04	0.79	0.209	0.001
1873.15	119990.132	0.04	9.43E-05	8.93E-04	0.79	0.209	0.001
1923.15	119990.132	0.04	9.43E-05	8.65E-04	0.79	0.209	0.001
1973.15	119990.132	0.04	9.43E-05	8.38E-04	0.79	0.209	0.001
2023.15	119990.132	0.04	9.43E-05	8.13E-04	0.79	0.209	0.001
2073.15	119990.132	0.04	9.43E-05	7.89E-04	0.79	0.209	0.001

T_{reactor} (K)	F_{N_2} (mol/s)	F_{O_2} (mol/s)	F_{CH_4} (mol/s)	True Q_{N_2} (n mL/min)	Set Point N_2 (n L/min)	True Q_{O_2} (n mL/min)	Set Point O_2 (n L/min)	Set Point CH_4 (n mL/min)
1423.15	7.56E-04	2.00E-04	9.56E-07	1016.11	1.43	268.48	0.39	1.30E+00
1473.15	7.30E-04	1.93E-04	9.23E-07	981.63	1.38	259.37	0.37	1.26E+00
1523.15	7.06E-04	1.87E-04	8.93E-07	949.40	1.34	250.85	0.36	1.22E+00
1573.15	6.84E-04	1.81E-04	8.65E-07	919.23	1.30	242.88	0.35	1.18E+00
1623.15	6.63E-04	1.75E-04	8.38E-07	890.91	1.26	235.40	0.34	1.14E+00
1673.15	6.43E-04	1.70E-04	8.13E-07	864.29	1.22	228.36	0.33	1.11E+00
1723.15	6.24E-04	1.65E-04	7.89E-07	839.21	1.18	221.74	0.32	1.08E+00
1773.15	6.07E-04	1.60E-04	7.67E-07	815.54	1.15	215.48	0.31	1.05E+00
1823.15	5.90E-04	1.56E-04	7.46E-07	793.18	1.12	209.58	0.30	1.02E+00
1873.15	5.74E-04	1.52E-04	7.26E-07	772.00	1.09	203.98	0.29	0.989
1923.15	5.59E-04	1.48E-04	7.07E-07	751.93	1.06	198.68	0.29	0.964
1973.15	5.45E-04	1.44E-04	6.89E-07	732.88	1.03	193.64	0.28	0.939
2023.15	5.32E-04	1.41E-04	6.72E-07	714.77	1.01	188.86	0.27	0.916
2073.15	5.19E-04	1.37E-04	6.56E-07	697.53	0.98	184.30	0.27	0.894

X.2 Experimental data of biogas components

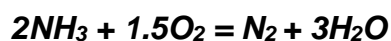
X.2.1 Pyrolysis of neat ammonia in the FR1



Reactor type	FR1
Temperature (K)	1373-1873
Pressure (Bar)	1.13
Residence time (s)	0.25
NH ₃ inlet mole fraction (ppm)	1000
Dilution gas	Helium
Data type	Mole fractions (ppm)

T (K)	NH ₃ (ppm)	N ₂ (ppm)	H ₂ (ppm)
1373	1.00E+03	0.00E+00	0.00E+00
1423	9.86E+02	2.50E+01	2.10E+01
1473	9.49E+02	7.10E+01	7.70E+01
1523	8.22E+02	7.70E+01	1.58E+02
1573	6.77E+02	1.46E+02	3.47E+02
1623	4.65E+02	2.59E+02	6.60E+02
1673	2.39E+02	3.84E+02	1.10E+03
1723	7.30E+01	4.68E+02	1.39E+03
1773	3.30E+01	4.81E+02	1.46E+03
1823	6.00E+00	4.95E+02	1.49E+03
1873	0.00E+00	5.00E+02	1.50E+03

X.2.2 Oxidation of neat ammonia



Set 1:

Reactor type	JSR
Temperature (K)	500-1200
Pressure (Bar)	1.07
Residence time (s)	1.5
NH ₃ inlet mole fraction (ppm)	500
O ₂ inlet mole fraction (ppm)	0, 0.02, 0.04
Dilution gas	Helium
Data type	Mole fractions (ppm)

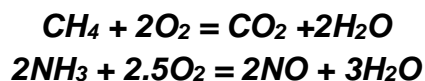
T (K)	NH ₃ (ppm)			NO (ppm)			NO ₂ (ppm)		
	0.02	0.04	0	0.02	0.04	0	0.02	0.04	0
x ⁱⁿ _{O₂}	0.02	0.04	0	0.02	0.04	0	0.02	0.04	0
500	5.04E+02	5.04E+02	5.08E+02						
525									
550									
575									
600	5.01E+02		5.08E+02						
625									
650									
675									
700	4.97E+02		5.02E+02						
725									
750	4.97E+02		4.97E+02						
775									
800	4.98E+02		5.03E+02						
825									
850									
875									
900	5.02E+02		5.05E+02		8.00E-01			0.00E+00	
925									
950	5.07E+02		5.08E+02	2.00E-01	1.10E+00		0.00E+00	0.00E+00	
975									
1000	4.95E+02	4.94E+02	4.98E+02	2.00E-01	1.30E+00		0.00E+00	0.00E+00	
1025		4.93E+02							
1050	4.91E+02	4.85E+02	4.94E+02		1.60E+00			0.00E+00	
1075		4.83E+02							
1100	4.93E+02	4.67E+02	4.98E+02	1.00E+00	4.10E+00		0.00E+00	0.00E+00	
1125				1.80E+00	4.50E+00		0.00E+00	0.00E+00	
1150	4.39E+02	3.93E+02	5.03E+02	1.80E+00	5.10E+00		0.00E+00	0.00E+00	
1175				2.30E+00			0.00E+00		
1200	2.74E+02	1.10E+02	4.97E+02	3.10E+00	5.30E+00		0.00E+00	0.00E+00	

Set 2:

Reactor type	FR1
Temperature (K)	1073-1973
Pressure (Bar)	1.27
Residence time (s)	0.05
NH ₃ inlet mole fraction (ppm)	1000
O ₂ inlet mole fraction (ppm)	2000
Dilution gas	Helium
Data type	Mole fractions (ppm)

T (K)	NH ₃ (ppm)	O ₂ (ppm)	NO (ppm)	N ₂ (ppm)	H ₂ O (ppm)	H ₂ (ppm)
1073	9.93E+02	1.97E+03	0.00E+00	2.00E+00	7.40E+01	0.00E+00
1123	1.02E+03	1.98E+03	0.00E+00	2.00E+00	4.50E+01	0.00E+00
1173	9.82E+02	1.97E+03	0.00E+00	2.00E+00	1.50E+01	0.00E+00
1223	9.89E+02	1.95E+03	1.00E+00	0.00E+00	9.00E+00	0.00E+00
1273	9.72E+02	2.00E+03	1.00E+00	3.00E+00	0.00E+00	0.00E+00
1323	9.58E+02	2.00E+03	1.00E+00	6.00E+00	3.00E+00	0.00E+00
1373	1.00E+03	1.93E+03	2.00E+00	1.80E+01	1.50E+01	0.00E+00
1423	8.53E+02	2.02E+03	2.00E+00	5.20E+01	8.60E+01	1.90E+01
1473	3.51E+02	1.57E+03	5.00E+00	1.71E+02	5.11E+02	5.30E+01
1523	0.00E+00	1.51E+03	1.60E+01	3.81E+02	8.64E+02	0.00E+00
1573	0.00E+00	1.22E+03	8.20E+01	4.76E+02	1.48E+03	0.00E+00
1623	0.00E+00	1.21E+03	1.08E+02	5.13E+02	1.50E+03	0.00E+00
1673	0.00E+00	1.19E+03	1.30E+02	4.51E+02	1.50E+03	0.00E+00
1723	0.00E+00	1.19E+03	1.51E+02	4.26E+02	1.63E+03	0.00E+00
1773	0.00E+00	1.17E+03	1.64E+02	4.18E+02	1.58E+03	0.00E+00
1823	0.00E+00	1.17E+03	1.78E+02	4.08E+02	1.50E+03	0.00E+00
1873	0.00E+00	1.16E+03	1.85E+02	4.05E+02	1.50E+03	0.00E+00
1923	0.00E+00	1.15E+03	1.88E+02	4.05E+02	1.50E+03	0.00E+00
1973	0.00E+00	1.16E+03	1.94E+02	4.00E+02	1.47E+03	0.00E+00

X.2.3 Oxidation of methane-ammonia



Set 1:

Reactor type	JSR
Temperature (K)	500-1200
Pressure (Bar)	1.07
Residence time (s)	1.5
CH ₄ inlet mole fraction (ppm)	1000
NH ₃ inlet mole fraction (ppm)	500
Equivalence ratio	0.5, 1 and 2
Dilution gas	Helium
Data type	Mole fractions (ppm)

T (K)	NH ₃ (ppm)			NO (ppm)			NO ₂ (ppm)		
	Phi=0.5	Phi=1	Phi=2	Phi=0.5	Phi=1	Phi=2	Phi=0.5	Phi=1	Phi=2
500	4.95E+02	5.01E+02	5.04E+02						
525									
550									
575									
600		4.95E+02							
625									
650									
675									
700		4.86E+02							
725									
750									
775									
800	4.89E+02	4.84E+02							
825									
850									
875									
900	4.92E+02	4.87E+02		7.00E-01	2.43E-01		0.00E+00		
925									
950	4.95E+02			9.47E-01			0.00E+00		
975	4.94E+02			1.03E+00			0.00E+00		
1000	4.85E+02	4.87E+02	4.91E+02	1.40E+00	5.33E-01		0.00E+00		
1025	5.54E+01			1.52E+01			4.40E+01		
1050	2.77E+01			1.68E+01			2.45E+01		
1075				1.87E+01			1.49E+01		
1100		4.75E+02	4.93E+02	2.00E+01	1.19E+00	4.73E-01	8.40E+00	1.30E+00	
1125				2.26E+01	1.96E+01	5.15E-01	5.30E+00	7.50E+00	
1150			4.89E+02	2.39E+01	1.68E+01	7.14E-01	3.50E+00	1.14E+01	
1175			4.97E+02	2.65E+01	1.96E+01	7.64E-01	2.60E+00	5.70E+00	1.36E+00
1200			4.15E+02	2.93E+01	1.72E+01	1.30E+00	2.10E+00	8.00E+00	2.51E+01

T (K)	CH ₄			CO			CO ₂		
	Phi=0.5	Phi=1	Phi=2	Phi=0.5	Phi=1	Phi=2	Phi=0.5	Phi=1	Phi=2
500	1.03E-02	1.03E-02	1.03E-02						
525									
550									
575									
600		1.04E-02							
625									
650									
675									
700		1.04E-02							
725									
750									
775									
800	1.03E-02	1.03E-02							
825									
850									
875									
900	1.03E-02	1.04E-02							
925									
950	1.02E-02								
975	1.02E-02								
1000	1.00E-02	1.04E-02	1.04E-02	7.06E-05			4.51E-06		
1025	1.48E-03	1.02E-02		2.77E-03	1.13E-05		5.48E-03	1.35E-05	
1050	1.14E-03	1.02E-02		1.72E-03	3.36E-05		7.15E-03	3.13E-06	
1075	9.45E-04	9.95E-03		1.06E-03	1.01E-04		8.04E-03	2.19E-05	
1100	8.46E-04	4.90E-03	1.02E-02	6.41E-04	4.15E-04	2.41E-05	8.67E-03	2.49E-05	
1125	7.25E-04			4.42E-04			8.94E-03		
1150	5.72E-04	3.97E-03	9.87E-03	3.82E-04	1.14E-03	1.32E-04	9.28E-03	3.40E-03	
1175	3.85E-04			3.53E-04			9.35E-03		
1200	1.17E-04	1.75E-03	4.27E-03	3.93E-04	8.35E-04	3.70E-03	9.65E-03	7.43E-03	7.49E-04

T (K)	C ₂ H ₄			C ₂ H ₆		
	Phi=0.5	Phi=1	Phi=2	Phi=0.5	Phi=1	Phi=2
500						
525						
550						
575						
600						
625						
650						
675						
700						
725						
750						
775						
800						
825						
850						
875						
900						
925						
950						
975						
1000	2.23E-05			1.48E-05		
1025	9.85E-05			3.19E-05		
1050	6.48E-05	9.34E-06		2.53E-05	2.60E-05	
1075	4.82E-05	6.09E-05		1.56E-05	5.64E-05	
1100	4.40E-05	2.58E-04		2.52E-05	1.22E-04	
1125	5.03E-05			2.41E-05		
1150	4.94E-05	5.87E-04	9.32E-05	2.35E-05	1.45E-04	6.50E-05
1175	5.82E-05			2.09E-05		
1200	3.47E-05	2.64E-04	1.11E-03	1.27E-06	6.82E-05	1.19E-04

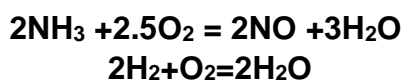
Set 2:

Reactor type	FR1
Temperature (K)	1223-1973
Pressure (Bar)	1.27
Residence time (s)	0.025
CH ₄ inlet mole fraction (ppm)	1000
NH ₃ inlet mole fraction (ppm)	1000
O ₂ inlet mole fraction (ppm)	3250 (phi = 1)
Dilution gas	Helium
Data type	Mole fractions (ppm)

T (K)	CH4 (ppm)	NH3 (ppm)	O2 (ppm)	NO (ppm)	NO2 (ppm)	N2 (ppm)	CO (ppm)	CO2 (ppm)	C2H4 (ppm)
1223	1.00E+03	1.00E+03	3.25E+03	1.00E+00	-1.00E+00	0.00E+00	0.00E+00	0.00E+00	0.00E+00
1273	9.87E+02	1.00E+03	3.25E+03	1.00E+00	-1.00E+00	0.00E+00	0.00E+00	0.00E+00	0.00E+00
1323	9.78E+02	9.79E+02	3.25E+03	2.00E+00	0.00E+00	0.00E+00	0.00E+00	0.00E+00	0.00E+00
1373	9.69E+02	9.59E+02	3.17E+03	4.00E+00	0.00E+00	0.00E+00	0.00E+00	0.00E+00	0.00E+00
1423	9.65E+02	9.32E+02	3.09E+03	7.00E+00	1.00E+00	6.00E+00	0.00E+00	0.00E+00	1.00E+00
1473	9.26E+02	9.06E+02	3.00E+03	1.00E+01	7.00E+00	3.00E+01	1.40E+01	0.00E+00	7.00E+00
1523	5.49E+02	8.14E+02	2.75E+03	1.40E+01	5.60E+01	1.04E+02	1.29E+02	1.30E+01	3.70E+01
1573	0.00E+00	1.90E+01	6.28E+02	2.14E+02	2.10E+01	2.99E+02	4.95E+02	4.56E+02	0.00E+00
1623	0.00E+00	1.40E+01	5.65E+02	2.24E+02	4.00E+00	3.90E+02	2.42E+02	6.94E+02	0.00E+00
1673	0.00E+00	1.20E+01	5.26E+02	2.36E+02	1.00E+00	3.80E+02	1.81E+02	7.81E+02	0.00E+00
1723	0.00E+00	9.00E+00	5.01E+02	2.37E+02	0.00E+00	3.89E+02	1.28E+02	8.43E+02	0.00E+00
1773	0.00E+00	1.00E+01	4.76E+02	2.34E+02	0.00E+00	3.93E+02	8.00E+01	9.04E+02	0.00E+00
1823	0.00E+00	8.00E+00	4.57E+02	2.37E+02	0.00E+00	3.86E+02	4.40E+01	9.56E+02	0.00E+00
1873	0.00E+00	1.10E+01	4.43E+02	2.38E+02	0.00E+00	3.80E+02	2.40E+01	9.83E+02	0.00E+00
1923	0.00E+00	3.00E+00	4.41E+02	2.38E+02	0.00E+00	3.81E+02	2.00E+01	9.87E+02	0.00E+00
1973	0.00E+00	0.00E+00	4.63E+02	2.37E+02	0.00E+00	3.80E+02	2.40E+01	9.92E+02	0.00E+00

T (K)	C2H2 (ppm)	C2H6 (ppm)	C3H6 (ppm)	HCN (ppm)	H2O (ppm)
1223	0.00E+00	0.00E+00	0.00E+00	0.00E+00	0.00E+00
1273	0.00E+00	0.00E+00	0.00E+00	0.00E+00	0.00E+00
1323	0.00E+00	2.00E+00	0.00E+00	0.00E+00	0.00E+00
1373	0.00E+00	5.00E+00	0.00E+00	0.00E+00	0.00E+00
1423	0.00E+00	7.00E+00	0.00E+00	0.00E+00	0.00E+00
1473	0.00E+00	1.60E+01	0.00E+00	0.00E+00	0.00E+00
1523	9.00E+00	2.20E+01	0.00E+00	0.00E+00	3.26E+02
1573	0.00E+00	0.00E+00	0.00E+00	2.90E+01	3.68E+03
1623	0.00E+00	0.00E+00	1.10E+01	1.60E+01	3.63E+03
1673	0.00E+00	0.00E+00	0.00E+00	0.00E+00	3.58E+03
1723	0.00E+00	0.00E+00	0.00E+00	0.00E+00	3.45E+03
1773	0.00E+00	0.00E+00	0.00E+00	0.00E+00	3.47E+03
1823	0.00E+00	0.00E+00	0.00E+00	0.00E+00	3.47E+03
1873	0.00E+00	0.00E+00	0.00E+00	0.00E+00	3.45E+03
1923	0.00E+00	0.00E+00	0.00E+00	0.00E+00	3.45E+03
1973	0.00E+00	0.00E+00	0.00E+00	0.00E+00	3.50E+03

X.2.4 Oxidation of ammonia-hydrogen in the FR1



Set 1: 50% H₂- 50% NH₃

Reactor type	FR1
Temperature (K)	873-1773
Pressure (Bar)	1.27
Residence time (s)	0.05
NH ₃ inlet mole fraction (ppm)	1000
H ₂ inlet mole fraction (ppm)	1000
O ₂ inlet mole fraction (ppm)	1750 (phi = 1)
Dilution gas	Helium
Data type	Mole fractions (ppm)

Species were quantified using Mass Spectrometry (MS), except H₂ which was quantified by MS and Gas Chromatography (GC).

T(K)	H ₂ ppm		NH ₃ ppm		H ₂ O ppm		NO ppm	
	MS	GC	MS	MS	MS	MS	MS	MS
873.15	1000	1000	969	1738	36	3	0	
923.15	1000	971	981	1750	0	3	0	
973.15	991	971	984	1721	0	2	3	
1023.15	982	971	984	1723	0	0	5	
1073.15	947	955	969	1699	71	11	13	
1123.15	876	867	943	1633	261	62	12	
1173.15	693	716	771	1394	964	245	1	
1073.15	953	942	1000	1705	138	24		
1123.15	859	874	935	1629	198	31		
1173.15	699	730	730	1321	605	135	1	
1223.15	480	531	335	967	1308	305		
1273.15	18	17	106	467	2500	470	42	
1323.15	4	0	65	456	2456	437	20	
1373.15	2	0	48	418	2446	410	111	
1423.15	1	0	42	416	2454	407	151	
1473.15	0	0	30	426	2426	407	174	
1523.15	1	0	30	416	2453	407	180	
1573.15	0	0	12	409	2424	397	182	
1623.15	0	0	9	409	2451	397	186	
1673.15	0	0	9	403	2479	397	186	
1723.15	0	0	0	422	2469	393	190	
1773.15	0	0	2	411	2478	393	190	

relative uncertainties MS : +/- 10% (+/- 20% for water)

relative uncertainties GC : +/- 5%

Set 2: 35% H₂- 65% NH₃

Reactor type	FR1
Temperature (K)	873-1773
Pressure (Bar)	1.27
Residence time (s)	0.05
NH ₃ inlet mole fraction (ppm)	1000
H ₂ inlet mole fraction (ppm)	538
O ₂ inlet mole fraction (ppm)	1519 (phi = 1)
Dilution gas	Helium
Data type	Mole fractions (ppm)

Species were quantified using Mass Spectrometry (MS), except H₂ which was quantified by MS and Gas Chromatography (GC).

T(K)	H ₂ ppm		NH ₃ ppm		H ₂ O ppm		NO ppm
	MS	GC	MS	MS	MS	MS	MS
873.15	504	512	1000	1500	8	10	0
923.15	529	523	959	1487	0	2	3
973.15	536	536	948	1487	21	1	3
1023.15	539	538	936	1496	66	0	4
1073.15	537	533	924	1519	81	0	4
1123.15	519	518	912	1514	76	6	7
1173.15	487	490	884	1492	112	24	8
1223.15	438	426	792	1375	257	68	10
1273.15	368	382	596	1218	608	160	14
1323.15	279	303	238	864	1234	312	21
1373.15	4	0	27	481	2001	416	89
1423.15	0	0	25	495	2028	422	91
1473.15	0	0	17	477	2039	427	91
1523.15	0	0	8	489	2017	435	96
1573.15	0	0	1	478	2011	440	100
1623.15	0	0	0	477	2006	439	101
1673.15	1	0	2	486	2000	438	106
1723.15	1	0	3	500	2028	440	112
1773.15	1	0	1	501	2023	441	117

relative uncertainties MS : +/- 10% (+/- 20% for water)

relative uncertainties GC : +/- 5%

Set 3: 30% H₂- 70% NH₃

Reactor type	Flow Tube Reactor
Temperature (K)	873-1773
Pressure (Bar)	1.27
Residence time (s)	0.05
NH ₃ inlet mole fraction (ppm)	1000
H ₂ inlet mole fraction (ppm)	429
O ₂ inlet mole fraction (ppm)	1464 (phi = 1)
Dilution gas	Helium
Data type	Mole fractions (ppm)

Species were quantified using Mass Spectrometry (MS), except H₂ which was quantified by MS and Gas Chromatography (GC).

T(K)	H ₂ ppm		NH ₃ ppm		H ₂ O ppm		NO ppm	
	MS	GC	MS	MS	MS	MS	MS	MS
873.15	429	429	1002	1290	0	5	0	0
923.15	427	429	1000	1306	29	4	0	0
973.15	427	423	991	1287	0	1	0	0
1023.15	427	426	995	1284	31	0	0	0
1073.15	433	421	1006	1287	75	1	0	0
1123.15	426	411	998	1276	73	2	0	0
1173.15	412	397	979	1239	88	7	0	0
1223.15	380	362	940	1191	171	23	0	0
1273.15	346	324	861	1122	216	54	0	0
1323.15	305	274	715	1029	263	113	0	0
1373.15	262	228	547	906	983	193	0	0
1423.15	207	176	311	716	1787	318	0	0
1473.15	68	52	0	512	1929	453	3	3
1523.15	1	0	0	443	1929	479	29	29
1573.15	0	0	0	437	1929	462	59	59
1623.15	0	0	0	422	1929	460	75	75
1673.15	1	0	0	417	1929	453	86	86
1723.15	0	0	0	422	1929	451	97	97
1773.15	1	0	0	417	1929	451	100	100

relative uncertainties MS : +/- 10% (+/- 20% for water)

relative uncertainties GC : +/- 5%

Set 4: 26% H₂- 74% NH₃

Reactor type	FR1
Temperature (K)	873-1773
Pressure (Bar)	1.27
Residence time (s)	0.05
NH ₃ inlet mole fraction (ppm)	1000
H ₂ inlet mole fraction (ppm)	351
O ₂ inlet mole fraction (ppm)	1426(phi = 1)
Dilution gas	Helium
Data type	Mole fractions (ppm)

Species were quantified using Mass Spectrometry (MS), except H₂ which was quantified by MS and Gas Chromatography (GC).

T(K)	H ₂ ppm		NH ₃ ppm		H ₂ O ppm		NO ppm	
	MS	GC	MS	MS	MS	MS	MS	MS
873.15	350	350	1012	1401	20	0	1	
923.15	344	351	1007	1425	14	0	1	
973.15	344	351	988	1415	0	0	0	
1023.15	347	350	996	1359	3	1	0	
1073.15	350	350	991	1351	0	0	0	
1123.15	352	347	1014	1346	3	0	0	
1173.15	343	340	1008	1327	7	0	0	
1223.15	326	313	1002	1297	26	3	0	
1273.15	300	284	965	1261	66	3	1	
1323.15	273	254	832	1171	72	3	0	
1373.15	241	217	622	1039	91	0	0	
1423.15	206	181	401	857	572	27	4	
1473.15	105	92	0	593	747	36	6	
1523.15	1	0	0	455	1364	220	36	
1573.15	1	0	0	469	1608	389	63	
1623.15	1	0	0	457	1795	431	70	
1673.15	0	0	0	459	1850	458	74	
1723.15	0	0	0	462	1755	462	75	
1773.15	0	0	0	466	1817	462	75	

relative uncertainties MS : +/- 10% (+/- 20% for water)

relative uncertainties GC : +/- 5%

Set 5: 21% H₂- 79% NH₃

Reactor type	FR1
Temperature (K)	873-1773
Pressure (Bar)	1.27
Residence time (s)	0.05
NH ₃ inlet mole fraction (ppm)	1000
H ₂ inlet mole fraction (ppm)	266
O ₂ inlet mole fraction (ppm)	1383 (phi = 1)
Dilution gas	Helium
Data type	Mole fractions (ppm)

Species were quantified using Mass Spectrometry (MS), except H₂ which was quantified by MS and Gas Chromatography (GC).

T(K)	H ₂ ppm		NH ₃ ppm		H ₂ O ppm		NO ppm	
	MS	GC	MS	MS	MS	MS	MS	MS
873.15	272	263	1000	1383	0	3	7	
923.15	266	273	972	1402	0	2	4	
973.15	267	265	962	1376	0	2	3	
1023.15	266	264	975	1395	0	1	3	
1073.15	268	265	956	1358	0	4	3	
1123.15	271	264	905	1367	0	1	3	
1173.15	270	267	934	1362	0	0	3	
1223.15	263	256	954	1363	55	3	3	
1273.15	253	230	977	1357	113	8	3	
1323.15	235	206	992	1350	214	18	3	
1373.15	212	183	998	1307	394	45	3	
1423.15	197	160	870	1181	754	125	1	
1473.15	166	139	261	781	1404	364	0	
1523.15	10	0	0	577	1766	479	12	
1573.15	0	0	0	579	1766	479	28	
1623.15	0	0	0	584	1766	479	36	
1673.15	1	0	0	576	1766	479	41	
1723.15	0	0	0	579	1766	479	47	
1773.15	0	0	0	583	1766	479	50	

relative uncertainties MS : +/- 10% (+/- 20% for water)

relative uncertainties GC : +/- 5%

X.2.5 Oxidation of neat hydrogen in the FR1



Reactor type	FR1
Temperature (K)	1073-1773
Pressure (Bar)	1.27
Residence time (s)	0.05
H ₂ inlet mole fraction (ppm)	1000
O ₂ inlet mole fraction (ppm)	3000 (phi=1)
Dilution gas	Helium
Data type	Mole fractions (ppm)

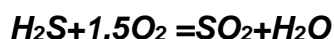
Species were quantified using Mass Spectrometry (MS), except H₂ which was quantified by MS and Gas Chromatography (GC).

T(K)	H ₂ ppm MS	H ₂ ppm GC	O ₂ ppm MS	H ₂ O ppm MS	H balance	O balance
1073.15	1000	997	475	0	1.00	0.95
1123.15	997	997	478	0	1.00	0.96
1173.15	1000	1001	500	0	1.00	1.00
1223.15	342	367	124	728	1.07	0.98
1273.15	273	266	100	788	1.06	0.99
1323.15	252	248	110	849	1.10	1.07
1373.15	230	260	117	849	1.08	1.08
1423.15	207	204	110	889	1.10	1.11
1473.15	189	175	99	889	1.08	1.09
1523.15	175	159	92	930	1.10	1.11
1573.15	158	143	88	910	1.07	1.09
1623.15	146	131	83	899	1.05	1.06
1673.15	126	107	74	930	1.06	1.08
1723.15	89	68	59	930	1.02	1.05
1773.15	70	51	45	950	1.02	1.04

relative uncertainties MS : +/- 10% (+/- 20% for water)

relative uncertainties GC : +/- 5%

X.2.6 Oxidation of neat hydrogen sulfide



Reactor type	JSR
Temperature (K)	400-1200
Pressure (MPa)	0.107
Residence time (s)	2
H ₂ S inlet mole fraction (ppm)	500
O ₂ inlet mole fraction (ppm)	3000 ($\phi = 0.25$), 20400 ($\phi = 0.037$), 40800 ($\phi = 0.018$) & 81600 ($\phi = 0.009$)
Dilution gas	Helium
Data type	Mole fractions (ppm)

Species were quantified using mass spectrometry

T (K)	H ₂ S				SO ₂			
	3 000 ppm O ₂	20 400 ppm O ₂	40 800 ppm O ₂	81 600 ppm O ₂	3 000 ppm O ₂	20 400 ppm O ₂	40 800 ppm O ₂	81 600 ppm O ₂
1200	4		6	5	482	549	479	500
1150	4	23	9	4	494	528	506	494
1100	3	2	13	2	486	496	513	482
1050	3	6	4	5	493	500	515	468
1000	3	6	6	6	491	488	513	453
950	4	7	3	6	500	500	513	443
900	3	3	3	10	495	483	507	434
850	4	1	6	9	500	467	503	419
800	4	4	9	10	494	444	480	416
750	4	4	3	6	486	395	477	400
700	37	5	4	3	404	325	446	378
650	163	21	14	12	252	297	414	326
600	254	74	45	20	172	255	376	286
550	328	137	86	47	130	230		
500	381	195	114	59	113	215		
450	428	235	129	70	87	185		
400	459	289	139	77	68			

relative uncertainties MS : +/- 10%

X.2.7 Oxidation of neat H₂S in the FR

Reactor type	FR1
Temperature (K)	773.15-1423.15 (set 1) – 673.15-1273.15 (set 2)
Pressure (Bar)	1.267
Residence time (s)	0.1 s (set 1) – 0.25 s (set 2)
H ₂ S inlet mole fraction (-)	0.0005
Equivalence ratio	0.25 (set 1) – 0.1 (set 2)
Dilution gas	Helium
Data type	Mole fractions (- or ppm when specified)

Species were quantified using mass spectrometry except O₂ which was quantified by gas chromatography

Set 1:

T (K)	H ₂ S	O ₂	H ₂	H ₂ O	SO ₂
773.15	486	2923	0	0	0
823.15	472	2938	1	0	0
873.15	497	2954	0	0	0
923.15	500	3000	3	0	14
973.15	12	2304	148	379	472
1023.15	7	2320	87	493	485
1073.15	4	2281	32	496	474
1123.15	2	2276	13	500	474
1173.15	2	2273	7	445	484
1223.15	1	2273	4		480
1273.15	1	2273	3		483
1323.15	0	2304	3		486
1373.15	1	2289	3	458	496
1423.15	0	2289	3	461	500

Set 2:

T (K)	H ₂ S	O ₂	H ₂	H ₂ O*	SO ₂
673.15	495	7440	3	0	5
723.15	489	7149	0	0	0
773.15	481	7260	3	0	10
823.15	500	7500	4	9	16
873.15	30	6514	129	294	451
848.15	41	6569	112	173	409
923.15	11	6633	137	216	475
973.15	7	6740	137	254	494
1023.15	5	6794	106	294	500
1073.15	4	6775	22	386	474
1123.15	1	6656	9	431	483
1173.15	1	6673	5	478	485
1223.15	0	6710	5	500	487
1273.15	0	6750	4	551	485

relative uncertainties MS : +/- 10% (+/- 20% for water)

relative uncertainties GC : +/- 5%

X.2.8 Pyrolysis of neat H₂S in the JSR:

Reactor type	JSR
Temperature (K)	600-1200 K
Pressure (Bar)	1.067
Residence time (s)	2 s
H ₂ S inlet mole fraction (ppm)	500
Dilution gas	Helium
Data type	Mole fractions (ppm)

Species were quantified using mass spectrometry.

T (K)	H ₂ S ppm	H ₂ ppm
1200	440	54
1150	471	23
1100	487	10
1050	503	5
1000	506	2
950	514	2
900	518	2
850	516	1
800	519	1
750	520	1
700	515	1
650	516	0
600	501	0

relative uncertainties MS : +/- 10%

X.2.9 Pyrolysis of neat H₂S in the FR:

Reactor type	FR1
Temperature (K)	973.15-1923.15 K
Pressure (Bar)	1.20
Residence time (s)	0.25 s
H ₂ S inlet mole fraction (ppm)	500
Dilution gas	Helium
Data type	Mole fractions (ppm)

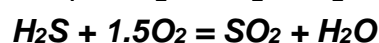
Species were quantified using mass spectrometry (MS) and gas chromatography (GC).

T(K)	H ₂ (ppm, MS)	H ₂ (ppm, GC)	H ₂ S (ppm, MS)
973.15	0	0	483
1023.15	1	0	490
1073.15	0	0	476
1123.15	0	0	493
1173.15	1	0	487
1223.15	4	0	500
1273.15	11	0	500
1323.15	28	15	490
1373.15	73	49	443
1423.15	171	134	315
1473.15	370	329	102
1523.15	448	425	22
1573.15	471	449	17
1623.15	483	463	13
1673.15	488	469	9
1723.15	492	484	6
1773.15	494	490	4
1823.15	499	499	2
1873.15	500	500	1
1923.15	492	497	0

relative uncertainties MS : +/- 10%

relative uncertainties GC : +/- 5%

X.2.10 Oxidation of methane-hydrogen sulfide in the JSR



Reactor type	JSR
Temperature (K)	650-1200 K
Pressure (Bar)	1.067
Residence time (s)	2 s
CH ₄ inlet mole fraction (-)	0.02
H ₂ S inlet mole fraction (ppm)	500
O ₂ inlet mole fraction (-)	0.0204 (phi = 2), 0.0408 (phi = 1) & 0.0816 (phi = 0.5)
Dilution gas	Helium
Data type	Mole fractions (ppm)

Gas chromatography data:

T (K)	CO (Carbosphere)			O ₂ (Carbosphere)			CO ₂ (Carbosphere)		
	phi = 0.5	phi = 1	phi = 2	phi = 0.5	phi = 1	phi = 2	phi = 0.5	phi = 1	phi = 2
650	0	4.84E-05	2.50E-05	7.78E-02	3.87E-02	1.83E-02	0	0	0
700	6.23E-05	7.77E-05	8.59E-05	7.75E-02	3.85E-02	1.76E-02	0	0	0
750	1.22E-04	1.42E-04	1.22E-04	7.68E-02	3.82E-02	1.73E-02	0	0	0
800	1.81E-04	1.80E-04	1.23E-04	7.80E-02	3.81E-02	1.71E-02	0	0	0
825	1.77E-04	2.11E-04	1.22E-04	7.68E-02	3.77E-02	1.70E-02	0	0	0
850	2.06E-04	2.23E-04	1.41E-04	7.60E-02	3.82E-02	1.71E-02	0	0	0
875	2.09E-04	1.72E-04	1.16E-04	7.56E-02	3.74E-02	1.68E-02	0	0	0
900	2.84E-04	2.00E-04	1.13E-04	7.52E-02	3.70E-02	1.69E-02	0	0	0
925	4.02E-04	1.56E-04	1.02E-04	7.59E-02	3.71E-02	1.70E-02	0	0	0
950	5.97E-04	1.77E-04	1.19E-04	7.52E-02	3.68E-02	1.67E-02	0	0	0
975	1.11E-03	2.19E-04	1.27E-04	7.35E-02	3.65E-02	1.70E-02	4.44E-05	0	0
1000	3.29E-03	3.93E-04	1.77E-04	6.98E-02	3.60E-02	1.66E-02	3.08E-04	0	0
1025	3.35E-03	4.88E-04	1.91E-04	5.63E-02	3.58E-02	1.64E-02	7.49E-03	0	0
1050	6.24E-03	8.91E-04	2.41E-04	4.07E-02	3.52E-02	1.66E-02	1.41E-02	5.14E-05	0
1075	4.10E-03	2.46E-03	3.86E-04	3.74E-02	3.27E-02	1.63E-02	1.68E-02	1.96E-04	0
1100	2.49E-03	1.09E-02	5.23E-04	3.57E-02	9.41E-03	1.62E-02	1.92E-02	7.24E-03	0
1125	2.13E-03	1.01E-02	9.47E-04	3.51E-02	5.60E-03	1.54E-02	1.98E-02	8.98E-03	0
1150	1.05E-03	8.44E-03	2.19E-03	3.34E-02	3.63E-03	1.34E-02	2.11E-02	1.14E-02	0
1175	8.72E-04	8.02E-03	5.22E-03	3.36E-02	2.87E-03	8.76E-03	2.11E-02	1.25E-02	6.92E-04
1200	2.27E-04	8.01E-03	7.39E-03	3.18E-02	1.63E-03	5.54E-03	2.24E-02	1.26E-02	1.28E-03

T (K)	CH ₄ (Q-Bond TCD)			C ₂ H ₄ (Q-Bond FID)			C ₂ H ₂ (Q-Bond FID)		
	phi = 0.5	phi = 1	phi = 2	phi = 0.5	phi = 1	phi = 2	phi = 0.5	phi = 1	phi = 2
650	1.82E-02	2.00E-02	1.92E-02	0	0	0	0	0	0
700	1.77E-02	1.88E-02	1.90E-02	0	0	0	0	0	0
750	1.95E-02	1.92E-02	1.89E-02	0	0	1.82E-06	0	0	0
800	1.88E-02	1.88E-02	1.89E-02	2.14E-06	2.61E-06	3.93E-06	0	0	0
825	1.88E-02	1.90E-02	1.88E-02	3.43E-06	5.36E-06	6.79E-06	0	0	0
850	1.95E-02	1.91E-02	1.93E-02	5.36E-06	7.86E-06	9.64E-06	0	0	0
875	1.93E-02	1.77E-02	1.89E-02	7.14E-06	6.79E-06	1.21E-05	0	0	0
900	1.81E-02	1.78E-02	1.88E-02	1.18E-05	1.18E-05	1.39E-05	0	0	0
925	1.81E-02	1.75E-02	1.89E-02	2.29E-05	1.25E-05	1.54E-05	0	0	0
950	1.86E-02	1.77E-02	1.90E-02	3.97E-05	1.93E-05	1.96E-05	0	0	0
975	1.78E-02	1.74E-02	1.87E-02	8.43E-05	2.54E-05	2.32E-05	0	0	0
1000	1.38E-02	1.86E-02	1.89E-02	2.25E-04	4.18E-05	3.18E-05	0	0	0
1025	8.24E-03	1.87E-02	1.87E-02	6.11E-05	6.43E-05	4.11E-05	0	0	0
1050	2.16E-03	1.83E-02	1.92E-02	5.79E-05	1.20E-04	5.86E-05	0	0	0
1075	1.24E-03	1.60E-02	1.88E-02	4.07E-05	2.93E-04	8.47E-05	9.29E-07	1.94E-06	0
1100	9.14E-04	3.18E-03	1.87E-02	3.54E-05	2.79E-04	1.23E-04	1.39E-06	2.86E-06	6.43E-07
1125	4.78E-04	2.61E-03	1.80E-02	3.39E-05	2.11E-04	2.11E-04	1.18E-06	5.36E-06	4.29E-06
1150	3.51E-04	1.88E-03	1.65E-02	3.11E-05	1.54E-04	4.07E-04	1.11E-06	4.64E-06	9.29E-06
1175	6.04E-05	8.29E-04	1.26E-02	1.50E-05	1.40E-04	5.86E-04	2.36E-06	1.25E-05	2.68E-05
1200	9.14E-05	6.47E-04	1.03E-02	0	1.30E-04	5.92E-04	0	3.18E-05	7.89E-05

T (K)	C ₂ H ₆ (Q-Bond FID)			CH ₂ O (Q-Bond TCD)		
	phi = 0.5	phi = 1	phi = 2	phi = 0.5	phi = 1	phi = 2
650	0	0	0	2.67E-04	6.04E-04	1.69E-04
700	0	0	1.39E-06	3.94E-04	2.81E-04	3.51E-04
750	2.14E-06	4.29E-06	6.79E-06	5.34E-04	6.47E-04	4.50E-04
800	1.00E-05	1.46E-05	2.21E-05	7.31E-04	6.04E-04	5.06E-04
825	1.75E-05	2.71E-05	3.39E-05	8.01E-04	7.45E-04	4.64E-04
850	2.96E-05	4.00E-05	4.50E-05	7.45E-04	6.32E-04	5.76E-04
875	4.36E-05	4.97E-05	5.50E-05	6.61E-04	6.04E-04	6.32E-04
900	2.50E-05	6.64E-05	6.64E-05	8.01E-04	1.18E-03	6.32E-04
925	7.86E-05	7.18E-05	7.89E-05	1.22E-03	7.73E-04	5.06E-04
950	1.09E-04	8.79E-05	8.82E-05	1.57E-03	8.29E-04	5.48E-04
975	1.50E-04	1.08E-04	9.75E-05	2.05E-03	9.70E-04	5.34E-04
1000	2.11E-04	1.23E-04	1.13E-04	4.98E-03	1.10E-03	6.32E-04
1025	8.79E-05	1.54E-04	1.26E-04	1.17E-02	1.08E-03	5.90E-04
1050	4.07E-05	1.92E-04	1.42E-04	1.89E-02	1.77E-03	9.14E-04
1075	2.96E-05	2.51E-04	1.48E-04	7.03E-04	3.54E-03	1.11E-03
1100	2.50E-05	1.14E-04	1.76E-04	7.87E-04	1.90E-02	1.07E-03
1125	2.21E-05	7.68E-05	2.00E-04	1.57E-02	1.80E-02	1.69E-03
1150	1.89E-05	5.29E-05	2.38E-04	2.00E-02	1.33E-02	2.77E-03
1175	5.72E-06	3.82E-05	2.15E-04	1.60E-02	1.37E-02	5.48E-03
1200	0	2.68E-05	1.65E-04	1.61E-02	1.31E-02	6.63E-03

Mass spectrometry data:

T (K)	H ₂ S			SO ₂		
	20 400 ppm O ₂	40 800 ppm O ₂	81 600 ppm O ₂	20 400 ppm O ₂	40 800 ppm O ₂	81 600 ppm O ₂
1200						
1150				420	429	495
1100	-3			433	433	510
1050	8	7	13	436	485	500
1000	6	6	11	432	487	435
950	6	5	9	435	473	493
900	6	7	9	435	471	533
850	5	3	8	434	456	524
800	5	5	7	432	423	518
750	8	9	9	421	408	500
700	14	16	11	421	414	459
650	25	29	12	415	396	441
600	63	49	18	386	402	448
550	120	73	27	349	397	452
500	201	87	36	316	412	438
450	229	96	58	304	426	458
400	257	105	66	304	437	479

relative uncertainties MS : +/- 10%

relative uncertainties GC : +/- 5%

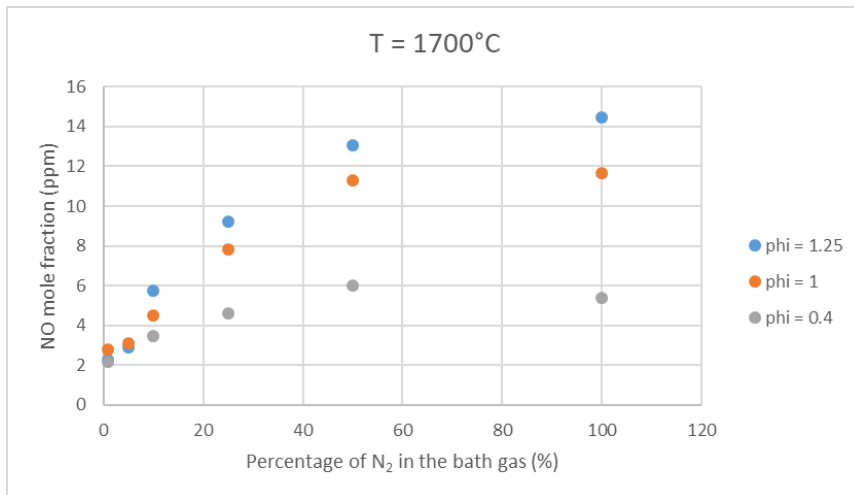
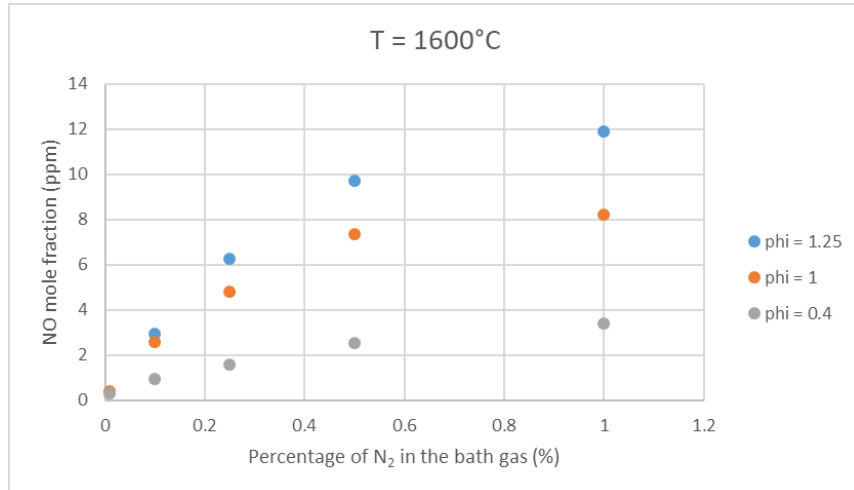
X.2.11 Oxidation of neat methane in the FR: simulation of a leak of N₂ (unpublished data)

Reactor type	FR1
Temperature (K)	1600-1700
Pressure (Bar)	1.33
Equivalence ratio	0.04, 1 and 1.25
CH ₄ inlet mole fraction (-)	0.001
Bath gas	He+N ₂
N ₂ fraction in the bath gas (%)	1-100
Data type	Mole fraction (ppm)

1700 °C

1600 °C		Phi = 0.4	
Phi = 0.4		mol% N ₂ in bath gas	NO (ppm)
mol% N ₂ in bath gas	NO (ppm)	1	2.18E+00
1	3.29E-01	10	3.48E+00
10	9.50E-01	25	4.58E+00
25	1.60E+00	50	6.00E+00
50	2.52E+00	100	5.38E+00
100	3.42E+00		
Phi = 1.0		Phi = 1.0	
Phi = 1.0		mol% N ₂ in bath gas	NO (ppm)
mol% N ₂ in bath gas	NO (ppm)	1	2.77E+00
1	4.25E-01	5	3.10E+00
10	2.60E+00	10	4.48E+00
25	4.81E+00	25	7.84E+00
50	7.35E+00	50	1.13E+01
100	8.23E+00	100	1.17E+01
Phi = 1.25		Phi = 1.25	
Phi = 1.25		mol% N ₂ in bath gas	NO (ppm)
mol% N ₂ in bath gas	NO (ppm)	1	2.27E+00
1	5.36E-01	5	2.88E+00
10	2.97E+00	10	5.77E+00
25	6.28E+00	25	9.20E+00
50	9.72E+00	50	1.31E+01
100	1.19E+01	100	1.44E+01

*No NO₂ has been observed



X.3 Experimental data of the formation of NO_x

X.3.1 Oxidation of N₂ in the FR1



Reactor type	FR1
Temperature (K)	1273-2073
Pressure (Bar)	1.2
Residence time (s)	0.04
N ₂ inlet mole fraction (-)	0.791, 0.781
O ₂ inlet mole fraction (-)	0.209
H ₂ O inlet mole fraction (-)	0, 0.01
Data type	Mole fraction (ppm)

T(K)	NO (N ₂ /O ₂)	NO (N ₂ /O ₂ /H ₂ O)
1373.15	0	0
1423.15	0	0
1473.15	0	1.2
1523.15	0	0
1573.15	4.5	7.3
1623.15	2	9
1673.15	4	10.36
1723.15	7	10.6
1773.15	8	15.3
1823.15	11	16.3
1873.15	11	20.7
1923.15	17	27.1
1973.15	27	34
2023.15	56	63
2073.15	114	126.7

X.3.2 Oxidation of CH₄ in the FR1

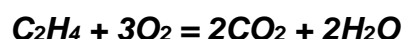


Reactor type	FR1
Temperature (K)	1073-2073
Pressure (Bar)	1.2
Residence time (s)	0.04
CH ₄ inlet mole fraction (-)	0.001
O ₂ inlet mole fraction (-)	0.209
N ₂ inlet mole fraction (-)	0.79
Data type	Mole fraction (ppm)

T(K)	H ₂ O	CH ₄	CO ₂	NO	CO
1073.15	0	969	0	0	0
1123.15	0	1006	0	0	0
1173.15	0	1000	0	0	0
1223.15	4.7	851	12	0	71
1273.15	816	296	53	0	552
1323.15	1676	120	605	0	686
1373.15	1911	0	841	0	98
1423.15	1955	0	933	0	51
1473.15	1991	0	977	0	0
1523.15	1941	0	986	0	0
1573.15	1922	0	985	0	0
1623.15	1758	0	980	0	0
1673.15	1774	0	976	0	0
1723.15	1980	0	991	0	0
1773.15	1741	0	int	0	0
1823.15	1998	0	996	0	0
1873.15	1798	0	1002	0	0
1923.15	1911	0	994	6.09	0
1973.15	2000	0	998	21.64	0
2023.15	1948	0	993	50.53	0
2073.15	1984	0	1000	112.1351	0

int = interference with other species

X.3.3 Oxidation of C₂H₄ in the FR1



Reactor type	FR1
Temperature (K)	973-2073
Pressure (Bar)	1.23
Residence time (s)	0.04
C ₂ H ₄ inlet mole fraction (-)	0.0005
O ₂ inlet mole fraction (-)	0.15%, 0.3%
Equivalence ratio	0.5 and 1
Dilution gas	N ₂
Data type	Mole fraction (ppm)

T(K)	C ₂ H ₄		O ₂		CO ₂		H ₂ O		NO	
	φ= 0.5	φ= 1	φ= 0.5	φ= 1	φ= 0.5	φ= 1	φ= 0.5	φ= 1	φ= 0.5	φ= 1
973.15	500	454	3000	1635	0	9	0	0	0	0
1023.15	423	500	3000	1539	0	5	30	0	0	0
1073.15	407	int	2884	1475	12	1	154	2	0	0
1123.15	207	403	2419	1486	62	0	470	173	0	0
1173.15	0	266	1605	1315	680	13	966	217	0	0
1223.15	0	0	1547	823	759	114	974	455	0	0
1273.15	0	0	1512	127	871	692	983	945	0	0
1323.15	0	0	1500	50	923	894	1000	984	0	0
1373.15	0	0	1477	12	971	1000	983	1000	0	0
1423.15	0	0	1465	5	990	1026	940	992	0	0
1473.15	0	0	1442	0	1000	1000	957	929	0	0
1523.15									0	0
1573.15									0	3
1623.15									0	3
1673.15									0	3
1723.15									0	3
1773.15									0	3
1823.15									1	3
1873.15									1	4
1923.15									2	4
1973.15									3	4
2023.15									5	5
2073.15									11	6

int = interference with other species

X.4 Experimental data of bio-oils surrogates

X.4.1 Pyrolysis of pyrrole in a JSR

Reactor type	JSR
Temperature (K)	925-1200
Pressure (Bar)	1.067
Residence time (s)	2
Pyrrole inlet mole fraction (-)	0.01
Dilution gas	Helium
Data type	Mole fractions (-)

T (K)	CH ₄	C ₂ H ₄	C ₂ H ₂	C ₂ H ₆	C ₃ H ₆	aC ₃ H ₄	pC ₃ H ₄	HCN	C ₄ H _x
925	0	0	0	0	0	0	0	0	0
950	0	0	0	0	0	0	4.91E-06	0	0
975	0	0	0	0	0	0	4.91E-06	0	0
1000	0	0	0	0	0	0	1.78E-05	0	0
1025	9.20E-06	0	7.82E-06	0	0	9.20E-06	3.56E-05	1.47E-05	0
1050	1.29E-05	5.06E-06	2.71E-05	0	0	2.58E-05	9.84E-05	4.14E-05	0
1075	6.44E-05	1.38E-05	1.09E-04	0	0	6.16E-05	1.93E-04	1.59E-04	4.37E-06
1100	2.52E-04	6.30E-05	3.83E-04	0	8.59E-06	9.72E-05	2.96E-04	6.37E-04	1.61E-05
1125	5.88E-04	1.59E-04	7.77E-04	8.28E-06	1.47E-05	1.05E-04	2.97E-04	9.01E-04	2.67E-05
1150	1.15E-03	3.15E-04	1.31E-03	1.61E-05	1.84E-05	1.00E-04	2.86E-04	1.71E-03	3.50E-05
1175	1.59E-03	4.32E-04	1.70E-03	1.38E-05	1.99E-05	7.97E-05	2.15E-04	1.82E-03	3.40E-05
1200	2.01E-03	4.88E-04	2.05E-03	1.84E-05	1.63E-05	7.18E-05	1.84E-04	2.18E-03	3.86E-05

*C₄H_x is the sum of 1,2-butadiene and but-1-en-3-yne

T (K)	CH ₃ CN	2PN	butene-nitrile	C ₆ H ₆	butene-nitrile	Pyrrole	toluene
925	0	0	2.53E-06	0	0	3.91E-06	9.73E-03
950	0	0	3.91E-06	0	0	4.37E-06	9.14E-03
975	0	0	7.59E-06	0	0	7.13E-06	9.34E-03
1000	0	0	2.16E-05	0	4.83E-06	1.63E-05	9.62E-03
1025	5.06E-06	3.07E-06	4.19E-05	1.53E-06	1.27E-05	3.17E-05	8.69E-03
1050	1.24E-05	8.59E-06	1.12E-04	3.22E-06	2.90E-05	8.28E-05	9.16E-03
1075	5.61E-05	3.86E-05	2.20E-04	1.03E-05	5.54E-05	1.67E-04	8.25E-03
1100	2.05E-04	1.78E-04	3.52E-04	4.80E-05	1.08E-04	2.68E-04	6.83E-03
1125	4.74E-04	4.20E-04	3.29E-04	7.82E-05	9.20E-05	2.69E-04	4.99E-03
1150	7.59E-04	6.69E-04	2.88E-04	1.29E-04	8.46E-05	2.37E-04	3.42E-03
1175	7.45E-04	6.59E-04	1.80E-04	1.48E-04	5.64E-05	1.40E-04	1.69E-03
1200	7.13E-04	6.26E-04	1.39E-04	1.73E-04	3.50E-05	1.08E-04	9.07E-04

X.4.2 Oxidation of pyrrole in the JSR



Reactor type	JSR
Temperature (K)	700-1200
Pressure (Bar)	1.067
Residence time (s)	2
Pyrrole inlet mole fraction (-)	0.01
Equivalence ratio	0.5, 1 & 2
Dilution gas	Helium
Data type	Mole fractions (- or ppm when specified)

Species with a * symbol were quantified using FTIR. Species with a ** symbol were quantified with the gas chromatograph equipped with the carbosphere packed column. All other species were quantified with the gas chromatograph equipped with the Plot Q column.

T (K)	HCN* (ppm)			CO* (ppm)			CO ₂ *		
	phi = 0.5	phi = 1	phi = 2	phi = 0.5	phi = 1	phi = 2	phi = 0.5	phi = 1	phi = 2
650	0	0	int	0	0	0	4.46E-06	1.53E-06	1.77E-06
700	0	0	int	0	0	0	1.17E-05	1.59E-06	5.07E-06
750	0	0	int	0	23	0	2.16E-05	4.18E-06	8.21E-06
800	0	0	int	0	137	0	4.28E-05	1.07E-05	1.61E-05
850	0	34	int	1621	572	0	8.09E-05	1.79E-05	2.34E-05
875	0	350	int	0	1167	0	3.44E-04	4.33E-05	3.19E-05
900	1393	454	int	8229	1189	906	1.29E-04	3.12E-05	3.91E-05
925	2462	886	int	12075	3025	1455	2.65E-04	6.70E-05	5.12E-05
950	2884	1993	int	11465	6346	2219	3.84E-04	5.79E-05	5.39E-05
975	2932	2560	int	10694	10578	2805	6.42E-04	1.48E-04	6.17E-05
1000	2333	2900	int	7723	11225	5180	1.69E-03	2.91E-04	7.21E-05
1025	1652	3353	int	5513	14469	7674	3.99E-03	3.84E-04	8.60E-05
1050	1004	1831	int	3122	6166	11465	4.07E-03	4.02E-03	1.15E-04
1075	567	826	int	1845	1297	11952	3.95E-03	3.86E-03	1.55E-04
1100	259	551	int	1744	1432	15710	4.15E-03	4.22E-03	1.64E-04
1125	0	342	int	0	1105	16278	3.64E-03	sig sat	2.33E-04
1150	0	0	int	0	0	18041	3.45E-03	sig sat	2.62E-04
1175	0	0	int	0	0	15222	3.65E-03	sig sat	2.86E-04
1200	0	0	int	0	0	14267	3.96E-03	sig sat	3.18E-04

int = interference with other species

sig sat = signal saturated

T (K)	O ₂ **			CO**			CH ₄ **		
	Phi=0.5	Phi=1	Phi=2	Phi=0.5	Phi=1	Phi=2	Phi=0.5	Phi=1	Phi=2
700	1.26E-01	6.33E-02	3.05E-02	0	0	0	0	0	0
750	1.24E-01	6.39E-02	3.05E-02	0	0	0	0	0	0
800	1.23E-01	6.35E-02	3.29E-02	7.19E-05	0	0	0	0	0
850	1.22E-01	6.27E-02	3.05E-02	3.91E-04	0	9.38E-05	0	0	0
875	1.23E-01	5.98E-02	3.11E-02	7.63E-04	0	0	0	0	0
900	1.24E-01	5.68E-02	3.28E-02	1.61E-03	7.03E-04	3.28E-04	0	0	0
925	9.27E-02	5.32E-02	3.38E-02	1.42E-02	1.51E-03	3.05E-04	0	0	0
950	9.21E-02			1.21E-02	0	1.25E-03	0	0	0
975	8.60E-02	4.53E-02	2.85E-02	1.11E-02	1.21E-02	2.28E-03	0	0	0
1000	8.47E-02	3.34E-02	2.50E-02	8.81E-03	1.54E-02	4.98E-03	0	0	0
1025	7.96E-02	2.68E-02	1.88E-02	4.80E-03	1.42E-02	9.49E-03	0	0	0
1050	8.41E-02	1.94E-02	1.07E-02	2.84E-03	7.32E-03	1.40E-02	0	0	3.15E-04
1075	8.76E-02	1.39E-02	5.16E-03	1.61E-03	2.74E-03	1.53E-02	0	0	7.90E-04
1100	9.25E-02	1.22E-02	5.49E-03	7.08E-04	1.18E-03	1.72E-02	0	0	6.57E-04
1125	9.00E-02	1.75E-02	1.30E-03	0	5.06E-04	1.75E-02	0	0	6.80E-04
1150	8.45E-02	1.58E-02	9.55E-04	0	2.13E-04	1.74E-02	0	0	3.47E-04
1175	6.81E-02	7.12E-03	1.49E-03	0	1.25E-04	1.66E-02	0	0	5.46E-04
1200	6.82E-02	7.24E-03	1.46E-03	0	6.56E-05	1.42E-02	0	0	0

T (K)	CO ₂ **			CO			CO ₂		
	Phi=0.5	Phi=1	Phi=2	Phi=0.5	Phi=1	Phi=2	Phi=0.5	Phi=1	Phi=2
700	0	0	0	2.76E-05	7.36E-06	0	1.58E-04	4.88E-05	1.84E-05
750	0	0	0	2.76E-05	3.04E-05	3.68E-05	1.10E-04	7.36E-05	6.44E-05
800	1.94E-04	0	0	1.56E-04	5.70E-05	3.31E-05	2.85E-04	1.54E-04	9.84E-05
850	5.14E-04	0	2.17E-04	4.23E-04	1.84E-04	1.00E-04	6.44E-04	4.12E-04	2.22E-04
875	7.78E-04	2.47E-04	1.07E-04	1.31E-03	3.10E-04	2.02E-04	1.22E-03	5.18E-04	6.72E-04
900	1.22E-03	8.10E-04	5.69E-04	5.39E-03	7.91E-04	3.28E-04	7.69E-03	1.35E-03	5.53E-04
925	1.23E-02	1.20E-03	4.65E-04	1.39E-02	1.78E-03	6.99E-04	1.36E-02	1.58E-03	9.20E-04
950	1.71E-02	0	9.83E-04	1.19E-02	5.86E-03	1.44E-03	1.64E-02	2.91E-03	1.20E-03
975	1.88E-02	4.65E-03	1.46E-03	9.14E-03	1.17E-02	2.52E-03	1.74E-02	4.45E-03	2.07E-03
1000	2.36E-02	1.01E-02	2.32E-03	8.38E-03	1.51E-02	4.52E-03	2.51E-02	1.10E-02	2.45E-03
1025	2.96E-02	1.64E-02	4.74E-03	4.03E-03	1.32E-02	8.31E-03	2.75E-02	1.65E-02	3.28E-03
1050	3.72E-02	2.61E-02	5.13E-03	2.74E-03	7.06E-03	1.41E-02	3.61E-02	2.71E-02	6.54E-03
1075	4.19E-02	3.46E-02	9.35E-03	1.29E-03	2.57E-03	1.62E-02	3.60E-02	3.42E-02	6.96E-03
1100	4.07E-02	3.72E-02	8.25E-03	6.35E-04	1.10E-03	1.71E-02	3.56E-02	3.67E-02	9.12E-03
1125	3.66E-02	3.52E-02	1.25E-02	1.20E-04	4.97E-04	1.75E-02	3.39E-02	3.56E-02	9.94E-03
1150	3.51E-02	3.88E-02	1.20E-02	9.20E-05	1.56E-04	1.77E-02	3.93E-02	3.61E-02	1.18E-02
1175	4.48E-02	4.19E-02	1.22E-02	0	9.20E-05	1.82E-02	4.03E-02	3.70E-02	1.10E-02
1200	4.09E-02	4.02E-02	1.26E-02	0	0	1.72E-02	3.97E-02	3.91E-02	1.29E-02

T (K)	C ₂ H ₄			C ₂ H ₂			C ₂ H ₆		
	Phi=0.5	Phi=1	Phi=2	Phi=0.5	Phi=1	Phi=2	Phi=0.5	Phi=1	Phi=2
700	0	0	0	0	0	0	0	0	0
750	0	0	0	0	0	0	0	0	0
800	0	0	0	0	0	0	0	0	0
850	0	0	0	7.36E-06	0	0	0	0	0
875	0	0	0	3.73E-05	6.44E-06	0	0	0	0
900	1.15E-05	0	0	6.03E-05	2.53E-05	1.06E-05	0	0	0
925	1.70E-05	1.75E-05	5.06E-06	7.36E-05		1.79E-05	0	0	0
950	8.74E-06	4.69E-05	2.12E-05	4.42E-05	1.47E-04	4.32E-05	0	0	0
975	5.52E-06	1.01E-04	4.32E-05	1.79E-05	2.16E-04	9.75E-05	0	0	0
1000	0	7.73E-05	1.04E-04	1.93E-05	1.51E-04	1.92E-04	0	0	2.76E-06
1025	0	4.05E-05	2.13E-04	7.36E-06	5.20E-05	2.96E-04	0	0	7.36E-06
1050	0	1.93E-05	2.94E-04	0	3.63E-05	2.48E-04	0	0	1.66E-05
1075	0	7.36E-06	3.36E-04	0	1.10E-05	2.21E-04	0	0	2.30E-05
1100	0	0	2.92E-04	0	0	1.29E-04	0	0	2.30E-05
1125	0	0	2.31E-04	0	0	1.04E-04	0	0	2.25E-05
1150	0	0	1.52E-04	0	0	7.31E-05	0	0	1.38E-05
1175	0	0	1.40E-04	0	0	1.67E-04	0	0	1.38E-05
1200	0	0	9.06E-05	0	0	8.65E-05	0	0	8.28E-06

T (K)	propene			allene			propyne		
	Phi=0.5	Phi=1	Phi=2	Phi=0.5	Phi=1	Phi=2	Phi=0.5	Phi=1	Phi=2
700	0	0	0	0	0	0	0	0	0
750	0	0	0	0	0	0	0	0	0
800	0	0	0	0	0	0	0	0	0
850	0	0	0	0	0	0	0	0	0
875	0	0	0	0	0	0	0	0	0
900	0	0	0	0	0	0	0	0	0
925	0	0	0	0	0	0	0	0	0
950	0	0	0	0	0	0	0	0	2.15E-06
975	0	0	0	0	0	0	0	0	0
1000	0	0	2.21E-06	0	0	0	0	0	6.13E-06
1025	0	0	3.07E-06	0	0	0	0	0	4.91E-06
1050	0	0	4.60E-06	0	0	0	0	0	3.37E-06
1075	0	0	5.52E-06	0	0	0	0	0	3.68E-06
1100	0	0	3.99E-06	0	0	0	0	0	2.09E-06
1125	0	0	3.07E-06	0	0	0	0	0	0
1150	0	0	0	0	0	0	0	0	0
1175	0	0	0	0	0	0	0	0	0
1200	0	0	0	0	0	0	0	0	0

T (K)	HCN			acetonitrile			2-propene nitrile		
	Phi=0.5	Phi=1	Phi=2	Phi=0.5	Phi=1	Phi=2	Phi=0.5	Phi=1	Phi=2
700	0	0	0	0	0	0	0	0	0
750	0	0	0	0	0	0	0	0	0
800	0	0	0	0	0	0	0	0	0
850	0	0	0	0	0	0	1.96E-05	5.83E-06	2.15E-06
875	1.29E-05	3.22E-05	0	7.36E-06	0	0	9.78E-05	1.13E-05	4.91E-06
900	9.02E-05	1.38E-05	1.66E-05	1.38E-05	7.82E-06	0	1.84E-04	3.99E-05	1.10E-05
925	1.41E-03	2.48E-05	8.19E-05	2.35E-05	1.43E-05	5.98E-06	2.35E-04	1.08E-04	
950	2.77E-03	7.55E-04	3.68E-05	1.89E-05	4.00E-05	1.52E-05	1.72E-04	3.25E-04	1.06E-04
975	2.57E-03	2.14E-03	4.18E-04	1.15E-05	5.66E-05	2.44E-05	9.81E-05	4.91E-04	1.97E-04
1000	1.56E-03	3.05E-03	4.50E-04	1.29E-05	5.24E-05	4.46E-05	7.05E-05	3.34E-04	4.26E-04
1025	8.23E-04	2.68E-03	2.24E-03	6.44E-06	2.90E-05	8.23E-05	4.35E-05	1.73E-04	6.58E-04
1050	1.93E-04	9.48E-04	1.84E-03	5.06E-06	2.02E-05	9.66E-05	3.31E-05	1.15E-04	5.71E-04
1075	0	3.01E-04	3.34E-03	0		1.00E-04	1.32E-05	4.88E-05	4.78E-04
1100	0	2.58E-05	2.22E-03	0	5.52E-06	9.34E-05	0	2.79E-05	3.25E-04
1125	0	0	2.37E-03	0	0	8.28E-05	0	0	2.16E-04
1150	0	0	2.68E-03	0	0	5.93E-05	0	0	1.20E-04
1175	0	0	5.81E-03	0	0	6.07E-05	0	0	8.80E-05
1200	0	0	3.99E-03	0	0	3.86E-05	0	0	4.23E-05

T (K)	C ₄ H ₅ N			benzene			C ₄ H ₅ N		
	Phi=0.5	Phi=1	Phi=2	Phi=0.5	Phi=1	Phi=2	Phi=0.5	Phi=1	Phi=2
700	0	0	0	0	0	0	0	0	0
750	0	0	0	0	0	0	0	0	0
800	0	0	0	0	0	0	0	0	0
850	2.76E-06	0	0	0	0	0	0	0	0
875	1.26E-05	3.37E-06	0	0	0	0	0	0	0
900	2.67E-05	1.35E-05	7.05E-06	0	0	0	0	0	0
925	6.13E-06	2.82E-05	1.87E-05	0	0	0	0	0	0
950	3.68E-06	5.89E-05	5.34E-05	0	0	0	0	0	0
975	0	5.61E-05	7.27E-05	0	0	0	0	0	0
1000	0	2.33E-05	1.08E-04	0	0	4.91E-06	0	0	0
1025	0	1.01E-05	1.02E-04	0	0	9.20E-06	0	0	0
1050	0	7.36E-06	6.41E-05	0	0	6.13E-06	0	0	0
1075	0	4.91E-06	4.54E-05	0	0	7.97E-06	0	0	0
1100	0	0	2.91E-05	0	0	6.75E-06	0	0	0
1125	0	0	1.63E-05	0	0	7.67E-06	0	0	0
1150	0	0	8.89E-06	0	0	6.44E-06	0	0	0
1175	0	0	5.52E-06	0	0	7.36E-06	0	0	0
1200	0	0	0	0	0	5.52E-06	0	0	0

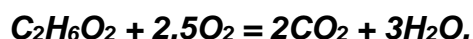
T (K)	C ₄ H ₅ N			pyrrole		
	Phi=0.5	Phi=1	Phi=2	Phi=0.5	Phi=1	Phi=2
700	0	0	0	1.04E-02	1.05E-02	9.72E-03
750	0	0	0	1.01E-02	1.02E-02	9.93E-03
800	0	0	0	1.04E-02	9.66E-03	1.08E-02
850	0	0	0	9.64E-03	1.03E-02	1.07E-02
875	3.68E-06	0	3.37E-06	6.93E-03	8.53E-03	9.76E-03
900	8.28E-06	6.75E-06	3.99E-06	4.05E-03	8.94E-03	1.04E-02
925	0	1.23E-05	9.81E-06	5.82E-04	6.44E-03	8.56E-03
950	0	2.85E-05	3.25E-05	3.57E-04	4.39E-03	8.12E-03
975	0	2.42E-05	4.57E-05	1.66E-04	2.56E-03	6.90E-03
1000	0	9.81E-06	7.39E-05	1.66E-04	6.81E-04	5.68E-03
1025	0	4.29E-06	6.65E-05	6.65E-05	2.35E-04	3.29E-03
1050	0	3.68E-06	4.05E-05	2.07E-05	1.48E-04	1.05E-03
1075	0	3.07E-06	2.91E-05	1.38E-05	1.35E-04	7.71E-04
1100	0	0	2.61E-05	1.15E-05	8.42E-05	2.58E-04
1125	0	0	1.26E-05	1.14E-04	9.20E-06	1.07E-04
1150	0	0	6.75E-06	2.30E-05	9.20E-06	4.62E-05
1175	0	0	3.68E-06	1.27E-05	9.20E-06	7.22E-05
1200	0	0	0	1.15E-05	1.61E-05	4.72E-05

X.4.3 Pyrolysis of ethylene glycol in the JSR

Reactor type	JSR
Temperature (K)	700-1200
Pressure (Bar)	1.067
Residence time (s)	2
Pyrrrole inlet mole fraction (-)	0.01
Equivalence ratio	∞
Dilution gas	Helium
Data type	Mole fractions (- or ppm when specified)

T (K)	CO	CH ₄	CO ₂	H ₂	Ethanal	C ₂ H ₄	C ₂ H ₆	C ₃ H ₆	C ₃ H ₆ O	C ₂ H ₆ O
650	4.61E-06	0.00E+00	0.00E+00	0.00E+00	0.00E+00	0	0	0	3.77E-06	0
675	5.65E-06	0.00E+00	0.00E+00	0.00E+00	0.00E+00	1.51E-06	0	0	1.98E-06	0
700	5.65E-06	0.00E+00	0.00E+00	0.00E+00	1.18E-06	0.00E+00	0	0	2.83E-05	0
725	7.06E-06	0.00E+00	0.00E+00	0.00E+00	2.97E-06	1.74E-06	0	0	1.7E-05	0
750	8.10E-06	0.00E+00	0.00E+00	0.00E+00	6.12E-06	7.53E-06	0	0	9.1E-06	0
775	9.42E-06	0.00E+00	0.00E+00	0.00E+00	1.65E-05	2.07E-05	0	0	6.28E-06	0
800	1.70E-05	1.04E-05	0.00E+00	0.00E+00	3.48E-05	4.71E-05	0	0	1.13E-05	5.89E-06
825	8.76E-05	8.19E-05	0.00E+00	8.63E-05	6.26E-05	8.90E-05	9.42E-07	8.12E-07	3.14E-06	2.07E-05
850	3.19E-04	3.25E-04	0.00E+00	1.98E-04	7.06E-05	1.25E-04	5.65E-06	2.14E-06	4.71E-06	2.35E-05
875	7.43E-04	7.72E-04	1.53E-05	3.67E-04	5.79E-05	1.34E-04	1.65E-05	3.25E-06	3.77E-06	3.15E-05
900	8.10E-04	8.48E-04	1.70E-05	6.10E-04	2.26E-05	9.56E-05	2.35E-05	3.25E-06	4.4E-06	1.88E-05
925	8.72E-04	8.53E-04	1.78E-05	9.39E-04	5.65E-06	7.25E-05	2.02E-05	5.52E-06	5.34E-06	9.89E-06
950	2.83E-03	2.62E-03	4.24E-05	1.67E-03	1.65E-06	2.47E-04	6.69E-05	2.73E-05	6.09E-05	2.07E-05
975	3.86E-03	3.33E-03	9.00E-05	2.78E-03	7.06E-07	3.71E-04	0.000129	2.31E-05	3.14E-05	2.07E-05
1000	4.99E-03	4.12E-03	1.09E-04	3.91E-03	0.00E+00	4.56E-04	0.000191	2.11E-05	1.16E-05	1.51E-05
1025	6.90E-03	5.66E-03	1.21E-04	5.24E-03	0.00E+00	6.40E-04	0.00025	1.56E-05	0	0
1050	8.01E-03	6.01E-03	1.05E-04	6.39E-03	0.00E+00	8.65E-04	0.000271	int	0	0
1075	8.63E-03	5.65E-03	1.09E-04	7.24E-03	0.00E+00	1.07E-03	0.000182	1.3E-05	0	0
1100	8.52E-03	5.62E-03	9.93E-05	7.96E-03	0.00E+00	1.07E-03	0.000141	int	0	0

X.4.4 Oxidation of ethylene glycol in the JSR



Reactor type	JSR
Temperature (K)	700-1200
Pressure (Bar)	1.067
Residence time (s)	2
Pyrrole inlet mole fraction (-)	0.01
Equivalence ratio	0.5, 1 & 2
Dilution gas	Helium
Data type	Mole fractions (- or ppm when specified)

T (K)	O ₂			CO			CH ₄		
	phi0.5	Phi=1	phi=2	phi0.5	Phi=1	phi=2	phi0.5	Phi=1	phi=2
600	5.01E-02	2.51E-02	1.11E-02	4.42E-05	0.00E+00	1.70E-05	0.00E+00	0.00E+00	0.00E+00
625	4.96E-02	2.45E-02	1.26E-02	4.68E-05	0.00E+00	3.96E-05	0.00E+00	0.00E+00	0.00E+00
650	4.90E-02	2.46E-02	1.21E-02	5.20E-05	0.00E+00	2.83E-05	0.00E+00	0.00E+00	0.00E+00
675	4.88E-02	2.37E-02	1.20E-02	6.58E-05	1.86E-05	4.99E-05	0.00E+00	0.00E+00	0.00E+00
700	4.73E-02	2.70E-02	1.27E-02	9.96E-05	5.40E-05	8.57E-05	0.00E+00	0.00E+00	0.00E+00
725	4.69E-02	2.68E-02	1.07E-02	1.70E-04	7.54E-05	8.01E-05	0.00E+00	0.00E+00	0.00E+00
750	4.59E-02	2.61E-02	1.19E-02	2.47E-04	1.71E-04	1.21E-04	0.00E+00	0.00E+00	0.00E+00
775	4.61E-02	2.44E-02	1.06E-02	7.81E-04	1.01E-03	2.79E-04	0.00E+00	7.25E-05	0.00E+00
800	4.31E-02	2.17E-02	6.81E-03	3.90E-03	2.34E-03	2.94E-03	1.30E-04	0.00E+00	1.90E-04
825	4.01E-02	1.88E-02	2.94E-03	7.14E-03	4.61E-03	6.79E-03	2.50E-04	4.65E-04	0.00E+00
850	3.77E-02	1.68E-02	3.27E-03	9.83E-03	5.90E-03	8.74E-03	4.13E-04	7.03E-04	8.50E-04
875	3.53E-02	1.62E-02	2.59E-03	1.07E-02	5.93E-03	1.10E-02	4.73E-04	3.70E-04	1.25E-03
900	2.82E-02	1.25E-02	2.90E-03	1.46E-02	7.31E-03	1.22E-02	5.88E-04	5.40E-04	1.18E-03
925	2.24E-02	1.00E-02	1.15E-03	1.32E-02	7.58E-03	1.25E-02	3.35E-04	4.90E-04	2.45E-03
950	int	8.44E-03	1.77E-03	9.15E-03	4.54E-03	1.36E-02	0.00E+00	1.23E-04	2.03E-03
975	1.50E-02	3.53E-03	1.87E-03	6.83E-03	1.63E-03	1.45E-02	0.00E+00	3.25E-05	2.18E-03
1000	1.72E-02	1.13E-03	1.89E-03	9.70E-04	2.38E-03	1.51E-02	0.00E+00	7.75E-05	2.08E-03
1025	2.04E-02	6.89E-05	1.38E-03	1.84E-04	7.52E-04	1.57E-02	0.00E+00	8.25E-05	2.00E-03
1050	2.23E-02	2.87E-03	9.68E-04	5.89E-05	1.22E-04	1.56E-02	0.00E+00	0.00E+00	1.68E-03
1075	1.89E-02	6.28E-03	5.56E-04	4.16E-05	1.12E-04	1.62E-02	0.00E+00	0.00E+00	1.48E-03
1100	2.35E-02	2.42E-03	0.00E+00	3.46E-05	1.05E-04	1.27E-02	0.00E+00	0.00E+00	int

T (K)	C ₂ H ₄			C ₂ H ₆			C ₃ H ₆		
	phi0.5	Phi=1	phi=2	phi0.5	Phi=1	phi=2	phi0.5	Phi=1	phi=2
600	0.00E+00	0.00E+00	0.00E+00	0.00E+00	0.00E+00	0.00E+00	0.00E+00	0.00E+00	0.00E+00
625	0.00E+00	0.00E+00	0.00E+00	0.00E+00	0.00E+00	0.00E+00	0.00E+00	0.00E+00	0.00E+00
650	0.00E+00	0.00E+00	0.00E+00	0.00E+00	0.00E+00	0.00E+00	0.00E+00	0.00E+00	0.00E+00
675	0.00E+00	0.00E+00	2.02E-06	0.00E+00	0.00E+00	0.00E+00	0.00E+00	0.00E+00	0.00E+00
700	2.50E-06	3.25E-06	1.98E-06	0.00E+00	0.00E+00	0.00E+00	0.00E+00	0.00E+00	0.00E+00
725	3.63E-06	6.59E-06	2.45E-06	0.00E+00	0.00E+00	0.00E+00	0.00E+00	0.00E+00	0.00E+00
750	4.38E-06	1.13E-05	3.96E-06	0.00E+00	0.00E+00	0.00E+00	0.00E+00	0.00E+00	0.00E+00
775	1.04E-05	2.26E-05	int	0.00E+00	0.00E+00	0.00E+00	0.00E+00	0.00E+00	0.00E+00
800	2.02E-05	4.05E-05	int	0.00E+00	1.41E-06	0.00E+00	0.00E+00	0.00E+00	0.00E+00
825	4.47E-05	9.61E-05	1.33E-04	2.87E-06	7.53E-06	2.35E-05	2.53E-06	9.74E-07	0.00E+00
850	6.50E-05	1.29E-04	2.22E-04	7.06E-06	1.65E-05	4.47E-05	2.86E-06	1.95E-06	5.85E-06
875	7.25E-05	1.13E-04	3.06E-04	8.01E-06	9.42E-06	8.01E-05	1.30E-06	9.74E-07	8.12E-06
900	9.18E-05	1.42E-04	3.39E-04	8.48E-06	1.55E-05	8.01E-05	0.00E+00	0.00E+00	6.50E-06
925	3.15E-05	1.11E-04	5.74E-04	4.52E-06	1.65E-05	1.76E-04	0.00E+00	0.00E+00	1.33E-05
950	7.06E-06	1.67E-04	4.68E-04	0.00E+00	3.15E-05	1.18E-04	0.00E+00	0.00E+00	7.47E-06
975	1.27E-05	1.22E-05	4.90E-04	3.30E-06	3.30E-06	1.18E-04	0.00E+00	0.00E+00	7.79E-06
1000	0.00E+00	9.42E-06	4.61E-04	0.00E+00	2.97E-06	9.89E-05	0.00E+00	0.00E+00	4.87E-06
1025	0.00E+00	0.00E+00	3.81E-04	0.00E+00	0.00E+00	6.12E-05	0.00E+00	0.00E+00	4.87E-06
1050	0.00E+00	0.00E+00	2.83E-04	0.00E+00	0.00E+00	3.81E-05	0.00E+00	0.00E+00	1.62E-06
1075	int	0.00E+00	2.37E-04	0.00E+00	0.00E+00	2.31E-05	0.00E+00	0.00E+00	0.00E+00
1100	int	0.00E+00	3.53E-04	0.00E+00	0.00E+00	3.77E-05	0.00E+00	0.00E+00	0.00E+00

T (K)	CO ₂			Ethanal			Acetone		
	phi0.5	Phi=1	phi=2	phi0.5	Phi=1	phi=2	phi0.5	Phi=1	phi=2
600	1.83E-04	7.35E-05	3.28E-04	2.92E-06	0.00E+00	0.00E+00	2.64E-06	1.85E-06	0.00E+00
625	1.50E-04	9.61E-05	1.56E-04	3.96E-06	0.00E+00	0.00E+00	2.29E-06	2.48E-06	0.00E+00
650	1.97E-04	1.56E-04	1.51E-04	2.68E-06	2.40E-06	2.26E-06	2.61E-06	2.79E-06	4.40E-06
675	2.59E-04	2.13E-04	2.02E-04	3.01E-06	3.30E-06	4.00E-06	2.10E-06	2.86E-06	4.40E-06
700	3.69E-04	1.08E-03	1.60E-04	3.86E-06	8.48E-06	2.40E-06	2.51E-06	1.48E-05	6.28E-06
725	4.63E-04	8.53E-04	1.18E-04	6.12E-06	1.32E-05	5.65E-06	3.05E-06	8.79E-06	3.14E-06
750	4.67E-04	6.72E-04	2.77E-04	1.32E-05	2.26E-05	7.06E-06	3.14E-06	1.07E-05	5.34E-06
775	7.97E-04	1.18E-03	3.17E-04	1.74E-05	2.73E-05	6.59E-06	2.45E-06	0.00E+00	0.00E+00
800	1.39E-03	9.28E-04	5.46E-04	2.50E-05	2.92E-05	9.89E-06	5.02E-06	0.00E+00	0.00E+00
825	1.84E-03	1.54E-03	7.67E-04	2.54E-05	3.48E-05	8.01E-06	5.34E-06	0.00E+00	0.00E+00
850	2.88E-03	1.86E-03	1.10E-03	2.35E-05	3.34E-05	1.88E-05	6.59E-06	0.00E+00	6.91E-06
875	3.26E-03	2.02E-03	1.45E-03	1.37E-05	6.59E-06	1.18E-05	0.00E+00	0.00E+00	5.02E-06
900	5.47E-03	2.94E-03	1.79E-03	1.88E-06	4.57E-06	6.12E-06	0.00E+00	0.00E+00	4.71E-06
925	8.80E-03	3.28E-03	1.02E-03	0.00E+00	1.84E-06	5.18E-06	0.00E+00	0.00E+00	4.71E-06
950	1.13E-02	5.31E-03	1.31E-03	0.00E+00	9.42E-07	4.71E-06	0.00E+00	0.00E+00	3.45E-06
975	1.53E-02	1.12E-02	1.41E-03	0.00E+00	0.00E+00	0.00E+00	0.00E+00	0.00E+00	2.45E-06
1000	1.84E-02	1.51E-02	1.34E-03	0.00E+00	0.00E+00	0.00E+00	0.00E+00	0.00E+00	0.00E+00
1025	1.86E-02	1.74E-02	1.62E-03	0.00E+00	0.00E+00	0.00E+00	0.00E+00	0.00E+00	0.00E+00
1050	2.01E-02	1.63E-02	1.61E-03	0.00E+00	0.00E+00	0.00E+00	0.00E+00	0.00E+00	0.00E+00
1075	1.82E-02	int	1.64E-03	0.00E+00	0.00E+00	0.00E+00	0.00E+00	0.00E+00	0.00E+00
1100	2.00E-02	1.66E-02	8.57E-04	0.00E+00	0.00E+00	0.00E+00	0.00E+00	0.00E+00	0.00E+00

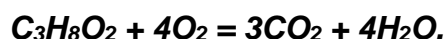
X.4.5 Pyrolysis of propylene glycol in the JSR

Reactor type	JSR
Temperature (K)	700-1200
Pressure (Bar)	1.067
Residence time (s)	2
Pyrrole inlet mole fraction (-)	0.01
Equivalence ratio	∞
Dilution gas	Helium
Data type	Mole fractions (- or ppm when specified)

T (K)	H ₂	Methane	CO	CO ₂	Ethylene	Ethane
650	0.00E+00	0.00E+00	0.00E+00	6.31E-05	0.00E+00	0.00E+00
675	0.00E+00	0.00E+00	0.00E+00	5.93E-05	0.00E+00	0.00E+00
700	0.00E+00	0.00E+00	0.00E+00	2.17E-05	0.00E+00	0.00E+00
725	0.00E+00	0.00E+00	0.00E+00	5.09E-05	0.00E+00	0.00E+00
750	0.00E+00	0.00E+00	0.00E+00	8.48E-05	0.00E+00	0.00E+00
775	0.00E+00	0.00E+00	0.00E+00	9.51E-05	5.65E-06	0.00E+00
800	5.78E-05	0.00E+00	0.00E+00	1.22E-04	2.54E-05	7.06E-06
825	1.35E-04	0.00E+00	1.42E-04	1.36E-04	8.48E-05	1.46E-05
850	3.05E-04	0.00E+00	2.59E-04	1.26E-04	2.35E-05	1.65E-05
875	7.15E-04	8.50E-04	2.01E-03	1.51E-04	7.51E-04	6.36E-05
900	1.34E-03	7.00E-04	2.78E-03	2.04E-04	2.09E-03	1.36E-04
925	2.22E-03	1.96E-03	5.13E-03	2.06E-04	2.80E-03	1.57E-04
950	3.13E-03	int	4.14E-03	1.66E-04	1.62E-03	1.13E-04
975	4.06E-03	2.56E-03	6.14E-03	1.92E-04	2.15E-03	1.76E-04
1000	4.45E-03	2.58E-03	5.85E-03	2.13E-04	3.19E-03	2.99E-04
1025	4.89E-03	5.08E-03	1.13E-02	1.57E-04	4.40E-03	1.92E-04
1050	5.89E-03	4.94E-03	1.14E-02	1.61E-04	3.80E-03	2.27E-04
1075	5.98E-03	5.27E-03	1.22E-02	1.54E-04	4.43E-03	3.68E-04
1100	7.08E-03	5.12E-03	1.21E-02	1.01E-04	4.20E-03	2.20E-04
1125	8.14E-03	5.45E-03	1.21E-02	1.51E-04	4.52E-03	1.34E-04
1150	8.63E-03	4.74E-03	1.26E-02	2.98E-04	1.34E-03	0.00E+00
1175	9.98E-03	5.03E-03	1.22E-02	1.74E-04	3.25E-03	2.78E-05
1200	1.47E-02	3.08E-03	1.12E-02	3.57E-04	5.90E-04	0.00E+00

T (K)	Propylene	Ethanal	Ethanol	Acetone	2-Propenal
650	0.00E+00	0.00E+00	0.00E+00	0.00E+00	0.00E+00
675	0.00E+00	0.00E+00	4.00E-06	5.34E-06	0.00E+00
700	0.00E+00	0.00E+00	1.55E-05	1.60E-05	0.00E+00
725	4.55E-06	0.00E+00	3.15E-05	3.55E-05	0.00E+00
750	1.04E-05	0.00E+00	7.44E-05	7.91E-05	1.76E-05
775	2.50E-05	7.06E-06	1.28E-04	1.38E-04	5.27E-05
800	6.66E-05	int	2.23E-04	2.60E-04	3.86E-05
825	1.15E-04	3.58E-05	1.87E-04	4.32E-04	2.54E-04
850	1.13E-04	5.60E-05	1.01E-04	4.73E-04	2.09E-04
875	1.78E-04	8.10E-05	1.13E-05	9.68E-04	1.19E-04
900	3.57E-04	int	4.52E-06	1.08E-03	
925	4.83E-04	8.95E-05	0.00E+00	1.09E-03	5.96E-05
950	3.71E-04	2.25E-04	0.00E+00	1.34E-03	4.46E-05
975	4.57E-04	2.36E-04	0.00E+00	1.32E-03	2.61E-05
1000	4.96E-04	1.79E-04	4.71E-06	1.01E-03	2.20E-05
1025	1.05E-04	2.73E-06	0.00E+00	5.65E-05	0.00E+00
1050	1.11E-04	int	0.00E+00	4.49E-05	0.00E+00
1075	1.41E-04	int	0.00E+00	9.51E-05	0.00E+00
1100	7.89E-05	5.65E-06	0.00E+00	8.79E-06	0.00E+00
1125	5.65E-05	0.00E+00	0.00E+00	0.00E+00	0.00E+00
1150	7.14E-06	0.00E+00	0.00E+00	2.89E-06	0.00E+00
1175	2.31E-05	0.00E+00	0.00E+00	0.00E+00	0.00E+00
1200	2.76E-06	0.00E+00	0.00E+00	0.00E+00	0.00E+00

X.4.6 Oxidation of propylene glycol in the JSR



Reactor type	JSR
Temperature (K)	700-1200
Pressure (Bar)	1.067
Residence time (s)	2
Pyrrole inlet mole fraction (-)	0.01
Equivalence ratio	1
Dilution gas	Helium
Data type	Mole fractions (- or ppm when specified)

T (K)	O ₂	CO	CH ₄	CO ₂	H ₂	C ₂ H ₄
600	0.040072	9.42E-06	0	3.673E-05	0	0
625	4.00E-02	3.20E-05	0.00E+00	4.24E-05	6.54E-05	0.00E+00
650	3.99E-02	2.26E-05	0.00E+00	6.40E-05	1.67E-04	0.00E+00
675	3.98E-02	4.90E-05	0.00E+00	1.21E-04	2.17E-04	0.00E+00
700	3.96E-02	6.88E-05	0.00E+00	2.01E-04	1.57E-04	0.00E+00
725	3.85E-02	1.21E-04	0.00E+00	4.00E-04	0.00E+00	0.00E+00
750	4.14E-02	2.78E-04	0.00E+00	5.07E-04	1.21E-04	8.48E-06
775	3.85E-02	5.10E-04	7.63E-05	5.62E-04	2.31E-04	1.74E-05
800	3.84E-02	1.39E-03	2.24E-04	4.33E-04	4.25E-04	8.76E-05
825	3.33E-02	6.53E-03	7.80E-04	7.29E-04	8.01E-04	2.84E-04
850	2.89E-02	1.28E-02	1.75E-03	1.95E-03	1.33E-03	5.39E-04
875	2.55E-02	1.46E-02	2.19E-03	2.89E-03	1.80E-03	6.31E-04
900	2.82E-02	1.51E-02	1.41E-03	3.10E-03	2.08E-03	7.24E-04
925	2.72E-02	1.83E-02	1.04E-03	4.39E-03	2.01E-03	7.70E-04
950	1.80E-02	1.55E-02	6.30E-04	9.62E-03	1.58E-03	3.00E-04
975	1.41E-02	8.06E-03	0.00E+00	1.95E-02	1.57E-03	1.68E-04
1000	1.10E-02	5.00E-03	0.00E+00	2.51E-02	1.13E-03	3.48E-05
1025	1.10E-02	2.63E-03	0.00E+00	2.69E-02	5.56E-04	4.00E-05
1050	9.07E-03	1.88E-04	0.00E+00	2.94E-02	8.42E-04	0.00E+00
1075	8.80E-03	7.53E-05	0.00E+00	2.85E-02	8.09E-04	0.00E+00
1100	1.05E-02	4.24E-05	0.00E+00	3.03E-02	6.63E-04	0.00E+00
1125	8.58E-03	4.66E-04	0.00E+00	3.04E-02	3.82E-04	0.00E+00
1150	1.03E-02	3.58E-05	0.00E+00	3.05E-02	3.62E-04	0.00E+00
1175	9.17E-03	3.77E-05	0.00E+00	3.04E-02	0.00E+00	0.00E+00
1200	9.88E-03	2.69E-04	0.00E+00	3.09E-02	0.00E+00	0.00E+00

T (K)	C ₂ H ₆	C ₃ H ₆	Acetone	Ethanol	Ethanal	2-Propenal
600	0.00E+00	0.00E+00	0.00E+00	0.00E+00	0.00E+00	0.00E+00
625	0.00E+00	0.00E+00	0.00E+00	0.00E+00	0.00E+00	0.00E+00
650	0.00E+00	0.00E+00	4.08E-06	5.18E-06	4.05E-05	0.00E+00
675	0.00E+00	0.00E+00	6.28E-06	7.53E-06	4.33E-05	0.00E+00
700	0.00E+00	3.25E-06	1.41E-05	1.37E-05	1.62E-04	0.00E+00
725	0.00E+00	5.85E-06	3.14E-05	2.92E-05	2.10E-04	0.00E+00
750	0.00E+00	9.09E-06	5.18E-05	4.52E-05	5.46E-04	2.10E-05
775	0.00E+00	1.20E-05	8.79E-05	5.04E-05	9.06E-04	3.70E-05
800	1.18E-05	1.27E-05	2.50E-04	3.48E-05	5.95E-04	4.65E-05
825	6.22E-05	3.41E-05	5.69E-04	1.04E-05	5.72E-04	3.36E-05
850	1.07E-04	3.64E-05	5.36E-04	0.00E+00	2.07E-04	8.79E-06
875	9.79E-05	5.68E-05	6.03E-04	0.00E+00	1.48E-04	1.32E-05
900	1.00E-04	5.00E-05	6.20E-04	0.00E+00	1.64E-04	1.57E-05
925	1.15E-04	4.74E-05	4.13E-04	0.00E+00	8.29E-05	6.91E-06
950	4.76E-05	1.07E-05	1.01E-04	0.00E+00	1.51E-05	0.00E+00
975	0.00E+00	0.00E+00	3.01E-05	0.00E+00	0.00E+00	0.00E+00
1000	0.00E+00	0.00E+00	0.00E+00	0.00E+00	0.00E+00	0.00E+00
1025	0.00E+00	0.00E+00	6.91E-06	0.00E+00	0.00E+00	0.00E+00
1050	0.00E+00	0.00E+00	0.00E+00	0.00E+00	0.00E+00	0.00E+00
1075	0.00E+00	0.00E+00	0.00E+00	0.00E+00	0.00E+00	0.00E+00
1100	0.00E+00	0.00E+00	0.00E+00	0.00E+00	0.00E+00	0.00E+00
1125	0.00E+00	0.00E+00	0.00E+00	0.00E+00	0.00E+00	0.00E+00
1150	0.00E+00	0.00E+00	0.00E+00	0.00E+00	0.00E+00	0.00E+00
1175	0.00E+00	0.00E+00	0.00E+00	0.00E+00	0.00E+00	0.00E+00
1200	0.00E+00	0.00E+00	0.00E+00	0.00E+00	0.00E+00	0.00E+00